

THE CEPHEIDS OF M33: DISTANCE AND
METALLICITY EFFECTS THROUGH SLOAN
FILTERS

Kevin Gah-Jan Tsang

A thesis submitted in partial fulfilment of the requirements of
Liverpool John Moores University
for the degree of
Doctor of Philosophy.
June 2019

Declaration

The work presented in this thesis was carried out at the Astrophysics Research Institute, Liverpool John Moores University. Unless otherwise stated, it is the original work of the author.

While registered as a candidate for the degree of Doctor of Philosophy, for which submission is now made, the author has not been registered as a candidate for any other award. This thesis has not been submitted in whole, or in part, for any other degree.

Kevin Gah-Jan Tsang
Astrophysics Research Institute
Liverpool John Moores University
IC2, Liverpool Science Park
146 Brownlow Hill
Liverpool
L3 5RF
UK

JUNE 18, 2019

Abstract

Cepheids are a class of variable stars that undergo regular pulsations in size and brightness. There exists a strong correlation between the period of pulsation and the average intrinsic brightness of a Cepheid; this correlation is known as the period-luminosity relation, or Leavitt Law. It is this Law that bestows Cepheids their importance as distance indicators on both interstellar and intergalactic scales, enabling accurate distance estimates and studies into galactic structure.

Cepheids are found in many different environments and are therefore imparted with varying levels of metallicity. The difference in Cepheid metallicities may give rise to variations in their observable characteristics, leading to changes in the Leavitt Law. These changes may manifest themselves as a metallicity dependence on the slope or zero-point of the Leavitt Law which, if not accounted for, introduce uncertainties into the resulting distance estimates.

Observational studies of Cepheids have typically used Johnson-Cousin filters. With the advent of large-scale sky surveys using Sloan-band filters, Cepheid studies in Sloan filters will become more prevalent. It is important that there exist baseline Leavitt Laws against which future work can be compared.

This thesis aims to provide Leavitt Laws in Sloan filters and to quantify the effects of metallicity on Leavitt Laws in said filters.

Sloan-band magnitudes were obtained with PSF photometry for over 1.3 million stars in the nearby spiral galaxy M33. Over 1500 Cepheids were identified and Leavitt Laws were empirically derived. The slopes were found to be consistent with semi-empirical

determinations. By adopting the semi-empirical slopes, a mean distance modulus of 24.57 ± 0.06 mag to the system and a reddening of $E(B - V) = 0.144 \pm 0.020$ mag were obtained.

Cepheids were found throughout the disk of M33 and so sample the galaxy's metallicity gradient. Cepheids were binned into galactocentric annuli and a series of Leavitt Laws were constructed to assess the effects of metallicity on the slopes and zero-points. For the slopes, no significant dependence on metallicity was found. For the zero-points, a metallicity effect is seen: metal-rich Cepheids are brighter than metal-poor Cepheids of the same pulsation period. Metallicity corrections of -0.089 ± 0.107 mag/dex in g' , -0.188 ± 0.071 mag/dex in r' , and -0.250 ± 0.080 mag/dex in i' were measured. In Wesenheit indices, the values all cluster around -0.468 mag/dex.

These metallicity parameter values are predicated upon the adoption of a metallicity gradient determined from beat Cepheids. Shallower metallicity gradients derived from HII regions produce unreasonably large corrections, suggesting that the use of chemical abundances derived from such tracers as a proxy for Cepheid metallicity is unreliable.

An independent distance determination to M33 was obtained with the tip of the red giant branch method. An average distance modulus of 24.53 ± 0.11 mag was found, consistent with the value derived from Cepheids.

Publications

In the course of completing the work presented in this thesis, the following papers have been submitted for publication in a refereed journal:

K. G.-J. Tsang, D. Bersier, L. Short, V. Scowcroft, et al.

The Cepheids of M33: Distance and metallicity effects, In prep.

Abbreviations

BSG	Blue Supergiant
CFHT	Canada–France–Hawaii Telescope
CMB	Cosmic Microwave Background
CMD	Colour-Magnitude Diagram
HP	Hertzsprung Progression
INT	Isaac Newton Telescope
LF	Luminosity Function
LMC	Large Magellanic Cloud
LSST	Large Synoptic Survey Telescope
M33	Messier 33
PSF	Point Spread Function
RRL	RR Lyrae
SDSS	Sloan Digital Sky Survey
SMC	Small Magellanic Cloud
SNe	Supernovae
TRGB	Tip of the Red Giant Branch
WFC	Wide Field Camera
WIYN	Wisconsin–Indiana–Yale–NOAO

Acknowledgements

My thanks first and foremost go to my supervisor David Bersier for providing a great deal of insight and support throughout both my master's and PhD projects. His guidance has been invaluable right from the start and all the way through to the end.

Of course, this project would have been impossible without the data. For that, I'd like to extend my thanks to Joel Hartman and collaborators for both their CFHT data and their catalogue of Cepheids. Thanks also go to Vicky Scowcroft and again to David Bersier for the INT data and their reductions, and to Lawrence Short for providing the INT stacks and astrometry.

And, finally, I give my thanks to my parents for always nurturing my sense of curiosity.

The funding for this PhD was jointly provided by the STFC and the LJMU Faculty of Engineering and Technology.

“There is a special sadness in achievement, in the knowledge that a long–desired goal has been attained at last, and that life must now be shaped towards new ends.”

– Arthur C. Clarke, *The City and the Stars*

“These are some of the things that hydrogen atoms do, given fifteen billion years of cosmic evolution.”

– Carl Sagan, *Cosmos*

“AC said, ‘THERE IS AS YET INSUFFICIENT DATA FOR A MEANINGFUL ANSWER.’ ”

– Isaac Asimov, *The Last Question*

Contents

Declaration	ii
Abstract	iii
Publications	v
Abbreviations	vi
Acknowledgements	vii
Contents	ix
List of Tables	x
List of Figures	xi
1 Introduction	1
1.1 A Brief History of Cepheids	1
1.1.1 Discovery	1
1.1.2 Leavitt Law	2
1.1.3 First calibration	2
1.1.4 Hubble’s discovery	3

1.1.5	Mistakes of magnitude	4
1.1.6	Proposed variability mechanisms	4
1.2	Physics of Cepheids	6
1.2.1	Key properties	6
1.2.2	Kappa mechanism	7
1.2.3	Post main-sequence evolution and blue loops	9
1.2.4	Pulsation modes	11
1.2.5	Mass discrepancy	14
1.3	Observed properties of Cepheids	17
1.3.1	Wavelength dependence	17
1.3.2	Hertzsprung Progression	18
1.3.3	Phase lag	18
1.3.4	Break in linearity	20
1.3.5	Theoretical and observed metallicity effects	22
1.4	Using Cepheids	23
1.4.1	Mathematical derivation of the PL relation	23
1.4.2	The Leavitt Law	25
1.4.3	The Baade–Wesselink method	25
1.4.4	Period-Age relation	27
1.4.5	Beat Cepheids as metallicity tracers	28
1.5	The Cosmic Distance Ladder	29
1.5.1	Parallax	30

1.5.2	Cepheids	32
1.5.3	Tip of the Red Giant Branch	32
1.5.4	Tully–Fisher relation	34
1.5.5	Type Ia supernovae	36
1.5.6	Hubble constant	37
1.6	Aims of this thesis	38
Introduction		1
2 The Triangulum Galaxy		40
2.1	Basic properties	40
2.1.1	Stellar distance estimates to M33	42
2.1.2	Metallicity gradients	42
3 Photometry and calibration		48
3.1	Image data	48
3.1.1	CFHT images	48
3.1.2	INT images	52
3.2	PSF photometry	53
3.2.1	SExtractor+PSFEx procedure	54
3.2.2	Aperture corrections	63
3.3	Calibration	64
3.3.1	INT	65
3.3.2	CFHT	69

4	Leavitt Laws	75
4.1	Identifying the Cepheids	75
4.2	Deprojection	80
4.3	Wesenheit magnitudes	83
4.4	Theoretical and semi-empirical Sloan-band Leavitt Laws	85
4.5	Empirical Leavitt Laws and the distance to M33	86
4.5.1	The $[Z] = [Z]_{\text{LMC}}$ Cepheid Sample	87
4.5.2	Creating and comparing period-Wesenheit relations	95
4.6	Effects of metallicity on the period-luminosity relation	100
4.6.1	Slopes	100
4.6.2	Zero-points	106
4.6.3	Metallicity correction values	113
4.6.4	Period-luminosity-metallicity relations	118
4.7	Predicting Wesenheit metallicity parameters	120
4.8	Wavelength dependency	120
5	Tip of the Red Giant Branch	124
5.1	Locating the tip	125
5.2	TRGB distances	127
6	Conclusions	135
6.1	Summary	135
6.2	M33 metallicity gradient	137

6.3 Outlook	138
A CFHT calibration solutions	140
Bibliography	144

List of Tables

2.1	Basic properties of M33.	40
2.2	Stellar M33 distances and adopted LMC distances.	43
2.3	A list of M33 metallicity gradient measurements in the literature, including the type of metallicity that is measured, the tracer that was used, and the adopted distance to M33.	47
3.1	Hartman Cepheid catalogue sample	50
3.2	CFHT stacks properties	51
3.3	Calibration solutions for the INT chips.	67
4.1	Semi-empirical and theoretical Sloan-band Leavitt Laws	86
4.2	Sloan band Leavitt Laws using M33 Cepheids with LMC metallicity.	92
4.3	Apparent distance moduli, extinctions and extinction-corrected distance moduli in the Sloan bands.	94
4.4	Predicted semi-empirical Sloan-band period-Wesenheit relations for LMC Cepheids.	96
4.5	Sloan-band period-Wesenheit relations using M33 Cepheids with LMC metallicity.	98

4.6	Distance moduli in various bands determined from Cepheids of LMC metallicity in M33.	99
4.7	Changes in observed distance modulus against galactocentric radius. .	108
4.8	Metallicity correction values for various metallicity gradients.	115
4.9	Sloan-band Leavitt Law terms with metallicity corrections for Cepheids in M33.	119
4.10	Metallicity parameters from several studies using multi-band data . .	123

List of Figures

1.1	First Leavitt Law plots	3
1.2	Partial ionisation zones	8
1.3	Post main-sequence track of $5M_{\odot}$ star	9
1.4	Cepheid internal standing waves	12
1.5	Light curves for fundamental mode and overtone mode Cepheids	13
1.6	Using Fourier parameters to distinguish Cepheids	14
1.7	Evolutionary tracks for intermediate mass stars	16
1.8	Cepheid light curves at various wavelengths	17
1.9	Observed pulsation curves for delta Cephei	19
1.10	Breaks in Leavitt Law linearity	21
1.11	Baade–Wesselink method	27
1.12	Petersen diagram	29
1.13	Parallax method	30
1.14	Cepheids detected by Gaia	31
1.15	Locating the tip of the red giant branch	34
1.16	Tully–Fisher relation	35

2.1	The Triangulum Galaxy	41
2.2	Petersen diagram with M33, Galactic and Magellanic beat Cepheids	44
2.3	Beat Cepheid deprojection	45
2.4	Updated beat Cepheid data	46
3.1	Sloan-band Cepheid light curves	49
3.2	Stacked sky-subtracted, r' -band CFHT image of M33.	51
3.3	CFHT MegaCam and INT WFC chip configurations	52
3.4	Background map	56
3.5	Mexican hat kernel	57
3.6	SExtractor's deblending procedure	58
3.7	PSF stars	60
3.8	PSFEx PSF model	60
3.9	PSF model subtraction	61
3.10	Number of stars detected and chosen for PSF modelling	62
3.11	Comparing PSF magnitudes	63
3.12	Sloan filters	64
3.13	INT residual magnitude radial dependence	66
3.14	LS stack r' versus $g' - r'$ CMD	68
3.15	LS stack i' versus $r' - i'$ CMD	68
3.16	Common CFHT chip regions in stacked images	69
3.17	Stars on CFHT MegaCam CCDs	70
3.18	CFHT stack r' versus $g' - r'$ CMD	71

3.19	CFHT stack i' versus $r' - i'$ CMD	72
3.20	Available SDSS data for M33	73
3.21	Comparisons between SDSS and calibrated CFHT stack magnitudes	74
4.1	Cepheids from Pellerin & Macri 2011	77
4.2	Cepheid matches from CFHT stack	78
4.3	CMD of Cepheids	79
4.4	Cepheids coloured by SExtractor flag value	80
4.5	Spatial distribution of Cepheids	82
4.6	Radial distribution of Cepheids	82
4.7	Sloan-band extinction ratios	85
4.8	Locating the LMC-metallicity Cepheids in M33	88
4.9	I -band amplitude distributions	89
4.10	Period distributions	90
4.11	Sloan-band period-luminosity relations of Cepheids in M33	91
4.12	Comparison between empirical and predicted slopes	92
4.13	Apparent distance moduli vs total-to-selective extinction ratios in the Sloan bands	94
4.14	Collection of M33 distances	95
4.15	Fitted period-Wesenheit relations	97
4.16	Slopes from empirical and predicted period-Wesenheit relations	98
4.17	Cepheid distance estimates for M33	99
4.18	Variations in slopes with galactocentric radius	103

4.19	Variations in slope with galactocentric radius from non-contaminated Cepheids	104
4.20	Changes in Leavitt Law slopes between fitting all Cepheids and using only isolated Cepheids	105
4.21	Period distributions of LMC Cepheids and Cepheids at the centre of M33	106
4.22	Variations in observed distance modulus with galactocentric radius	107
4.23	Reddening across M33	109
4.24	Variations in observed distance modulus with galactocentric radius with isolated Cepheids	112
4.25	Comparing gradients in distance modulus	113
4.26	Metallicity parameter curves	114
4.27	Comparison of measured γ values	121
4.28	Metallicity corrections against wavelength	122
5.1	TRGB magnitudes in Sloan bands	125
5.2	TRGB region	126
5.3	RGB metallicity gradient	127
5.4	Binned TRGB distances	129
5.5	TRGB response function heatmap	130
5.6	TRGB response function heatmap with distance moduli	131
5.7	Response functions and fitted Gaussians	132
5.8	TRGB distance against galactocentric radius	134

Chapter 1

Introduction

1.1 A Brief History of Cepheids

1.1.1 Discovery

Cepheids are an important class of variable stars that regularly pulsate in brightness and were among the first variables to be discovered. Cepheids inherit their name from the variable star designated δ Cephei located in the constellation of Cepheus. The variability of δ Cephei was first suspected by John Goodricke on the night of October 20th, 1784; three days later, he would write, “I am now *almost* convinced that δ Cephei varies.” (Hoskin, 1979). Interestingly, δ Cephei was not the first Cepheid to be discovered; that title belongs to η Aquilae, whose variability was observed a month earlier by Edward Pigott, a mentor and collaborator of Goodricke.

In the two and a half centuries since their discovery, Cepheids have played a pivotal role in many disparate fields of astronomy and astrophysics. From the physics of stars, the histories and dynamics of galaxies, and to the scale of the Universe itself, Cepheids have — and continue — to further our understanding of the most ancient of sciences.

1.1.2 Leavitt Law

It would take more than a century before the Cepheids' variable nature progressed from being an interesting curiosity to being a powerful tool to determine distances on interstellar and intergalactic scales by way of the famous period-luminosity (PL) relation, or Leavitt Law. The first hints of the potential of Cepheids were noted by [Leavitt \(1908\)](#) in a study of variable stars in the Magellanic Clouds. In her paper, periods for 16 variables in the Small Magellanic Cloud (SMC) were recorded against their magnitudes. An intriguing correlation between the periods and magnitudes was evident and Leavitt concisely remarked, "It is worthy of notice that...the brighter variables have the longer periods." However, she was reluctant to draw general conclusions as the sample size was small.

She and her supervisor Edward Charles Pickering later expanded upon and reinforced this relation ([Leavitt and Pickering, 1912](#)). With periods for 25 SMC Cepheids, they explicitly showed the existence of a relation between period and luminosity. A plot of the Cepheid magnitudes against the logarithm of their periods clearly reveals a linear correlation between the two quantities: the brighter the Cepheid, the longer its pulsation period (see [Figure 1.1](#)). They state, "Since the variables are probably at nearly the same distance from Earth, their periods are apparently associated with their actual emission of light." They also notice the similarity between the light curves of these SMC variables with variables in the Galaxy and write, "It is to be hoped, also, that the parallaxes of some variables of this type may be measured."

1.1.3 First calibration

A year later, [Hertzsprung \(1913\)](#) took on the parallax challenge. He would determine the parallaxes — hence, distances — of 13 Cepheid variables in the Galaxy, and arrive at the following Leavitt Law,

$$\langle M_V \rangle = -2.1 \log P - 0.6$$

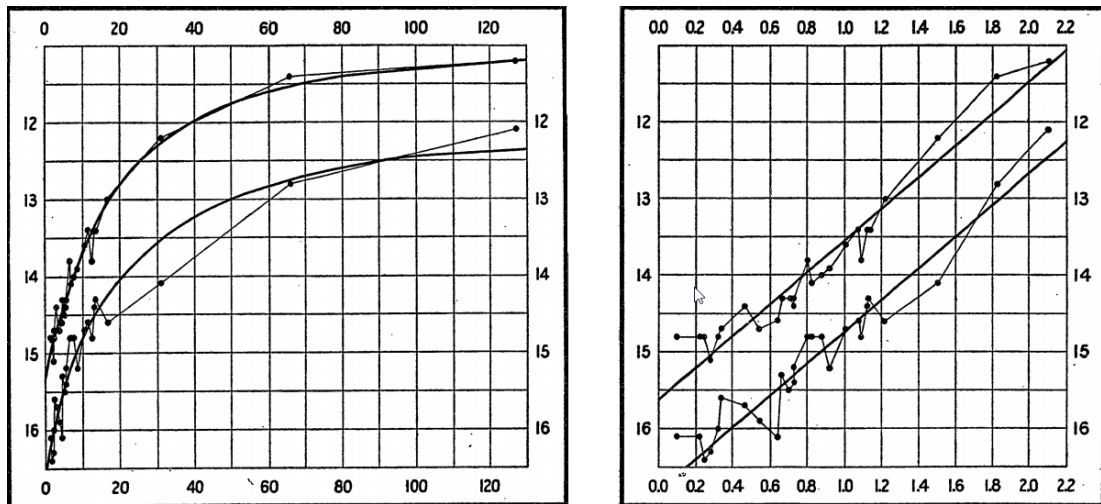


Figure 1.1: Leavitt’s plots of Cepheid maximum and minimum magnitudes against their pulsation periods. Left shows period linearly, right shows period logarithmically. Figure from [Leavitt and Pickering \(1912\)](#).

where $\langle M_V \rangle$ is the mean absolute V-band magnitude and P is the period measured in days. With his PL relation and Leavitt’s results, he would have derived a distance of 30000 light years (~ 9200 pc) to the SMC. Unfortunately — possibly due to a misprint or miscalculation — a value of 3000 light years (~ 920 pc) was presented in his paper instead ([Gautschy, 2003](#)). Regardless, Hertzsprung had pioneered the use of Cepheids to determine astronomical distances and, in fact, the use of the term “Cepheid” ([Ferne, 1969](#)). Had Hertzsprung decided differently, these pulsating variables could potentially have been dubbed “Aquilids” instead.

1.1.4 Hubble’s discovery

Just over a decade later, [Hubble \(1925\)](#) found Cepheids in two fuzzy spiral nebulae by their characteristic variability. Using the Leavitt Law, he would arrive at distances close to a million light years (~ 300 kpc) to the two “nebulae”. The vast distances to these systems conclusively placed them beyond the Milky Way, dispelling the notion that the Universe comprises only our Galaxy. Those two spiral “nebulae” are the local spiral galaxies M31 (Andromeda Galaxy) and M33 (Triangulum Galaxy). Modern estimates place these two galaxies at distances of ~ 2.5 million light years (~ 770 kpc). The factor of ~ 2 difference between Hubble’s determinations and modern values is a

symptom of a major oversight in the early determinations of the Leavitt Law.

1.1.5 Mistakes of magnitude

The historically accepted Leavitt Laws developed by Hertzsprung and others like Harlow Shapley suffered from an unfortunate offset of ~ 1.5 magnitudes towards the fainter direction; this offset arose primarily from neglecting the dimming effect of interstellar extinction and the effects of galactic rotation on geometric measurements. By coincidence, the intrinsic brightness of a fundamental mode¹ Population I (Classical) Cepheid is ~ 1.5 magnitudes brighter than a Population II (Type II) Cepheid of the same period. As a result, the inherently dimmer Type II Cepheids were incorporated into the Leavitt Laws with little suspicion.

The conflation of the two populations of Cepheids in the Leavitt Law would eventually be resolved by Walter Baade in the late 1940s (Osterbrock, 1998). With the recently discovered distinction between Population I and II stars and observations of the variables in the Andromeda Galaxy, Baade concluded that the Classical Cepheids of Population I should be 1.5 magnitudes brighter than the Type II Cepheids of the same period. This correction was applied to the Leavitt Law, the consequence of which was to double the distances to Classical Cepheids and the systems in which they reside, leading to the apocryphal statement: “The Lord made the universe — but Baade doubled it.”

1.1.6 Proposed variability mechanisms

Eight months after his discovery of the variability of the Cepheid prototype δ Cephei, Goodrick wrote to the Royal Society with his findings and a hypothesis on the origin of the observed variability. He suggested that the variability of δ Cephei was caused by fixed dark spots on its stellar surface which would result in periodic dimming as the star rotated on its axis (Hoskin, 1979). Curiously, for Algol (a non-Cepheid variable

¹(see Section 1.2.4)

star) he suggested another mechanism. He attributed Algol's variability to it being a two-body system, with eclipses causing the dimming.

A later and long-lasting theory attributed the variability of Cepheids to stellar binarity, where eclipsing events caused the observed dimming. The binary hypothesis was staunchly defended up until the 1930s despite mounting evidence to the contrary (Gautschy, 2003). The colour of a Cepheid varies over each cycle, changing its spectral type. Minor bumps and asymmetries in Cepheid light curves were accounted for by introducing complex orbital configurations of several star systems — reminiscent of Ptolemy's epicycles. Spectroscopic studies of Cepheids did not reveal the existence of more than one stellar signature. These drawbacks to the binary hypothesis were noted by Shapley (1914), who detailed his misgivings towards the accepted theory. Shapley presented an alternative explanation: the variations are intrinsic to the Cepheids themselves through some kind of internal pulsation mechanism, though he did not elaborate on it.

The first studies into stellar pulsation were undertaken by Ritter (1878). He considered gaseous spheres of constant density undergoing radial pulsations and arrived at a period-density relation: the pulsation period is proportional to the inverse square-root of the density. He postulated that the observed changes in the brightness of variables were intrinsic to the stars themselves through such radial pulsations and that they too follow a period-density relation.

Eddington (1926) expanded upon the intrinsic pulsation hypothesis by considering an engine-like mechanism as the driver of the pulsations. His key insight would be to assign a *variable transparency* to the stellar material as a means to modulate the energy flux. He also brought doubts to the idea that stellar contraction was the supposed energy source of stars according to the virial theorem. He reasoned that if stellar contraction were indeed the energy source of stars (and therefore the pulsations in Cepheids) then the increasing mean density of an evolving, contracting Cepheid would be observable as a change in its period via Ritter's period-density relation. The veracity of Eddington's valve-like mechanism would later be proven (see Section 1.2.2).

1.2 Physics of Cepheids

As this thesis is focused on Population I Classical Cepheids, they will be referred to simply as Cepheids for brevity.

1.2.1 Key properties

Cepheids are young, bright, intermediate to high-mass stars ($3\text{--}12 M_{\odot}$) in the post main sequence stage, fusing helium in their cores². Their ages are in the ~ 100 million year range. They undergo radial pulsations that give rise to their characteristic oscillations in observed brightness; these oscillations are extremely regular with periods that range from less than a day to several months. As mentioned earlier, there exists a correlation between the pulsation period of a Cepheid and its mean magnitude. This is the famous period-luminosity relation or Leavitt Law.

Cepheids belong to an important family of astrophysical objects whose intrinsic brightness is known or can be determined using other parameters. Objects like Cepheids occupy rungs on the *cosmic distance ladder*, a series of methods to determine distances to progressively more distant celestial objects. Cepheids rely upon accurate calibrations of their Leavitt Laws to provide reliable distance estimates. As discussed in the history section, this was first achieved through parallax measurements of Cepheids. In the same vein, the rungs representing type Ia supernovae, the Tully-Fisher relation and other methods on the cosmic distance ladder depend upon reliable Cepheid Leavitt Laws for calibration.

There exists a narrow, near-vertical region on the Hertzsprung-Russell (HR) diagram spanning a small range in temperature that is referred to the instability strip. Stars residing in this strip are unstable to pulsations because of the location of the partial helium ionisation zone in relation to the low-density outer zone and the heat-dense inner zone. Many classes of variable stars are found in this strip: Cepheids, RR Lyrae

²The mass of a Cepheid progenitor is sufficiently high to avoid the development of a degenerate core, which would otherwise have led to a Helium Flash — a rapid runaway fusion reaction in the core.

stars, and δ Scuti stars are a few examples ([Carroll and Ostlie, 2007](#)).

1.2.2 Kappa mechanism

The partial helium ionisation zone is the source of the pulsations observed in Cepheids. The helium in this zone is partially ionised in the He II state, permitting the opacity of the region to increase under compression. This is the physical realisation of Eddington's *variable transparency* mechanism.

When under compression, the layers of a Cepheid undergo an increase in density and temperature which in most cases will result in a decrease in opacity according to Kramers' opacity law

$$\kappa \propto \rho T^{-3.5} \quad (1.1)$$

where κ represents opacity, ρ is density, and T is temperature and is also dominating term. In order for the opacity of a region to increase when compressed, special conditions are necessary.

In the partial ionisation zone, the act of compression increases the density of the region while the work done by compression will mostly be expended in the ionisation of the helium content rather than in the raising of the temperature. The increase in density outweighs the small rise in temperature, leading to an increase in the opacity of the zone. With the increase in opacity, more radiation is trapped in the zone and the internal pressure rises. The zone expands and elevates the material above it, causing the Cepheid to swell. As the Cepheid expands, the density of the partial ionisation zone decreases and the helium ions recombine with the free electrons; the temperature decrease during this phase is smaller than expected because of the release of energy from recombination processes. The decrease in density leads to the decrease in opacity and so radiation passes through the zone more freely and the internal pressure of the region drops. Gravity eventually halts and reverses the expansion and the Cepheid contracts once more, repeating the cycle ([Carroll and Ostlie, 2007](#)).

The cycling between opacity and transparency of the partial ionisation zone — allowing the build up and subsequent dissipation of energy — is the fundamental mechanism driving the variations in brightness, radius and other observables. This process is referred to as the Eddington valve or κ -mechanism. Large-scale pulsations generated by the κ -mechanism are permitted for a narrow range of effective temperature, defining the location and shape of the instability strip on the HR diagram. At too high an effective temperature ($T_{\text{eff}} > 7500$ K), the partial ionisation zone is too close to the surface for significant pulsation to take place as the density of available material is too low. At too low temperatures ($T_{\text{eff}} < 5500$ K), the zone is close to the core and convection processes dominate as the energy transfer mechanism, acting to dampen pulsations that occur (Carroll and Ostlie, 2007). Figure 1.2 shows the locations of these zones in the three cases.

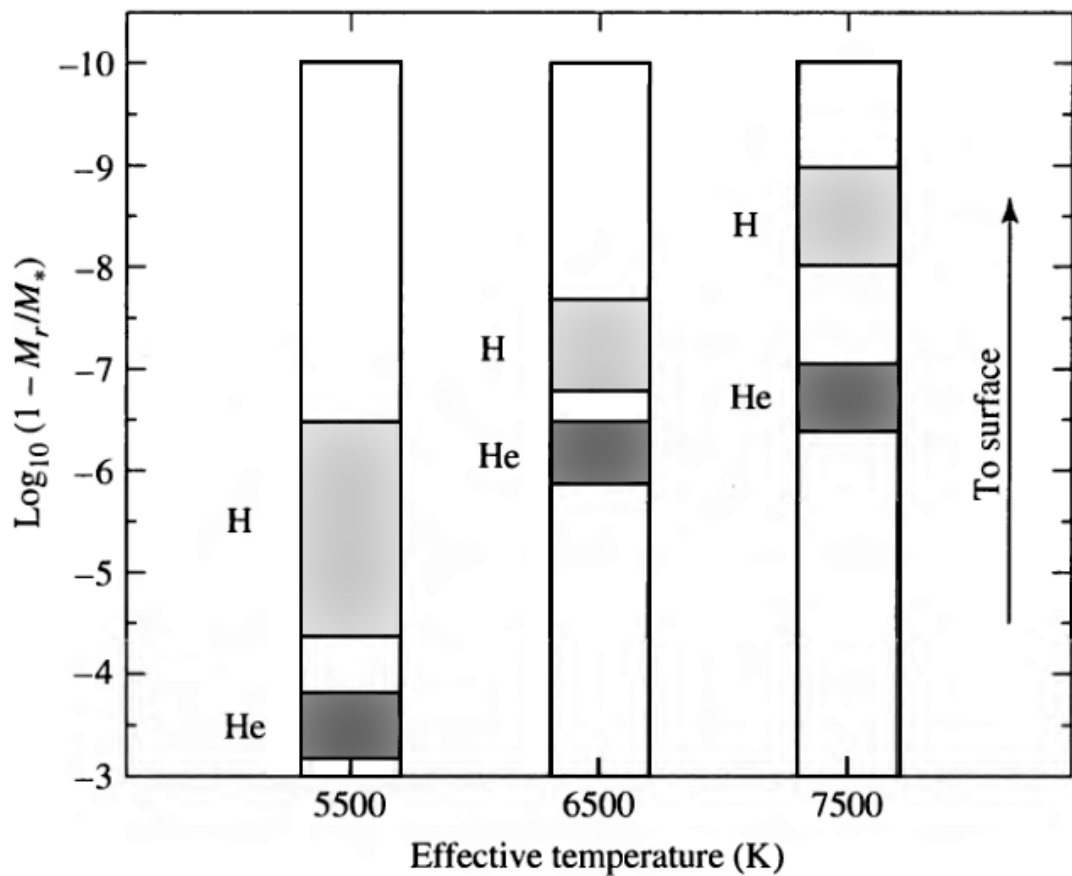


Figure 1.2: The locations of the partial ionisation zones for hydrogen and helium in stars of different effective temperatures. The locations of the zones vary with effective temperature. Figure from Carroll and Ostlie (2007).

1.2.3 Post main-sequence evolution and blue loops

Figure 1.3 shows the evolutionary track of a $5 M_{\odot}$ star along with the approximate location of the instability strip. The track crosses the instability strip multiple times. It is only during these crossings when the star becomes unstable to pulsations, meaning that Cepheids are transient phenomena. For the following section, the evolution of a star of mass $5 M_{\odot}$ will be examined.

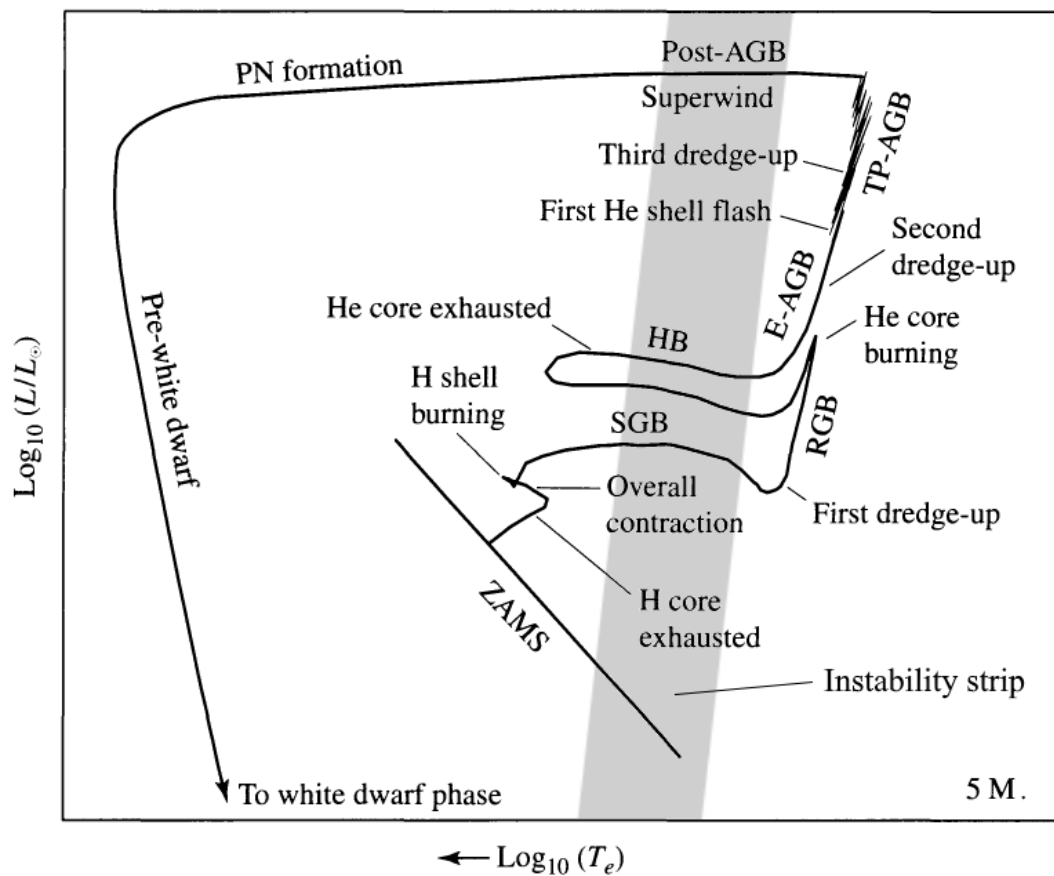


Figure 1.3: Post main-sequence evolutionary track of a $5 M_{\odot}$ star with the approximate location of the instability strip superimposed. Adapted from [Carroll and Ostlie \(2007\)](#).

When the core of the progenitor is depleted of hydrogen — leaving behind a core of inert helium — the entire star contracts on a thermal timescale. The liberation of gravitational potential energy has the following effects: the luminosity of the star increases slightly, the radius of the star decreases, and the effective temperature rises. The temperature of the hydrogen surrounding the inert helium core will eventually reach the point where fusion can take place, forming a shell of fusing material.

The shell where fusion takes place continuously consumes the hydrogen above the core, supplying the inert core with additional helium. The mass of the core will reach a point — the Schönberg–Chandrasekhar limit — where it becomes too great and cannot support the material above it. The core rapidly contracts and gravitational energy is released, causing the stellar envelope to expand and cool. This is the sub-giant branch phase and is represented by the red-ward path labelled SGB on the HR diagram (see Figure 1.3). It is during this phase when the post-main sequence, intermediate mass star is first unstable to pulsations as it crosses the instability strip. The star is now in its first Cepheid phase. The timescale on which this process takes place is very short in relation to other evolutionary stages; therefore, very few stars will be observed undergoing this phase. The expected fraction of Cepheids making their first crossing of the instability strip is around one per hundred (Poleski, 2008). The famous star Polaris is suspected to be such a first-crossing Cepheid (Anderson, 2018).

With the expansion and cooling of the stellar envelope, the Cepheid phase terminates and an extensive convection zone forms, joining the near-surface of the star with its deep interior. The efficiency of energy transport from the hydrogen-burning shell to the surface increases, and the luminosity of the star grows drastically, taking it up the red-giant branch (RGB section in Figure 1.3).

At the tip of the RGB, the central density and temperature of the star are sufficient to initiate helium fusion with the aid of quantum tunnelling to overcome electrostatic repulsion. The rate of energy production via helium fusion in the core is strongly sensitive to temperature and the core expands, pushing the hydrogen-fusing shell above it outwards. The shell cools and its energy production rate drops slightly, resulting in a sudden decrease in the star's luminosity and the contraction of the stellar envelope which raises the effective temperature. The path of the star along the RGB reverses.

The star travels horizontally blue-ward on the HR diagram during the helium-core fusing stage. This is the second crossing of the instability strip and the start of the *blue loop*. The star is once again unstable to pulsations and reprises its role as a Cepheid. The star continues to travel horizontally towards higher temperatures until the helium fraction in the core is $Y \sim 0.5$. The core contracts and the stellar envelope expands

and cools again, decreasing the energy output of the hydrogen shell, bringing the star back towards the red side of the HR diagram. The helium content available for fusion in the core is ultimately exhausted; helium continues to burn in a shell surrounding the core of inert helium-fusion products — namely carbon and oxygen. During this process, the star continues its red-ward path, finishing the blue loop.

For the $5 M_{\odot}$ star, the blue loop is a long lasting phase. The helium-core fusing phase lasts $\sim 20\%$ of the hydrogen-core fusing lifetime — or roughly 15 million years. An important consequence of the longevity of the blue loop and its juxtaposition with the instability strip is that a considerable number of post-main-sequence stars of intermediate mass are observed to pulsate as Cepheids.

1.2.4 Pulsation modes

The radial pulsation of a Cepheid can be considered to be a standing acoustic wave of stellar material; the core acts as a stationary node and the surface as an antinode. This configuration is not dissimilar to an organ pipe with a closed end where air does not move and an open end where air undergoes maximum displacement. An organ pipe with air oscillating in the fundamental mode contains a standing wave with a single node at the closed end; all the non-stationary air moves in the same direction. For first overtone oscillations, a node exists between the closed and open ends; air on either side moves in opposing directions. Higher overtones introduce more nodes. Like organ pipes, some Cepheids possess one or more nodal surfaces between the centre and the outer surface, resulting in overtone mode pulsations (see Figure 1.4). The majority of Cepheids pulsate in the fundamental mode (F). Overtone mode (O1, O2, etc) Cepheids with more than one nodal surface are progressively rarer.

For a given pulsation period shorter than ~ 8 days, O1 Cepheids are brighter than their F Cepheid counterparts by ~ 1 mag in optical bands (Beaulieu et al., 1995). Cepheids with periods longer than ~ 8 days do not undergo overtone mode pulsations (Pellerin and Macri, 2011).

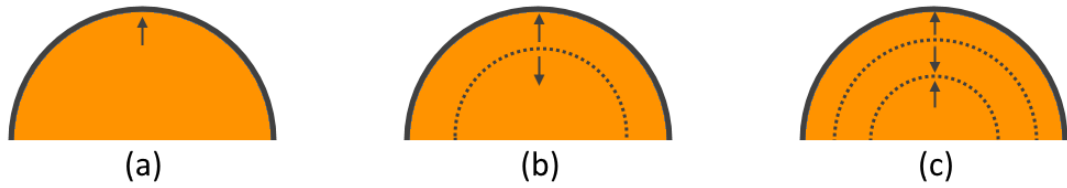


Figure 1.4: Cepheid standing wave configurations for (a) fundamental, (b) first overtone, and (c) second overtone pulsation modes. Dashed lines are the nodal surfaces and arrows represent the relative motions of stellar material.

Fundamental mode Cepheids generally produce asymmetric light curves with relatively large amplitudes. Overtone mode Cepheids, meanwhile, typically exhibit near-symmetric, sinusoidal light curves with small amplitudes. Cepheids with symmetric, sinusoidal and small-amplitude light curves have historically been referred to as s-Cepheids; some s-Cepheids, however, are actually fundamental mode pulsators and, conversely, some fundamental mode Cepheids show small amplitude variations (Klagyivik and Szabados, 2009). Figure 1.5 shows the light curves of Cepheids of varying periods and modes of pulsation. In the fundamental mode panel, the effects of the Hertzsprung progression are visible (see Section 1.3.2). To unequivocally determine a Cepheid's pulsation mode, more metrics than just the shape of its light curve are needed.

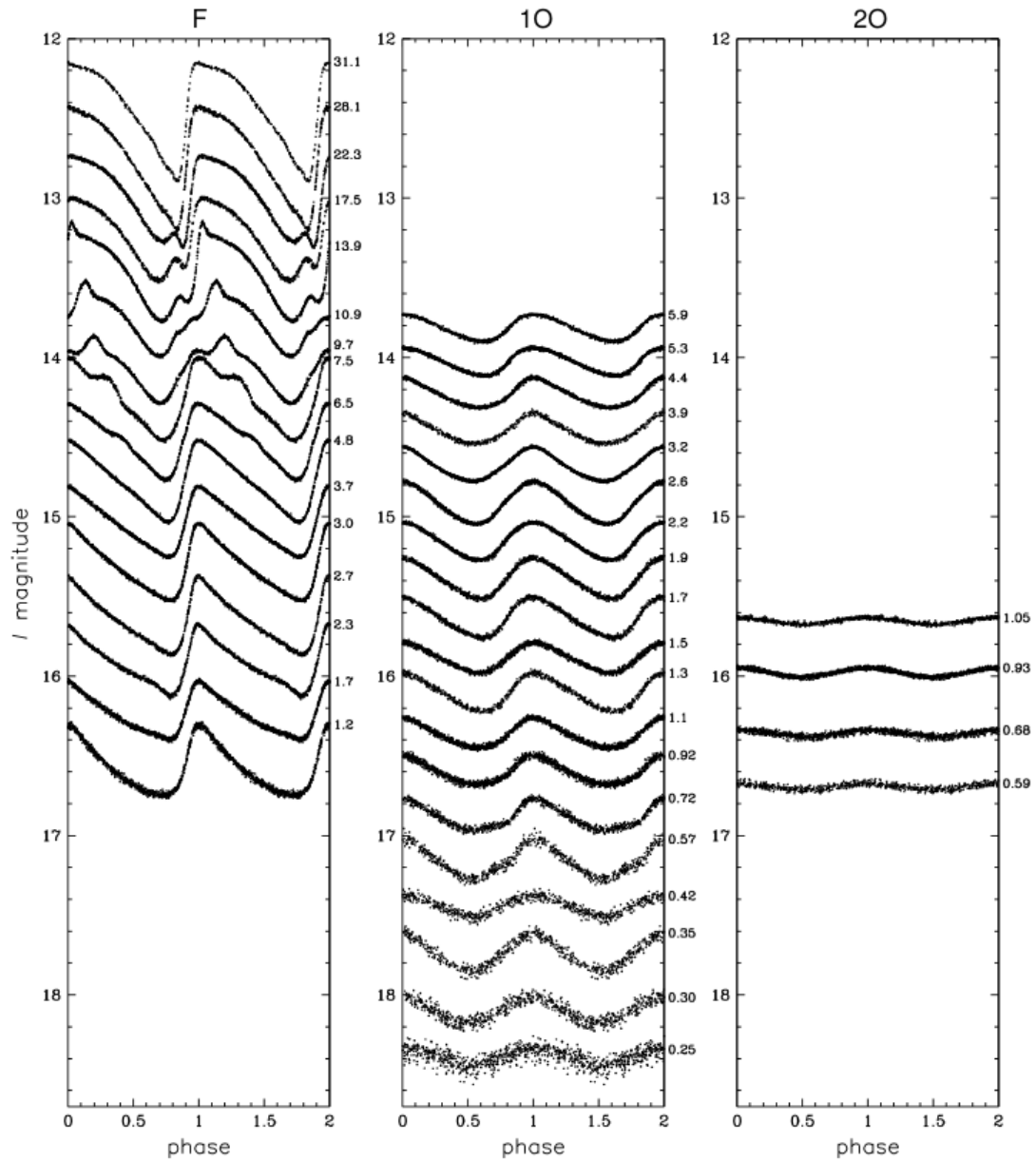


Figure 1.5: *Left*: Light curves for F Cepheids. *Centre*: Light curves for O1 Cepheids. *Right*: Light curves for O2 Cepheids. The Hertzsprung progression is visible in the F-mode light curves. Figure from [Soszynski et al. \(2008\)](#).

To reliably classify Cepheids in terms of pulsation mode, Fourier decomposition of their light curves is the method of choice. The magnitude variations of a Cepheid are fitted with the Fourier series

$$m(t) = A_0 + \sum_{i=1}^N A_i \cos(2\pi i(t - T_0)/P + \phi_i) \quad (1.2)$$

where $m(t)$ is the Cepheid magnitude at time t , A_0 is the average magnitude, A_i is the i th amplitude term, P is the pulsation period, and ϕ_i is the i th phase term. The key Fourier parameters A_i and ϕ_i are extracted for Cepheid classification.

Antonello et al. (1990) found two quantities that, when plotted against the pulsation period, can be used to distinguish between Cepheids with typical asymmetric light curves and s-Cepheids. Plots of $R_{21} = A_2/A_1$ and $\phi_{31} = \phi_3 - 3\phi_1$ against pulsation period separate these two classes of Cepheids into different sequences (see Figure 1.6).

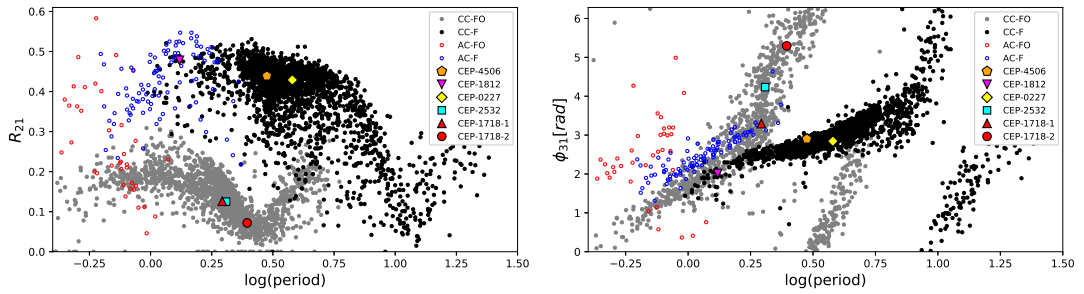


Figure 1.6: *Left:* R_{21} vs period. *Right:* ϕ_{31} vs period. Black points are F Cepheids and grey points are O1 Cepheids and the two populations are clearly separated. Figures are from Pilecki et al. (2018).

1.2.5 Mass discrepancy

For the past 40 years, there has been a significant discrepancy in the theoretical masses of Cepheids when estimated through either stellar evolution models or stellar pulsation models. For a Cepheid with a given luminosity and effective temperature, stellar evolution models predict a mass that is larger by 10–20% than a mass derived from stellar pulsation models.

With the stellar positions reported by the HIPPARCOS and Gaia missions and by searching for anomalies in their proper motions, (Kervella et al., 2019) identified a sample of Milky Way Cepheids with close-by orbiting companions. In their study, they estimate a binary fraction of $\sim 80\%$ for Cepheids. However, only a handful of Cepheids have been identified as part of eclipsing binary systems and have had their masses determined through the analysis of their orbital dynamics (Neilson et al.,

2011). The dynamic masses agree well with pulsation models; masses inferred from stellar evolution models are therefore overestimates of the true mass.

The inability of stellar evolution models to accurately predict the mass of a Cepheid suggests that there are physical processes that have not been considered or incorporated into the models. Various mechanisms have been proposed to explain the discrepancy: these include introducing convective core overshooting in the Cepheid's progenitor during its main-sequence phase (Chiosi et al., 1992), pulsation-driven mass loss during the Cepheid stage of evolution (Neilson et al., 2011), and rotational mixing (Anderson et al., 2014).

Convective core overshooting introduces extra hydrogen into the core during the main sequence. Convective cells in the core retain momentum as they cross beyond the boundary of the convective zone, mixing material from the upper stable layer into the core. The core's hydrogen reserves are continuously topped up, leading to a more massive helium core once the star leaves the main sequence to become a Cepheid. This has the effect of making the Cepheid more luminous or equivalently results in a Cepheid of lower mass mimicking a brighter Cepheid of higher mass with no convective core overshooting (Rosenfield et al., 2017).

Pulsation-driven mass loss allows a Cepheid to lose mass while maintaining the same luminosity. The total amount of mass that is lost depends strongly upon the longevity of the Cepheid phase. Neilson et al. (2011) find that mass loss due to pulsations alone is not enough to fully account for the discrepancy; a contribution from a small amount of convective core overshooting is sufficient to account for the offset.

The effects of rotation in Cepheids have largely been disregarded under the impression that since Cepheids are giant stars, they would rotate slowly, leading to negligible consequences. However, Cepheid progenitors (B-type stars) have been observed to be fast rotators. Rapid rotation leads to an increase in the size of the progenitor's core and to the extension of the progenitor's main-sequence lifetime through the mixing of hydrogen from outer layers into the core. Like convective core overshooting, Cepheids whose progenitors rapidly rotated have a higher luminosity than their mass would dic-

tate. Unlike overshooting, progenitor rotations provide many testable predictions. [Anderson et al. \(2014\)](#) show that rotation is sufficient to explain the mass discrepancy without the need to invoke convective core overshooting or pulsation-driven mass loss. A consequence of introducing convective core overshooting and stellar rotation is the suppression of the blue loops that occur post-helium core ignition and that intersect with the instability strip. For stars less massive than $5 M_{\odot}$, the suppression is enough to prevent the loop from entering the instability strip, averting the stars' Cepheid phases (see [Figure 1.7](#)) ([Evans et al., 2018](#)). The cause of the mass discrepancy has yet to be fully resolved though it is likely that it may be due to a mixture of the mechanisms discussed thus far.

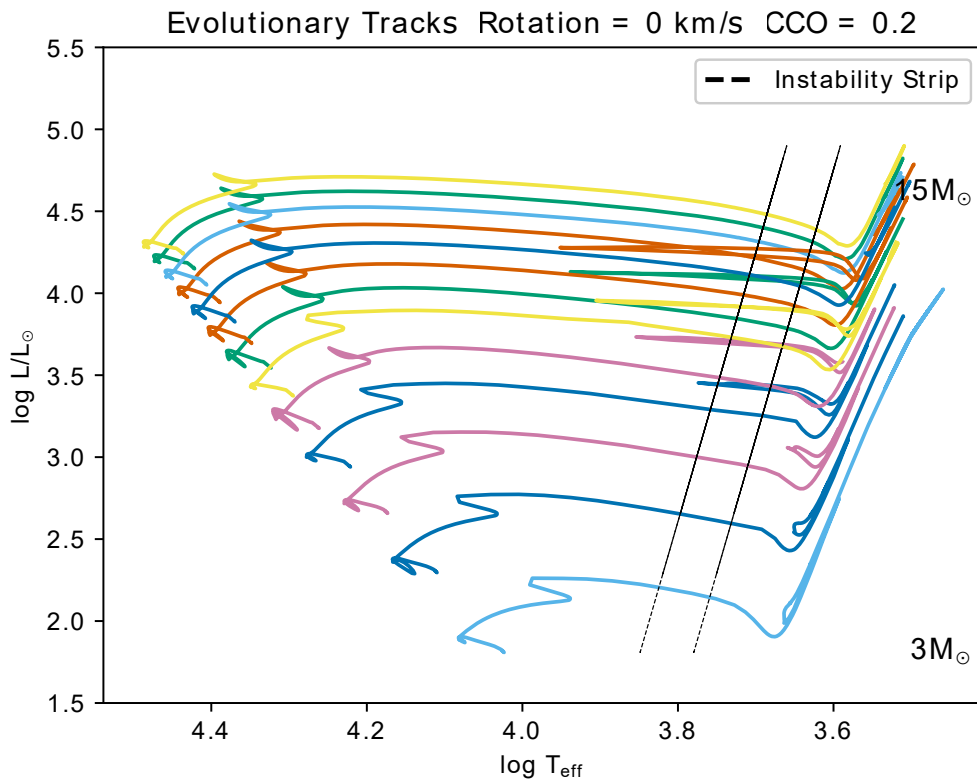


Figure 1.7: Computed post main-sequence stellar evolution tracks for stars of various masses with moderate convective core overshooting and no rotation. Figure from [Miller et al. \(2018\)](#).

1.3 Observed properties of Cepheids

1.3.1 Wavelength dependence

The light curves of Cepheids are very regular with a sharp rise to maximum brightness then a slow decline to the minimum in the optical and shorter wavelengths. The amplitudes of the brightness variations are sensitive to the Cepheid's period and the wavelength at which the measurements are made; the amplitudes decrease monotonically with increasing wavelength (Bhardwaj et al., 2015). The shape of the light curve also becomes more symmetric and sinusoidal towards redder wavelengths (see Figure 1.8).

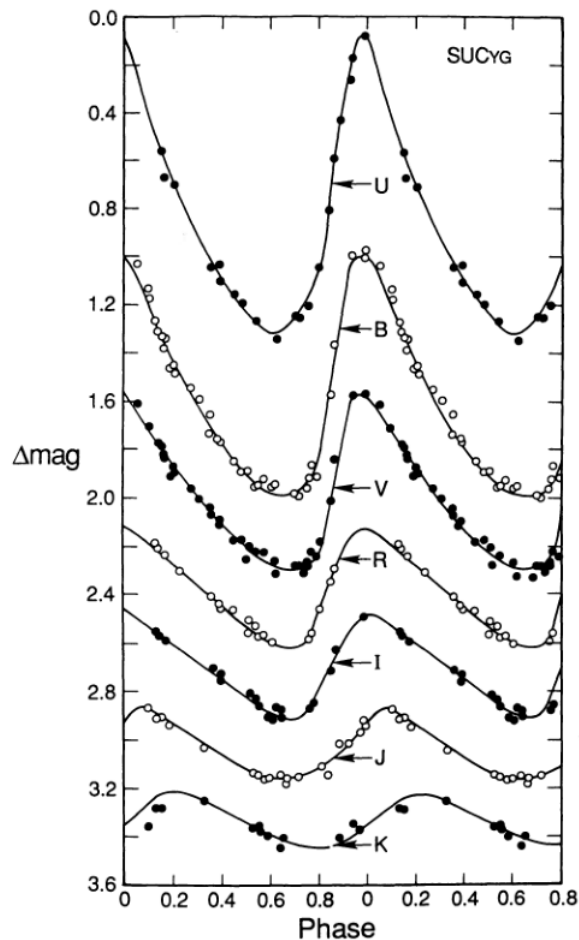


Figure 1.8: Light curves of a Cepheid as observed through various filters. At longer wavelengths, the amplitudes decrease and the curve takes on a more symmetric and sinusoidal shape. Figure from Madore and Freedman (1991).

1.3.2 Hertzsprung Progression

The light curve for a Cepheid with a period in the range 6–16 days exhibits a secondary bump. The phase of this bump is correlated with the period of the Cepheid; this phase-period phenomenon is referred to as the Hertzsprung Progression (HP) and Cepheids with this feature are often categorised as Bump Cepheids. For Bump Cepheids with periods in the range 6–9 days, the HP bump is located on the descending section of the light curve; for Cepheids with periods around 10 days, the bump coincides with the primary peak; for longer periods, the bump travels down the ascending branch before disappearing entirely (García-Varela et al., 2016). The HP is visible in the light curves for Fundamental mode Cepheids in Figure 1.5.

Two models have been proposed to explain this phenomenon: Christy’s *echo model* (Christy, 1975) and Simon and Schmidt’s *resonance model* (Simon and Schmidt, 1976). The echo model proposes that the bump originates from a pressure excess in the first helium ionisation zone. The excess pressure occurs at the phase of maximum compression and gives rise to two pressure waves — one travelling inwards towards the core and one outwards towards the stellar surface. The inward-travelling wave is reflected off the core and reaches the surface one period later, resulting in the observed bump in brightness. The resonance model suggests that the fundamental mode of oscillation drives an oscillation of the second overtone; a period ratio of $P_2/P_0 = 0.5$ arises, hence a resonance which manifests itself as a bump in the light curve. The mechanism behind the HP is not yet fully understood though the consensus is leaning towards the resonance model (Gastine and Dintrans 2008, Buchler 2009, Smolec 2017).

1.3.3 Phase lag

The velocity curve of a Cepheid closely resembles its light curve with maximal outward velocity coinciding with maximal brightness followed by a similarly slow drop. The maximum brightness of a Cepheid is expected to occur at the same phase as minimum radius. However, what is observed is a phase lag between the two points: the

time of maximum brightness occurs $\sim 90^\circ$ after minimum radius is achieved (see Figure 1.9).

Early models of variable stars were unable to recreate this phase lag when considering only a single partial ionisation zone of helium. It wasn't until the inclusion of a hydrogen partial ionisation zone above the helium that the models agreed with observations. During the compression stage, the hydrogen partial ionisation zone acts to temporarily store energy from the heat flow, increasing its ionisation fraction. This has the effect of keeping the temperature approximately constant and increasing the opacity. The increase in opacity slows the outward flux from lower layers, delaying the Cepheid's rise to maximum brightness (Szabó et al., 2007).

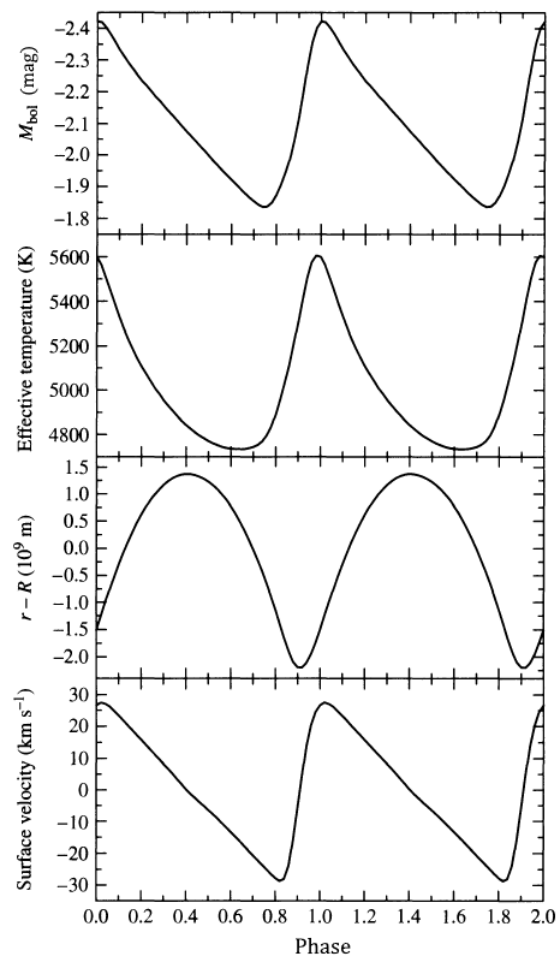


Figure 1.9: The magnitude, effective temperature, radius, and velocity curves of δ Cephei. A phase lag between maximal compression (minimum radius) and maximal luminosity is visible. Figure from Carroll and Ostlie (2007).

1.3.4 Break in linearity

The Leavitt Law has long been presumed to be linear across the permitted period range $0.3 < \log P < 2$. Recent studies of Cepheids in the Large Magellanic Cloud, however, strongly suggest the existence of a significant but subtle non-linearity in the Leavitt Law: a break in the optical-band PL relations for F mode Cepheids occurs at $\log P = 1$ (or $P = 10$ days) with the Leavitt Laws on either side of the break possessing differing slopes (Tammann et al. 2003, Ngeow et al. 2005, Ngeow and Kanbur 2006, García-Varela et al. 2013).

Bhardwaj et al. (2016) quantified the changes in the Leavitt Laws in optical, near-infrared, and multi-band magnitudes³ with a variety of statistical tests. They find that the slopes differs by at most $\sim 10\%$ on either side of $\log P = 1$ in optical bands, while in near-infrared bands, small non-linearities arise around $\log P = 1.25$ (~ 18 days). Figure 1.10 plots their period-luminosity and period-Wesenheit relations. They suggest that the physical mechanism behind the non-linearities is the variations in the envelope structure of Cepheids as a function of pulsation period, for a given mass-luminosity relation and a fixed topology of the instability strip.

Gieren et al. (2018) acknowledge the presence of Leavitt Law non-linearities in their study of the effects of metallicity on Cepheids though they find that the consequences on their results are insignificant.

³These multi-band magnitudes are constructed in such a way so that they are reddening-free and are referred to as Wesenheit magnitudes. See Section 4.3 for more details.

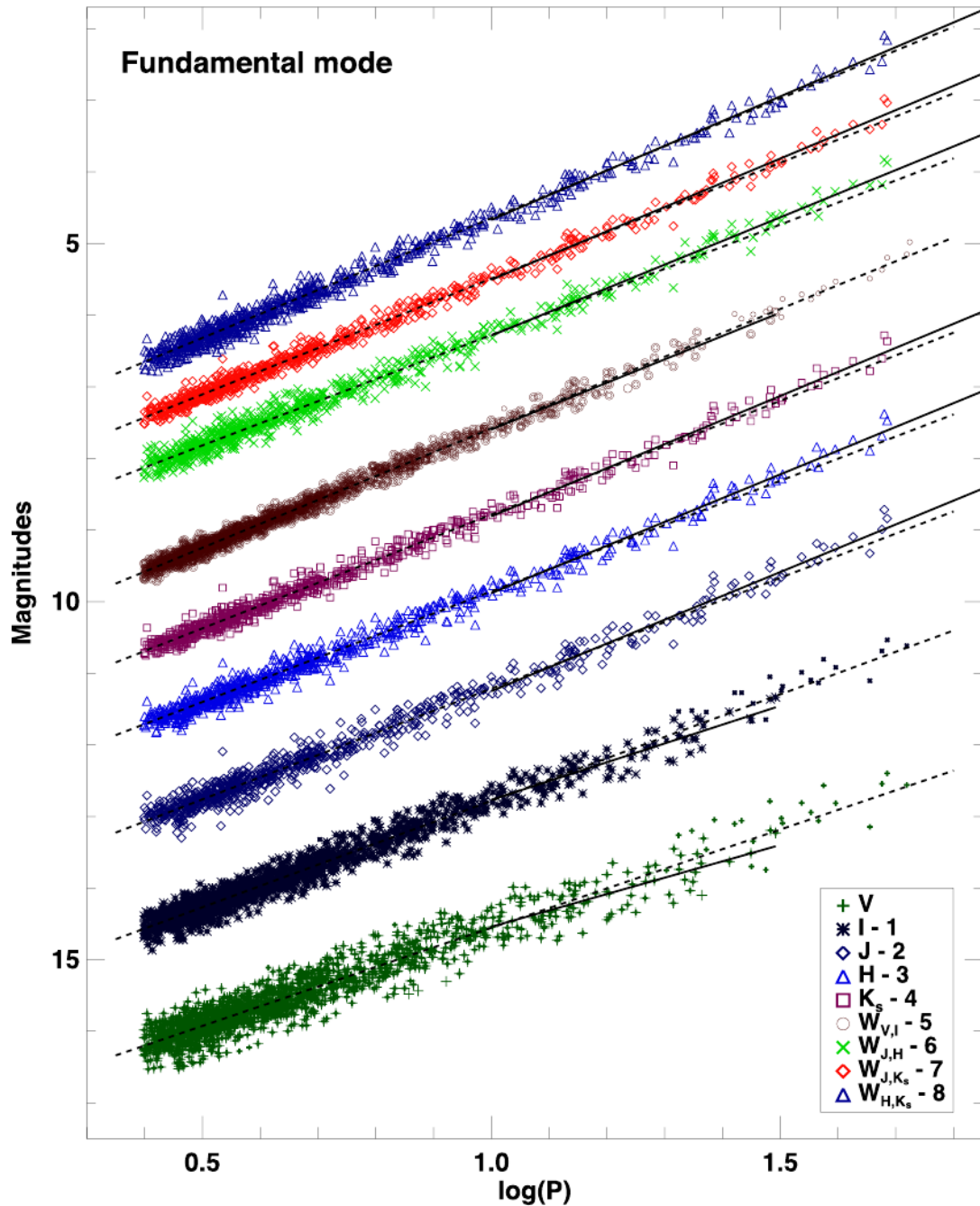


Figure 1.10: The break in the period-luminosity relations for various optical and infrared bands and for Wesenheit indices. The dashed lines represent the fitted Laws for Cepheids with periods shorter than 10 days. The solid lines represent the fits for the longer-period Cepheids. Figure from [Bhardwaj et al. \(2016\)](#).

With over 300 Cepheids in M31, [Kodric et al. \(2015\)](#) find evidence for non-linearity in the Leavitt Laws in near-infrared bands. In a follow-up study, [Kodric et al. \(2018\)](#) increased the sample size to over 500 Cepheids; however, they do not find significant

signs of a broken slope. They suggest that the non-linearity that was reported in [Kodric et al. \(2015\)](#) was caused by the presence of a large number of Cepheids with anomalous colours. With the larger sample size in the follow-up study, the influence of those atypical Cepheids is suppressed and the non-linearity of the slopes vanishes.

The existence of non-linearities in the period-luminosity relation still remains a contentious issue, particularly in the near-infrared regime.

1.3.5 Theoretical and observed metallicity effects

With nonlinear convective pulsation models, [Caputo et al. \(2000\)](#) investigated the effects of metallicity on Cepheid pulsation and, hence, Leavitt Laws. Cepheid models of varying levels of metallicity and mass were created and their resulting pulsational properties were explored. They find that as the metallicity increases, the location of the instability strip shifts to redder colours and the Cepheids, at fixed period, become dimmer. Quantitatively, they arrive at a positive metallicity correction of $\Delta\mu/\Delta\log Z = 0.27$ mag/dex where $\Delta\mu$ is the change in apparent distance modulus for a given difference in metallicity ($\Delta\log Z$) between the Cepheids and that of the Large Magellanic Cloud.

The theoretical dimming of Cepheids with increasing metallicity is in line with the luminosity-metallicity relation for stars in hydrostatic equilibrium whereby an increase in metallicity (assuming a fixed helium abundance) leads to a lower luminosity ([Salaris and Cassisi, 2005](#)).

With their models, [Marconi et al. \(2005\)](#) also find that as the metal content increases from $Z = 0.004$ to 0.03 at a fixed value for $\Delta Y/\Delta Z$ (where Y is the helium content), the instability strip moves towards lower effective temperatures. They also show that as metallicity increases from $Z = 0.03$ to 0.04 , the width of the instability strip becomes narrower because of the lower pulsation efficiency from the low abundance of hydrogen.

Empirical studies, however, generally find the opposite result concerning the relation

between metallicity and Cepheid brightness — that is, for the same period, a Cepheid with higher metallicity is observed to be brighter than a Cepheid of lower metallicity. See [Macri et al. \(2006\)](#), [Scowcroft et al. \(2009\)](#), [Gerke et al. \(2011\)](#), [Shappee and Stanek \(2011\)](#), [Storm et al. \(2011\)](#), [Mager et al. \(2013\)](#), [Fausnaugh et al. \(2015\)](#) and [Gieren et al. \(2018\)](#) for such examples. In line with theoretical predictions, [Romaniello et al. \(2008\)](#) measure a positive metallicity correction using direct measurements of the iron content of 68 Cepheids in the Milky Way and Magellanic Clouds.

Contrary to the previous results, [Wielgórski et al. \(2017\)](#) do not empirically detect any significant metallicity effect across a wide range of passbands.

It should be noted that most observational studies into the metallicity parameter relied on indirect measurements of Cepheid metallicities. One method of acquiring indirect Cepheid metallicities is to adopt a galactic metallicity gradient as determined from spectroscopy of HII regions and to assign a metallicity value to a given Cepheid according to its galactocentric distance; this method, however, introduces considerable uncertainty. Ideally, metallicities should be obtained on Cepheid-by-Cepheid basis through spectroscopy. Alternatively, if spectroscopy is infeasible, a metallicity gradient determined from beat Cepheids would be better suited than one obtained with HII regions since Cepheid metallicity is strongly constrained for a given period ratio.

1.4 Using Cepheids

1.4.1 Mathematical derivation of the PL relation

The functional form of the PL relation, or Leavitt Law, can be derived from the dimensional analysis of various stellar parameters pertaining to Cepheids.

We start with Ritter's period-density relation for a pulsating sphere of gas

$$\begin{aligned}
 P &\sim \frac{1}{\sqrt{\rho}} \\
 &\sim \frac{R^{3/2}}{M^{1/2}}.
 \end{aligned}
 \tag{1.3}$$

The mass and radius terms can be substituted using the mass-luminosity relation and the Stefan-Boltzmann law respectively

$$M \sim L^{1/\alpha} \quad \text{and} \quad R \sim \left(\frac{L}{T_{\text{eff}}^4}\right)^{1/2}$$

which yields

$$P \sim \frac{\left(L/T_{\text{eff}}^4\right)^{3/4}}{L^{1/2\alpha}}. \tag{1.4}$$

Taking the base-10 logarithm and collating the terms gives

$$\log P = A \times \log L + B \times \log T_{\text{eff}} + c \tag{1.5}$$

or, equivalently, using observable quantities

$$\log P = A' \times M + B' \times \text{colour} + c'. \tag{1.6}$$

This is the period-luminosity-colour relation. As previously mentioned, for a given luminosity, Cepheids exist in a narrow range in temperature in order for significant radial pulsations via the κ -mechanism to occur. The near-verticality and small width of the instability strip shows that effective temperature changes very slowly in relation with average luminosity. With this in consideration, the temperature (i.e. colour) term in the period-luminosity-colour relation can be absorbed into the constant term at the expense of a slightly higher dispersion

$$\log P = A' \times M + c'' . \quad (1.7)$$

Rearranging into its usual form yields

$$M = A'' \times \log P + c''' . \quad (1.8)$$

The coefficient on the period term and the constant can be derived either through observations of Cepheids of known distances or through theoretical considerations. Once those values have been established for a particular passband, the absolute magnitude for a Cepheid is easily inferred by measuring its pulsation period. With an absolute magnitude, a distance can be derived after measuring the apparent magnitude (assuming no extinction is present, or extinction effects have been accounted for).

1.4.2 The Leavitt Law

The intrinsic brightness of a Cepheid is tightly correlated with its pulsation period. Of the many stellar observables, pulsation period is one of the easiest to measure to a high level of precision. A series of photometric observations of a Cepheid produces a light curve, from which a period (or multiple periods for multi-mode Cepheids) can be extracted with Fourier analysis. As can be seen in Figure 1.8, the amplitude of pulsation monotonically increases with decreasing wavelength; periods measured from light curves with large amplitudes are more reliable. While optical band light curves are ideal for determining periods, their large amplitudes hinder mean magnitude measurements. In the mid-infrared, the pulsation amplitudes, the intrinsic scatter in the Leavitt Law and interstellar extinction are significantly reduced compared to those in the optical, making mid-infrared observations particularly attractive for Cepheid-based distance studies.

With a Cepheid's period and a calibrated Leavitt Law for a given passband, the absolute magnitude in that passband is calculated. With an extinction-corrected apparent

magnitude in the same passband, a measure of distance is given by the difference in calculated absolute magnitude and measured apparent magnitude.

1.4.3 The Baade–Wesselink method

The radial oscillations of a Cepheid provide a geometric method for measuring its distance. As the radius $R(\phi)$ of a Cepheid varies with phase, so too does its angular size $\theta(\phi)$ on the sky. The distance d to the Cepheid acts as a conversion factor between the two quantities

$$\theta(\phi) = \frac{2R(\phi)}{d} \quad (1.9)$$

thereby providing a means to estimate Cepheid distances independent of the Leavitt Law. This is the Baade–Wesselink method (Gautschy, 1987). Acquiring accurate values for the radius and angular diameter, however, requires more elaborate methods than those used in determining periods and magnitudes.

Direct measurement of the angular size of a Cepheid is achievable through interferometric techniques. Kervella et al. (2004b) determined the average angular diameters of seven nearby Galactic Cepheids through long-baseline interferometry and find values in the range of 1–3 milliarcseconds. It is also possible to infer the angular size variations of a Cepheid through purely photometric means by measuring its magnitude and colour variations.

The surface brightness of a star is related to its angular diameter via the relation

$$F_V(\phi) = 4.2207 - 0.1V_0(\phi) - 0.5 \log \theta(\phi) \quad (1.10)$$

where F_V is the V-band surface brightness, V_0 is the de-reddened visual magnitude, θ is the stellar angular diameter, and ϕ is the phase.

With their direct measurements of Cepheid angular sizes, Kervella et al. (2004a) derive

the following relation between surface brightness and $V - K$ colour

$$F_V = -0.1336(V - K)_0 + 3.950 \quad (1.11)$$

thereby allowing the indirect determinations of the angular sizes of Cepheids through measurements of their colours when interferometry is not feasible.

Spectroscopic measurements of a Cepheid's photosphere reveal its radial velocity variations superimposed on the Cepheid's systemic velocity with respect to the Earth. However, the measured radial velocity V_{rad} is not the pulsational velocity V_{puls} that is required for the Baade–Wesselink method but a convolution of V_{puls} with various phenomena. Limb darkening, the spherical geometry and the difference in velocity between the photosphere (optical depth of $\tau \approx 1$) and line-forming regions ($\tau = 2/3$) all contribute to the convolution which is parametrised as the projection factor p (Kervella et al., 2017).

Integration of the pulsational velocity (radial velocity multiplied by the projection factor) curve over a portion of a pulsation cycle yields the change in stellar radius between the phases ϕ_1 and ϕ_2

$$\Delta R = -p \int_{\phi_1}^{\phi_2} (V_{\text{rad}}(\phi) - V_{\text{sys}}) d\phi \quad (1.12)$$

By taking the variations in radius along a Cepheid's oscillation cycle from spectroscopy and the corresponding changes in angular size from photometry or interferometry, a distance can be estimated. Figure 1.11 illustrates various techniques involved with the Baade-Wesselink method.

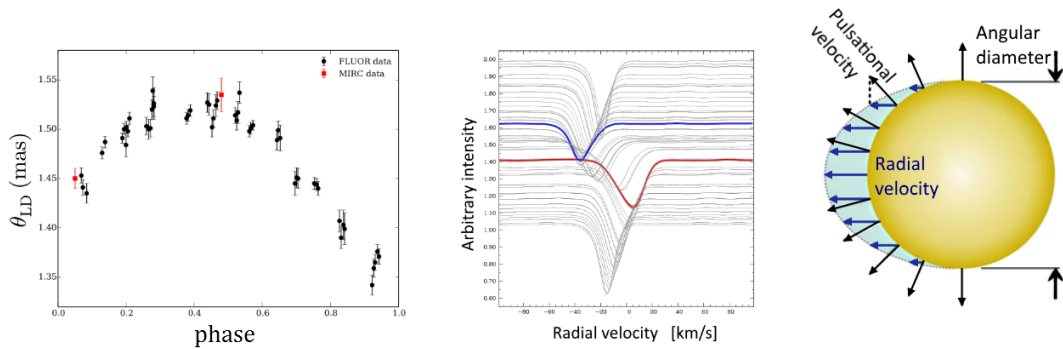


Figure 1.11: *Left*: Angular variations of δ Cephei from interferometry; figure from [Gallenne et al. \(2016\)](#). *Centre*: Line profile variations of δ Cephei from spectroscopy; figure from [Nardetto et al. \(2017\)](#). *Right*: Difference between radial and pulsation velocity; figure adapted from [Kervella et al. \(2018\)](#).

1.4.4 Period-Age relation

From theory of stellar evolution, stars of higher mass are found to leave the main sequence earlier and have lower densities, resulting in longer pulsation periods when those stars enter the instability strip. A relationship therefore exists between the pulsation period of a Cepheid and its age: younger Cepheids will have longer pulsation periods ([Efremov, 2003](#)).

[Senchyna et al. \(2015\)](#) arrive at the following period-age relation using Cepheids in the Andromeda Galaxy

$$\log A = -0.69 \log P + 8.38 \quad (1.13)$$

where A is the age in years and P is the period in days.

With the period-age relation, Cepheids can act as age-tracers as well as distance markers, making them useful for investigating localised star formation history and age distributions.

1.4.5 Beat Cepheids as metallicity tracers

A rare class of Cepheids pulsate simultaneously in two adjacent modes, typically fundamental/first overtone (F/O1) or first/second overtone (O1/O2). These Cepheids are aptly named double-mode or beat Cepheids and were first identified by [Oosterhoff \(1957\)](#). Unless otherwise stated, the term *beat Cepheids* will refer to Cepheids pulsating in the F/O1 modes.

Through models of stellar evolution and pulsation, the mass, luminosity, effective temperature and metallicity of a beat Cepheid are tightly constrained. A limited region of the parameter space permits the simultaneous pulsations in both the fundamental and first overtone modes. [Beaulieu et al. \(2006\)](#) find that the metallicity is especially tightly constrained in their models and have used this fact to determine the metallicities of five beat Cepheids in the Triangulum Galaxy. They also demonstrate the efficacy of the Petersen diagram ([Petersen, 1973](#)) as a means to photometrically extrapolate the metallicities of beat Cepheids.

A Petersen diagram is simply a plot of the ratio between two pulsation periods against the pulsation period of the lower harmonic. Since the metallicities of beat Cepheids are tightly correlated with their pulsation periods, different regions of a Petersen diagram correspond to different metallicities. One can therefore infer the metallicity of a beat Cepheid simply by its position on the plot (see [Figure 1.12](#)).

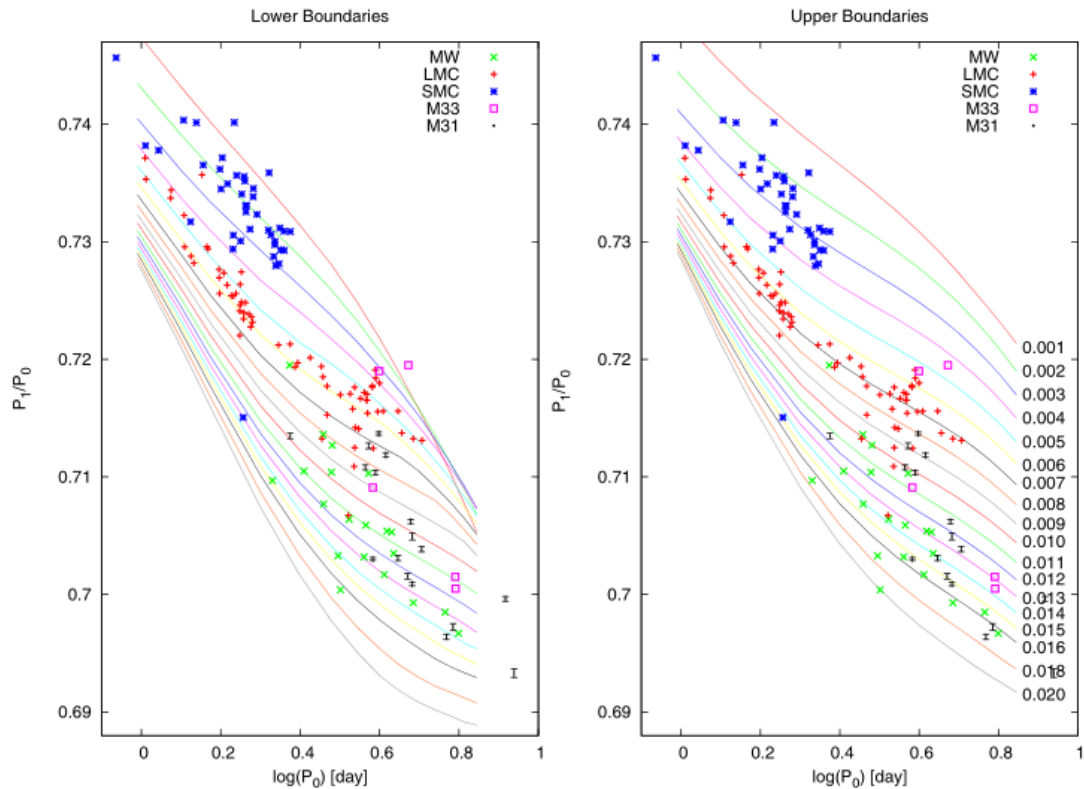


Figure 1.12: Petersen diagram of a selection of beat Cepheids. The Z metallicity tracks are presented as lower and upper boundaries in the left and right plots respectively. The overall metallicities of the Magellanic Clouds are lower than the Milky Way as expected. Figure from [Lee et al. \(2013\)](#).

1.5 The Cosmic Distance Ladder

Cepheids occupy a vital rung on the so-called cosmic distance ladder, a succession of methods with which to estimate distances to celestial objects. The rungs on the ladder represent different astrophysical phenomena, ranging from the minuscule parallactic motion of stars to the cataclysmic collapse of exposed stellar cores.

Many distance estimators rely on the accurate characterisation of Cepheids and the Leavitt Law as a means for calibration.

1.5.1 Parallax

At the base of the ladder is the parallax method, a purely geometric technique well suited for nearby stars and stellar clusters. As the Earth (and its resident observers and telescopes) orbits the Sun, the nearest stars appear to trace ellipses on the sky while the faraway background stars remain stationary (see Figure 1.13). With a measured apparent elliptical motion (parallax angle) $\bar{\omega}$, and a reddening-corrected apparent magnitude m_0 for a star, the absolute magnitude M for that star can be calculated with the following relation

$$M = m_0 + 5 \log(\bar{\omega}) - 10 \quad (1.14)$$

where $\bar{\omega}$ is measured in milliarcseconds. After the absolute magnitude, a distance estimate easily follows.

This method of inverting a parallax into an absolute magnitude is, however, only suitable for parallax angles with errors of less than 10%, otherwise the error in the absolute magnitudes will be significantly asymmetric, which can lead to biases; the parallax angles must also be measured to be positive in value for the relation to function.

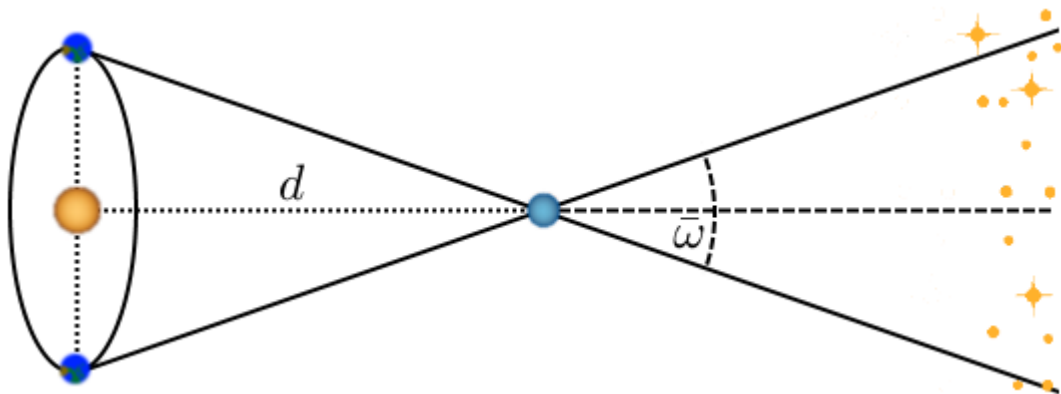


Figure 1.13: The parallax method. A nearby star will appear to trace out a small ellipse as the Earth orbits the Sun. Image not to scale.

The parallax angle for the nearest star to the Sun, Proxima Centauri, is $\bar{\omega} = 0.77''$, corresponding to a distance of 1.3 parsecs. Ground-based measurements are able to detect parallax angles down to $\sim 0.01''$, which would ideally translate to a maximum

measurable distance of 100 parsecs. In practice, the distance limit is several tens of parsecs, restricting the ground-based parallax method to the nearest few hundred stars (de Grijs, 2011).

The space-based Gaia mission is — as of writing — observing the positions, proper motions, parallaxes, and brightnesses of 1.7 billion sources. At the end of its mission, the parallax errors are expected to be of order 10^{-5} arcseconds for sources brighter than $V \sim 13$ mag. As part of *Gaia Data Release 2*, the characteristics of $\sim 10,000$ Cepheids were published, 350 of which are likely to be new discoveries (see Figure 1.14) (Clementini et al., 2018).

With the vast wealth of Galactic Cepheid data, the Leavitt Laws can be calibrated to a great level of precision and accuracy, solidifying the foundation of the cosmic distance ladder.

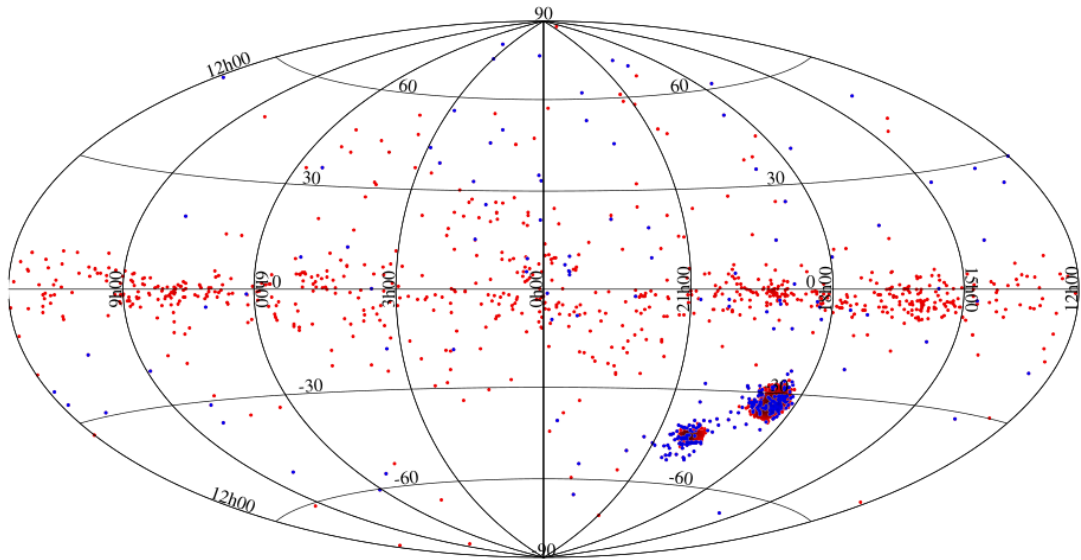


Figure 1.14: Positions of $\sim 10,000$ Galactic and Magellanic Cepheids (classical, type II and anomalous) from the *Gaia Data Release 2*. Red points are known Cepheids and blue points are new Cepheids discovered by Gaia. Figure from Clementini et al. (2018).

One key issue that plagues the parallax method is the Lutz–Kelker bias. For a given measured parallax angle ω_m and its associated error σ , an upper and lower bound on a distance d is provided. When being measured, stars with true parallaxes larger and smaller than that range in parallax can scatter into $\omega_m \pm \sigma$, and stars with true parallaxes

within $\omega_m \pm \sigma$ can scatter out. Assuming that stars are uniformly distributed in space, the number of stars per parallax interval varies as $1/\omega^4$. More stars with parallaxes smaller than ω_m will scatter into $\omega_m \pm \sigma$ than those with larger values. Therefore, the average true parallax of stars with a measured parallax of ω_m is smaller than ω_m , which in turn yields distances that are too small. To counter this bias, a Lutz–Kelker correction may be applied (Lutz and Kelker, 1973).

1.5.2 Cepheids

Cepheids play a vital role in the context of the extragalactic distance scale by extending the reach of the cosmic distance ladder to galaxies beyond the Local Group. Owing to their intrinsic brightness, Cepheids can be detected out to several tens of Mpc (Bird et al., 2009), well beyond the Local Group of galaxies which spans a few Mpc in diameter (Mateo, 1998). For the more distant extragalactic distance determination methods to be viable, those methods require calibration; this can be provided by observable Cepheids that are within the systems from which the secondary distance methods originate.

1.5.3 Tip of the Red Giant Branch

Stars of low mass ($M < 2 M_\odot$) undergo a helium flash event when reaching the top of the red giant branch. The helium flash is the runaway fusion of the degenerate core, converting around 5% of the helium content into carbon via the triple- α process. In just a few seconds, the power output of the core reaches $\sim 10^{10} L_\odot$ though almost none of this energy reaches the surface as it is absorbed by the intervening layers of the star. The RGB phase of the star’s evolution terminates and it subsequently travels down to lower luminosities, and begins to fuse helium in a stable manner.

For stars of mass $M < 1.8 M_\odot$ and with solar chemical abundances, the luminosity at which the helium flash occurs is approximately constant. A star of higher metallicity burns its hydrogen more efficiently in its hydrogen-burning shell, making the star

brighter; the helium core heats up faster due to the more efficient shell burning and therefore ignites at a lower mass. The lower mass of the core during ignition would correspond to a dimmer star but the efficient hydrogen shell more than compensate for that effect. The net result is that the more metal-rich stars are brighter at the helium flash point than their lower metallicity counterparts.

The brightness of an RGB star at its helium flash is referred to as the tip of the RGB (TRGB) magnitude and it generally varies with metallicity. At a fixed age, the bolometric magnitude at the flash decreases with increasing metallicity; the relationship between the magnitude of the TRGB star will vary between different photometric filters due to metallicity effects on bolometric corrections. The dependence of the TRGB brightness on metallicity is minimal in the *I*-band for metallicities $[\text{Fe}/\text{H}] < -0.7$ dex. The consistency of the *I*-band TRGB magnitude for low metallicity RGB stars makes them well suited as standard candles out to distances of ~ 20 Mpc. Unlike Cepheids, which are only found in spiral galaxies, RGB stars are readily found in galaxies of many morphologies and in other stellar systems.

Along the RGB in the *I*-band, the tip is delineated by a sudden change in the number of stars, i.e., a large gradient in the luminosity function (LF). A common technique for locating the sharp change in the LF is to convolve it with an edge-detection kernel. The peak of the output is located at the discontinuity or “edge” of the LF and the magnitude is read off accordingly as the TRGB magnitude (Salaris and Cassisi, 2005). The absolute TRGB magnitude is well established at a value of $M_I^{\text{TRGB}} \approx -4$ mag. A distance is then found simply by taking the difference between the observed TRGB magnitude and the absolute TRGB magnitude. Figure 1.15 shows a CMD of the RGB stars in the nearby spiral galaxy NGC 4258 and the location of the TRGB determined with an edge detection filter.

It is expected that a precise and accurate calibration of the absolute TRGB magnitude will be attained with parallax measurements of Milky Way red giants with Gaia.

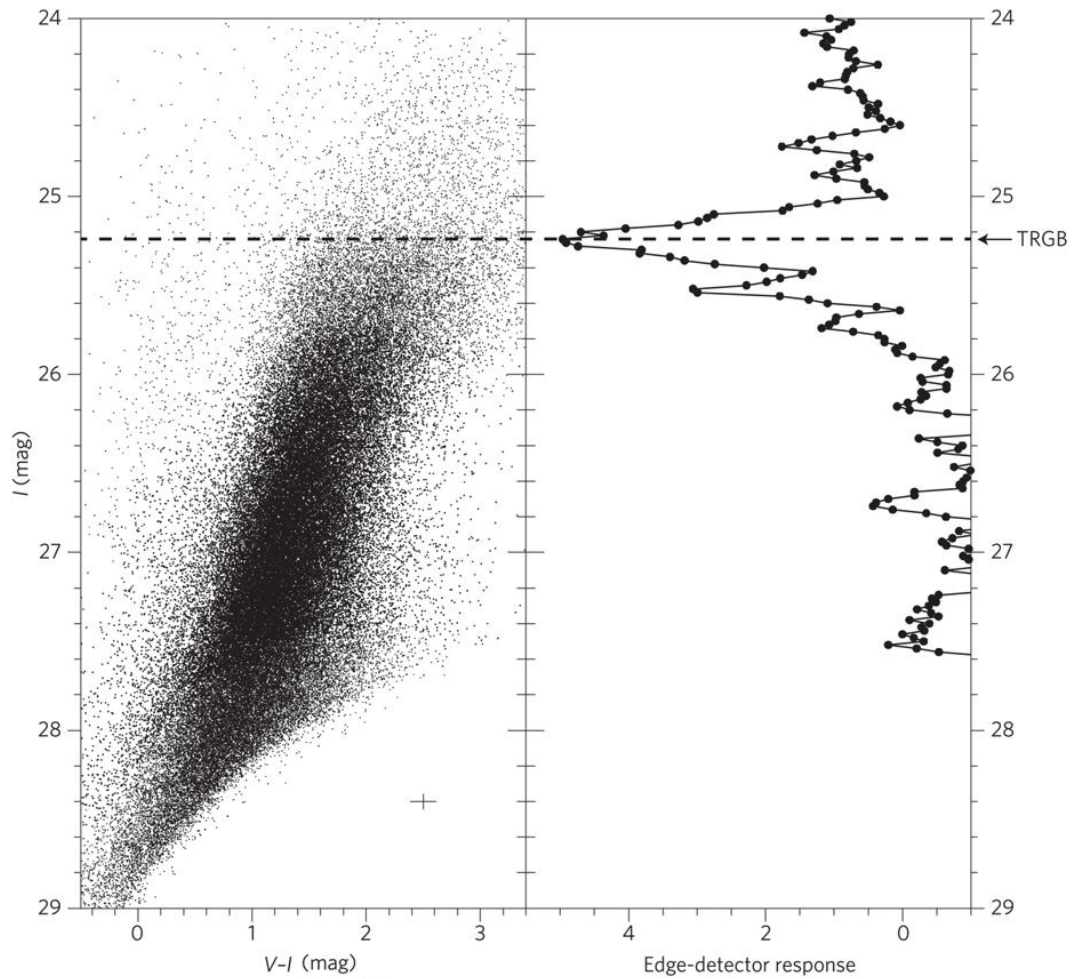


Figure 1.15: *Left*: I vs $(V - I)$ CMD of the RGB stars in the nearby spiral galaxy NGC 4258. *Right*: The response of the edge detection filter on the LF of the branch stars. The peak of the response marks the location of the TRGB (dashed line). Figure from [Freedman \(2017\)](#).

1.5.4 Tully–Fisher relation

Entire galaxies can themselves act as distance indicators. [Tully and Fisher \(1977\)](#) demonstrate this by showing that there exists a relation between the luminosity of a spiral galaxy and its disc circular velocity. The rotational velocity is framed as the measured width of the global neutral hydrogen (HI) line profile since it is strong in spiral galaxies and it samples the line-of-sight velocity over the entire disc. The rotational velocity, after being corrected for inclination and random motion, provides a measure of the mass of a spiral galaxy’s dark matter halo while the luminosity is an indication of the total stellar mass. The correlation between luminosity and rotational

velocity is thought to arise from a relationship between the dark matter halo and the baryonic content that it hosts, with the assumption that the luminosity is a direct result of the total baryonic mass (Ponomareva et al., 2017).

Calibration of the Tully–Fisher relation is typically attained by using Cepheids or the tip of the red giant branch method to acquire independent distances to those galaxies. Cepheids can be readily found in spiral galaxies since such galaxies host young and massive stars. Sorce et al. (2013) combined colour-corrected mid-infrared magnitudes and HI line widths for 213 galaxies — of which, 26 had known distances — and arrive at the relation

$$M_{C_{[3.6]}} = -(20.34 \pm 0.08) - (9.13 \pm 0.22)(\log W_{mx}^i - 2.5) \quad (1.15)$$

where $M_{C_{[3.6]}}$ is the colour-corrected mid-infrared ($3.6\mu\text{m}$) magnitude and W_{mx}^i is approximately twice the maximum rotation velocity of the galaxy (see Figure 1.16).

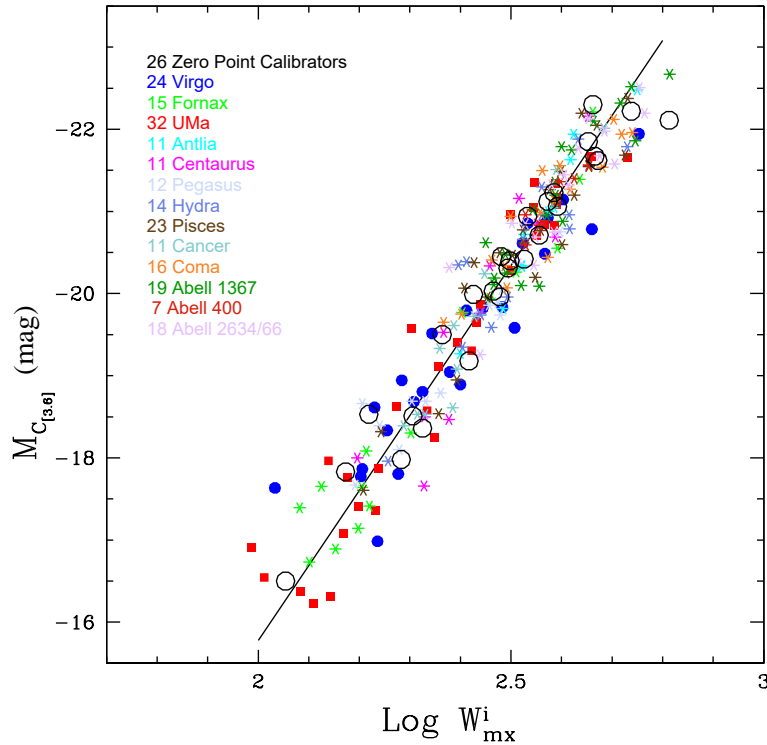


Figure 1.16: Mid-infrared Tully–Fisher relation derived from 213 spiral galaxies. Figure from Sorce et al. (2013).

With this method, distances of up to 200 Mpc are measurable, where the effects of the Hubble Flow are present and dominate over peculiar velocities.

1.5.5 Type Ia supernovae

Astrophysical objects or phenomena with intrinsic luminosities that are known are given the colloquial term *standard candle*. A type of astrophysical phenomenon with the standard candle classification is Type Ia supernovae (SNe Ia). These supernovae mark the death throes of white dwarfs — the remnant degenerate carbon-oxygen cores of low- to intermediate-mass stars. The favoured model describing the mechanism behind the eruptive event involves the passing of matter from an evolving secondary star onto the C-O white dwarf. One version of this model has the helium from the secondary star settling onto the surface of the white dwarf, becoming degenerate. Eventually, the white dwarf will accumulate enough surface helium and a helium flash will occur, sending shock waves into the dwarf’s interior, prompting the ignition of the degenerate carbon-oxygen material. Another version forgoes the helium flash; instead, the contribution of mass from the added helium eventually brings the total mass of the white dwarf over the Chandrasekhar limit. Beyond this limit, the degeneracy pressure from the carbon and oxygen is no longer sufficient to resist gravity and to prevent nuclear fusion.

Regardless of the ignition mechanism, SNe Ia reach a peak luminosity of

$$\langle M_B \rangle \simeq \langle M_V \rangle \simeq -19.3 \pm 0.3 \text{ mag} \quad (1.16)$$

before dimming over a period of weeks. There exists a correlation between the rate of decline in brightness and the peak brightness: the more rapid the rate of dimming, the fainter the supernovae at its peak. This is the Phillips relation (Phillips, 1993). Cepheid magnitudes peak at around $M \simeq -6$ mag, 13.3 magnitudes dimmer than SNe Ia. This difference corresponds to a maximum observable distance that is greater than that of Cepheids by a factor of ~ 400 (Carroll and Ostlie, 2007).

To date, 19 galaxies with Cepheid-calibrated distances have been observed to host a recent Type Ia supernova event (Riess et al., 2016). With the anchoring of distances derived from SNe Ia observations to Cepheids, the distance ladder is able to reach cosmologically significant distances.

1.5.6 Hubble constant

One of the key parameters in cosmology is the Hubble constant H_0 and great effort has been expended in determining its value. Riess et al. (2016) determined a local value of $H_0 = 73.24 \pm 1.74 \text{ km s}^{-1}\text{Mpc}^{-1}$, an uncertainty of 2.4%. This level of precision was achieved through the observations of Cepheids in 19 SNe Ia host galaxies, with the Cepheids imparting their precise calibration to the SNe Ia method of distance determination. The recession velocities of the host galaxies, combined with their distances, provides a local estimate for H_0 . This value was slightly improved to $H_0 = 73.52 \pm 1.62 \text{ kms}^{-1}\text{Mpc}^{-1}$ with the addition of parallax measurements of 50 Milky Way Cepheids from Gaia (Riess et al., 2018).

From the edge of the observable Universe, the cosmic microwave background (CMB) provides another measure of the Hubble constant. From their analysis of the variations in temperature and polarisation maps under the constraints of the Λ CDM cosmology, the Planck Collaboration (2018) find a value of $H_0 = 67.4 \pm 0.5 \text{ kms}^{-1}\text{Mpc}^{-1}$.

Between these two H_0 values derived from local and cosmological scales, there exists a significant tension of $\sim 4\sigma$. The difference may arise from unknown systematic errors from either system of methods or may be hints to new physics beyond the current standard model (Freedman, 2017).

1.6 Aims of this thesis

The characteristics of a star — such as its observed spectral energy distribution — vary with its chemical composition. For Cepheids, these metallicity-induced variations may introduce changes into the Leavitt Law, complicating their use as a primary distance indicator.

Observational studies of the effects of metallicity on Cepheids have been undertaken and the majority show a correlation between the observed Cepheid brightness and chemical abundance. For example, [Sasselov et al. \(1997\)](#), [Sakai et al. \(2004\)](#), [Scowcroft et al. \(2009\)](#) and [Mager et al. \(2013\)](#) find that Cepheids of higher metallicity are brighter in the optical, giving lower optical Leavitt Law zero-points and hence smaller observed distance moduli. However, it was argued whether this effect may instead be attributed to the effects of stellar crowding and blending ([Wagner-Kaiser et al., 2015](#)). [Freedman and Madore \(2011\)](#) arrive at the opposite conclusion regarding the dependence between metallicity and measured distance: they observe that metal-rich Cepheids are dimmer in optical wavelengths and that the size of the effect decreases at longer wavelengths until the sign reverses in the 3.6 μm filter. From their study of Cepheids in both Magellanic Clouds, [Wielgórski et al. \(2017\)](#) find no significant metallicity effect in optical and infrared bands. Counter to most empirical studies, [Romaniello et al. \(2008\)](#) measure a positive metallicity correction (at fixed period, metal-rich Cepheids are inherently dimmer) using direct measurements of the iron content of 68 Cepheids in the Milky Way and Magellanic Clouds.

Some theoretical investigations on the effect of metallicity on Cepheids suggest that the more metal-rich Cepheids ought to be dimmer and hence appear more distant, contrary to most empirical results ([Bono et al., 1999a](#), [Caputo et al., 2000](#), [Marconi et al., 2005](#)).

Under theoretical considerations, the slope of the Leavitt Law is expected to steepen with decreasing metallicity ([Marconi et al., 2010](#)) with the effect decreasing towards longer wavelengths ([Fiorentino et al., 2002, 2007](#)). Observational studies, however, tend to find no significant metallicity-slope effect ([Pietrzyński et al. 2007](#), [Mager et al. 2013](#), [Ripepi et al. 2018](#)).

These uncertainties are detrimental to the accuracy of secondary distance indicators that rely on accurate Cepheid calibrations (such as type Ia Supernovae and the Tully-Fisher relation). These cascading errors contribute to the systematic uncertainty on estimates of the Hubble constant and other cosmological parameters ([Freedman et al., 2011](#)).

To explore the possible effects of metallicity on the Leavitt Law, Cepheids residing in the nearby spiral Triangulum galaxy (M33) are investigated. M33 is an ideal test bed for extragalactic Cepheid studies as the galaxy is nearby, situated away from the plane of the Milky Way, has a low inclination angle and hosts thousands of Cepheids. M33 features a radial metallicity gradient and Cepheids are readily found throughout the disc. Cepheids at different galactocentric radii, therefore, sample different levels of metallicity, potentially affecting their observed characteristics. The effect of metallicity on the Leavitt Law can be empirically scrutinised and quantified with this bounty of Cepheid variables.

This study uses images of M33 taken in Sloan-like filters. Observational studies of Cepheids have typically used Johnson-Cousins filters. With the advent of large-scale sky surveys using Sloan-band filters, Cepheid studies in Sloan filters will become more prevalent. The Large Synoptic Survey Telescope will utilise Sloan filters and is expected to be able to detect and measure Cepheids in the southern sky out to distances of at least 10 Mpc ([Hoffmann and Macri, 2015](#)). This work will provide a baseline against which future Sloan-band studies of Cepheids can be compared.

Chapter 2

The Triangulum Galaxy

The Triangulum Galaxy (M33), along with the Milky Way and the Andromeda Galaxy (M31), are the dominant galaxies of the Local Group, a collection of ~ 50 gravitationally bound galaxies spanning a few Mpc. Under Hubble’s galaxy classification system, M33, with its loose spiral arms and lack of a central bar, is an Sc type galaxy.

2.1 Basic properties

With its close proximity and low inclination, M33 has been studied intensively for many decades. Many of its properties are, therefore, well constrained though some remain in slight dispute. Basic parameters are presented in Table 2.1.

Property	Value	Source
Coordinates (J2000)	RA = 01h33m50.9s, Dec = +30°39′35.8″	Wenger et al. (2000)
Distance	794 to 968 kpc	Table 2.2
Angular size	71′ × 42′	König and Binnewies (2017)
Stellar mass	$3.2 \times 10^9 M_{\odot}$	van der Marel et al. (2012)
Inclination	53°	Magrini et al. (2007)
Position angle	22°	Magrini et al. (2007)

Table 2.1: Basic properties of M33.



Figure 2.1: The Triangulum Galaxy. Copyright: Robert Gendler, Subaru Telescope, National Astronomical Observatory of Japan (NAOJ).

2.1.1 Stellar distance estimates to M33

M33 is close enough that its stars are spatially resolvable, enabling the use of many stellar methods of distance estimation. Stellar distances obtained with various techniques over the past two decades typically lie within the range $24.4 < \mu < 24.9$ mag where μ is the distance modulus and is defined as $\mu = (m - M)$ i.e., the difference between the apparent and absolute magnitudes of a celestial object. Converting a distance modulus (which is a logarithmic measure of distance) into a linear scale is achieved with the following relation

$$D = 10^{(\mu+5)/5} \text{ pc} \quad (2.1)$$

Table 2.2 lists a sample of distance estimates determined from various stellar distance indicators and, where applicable, the adopted distance to the Large Magellanic Cloud.

2.1.2 Metallicity gradients

Metallicity gradients are a common trait of spiral galaxies and M33 is no exception. Indeed, the first signs of the existence of metallicity gradients in spiral galaxies were first observed in M33 by [Aller \(1942\)](#). Gradients are usually presented as the change in iron or oxygen abundance as a function of galactocentric radius and are almost always negative in value, i.e., the inner regions of spiral galaxies are more metal rich than the outskirts.

Various studies into the metal content of M33 confirm the presence of a negative radial metallicity gradient. However, there is some dispute over the steepness of the gradient and whether or not the gradient is better represented by a multi-component profile. Recent results are shown in Table 2.3.

Implicit to most metallicity gradient studies in spiral galaxies is the assumption of an axisymmetric distribution of chemical abundances. A recent spectroscopic survey of 412 HII regions in M33 by [Lin et al. \(2017\)](#) supports the assumption that there is little

Distance modulus (mag)	Method	Adopted LMC distance (mag)	Source
24.56 ± 0.10	Cepheids	18.50	Freedman et al. (2001)
24.47 ± 0.13	Cepheids	18.50	Willick and Batra (2001)
24.53 ± 0.19	Cepheids	18.50	Lee et al. (2002)
24.53 ± 0.11	Cepheids	18.4	Scowcroft et al. (2009)
24.76 ± 0.02	Cepheids	18.5	Pellerin and Macri (2011)
24.62 ± 0.07	Cepheids	18.50	Gieren et al. (2013)
24.84 ± 0.16	RR Lyrae	18.5	Sarajedini et al. (2000)
24.67 ± 0.07	RR Lyrae		Sarajedini et al. (2006)
24.52 ± 0.11	RR Lyrae		Yang et al. (2010)
24.36 ± 0.09	RR Lyrae		Dambis et al. (2013)
24.85 ± 0.13	LPV	18.5	Pierce et al. (2000)
24.80 ± 0.06	Miras	18.493	Yuan et al. (2018)
24.80 ± 0.06	Red clump		Kim et al. (2002)
24.81 ± 0.24	HB		Sarajedini et al. (2000)
24.81 ± 0.14	TRGB		Kim et al. (2002)
24.72 ± 0.14	TRGB		Brooks et al. (2004)
24.64 ± 0.15	TRGB		Galleti et al. (2004)
24.50 ± 0.06	TRGB		McConnachie et al. (2004)
24.69 ± 0.07	TRGB		Tiede et al. (2004)
24.84 ± 0.10	TRGB		U et al. (2009)
24.93 ± 0.11	FGLR	18.50	U et al. (2009)
24.92 ± 0.12	Eclipsing binary		Bonanos et al. (2006)

Table 2.2: Stellar M33 distances and adopted LMC distances.

to no azimuthal variation across the disk within an uncertainty of 0.04 dex. They do find, however, that small local variations are present and are associated with the spiral arms.

Beat Cepheids

[Beaulieu et al. \(2006\)](#) found 5 beat Cepheids pulsating simultaneously in the fundamental and first overtone modes across M33 at different galactocentric radii. For each beat Cepheid, they constrain their metallicity value through the use of stellar pulsation models that incorporate their observed pulsation periods and exploratory values for effective temperature and metallicity. Cepheid models with known periods trace

different paths through the mass-luminosity plane as their assigned metallicity and effective temperature varies. If, at a given fixed metallicity and known periods, the path of Cepheid model in the $M - L$ plane intersects with the loci of known mass-luminosity relations, the assigned metallicity is presumed to be true for that Cepheid with those particular periods. This method is sensitive to the iron-group elements but it is relatively insensitive to the abundance of other metals and helium.

When these Cepheids are plotted on a Petersen diagram that is populated with known beat Cepheids from the Milky Way and Magellanic Clouds, the M33 beat Cepheids are indeed located where they are expected to be based on their computed metallicities (see Figure 2.2). The metal-poor M33 beat Cepheids (A and B) are aligned with those in the SMC, and the more metal-rich ones (C, D and E) with those of the LMC and Milky Way.

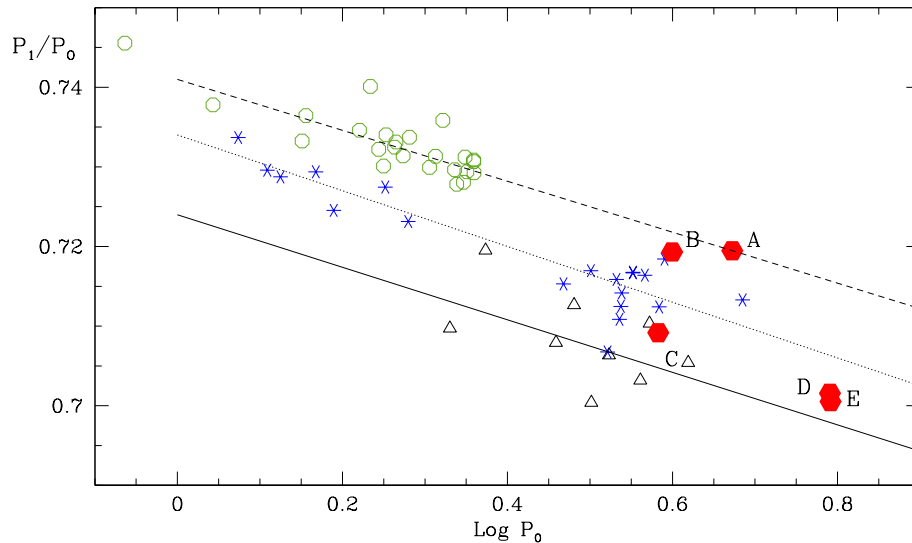


Figure 2.2: Petersen diagram with beat Cepheids from the Milky Way (triangles), Large Magellanic Cloud (stars), Small Magellanic Cloud (open circles) and M33 (filled circles). Figure from [Beaulieu et al. \(2006\)](#).

Those 5 beat Cepheids with known metallicities are located at various distances from the centre of M33, from which [Beaulieu et al. \(2006\)](#) determine a metallicity gradient of $d[Z]/d\rho = -0.20$ dex/kpc (where ρ is galactocentric radius and $[Z]$ is the relative abundance of the iron-group elements compared to that of the Sun, i.e., $\log(Z/Z_{\odot})$). However, this gradient value is suspected to be erroneous. The original deprojection of

the Cepheids' distances was performed with what was stated to be an assumed distance of 840 kpc to M33; no values for the position angle and inclination angle for M33 were given. If the reported celestial positions of the 5 Cepheids are now deprojected with a distance of 840 kpc, an inclination angle of 53° and a position angle of 22° , there are clear inconsistencies between these new radii and those reported in their paper. The new galactocentric radii of the 5 Cepheids determined here are all larger than the radii given by [Beaulieu et al. \(2006\)](#) (see Figure 2.3).

If, instead, the deprojection is performed with a much smaller distance of 540 kpc to M33 but with the same galactic orientation angles, the new galactocentric radii are very consistent with those reported by [Beaulieu et al. \(2006\)](#). It seems likely that the original deprojection for the 5 beat Cepheids' positions suffered an unfortunate miscalculation which would then have propagated to their metallicity gradient values. A redetermination of the galactocentric radii at a distance of 840 kpc yields larger radial distances and, therefore, a shallower metallicity gradient (see Figure 2.4). By applying linear regression to the updated data, a new metallicity gradient of $d[Z]/d\rho = -0.112$ dex/kpc is found and is appended to Table 2.3.

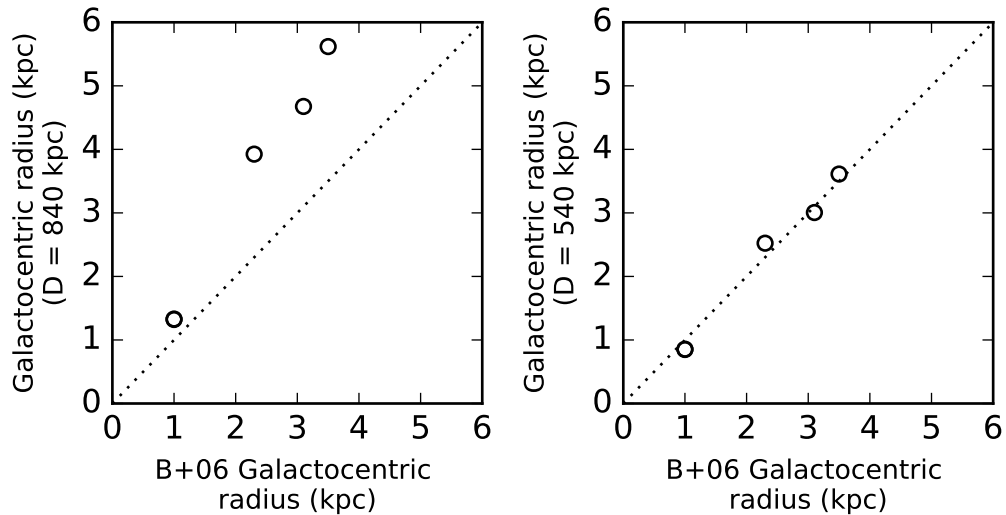


Figure 2.3: *Left*: Deprojected galactocentric radii of 5 beat Cepheids assuming a distance of 840 kpc against the radii reported by [Beaulieu et al. \(2006\)](#). *Right*: Same as the left plot but with an assumed M33 distance of 540 kpc. The dotted lines in both plots mark the locus of identical radii. Note that in both plots, the bottom-left circle is actually two data points representing two Cepheids with very similar angular distances from the galactic centre.

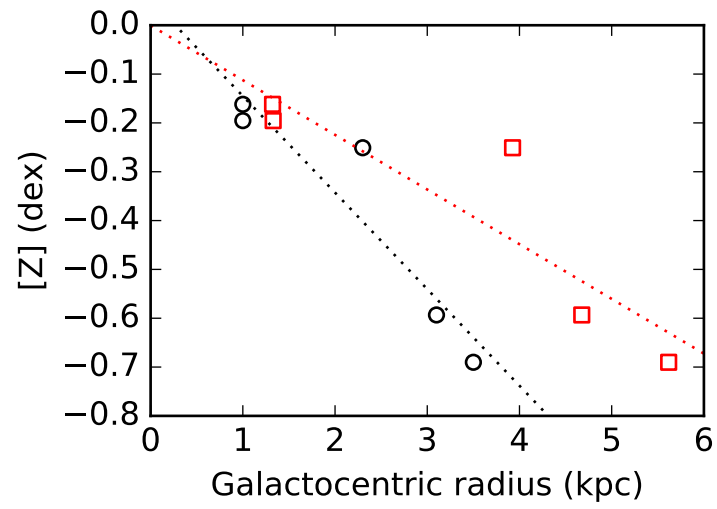


Figure 2.4: The red points represent the original data in [Beaulieu et al. \(2006\)](#). The black points represent the same data but with updated deprojected radii. Dotted lines are fits to the data and represent the metallicity gradients.

Metal	Gradient (dex/kpc)	Central abundance (dex)	Tracer	Distance used (kpc)	Source
12+[O/H]	-0.127 ± 0.011	9.08	HII regions	700	Zaritsky et al. (1994)
12+[O/H]	-0.11 ± 0.02	8.87	HII regions	840	Garnett et al. (1997)
12+[Ne/H]	-0.034 ± 0.015		HII regions	832	Willner and Nelson-Patel (2002)
12+[Ne/H]	-0.016 ± 0.017	7.7	HII regions	832	Crockett et al. (2006)
12+[O/H]	-0.012 ± 0.011	8.4	HII regions	832	Crockett et al. (2006)
12+[O/H]	$(-0.19 \pm 0.08)_{R < 3 \text{ kpc}},$ $(-0.038 \pm 0.015)_{R > 3 \text{ kpc}}$	8.95 ± 0.13	HII regions	840	Magrini et al. (2007)
12+[O/H]	-0.05 ± 0.01	8.60 ± 0.05	HII regions	840	Viironen et al. (2007)
12+[O/H]	-0.027 ± 0.012	8.36 ± 0.04	HII regions	840	Rosolowsky and Simon (2008)
[α /H]	-0.025 ± 0.006		HII regions + PNe	840	Bresolin et al. (2010)
[O/H]	$(-0.044 \pm 0.009)_{1 < R < 8 \text{ kpc}}$		HII regions	840	Magrini et al. (2010)
12+[O/H]	-0.033 ± 0.005		HII regions	840	Bresolin (2011b)
12+[O/H]	-0.024 ± 0.007		HII regions	840	Magrini et al. (2016)
12+[O/H]	$-0.024 \pm 0.004_{R < 8 \text{ kpc}}$	8.41 ± 0.11	HII regions	878	Lin et al. (2017)
12+[O/H]	-0.031 ± 0.013		Planetary nebulae	840	Magrini et al. (2009)
12+[O/H]	-0.16 ± 0.06		Blue supergiants	~ 967	Monteverde et al. (1997)
12+[O/H]	-0.06 ± 0.02	8.81 ± 0.11	Blue supergiants	820	Urbaneja et al. (2005)
[Z]	-0.07 ± 0.01	0.09 ± 0.04	Blue supergiants	968	U et al. (2009)
[Fe/H]	$(-0.078 \pm 0.003)_{R < 9 \text{ kpc}}$	-0.77 ± 0.02	AGB stars	840	Cioni (2009)
[Fe/H]	-0.07 ± 0.01	-0.48 ± 0.04	RGB stars	916	Kim et al. (2002)
[Fe/H]	-0.07 ± 0.01	-0.48 ± 0.04	RGB stars	867	Tiede et al. (2004)
[Z]	$(-0.2)_{R < 3.5 \text{ kpc}}$		Beat Cepheids	840(?)	Beaulieu et al. (2006)
12+[O/H]	$(-0.16)_{R < 3.5 \text{ kpc}}$		Beat Cepheids	840(?)	Beaulieu et al. (2006)
[Z]	$(-0.112)_{R < 5.7 \text{ kpc}}$		Beat Cepheids	840	Beaulieu et al. (2006)

Table 2.3: A list of M33 metallicity gradient measurements in the literature, including the type of metallicity that is measured, the tracer that was used, and the adopted distance to M33.

Chapter 3

Photometry and calibration

3.1 Image data

3.1.1 CFHT images

Deep images of M33 have been taken through Sloan-like filters g' , r' and i' , and cover the whole galaxy over many epochs. The images were obtained by [Hartman et al. \(2006\)](#) using the MegaCam instrument at the Canada–France–Hawaii Telescope (CFHT) on 27 separate nights as part of a variability survey spanning 17 months. The MegaCam detector comprises a mosaic of 9×4 operational 2048×4612 pixel CCDs at a scale of 0.185 arcsecond/pixel. This configuration allows each pointing to cover ~ 1 degree² of the sky, encompassing the entire disk of the galaxy.

Analysis with image subtraction techniques have been performed on the frames by Hartman et al. to detect variable sources and to create their corresponding light curves (see [Figure 3.1](#) for example light curves). Their magnitude calibrations were rudimentary with only zero-point terms, and may differ from the standard by a few tenths of a magnitude, depending on colour. They therefore recommended that these magnitudes should be treated as being instrumental. Over 36000 variable objects have been detected, more than 2000 of which were classified as Cepheids by their being

located within the instability strip and by their conformity to a period-luminosity relation. Catalogues of the variable objects were made publicly available¹. A sample of the catalogue of fundamental mode Cepheids is presented in Table 3.1.

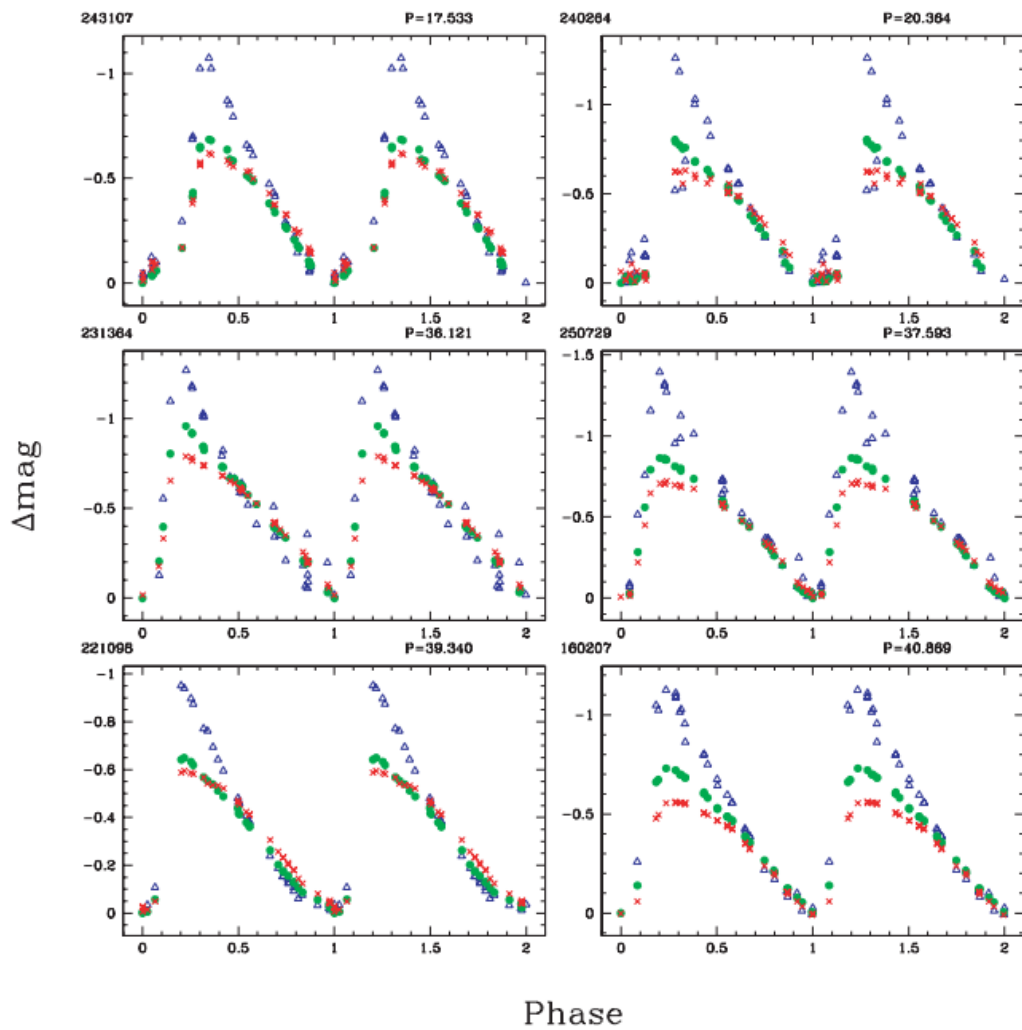


Figure 3.1: Example Sloan-band Cepheid light curves. Open blue triangles are g' observations, filled green circles are r' , and red crosses are i' . Figure from Hartman et al. (2006).

¹<http://www.astro.ljmu.ac.uk/~dfb/M33/>

NumEt	RA	DEC	Perd1	Perd2	Perd3	MeanMag	MaxAoV	Sigma	NbMes	R0	R1	Phi1	R21	Phi21	DR21	DPhi21	R31	Phi31	DR31	DPhi31	RA_deg	DEC_deg
20016	01:35:09.31	+31:05:43.6	2.30915	4.61847	1.75493	22.102	10.829	0.281	31	22.256	0.345	0.945	0.436	3.901	0.091	0.250	0.184	2.190	0.822	1.508	23.7887916666	31.0954444444
20019	01:35:09.69	+31:05:21.5	2.81125	1.90174	1.54568	22.288	16.754	0.195	31	22.292	0.205	-0.587	0.411	4.400	0.066	0.148	0.319	2.764	1.122	2.260	23.7903749999	31.0893055555
20020	01:35:09.71	+31:00:30.5	2.05397	4.10803	1.93805	22.378	15.091	0.288	31	22.393	0.324	2.291	0.576	3.904	0.052	0.119	0.274	1.362	0.693	1.046	23.7904583333	31.0084722222
20024	01:35:10.30	+30:56:17.4	3.94455	1.33469	7.8838	21.658	20.512	0.138	31	21.665	0.166	-0.070	0.331	4.286	0.065	0.213	0.209	2.506	1.122	4.771	23.7929166666	30.9381666666
20029	01:35:10.52	+31:05:15.0	2.30283	1.75843	4.63085	22.226	11.488	0.249	31	22.284	0.278	1.852	0.565	4.166	0.089	0.186	0.306	2.494	0.851	0.647	23.7938333333	31.0875000000
20045	01:35:12.39	+30:59:04.3	10.3426	2.71067	2.46307	20.757	12.562	0.203	31	20.846	0.326	-2.698	0.332	5.097	0.056	0.157	0.157	3.591	0.856	1.212	23.8016249999	30.9845277777
20083	01:35:16.51	+31:04:21.9	4.10030	1.31772	1.60447	21.625	34.249	0.249	31	21.558	0.320	1.819	0.442	4.171	0.041	0.141	0.123	2.272	0.820	0.919	23.8187916666	31.0727500000
20097	01:35:18.12	+31:05:18.2	2.27004	1.77850	4.53915	22.397	28.857	0.238	31	22.394	0.270	2.004	0.457	4.025	0.054	0.172	0.253	2.231	1.053	1.731	23.8255000000	31.0883888888
20099	01:35:18.19	+31:03:04.2	2.80549	1.55319	1.46920	22.341	11.284	0.118	31	22.323	0.145	2.807	0.419	4.363	0.097	0.275	0.202	2.168	1.899	4.063	23.8257916666	31.0511666666
20128	01:35:23.33	+31:02:29.9	3.27782	1.43368	6.55255	22.107	23.292	0.158	31	22.134	0.212	-2.262	0.487	4.623	0.064	0.187	0.243	3.149	0.674	5.112	23.8472083333	31.0416388888
20169	01:35:30.87	+30:58:05.9	2.48647	4.97248	1.66497	22.305	35.316	0.287	31	22.344	0.288	-0.702	0.610	4.245	0.042	0.105	0.338	2.514	0.432	2.937	23.8786250000	30.9683055555
20172	01:35:32.14	+31:02:50.9	2.23696	4.44909	1.80788	22.375	17.177	0.285	31	22.331	0.355	0.315	0.353	3.985	0.074	0.216	0.289	1.942	0.193	2.420	23.8839166666	31.0474722222
30006	01:34:37.30	+30:58:22.6	3.89166	1.34089	3.40322	21.708	26.923	0.334	31	21.765	0.351	-0.539	0.404	4.236	0.052	0.166	0.328	2.319	0.464	1.673	23.6554166666	30.9729444444
30013	01:34:37.53	+31:04:21.9	2.63878	1.60983	3.13000	22.368	14.801	0.237	31	22.362	0.293	-2.404	0.455	4.140	0.085	0.230	0.351	2.606	0.977	0.427	23.6563749999	31.0727500000
30018	01:34:37.81	+31:07:18.0	2.94302	5.88595	1.58979	22.294	13.481	0.124	31	22.310	0.156	0.097	0.230	5.926	0.109	0.482	0.134	3.43	0.931	10.626	23.6575416666	31.1216666666
30023	01:34:38.15	+30:55:53.3	2.60813	1.61480	5.21546	21.913	29.517	0.114	31	21.950	0.154	-1.245	0.055	3.697	0.039	0.694	0.075	4.124	0.709	22.954	23.6589583333	30.9314722222
30029	01:34:38.82	+31:01:41.9	8.60368	1.12786	2.16592	20.877	39.351	0.143	31	20.851	0.172	0.116	0.402	5.136	0.033	0.112	0.135	3.839	1.565	6.703	23.6617500000	31.0283055555
30035	01:34:38.97	+31:04:29.4	3.18205	2.90695	1.45789	21.880	22.998	0.240	31	21.794	0.333	-1.092	0.504	4.054	0.042	0.114	0.246	2.033	0.705	0.992	23.6623749999	31.0748333333
30044	01:34:39.35	+30:58:40.1	2.62828	1.60751	3.89333	22.394	16.788	0.308	31	22.461	0.325	-2.733	0.468	4.398	0.080	0.203	0.364	2.518	0.496	1.982	23.6639583333	30.9778055555
30047	01:34:39.41	+31:03:35.9	2.16583	1.84791	4.33356	22.420	33.544	0.250	31	22.507	0.264	1.243	0.458	4.142	0.057	0.172	0.189	2.087	0.585	6.104	23.6642083333	31.0599722222
30059	01:34:39.80	+30:56:18.8	2.75777	1.56204	1.15676	22.299	18.765	0.160	31	22.258	0.198	-2.353	0.368	4.361	0.065	0.245	0.121	2.191	1.415	1.922	23.6658333333	30.9385555555
30063	01:34:39.87	+31:06:50.0	2.74005	1.56829	1.56829	22.044	37.915	0.248	31	22.042	0.304	-2.360	0.474	4.197	0.033	0.089	0.234	2.305	0.820	0.271	23.6661250000	31.1138888888
30066	01:34:39.88	+31:04:29.5	2.58405	1.63143	1.43934	22.235	20.649	0.189	31	22.297	0.220	2.720	0.569	4.309	0.075	0.176	0.222	2.553	1.305	1.735	23.6661666666	31.0748611111
30073	01:34:40.07	+31:07:33.0	3.09878	1.47052	6.19723	21.939	34.760	0.291	31	21.910	0.328	1.700	0.447	4.157	0.070	0.213	0.319	2.579	0.994	0.627	23.6669583333	31.1258333333
30075	01:34:40.12	+30:59:05.6	3.14797	1.45977	1.81314	21.599	7.7750	0.210	31	21.602	0.206	-2.966	0.649	4.355	0.076	0.157	0.521	1.890	1.101	2.398	23.6671666666	30.9848888888
30076	01:34:40.26	+31:05:26.8	1.61462	4.24089	2.62446	22.714	18.335	0.202	31	22.705	0.205	-1.151	0.628	3.835	0.124	0.265	0.354	2.060	1.336	0.817	23.6677499999	31.0907777777
30081	01:34:40.58	+31:08:36.8	1.96763	1.96763	2.4696	22.415	21.246	0.301	31	22.395	0.318	-0.223	0.561	4.086	0.065	0.149	0.256	2.214	0.779	0.299	23.6690833333	31.1435555555
30088	01:34:40.80	+31:06:49.3	2.28268	1.77869	4.5657	22.078	20.389	0.263	31	22.101	0.304	-1.815	0.450	4.253	0.062	0.173	0.245	1.841	0.431	3.523	23.6699999999	31.1136944444
30090	01:34:40.84	+31:06:43.9	3.66939	7.33906	4.1933	21.964	11.870	0.117	31	21.985	0.154	2.831	0.385	4.395	0.067	0.213	0.177	2.340	1.775	1.684	23.6701666666	31.1121944444
30101	01:34:41.61	+31:08:43.8	2.08176	1.34833	3.8267	22.395	21.323	0.221	31	22.339	0.291	-0.923	0.422	4.110	0.066	0.194	0.149	2.020	0.737	5.304	23.6733750000	31.1455000000
:	:	:	:	:	:	:	:	:	:	:	:	:	:	:	:	:	:	:	:	:	:	:

Table 3.1: Sample of the fundamental mode Cepheid catalogue by Hartman et al. The J2000 celestial coordinates are stored under the RA/DEC columns, (most likely) periods are under Perd1, and mean instrumental r' -band magnitudes under MeanMag. Fourier parameters are also available.

Deep median stacks were created using the best-seeing images from the three filters with the MegaPipe Pipeline (Gwyn, 2008). Figure 3.2 shows the median stack in the r' band. Table 3.2 lists the number of input frames and quality for each stacked image.

Filter	Frames	Image quality (arcsec)
g'	17	0.88
r'	15	0.85
i'	17	0.74

Table 3.2: Number of input frames and resulting image quality for each CFHT stacked image.



Figure 3.2: Stacked sky-subtracted, r' -band CFHT image of M33.

3.1.2 INT images

Additional images of the galaxy were taken by V. Scowcroft in October 2008 with the Wide Field Camera (WFC) at the Isaac Newton Telescope (INT) with filters similar to the ones used by Hartman et al. at the CFHT facility. The WFC detector comprises four CCDs, each with a pixel count of 2048×4100 at a scale of 0.333 arcsecond/pixel. The chip configuration provides a field of view of ~ 0.3 degree². In the same observing run, observations were made of the Sloan Digital Sky Survey (SDSS) Stripe 82 Region to provide standard stars for calibration purposes. On a separate observing session, around 50 r' -band images of M33 were taken with the aim of identifying and analysing double-mode Cepheids. The debiasing and flat-fielding of the INT images were achieved with the IRAF CCDPROC packages.

Stacks of the INT images were created and provided by L. Short (priv. comm.) and will hereafter be referred to as the LS stacks.

Figure 3.3 shows the respective CCD configurations for CFHT's MegaCam and INT's WFC.

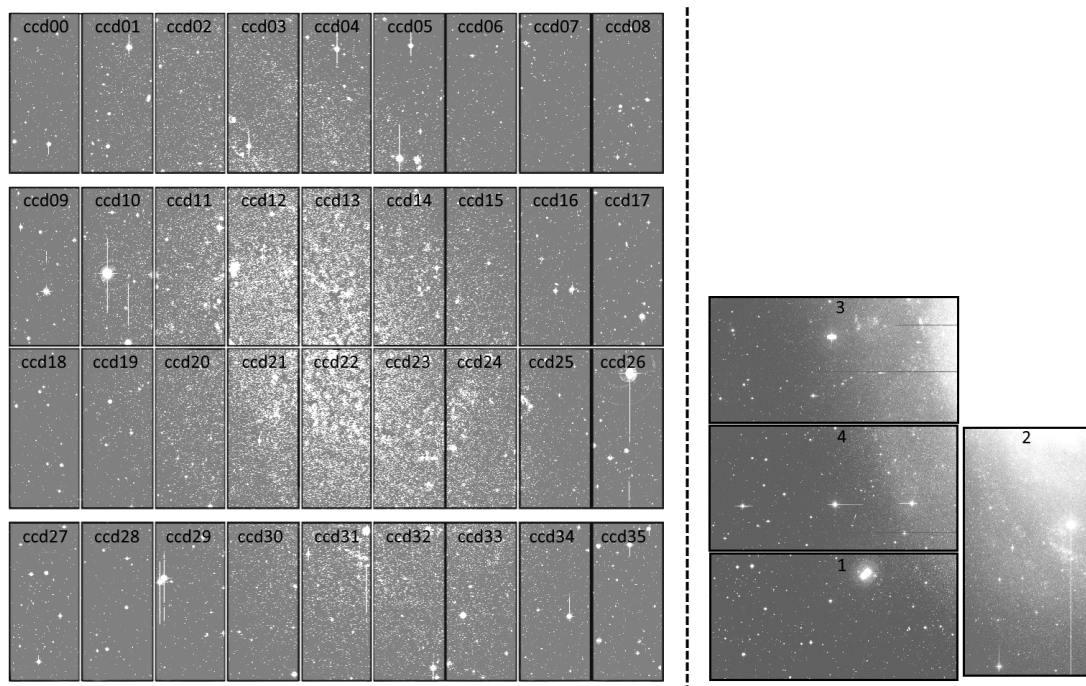


Figure 3.3: *Left*: Configuration of the CFHT MegaCam chips. *Right*: Configuration of the INT WFC chips.

3.2 PSF photometry

This section describes the procedure taken to acquire instrumental stellar magnitudes from the CFHT and INT images of M33.

The disk of the galaxy shows substantial levels of stellar crowding where the profiles of neighbouring stars are in close proximity or overlap, rendering aperture photometry unsuitable for acquiring accurate magnitudes. An aperture centred on a source is likely to pick up extraneous flux from neighbouring sources, thereby overestimating the brightness of the star being measured. Furthermore, estimating the sky value around the source would be unfeasible as the sky annulus itself can be substantially contaminated with stellar flux from neighbours. To mitigate the effects of crowding, point spread function (PSF) fitting photometry is used instead of solely aperture photometry.

Stars are sufficiently far away that they are effectively point sources of light. Atmospheric effects and the optics of the telescope will act to smear out the light before it reaches the CCD. The extended image of a star on the CCD (referred to as the PSF) is roughly Gaussian in appearance and its profile is reflective of the distortions encountered along its path. The profile can vary with position, time and filter.

PSF photometry relies on measuring the flux from a source through a small aperture and on creating a model of the stellar profile on the CCD (i.e., PSF modelling). The PSF model is fitted against the detected sources and scaled to match the flux measurements to acquire PSF magnitudes. The main advantage PSF photometry has over aperture photometry is that multiple sources can be fitted and measured simultaneously; the profiles of stars in close apparent proximity can be disentangled from one another, lessening the effects of flux contamination.

Instrumental photometry of the CFHT and INT images was undertaken with the photometry software packages Source Extractor (SExtractor; [Bertin and Arnouts 1996](#)) and PSF Extractor (PSFEx; [Bertin 2011](#)) with configuration files suitably modified for each set of images. The order of operations to acquire PSF magnitudes with these

software programs is:

1. Create a catalogue of small-aperture magnitudes of detected sources in the image with SExtractor.
2. Use PSFEx to build a (variable) PSF model using the output catalogue from the previous step as input.
3. Use the PSF model from PSFEx as an input for a second pass of SExtractor over the image to measure PSF-fitted magnitudes.

The SExtractor+PSFEx software suite were chosen over the PSF photometry applications DAOPHOT ([Stetson, 1987](#)) and ALLSTAR ([Stetson, 1994](#)) which have been traditionally used for crowded stellar fields for a variety of reasons:

1. SExtractor+PSFEx offers a finer level of control over the parameters governing the detection, extraction and fitting procedures.
2. It outputs a considerably greater number of useful parameters concerning stellar properties and effectiveness of the detection and extraction procedures.
3. It can generate useful diagnostic files concerning the input images and its flux sources such as a map of the measured stellar FWHM over the image.
4. It offers a multitude of file formats for the output catalogues, including formats that allows the catalogues to be readily viewed and manipulated using software like Python and TOPCAT (Tool for Operations on Catalogues And Tables, [Taylor 2005](#)).
5. It is able to go deeper by ~ 2 magnitudes in the B band than DAOPHOT+ALLSTAR while still being able to separate stars and background galaxies ([Annunziatella et al., 2013](#)).

3.2.1 SExtractor+PSFEx procedure

SExtractor identifies and performs aperture photometry on point-like and extended sources in astronomical images, producing a catalogue of various parameters. The aperture photometry procedure of SExtractor follows these steps: (1) a model of the background is created and subtracted from the image, (2) the image is filtered with an input convolution kernel, (3) thresholding and segmentation of the image is performed to detect sources, (4) composite objects are deblended, and finally (5) the fluxes from the sources are measured.

Background estimation SExtractor makes an initial pass through the pixel data of the image and calculates a local background value for each cell in a generated mesh covering the image. The background value is calculated by first iteratively clipping the background histogram until a convergence of $\pm 3\sigma$ around its median is reached, then by taking the mean of the final histogram. If σ changes by more than 20% during the clipping procedure, the field is considered to be crowded, and a “mode” is taken as the estimate background value. The “mode” in this case is calculated as

$$\text{mode} = 2.5 \times \text{median} - 1.5 \times \text{mean} \quad (3.1)$$

A median filter is then applied to compensate for overestimates due to potential bright stars. By applying a bicubic-spline interpolation to the filtered mesh, a background map is created. Figure 3.4 shows a subregion of the CFHT r' -band stack and its corresponding background map.

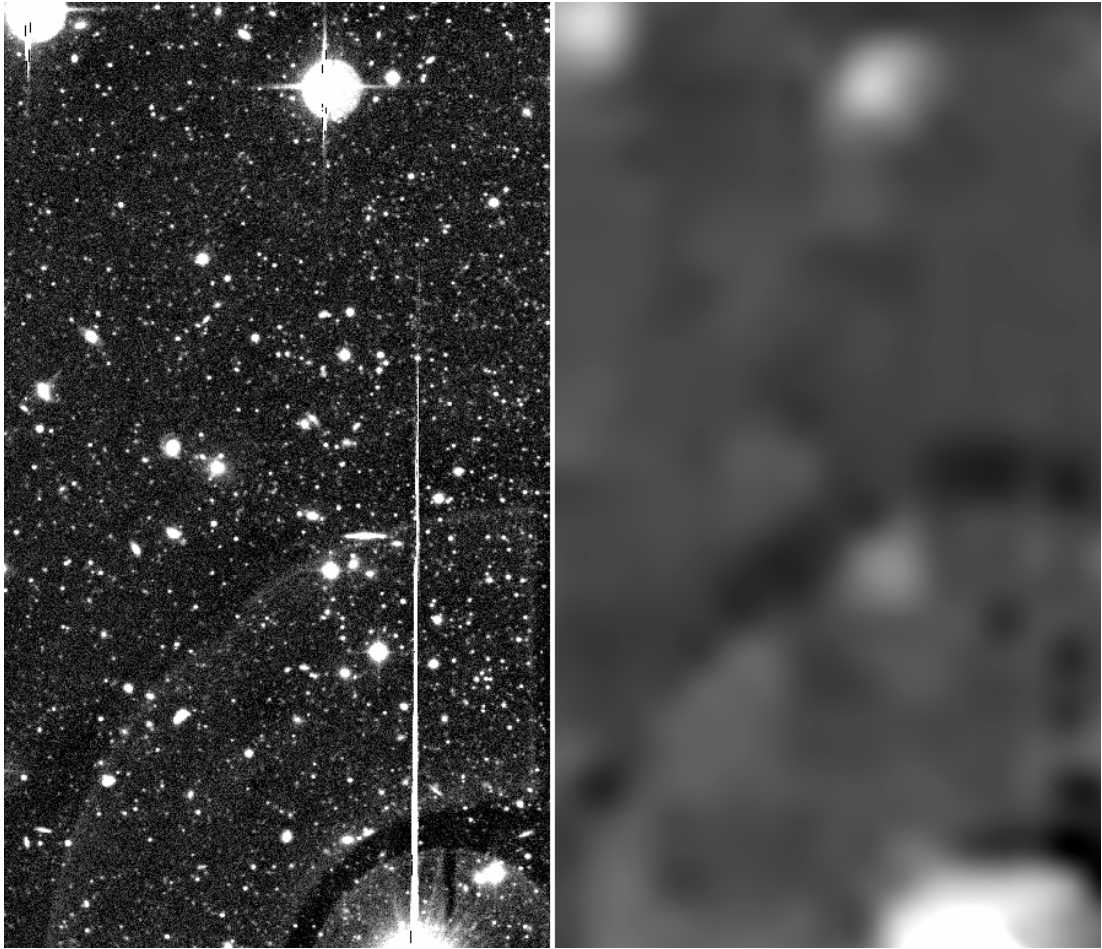


Figure 3.4: *Left*: 1000×2000 pixel subregion of the CFHT r' -band stack. *Right*: Background map of the subimage.

The background value for each detected source is then simply the value from the background map at the source's centroid. A rectangular annulus around a source can then be toggled on to calculate a local correction to the initial background value.

Image filtering To aid the detection of sources in an image, a filter can be applied. Bundled with SExtractor are various convolution kernels suited for aiding the detection of various object types in various environments. The crowded nature of the M33 images and seeing of $\text{FWHM} \simeq 5$ pixels makes the `mexhat_5.0_11x11.conv` (see Figure 3.5) well suited for the task.

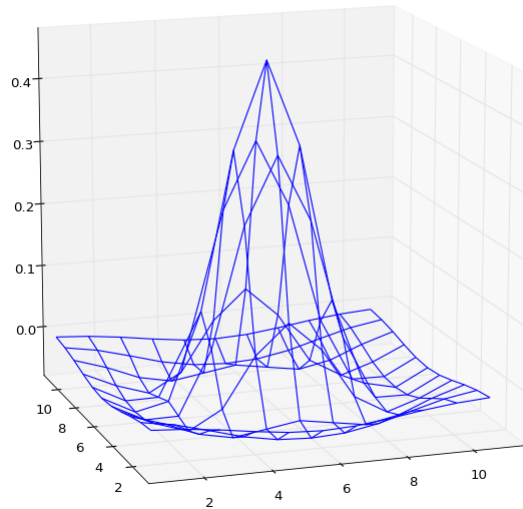


Figure 3.5: SExtractor’s Mexican hat kernel.

Thresholding and segmentation Every pixel with a value above a certain threshold is considered to be part of an object. The threshold is set to either some value relative to the background RMS or to an absolute value.

A contiguous group of pixels above the threshold may represent the profile of a single object — be it a star or galaxy — or may be several objects in close proximity with overlapping profiles. Each of these pixel groups are considered segments of the image. SExtractor attempts to separate these segments into their overlapping constituents with a deblending procedure.

Deblending For each group of adjacent pixels, SExtractor constructs a tree with each branch occurring at each saddle point (see Figure 3.6). Each branch is considered to be a separate object when the following conditions are met: (1) the branch contains more than a certain fraction of the total number of counts from the contiguous group of pixels, and (2) there is at least one other branch meeting the same fractional criteria that is also at the same level.

Magnitude measurements SExtractor offers various types of magnitude measurements. Most — but not all — are discussed in detail in the documentation; for brevity, only fixed-aperture, growth, and PSF-fitting flux measuring methods will be discussed here as these magnitudes were used in this work.

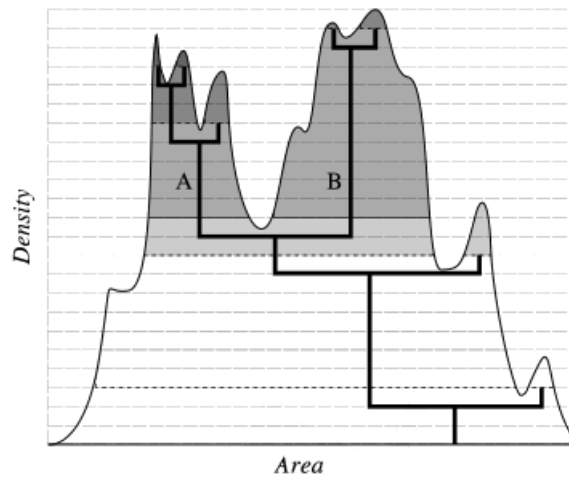


Figure 3.6: SExtractor’s deblending procedure. Two components labelled A and B are found in this segment.

For fixed-aperture, the user defines the aperture size(s) in the configuration file and SExtractor measures the total flux in a circular aperture centred on a detected source.

The growth magnitude is a magnitude measured through a circular aperture whose size is automatically adjusted on a source-by-source basis, depending on the FWHM of the source being measured. The radius is defined as the greater of the following two values: 3 times the source’s major axis of the RMS light distribution or the first “PHOT_AUTOAPERS” parameter in the configuration file.

SExtractor currently does not natively support PSF-fitting photometry by itself. The companion tool PSFEx is required for this purpose. PSFEx identifies objects in the first SExtractor catalogue of aperture magnitudes that are likely to be point sources. A subsample of point-like sources is then selected based on their characteristics to construct a PSF model; objects with too low signal-to-noise, too high ellipticity, etc. are discarded during the PSF model-building procedure. The final sample of stars is ideally distributed across the entire image so that position-dependent variations are properly traced. The PSF is modelled as a combination of basis vectors in the form of small images. Figure 3.7 shows a collection of stars chosen by PSFEx for PSF modelling and the residuals after subtracting the model. Figure 3.8 shows a grid of how a PSF model varies across an image. Figure 3.9 shows a stack subimage, a computed

model of the stars in that image, and the residuals after model subtraction.

The output PSF model and the image from which it was built are then fed into SExtractor for a second pass. From this second pass of SExtractor with a PSF model, new output parameters based on PSF fitting become available; these include PSF magnitudes and PSF positions. Multiple neighbouring sources can be fitted simultaneously with the PSF model to alleviate the effects of crowding, providing more robust magnitude measurements.

SExtractor provides a flag value for each measured object to indicate warnings during the magnitude measurement procedure. Warnings include the presence of bright neighbours that may bias aperture photometry and the blending² of the measured star with another object. Flag values are provided as sums of powers of 2 and each power of 2 represents a different warning. For example, a flag value of 1 indicates that the measured object has neighbours that are bright and close enough to bias photometry using an “automatic” aperture size or if the object profile contains bad pixels. A flag value of 2 means the object was originally blended with another object. A flag value of $3 = 2 + 1$ would therefore mean the object was originally blended and has bright neighbours and/or bad pixels.

For every instance of PSF photometry on CFHT and LS stacks, SExtractor’s double image mode was invoked. In double image mode, one image is used to identify the positions of the sources while the flux measurements are carried out on the other image at those same positions. This mode requires that the two images have the same dimensions and are registered so that the sources lie at the same pixel coordinates. The r' -band images were used as the detection image for their respective image sets as they go deeper and have better signal-to-noise than the other two filters.

²What SExtractor refers to as blending is the overlapping of stellar profiles even if the individual stars are separated by a distance greater than the Rayleigh Criterion and are therefore resolvable.

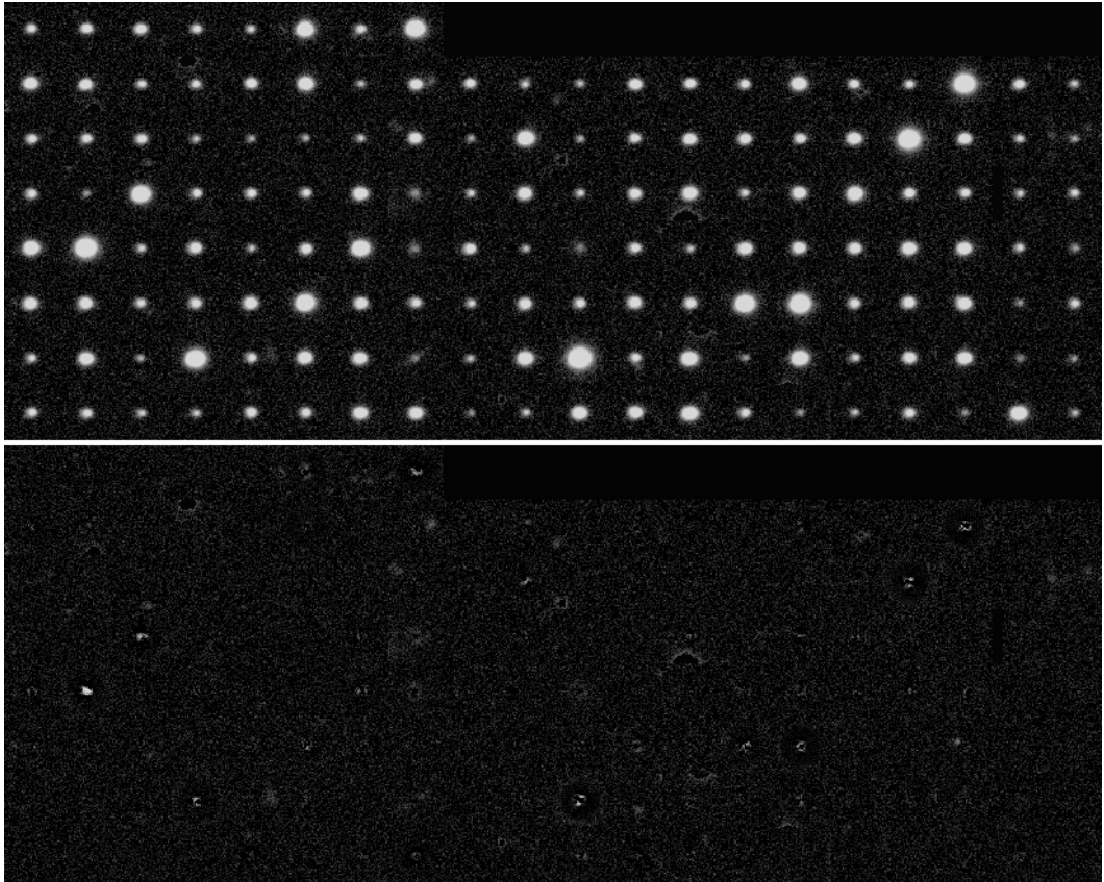


Figure 3.7: *Top*: Stars chosen by PSFEx for PSF modelling. *Bottom*: Residuals after fitting PSF stars with constructed PSF model. Images are on the same scale.

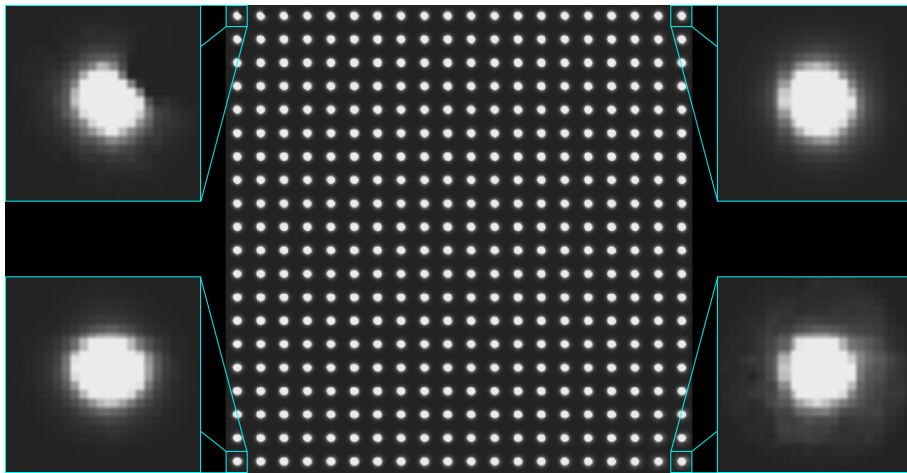


Figure 3.8: Grid of a position-dependent PSF model produced by PSFEx at various locations. The PSFs at the corners are magnified to illustrate the variation of the model across the field.

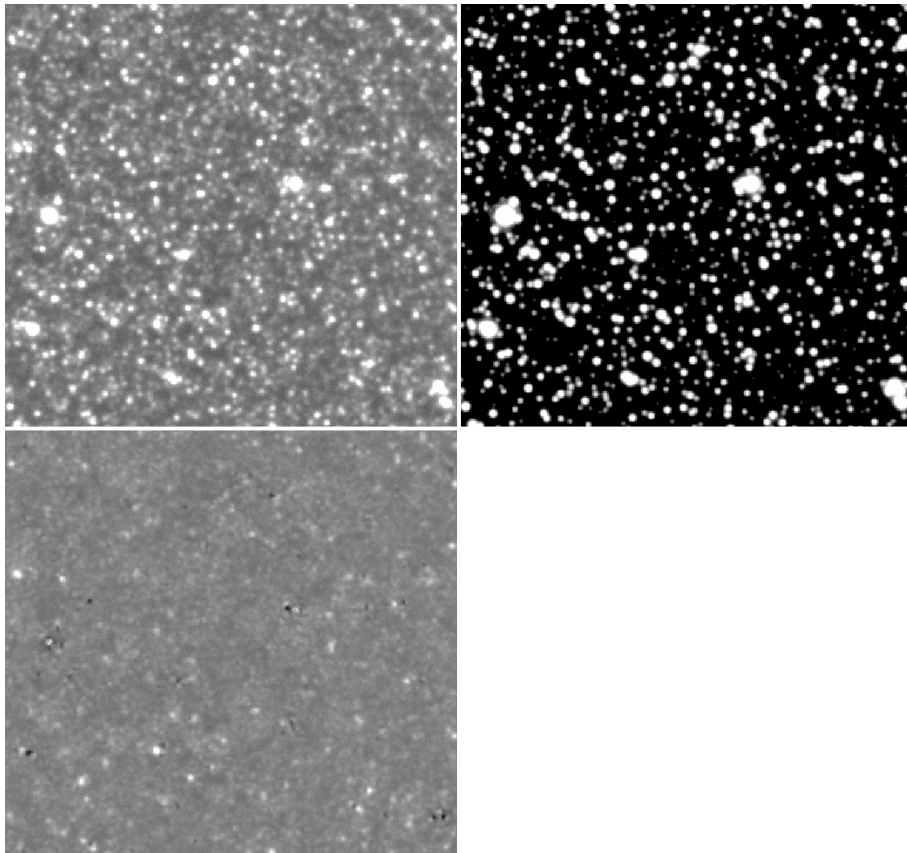


Figure 3.9: *Top left*: Sample image. *Top right*: Computed PSF models of the detected sources. *Bottom left*: Residual image after subtracting the PSF models from the original image.

The three CFHT stacked images are $\sim 20000 \times 20000$ pixels in size. Performing aperture and PSF-fitting photometry on an entire image would be computationally demanding. To alleviate this issue, each of the CFHT stacks is split into 16 subimages of size $\sim 5500 \times 5500$ pixels. The subimages overlap with each adjacent subimage by $\sim 500 \times 5500$ pixels. This was done to enable the direct comparison of measured PSF magnitudes of the same stars from two different subimages with the aim of identifying the presence of any systematic or differential inconsistencies. The total number of stars detected during the aperture photometry phase and the number of stars chosen for the PSF modelling procedure are shown for each subimage and filter in Figure 3.10. Figure 3.11 shows the difference in measured PSF magnitudes for the same stars in the overlapping region between two r' -band subimages; the mean difference here is 0.0004 mag with a standard deviation of 0.074 mag. All other comparisons yield similarly acceptable results.

128031 (2704)	164604 (2978)	129812 (2685)	67323 (603)
108542 (969)	127472 (1175)	85427 (669)	34301 (142)
240271 (3450)	256046 (4685)	242517 (3371)	220156 (742)
245504 (2452)	338140 (1813)	326026 (2472)	196667 (2979)
248658 (2340)	336953 (2371)	312011 (2784)	184174 (1520)
323393 (5847)	393213 (2631)	380092 (4282)	292027 (5460)
162820 (3092)	313314 (1739)	339623 (2151)	263216 (2194)
153275 (1842)	313373 (2318)	344319 (3107)	273592 (2125)
276950 (4735)	370757 (3738)	392410 (3221)	331249 (5408)
55619 (572)	110278 (1929)	148118 (2909)	109232 (1862)
31236 (524)	76116 (1211)	119346 (1952)	93999 (1308)
210412 (652)	227111 (2445)	241214 (4372)	216702 (2764)

Figure 3.10: In each square subimage, the number of stars detected during aperture photometry and the number of those stars that were automatically chosen for PSF modelling are respectively listed as the unbracketed and bracketed values. Green values represent the counts in the g' filter, red for r' , and orange for i' . The overlapping configuration of the subimages is not shown for clarity.

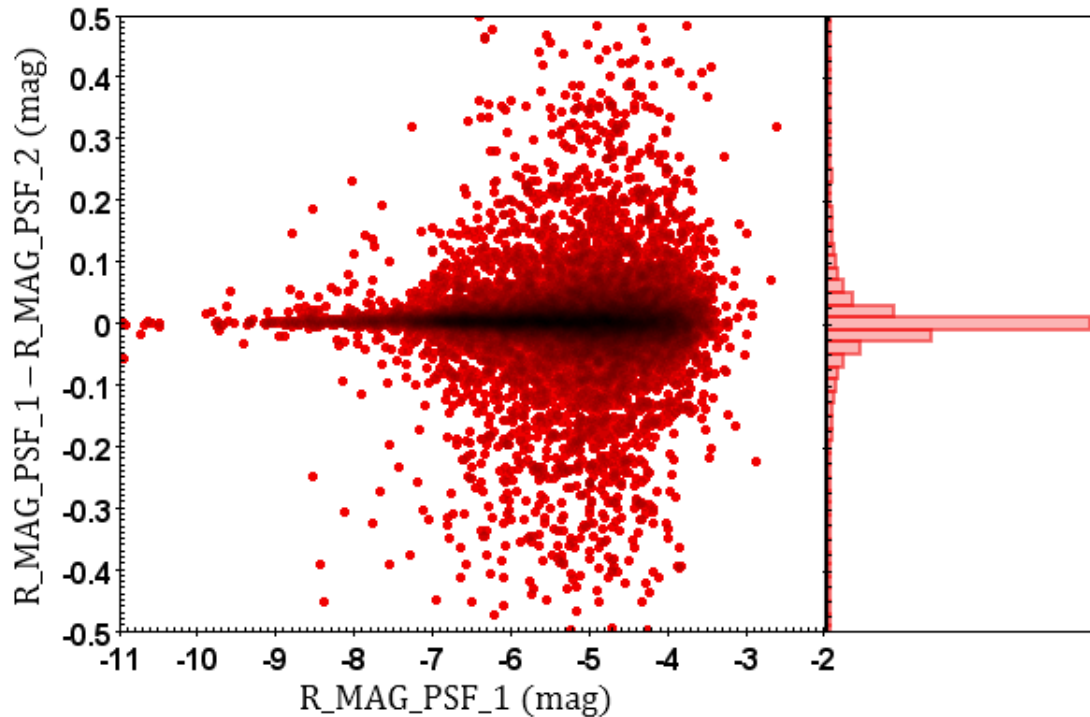


Figure 3.11: Comparison of measured PSF magnitudes for the same stars from the overlapping region of two adjacent r' -band subimages.

3.2.2 Aperture corrections

A caveat of PSF photometry is that it outputs *relative* magnitude values. It is necessary to bring the relative PSF magnitudes to a common instrumental photometric system with an aperture correction. This is usually achieved by measuring the magnitudes of bright, unsaturated and isolated stars through a large aperture to capture most if not all of the stellar flux and by determining the offset between the PSF and large-aperture magnitudes. Given that the images in the data set may not have stars that satisfy these criteria due to crowding, a slightly different approach was taken.

SExtractor has the ability to mask out nearby objects during the aperture photometry of a source to reduce flux contamination, a particular advantage in crowded fields. For the large aperture photometry step, SExtractor's *growth* magnitude is used as it yielded more consistent magnitudes for the same stars imaged during different epochs than straightforward fixed-aperture photometry.

3.3 Calibration

For the magnitude data to be scientifically viable and for meaningful comparisons to be made, it is necessary to calibrate them to a standard photometric system.

The images in this work have been taken through Sloan-like g' , r' , and i' filters at the CFHT and INT. As shown in Figure 3.12, the transmission profiles of the filters at these facilities do not match the SDSS system exactly. This introduces systematic errors in the measured magnitudes of stars as the slight differences in filter transmission results in slight differences in the sampling of a star's spectral energy distribution. These errors can manifest themselves as a colour-dependent parameter.

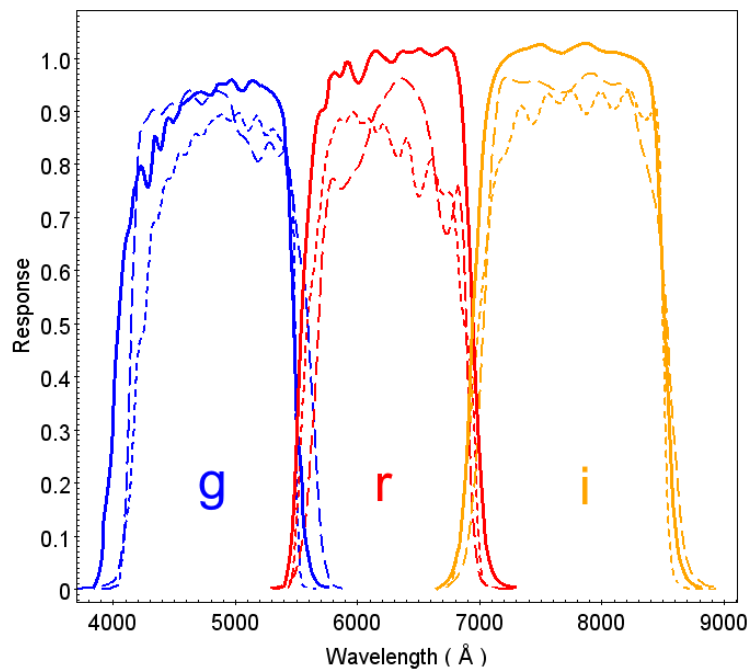


Figure 3.12: Filter curves from INT (short dashed lines), CFHT (long dashed lines) and SDSS (solid lines). The quantum efficiency of the CCDs at each facility and atmospheric effects (not shown here) impart additional variations.

The Earth's atmosphere acts to attenuate the light from celestial sources — the greater the path length through the atmosphere, the greater the attenuation. Over the course of an observation run on a given night, the sources being imaged will occupy different positions in the sky. For celestial sources observed closer to the horizon, more atmosphere is present along the line of sight than if the source were near zenith, resulting

in higher extinction. The path length through the atmosphere is known as the air mass and is a key parameter in the calibration of the instrumental INT data.

For the calibration procedure, Image Reduction and Analysis Facility (IRAF) software packages were used.

3.3.1 INT

The SDSS Stripe 82 region covers an area of ~ 300 degree² on the celestial equator that has been repeatedly observed in the Sloan *ugriz* filters (Jiang et al., 2014). A catalogue of Sloan magnitudes, sky positions and other parameters for the observed stars in this region was requested and downloaded from the SDSS website³.

The SDSS Stripe 82 catalogue stars were matched on the basis of sky position with the INT-observed stars in order to create solutions to transform instrumental magnitudes to the standard system. The solutions for each chip and filter initially took the form

$$m_{\text{Inst}} = m_{\text{SDSS}} + Z_p + (k \times l) + (c \times Col) \quad (3.2)$$

where m_{Inst} is the instrumental magnitude, m_{SDSS} is the SDSS catalogue magnitude, Z_p is the zero point, l is the air mass⁴, Col is the colour index. For the calibration of g' magnitudes, $g' - r'$ colours were used. Both r' and i' calibrations used $r' - i'$ colours.

During the initial calibrations, a radial dependence became apparent when comparing the residuals between the ‘‘calibrated’’ INT magnitudes and the SDSS catalogue magnitudes (see Figure 3.13). This radial dependence may be a symptom of a lack of a position-dependent aperture correction. Position terms were then included in the calibration solutions to account for this effect

$$m_{\text{Inst}} = m_{\text{SDSS}} + Z_p + (k \times l) + (c \times Col) + (d \times X) + (e \times Y) \quad (3.3)$$

³<http://skyserver.sdss.org/dr12/en/home.aspx>

⁴Air mass is usually represented with X .

where X is the horizontal position of the star on the CCD and Y is the vertical.

The air mass coefficient k should — in theory — be identical for all chips in a given filter as it is solely a measure of atmospheric extinction. Initial solutions show that the value for k varies slightly between the chips. Various exploratory solutions were determined for each chip with various fixed- k values. The quality of the solutions in terms of RMS and reduced- χ were found to vary with the fixed- k values, while the zero point term Z_p changes with k to compensate for the resulting residuals. For each filter, a value of k that produced minimal values for RMS and reduced- χ for all four chips was chosen as the adopted value.

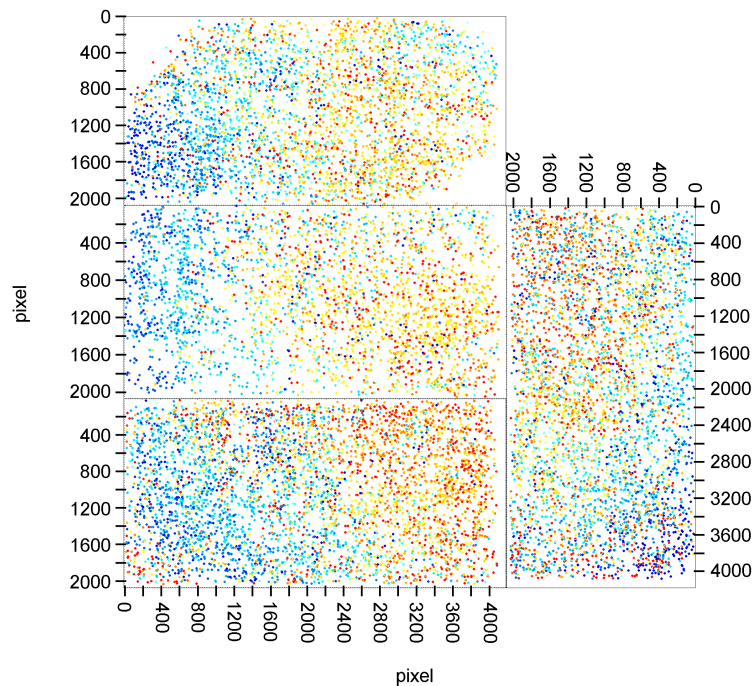


Figure 3.13: Stripe 82 stars that have their INT instrumental magnitudes calibrated are plotted on their observed positions on the INT chips and are colour coded based on their SDSS – INT magnitude residual. Bluer points have a more positive SDSS – INT magnitude residual, i.e., they are measured to be brighter. It is apparent that the further a star is from the focal point, the larger the discrepancy between the SDSS and INT magnitudes.

With the solutions for the INT chips now finalised, the instrumental magnitudes of the single-epoch INT M33 images were transformed to the standard system.

Photometry of the INT LS stacks revealed the presence of many more sources at dimmer magnitudes. The PSF magnitudes of the LS stacks were then calibrated against

Filter	Z	k	c	d	e	RMS
Chip 1						
g'	-30.411	0.166	-0.143	-0.589×10^{-5}	1.847×10^{-5}	0.034
r'	-30.053	0.089	-0.007	-2.524×10^{-5}	2.571×10^{-5}	0.027
i'	-29.593	0.056	-0.059	-3.365×10^{-5}	2.288×10^{-5}	0.032
Chip 2						
g'	-30.063	0.166	-0.134	1.511×10^{-5}	-1.595×10^{-5}	0.036
r'	-29.722	0.089	0.001	2.990×10^{-5}	-1.667×10^{-5}	0.031
i'	-29.242	0.056	-0.067	2.382×10^{-5}	-2.453×10^{-5}	0.034
Chip 3						
g'	-30.273	0.166	-0.147	-6.734×10^{-5}	2.628×10^{-5}	0.047
r'	-30.103	0.089	-0.005	0.155×10^{-5}	1.826×10^{-5}	0.027
i'	-29.683	0.056	-0.094	-0.804×10^{-5}	1.914×10^{-5}	0.028
Chip 4						
g'	-30.207	0.166	-0.142	-0.155×10^{-5}	1.719×10^{-5}	0.028
r'	-29.902	0.089	0.001	0.212×10^{-5}	1.892×10^{-5}	0.027
i'	-29.500	0.056	-0.067	-1.842×10^{-5}	2.149×10^{-5}	0.030

Table 3.3: Calibration solutions for the INT chips.

the calibrated single-epoch M33 magnitudes.

From the LS stacks, $\sim 580,000$ objects were detected across the g' , r' , and i' bands and were catalogued. Colour-magnitude diagrams (CMDs) of the LS stack M33 stars are presented in Figures 3.14 and 3.15. The main sequence is visible as the leftmost vertical structure and the giant branch is located to the right in the two CMDs. It should be noted that the CMDs have not been cleaned of foreground Milky Way stars.

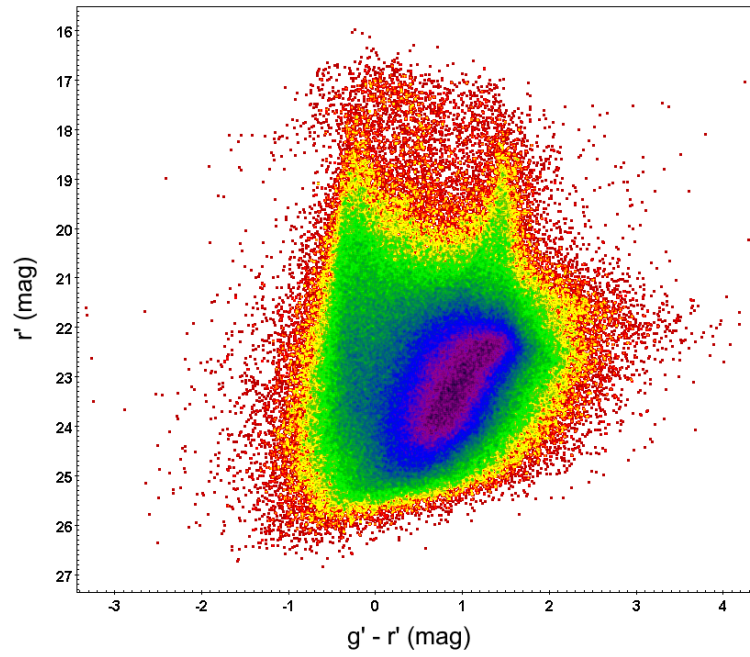


Figure 3.14: r' versus $g' - r'$ CMD using stars from the LS stack catalogue. Denser regions are more violet.

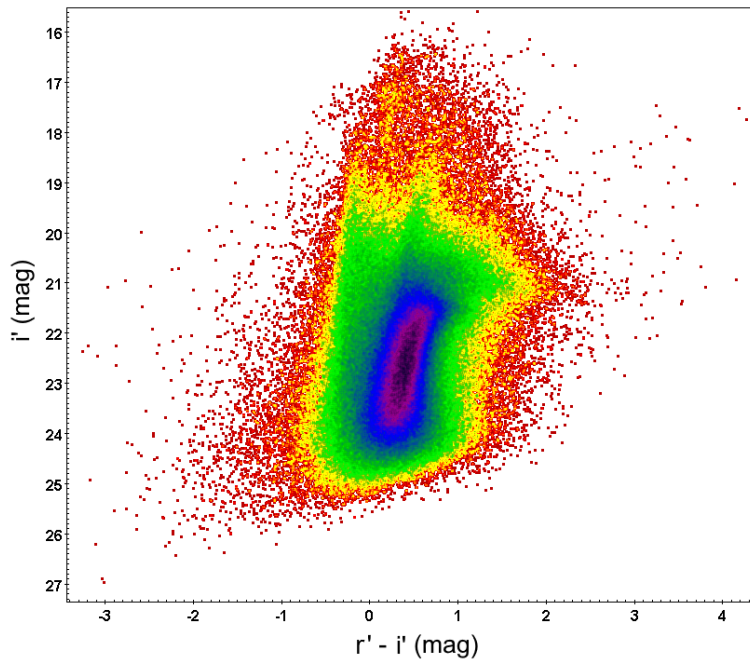


Figure 3.15: i' versus $r' - i'$ CMD using stars from the LS stack catalogue. Denser regions are more violet.

3.3.2 CFHT

The instrumental magnitudes of the deep CFHT stacks required calibration on a chip-by-chip basis. Each of the input mosaic frames for each stacked image comprise 36 subimages from 36 CCDs that are not necessarily identical in their response. The stars in the CFHT stacks were separated into 36 groups corresponding to the positions of the 36 CCDs and were calibrated separately with the stacked INT image magnitudes as reference.

The single-epoch g' and i' observations were dithered slightly such that there exists certain regions on the stacks — or equivalently, certain regions of the sky — that have been imaged on the same chip for all frames. Those regions cover a subsection of every chip and are shown schematically in Figure 3.16. The chip-by-chip calibration of the instrumental CFHT g' , r' , i' magnitude data relied upon the stars imaged exclusively on the same chip in all of the stacks' input frames. This is to ensure that the calibration solutions for each chip are not contaminated by magnitude data captured by neighbouring chips. Figure 3.17 shows the regions in the g' -band stack where the sky falls on the same chips in all input frames. From each chip subregion and filter, the 400 brightest stars were used for the calibration procedure.

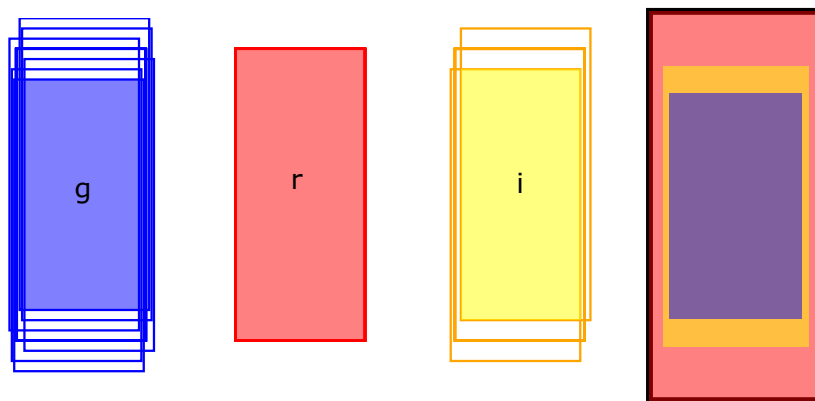


Figure 3.16: For the three leftmost images, the relative positions of the chip boundaries show the extent of the dithering in the three filters, and the shaded areas represent the chip subregions that have imaged the same regions of sky for all frames. The rightmost image compares the shaded regions for the three filters.

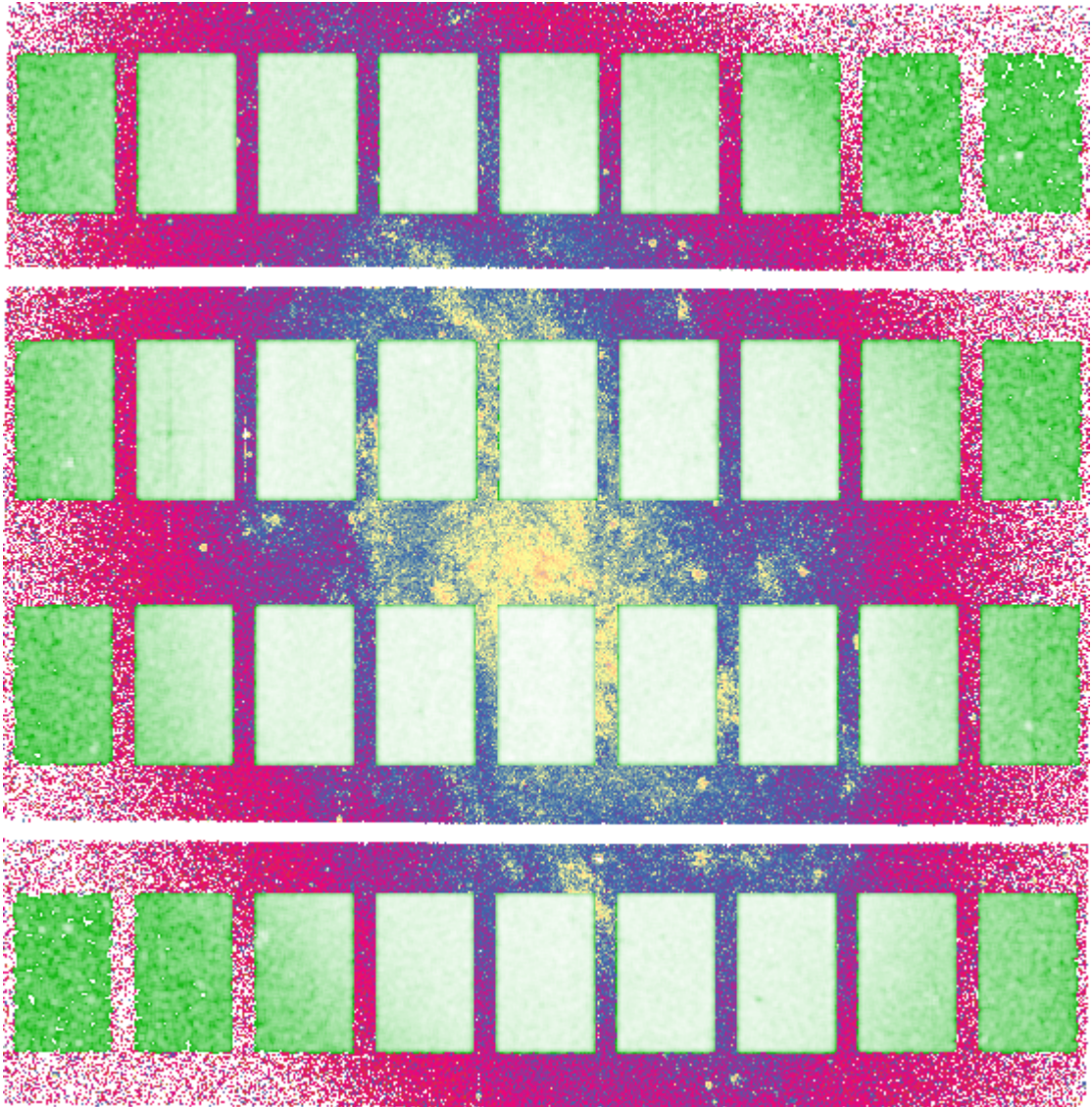


Figure 3.17: *Background*: all stars detected across all filters in the CFHT stacks. *Foreground*: regions of the sky that have been imaged by the same chips across all input frames and filters.

The calibration equation for the CFHT magnitudes for each chip is

$$m_{\text{Inst}} = m_{\text{INT}} + Z_p + (c \times \text{Col}) + (d \times X) + (e \times Y) \quad (3.4)$$

where m_{Inst} is the instrumental CFHT magnitude, m_{INT} is the calibrated INT magnitude, X is the horizontal position of the star on the CCD and Y is the vertical. Positional terms were included to account for spatial distortions that are present in such wide-field CFHT images (Betoule et al., 2013). No airmass term is included as the

stacks are composite images. The solution for each chip is listed in the Appendix. The calibration solutions determined from the subregion for each chip are then applied to the stars imaged on the entire chip.

The magnitudes of over 1.3 million stars are calibrated and catalogued along with other parameters. CMDs are shown in Figures 3.18 and 3.19. This new CFHT catalogue goes ~ 1 magnitude deeper than the LS stack.

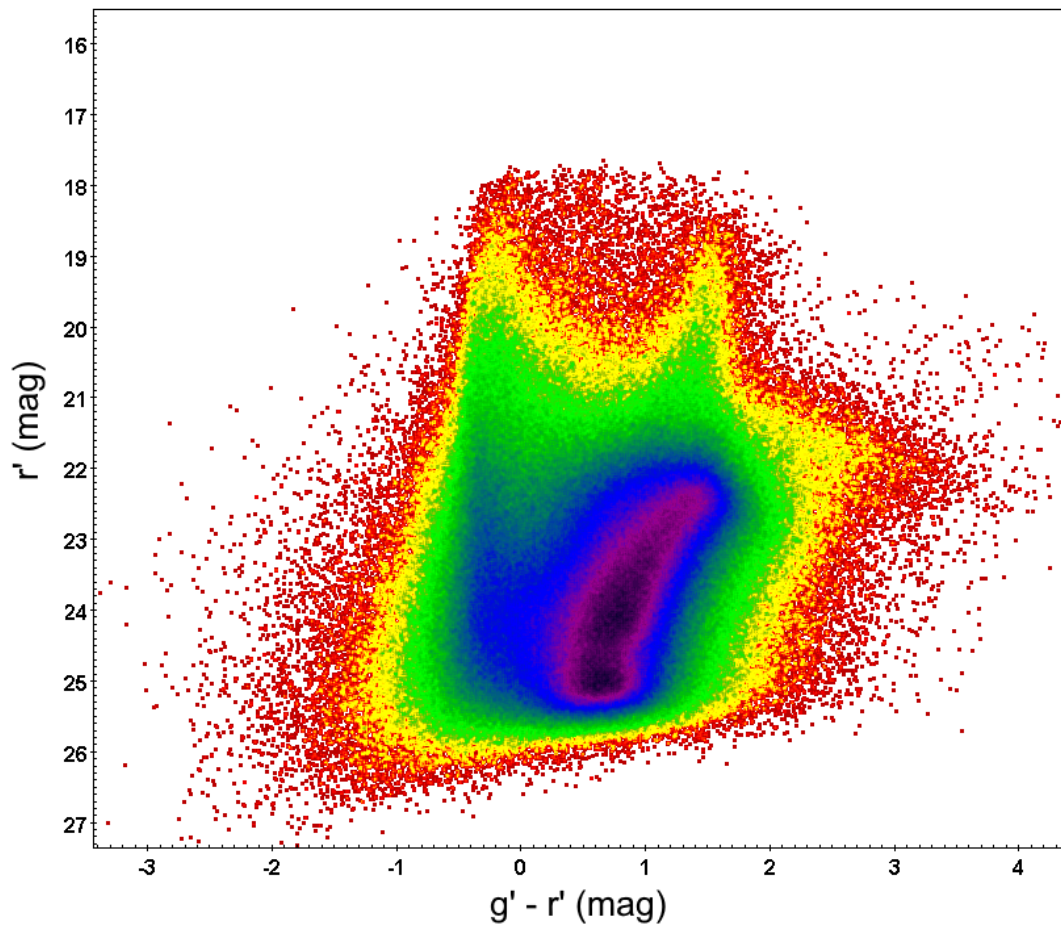


Figure 3.18: r' versus $g' - r'$ CMD using stars from the CFHT stack catalogue. Denser regions are more violet.

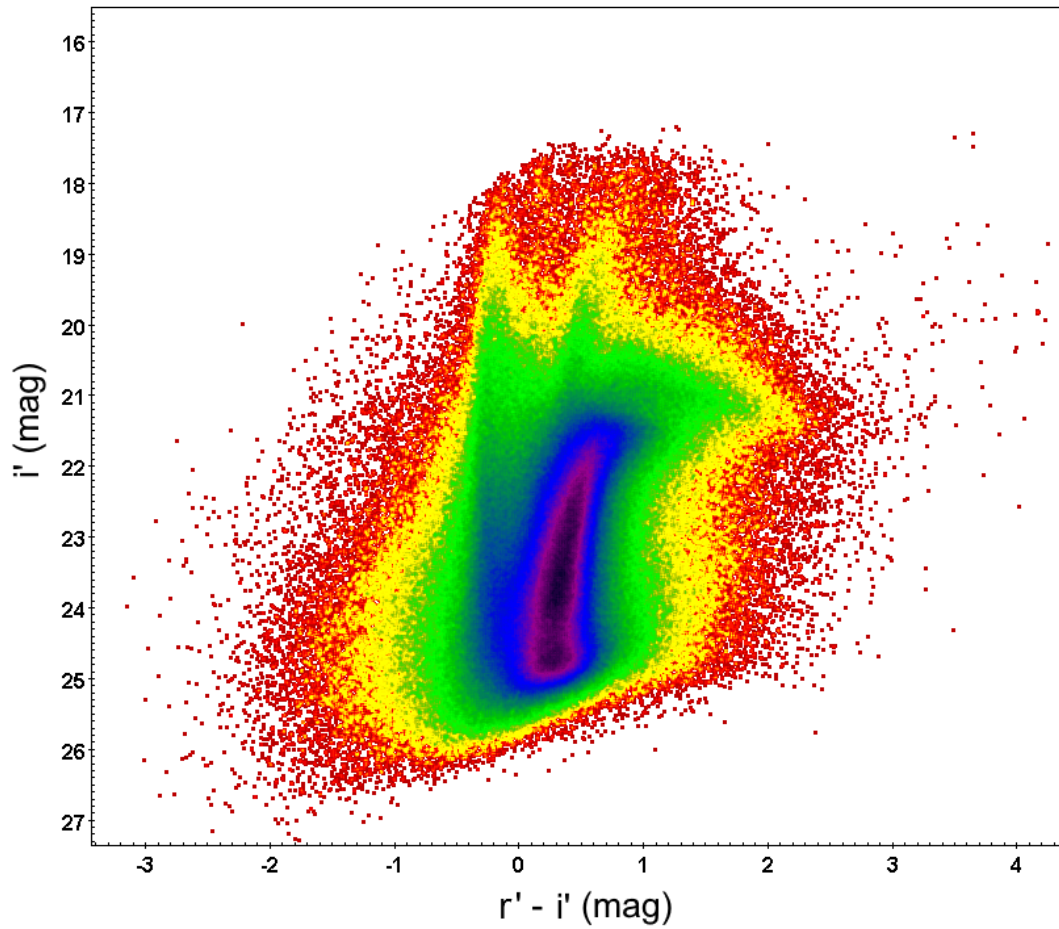


Figure 3.19: i' versus $r' - i'$ CMD using stars from the CFHT stack catalogue. Denser regions are more violet.

There is some SDSS data available for the outer regions of M33; Figure 3.20 shows the availability of M33 star data in the SDSS dataset. Figure 3.21 shows magnitude comparisons of that data with the calibrated CFHT stack and shows good agreement, supporting the accuracy of the photometry and calibration procedures.

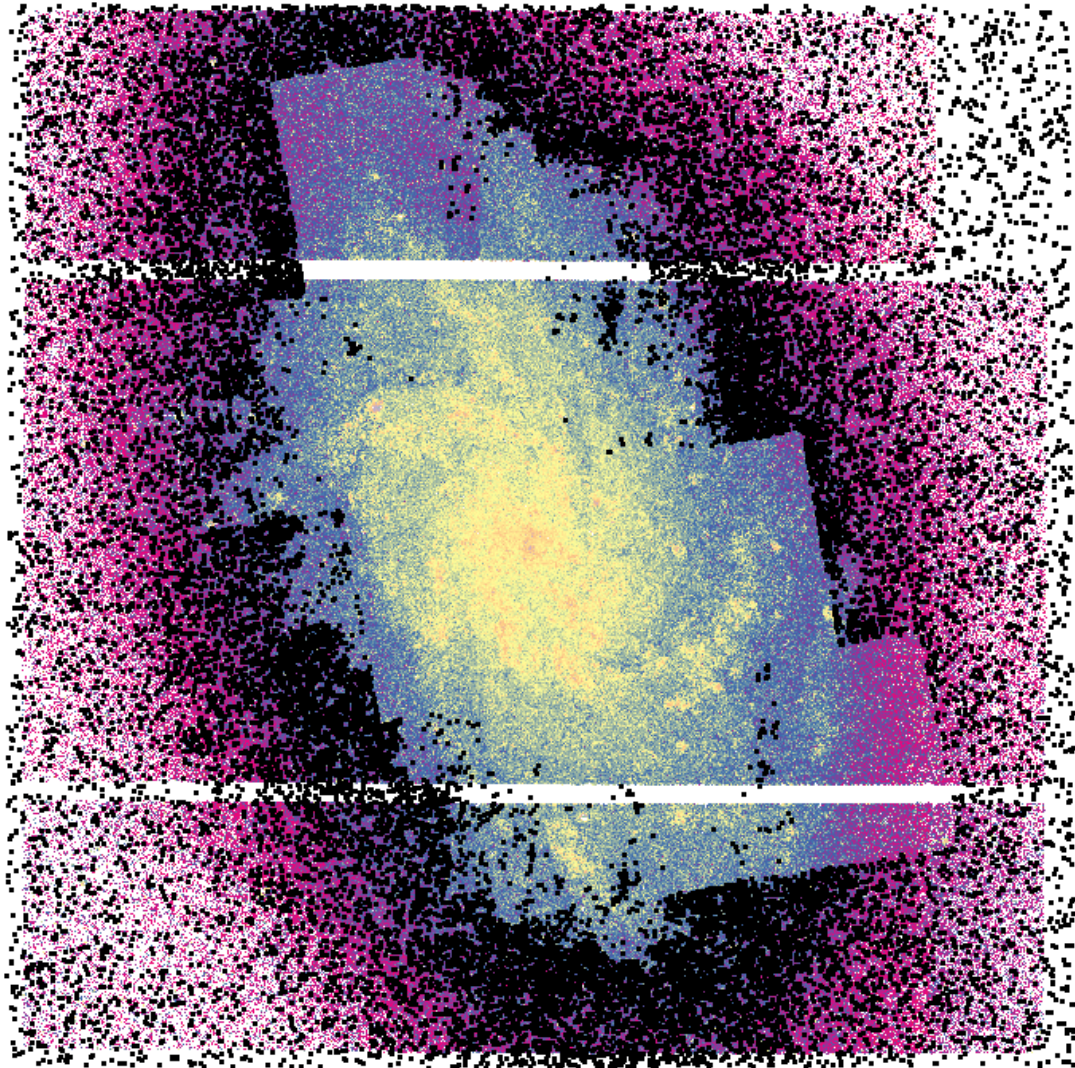


Figure 3.20: Available SDSS data for M33. Coloured background points are CFHT stack stars and foreground black points are stars in the SDSS reference catalogue. The majority of the stars in the disc of M33 do not have SDSS data available.

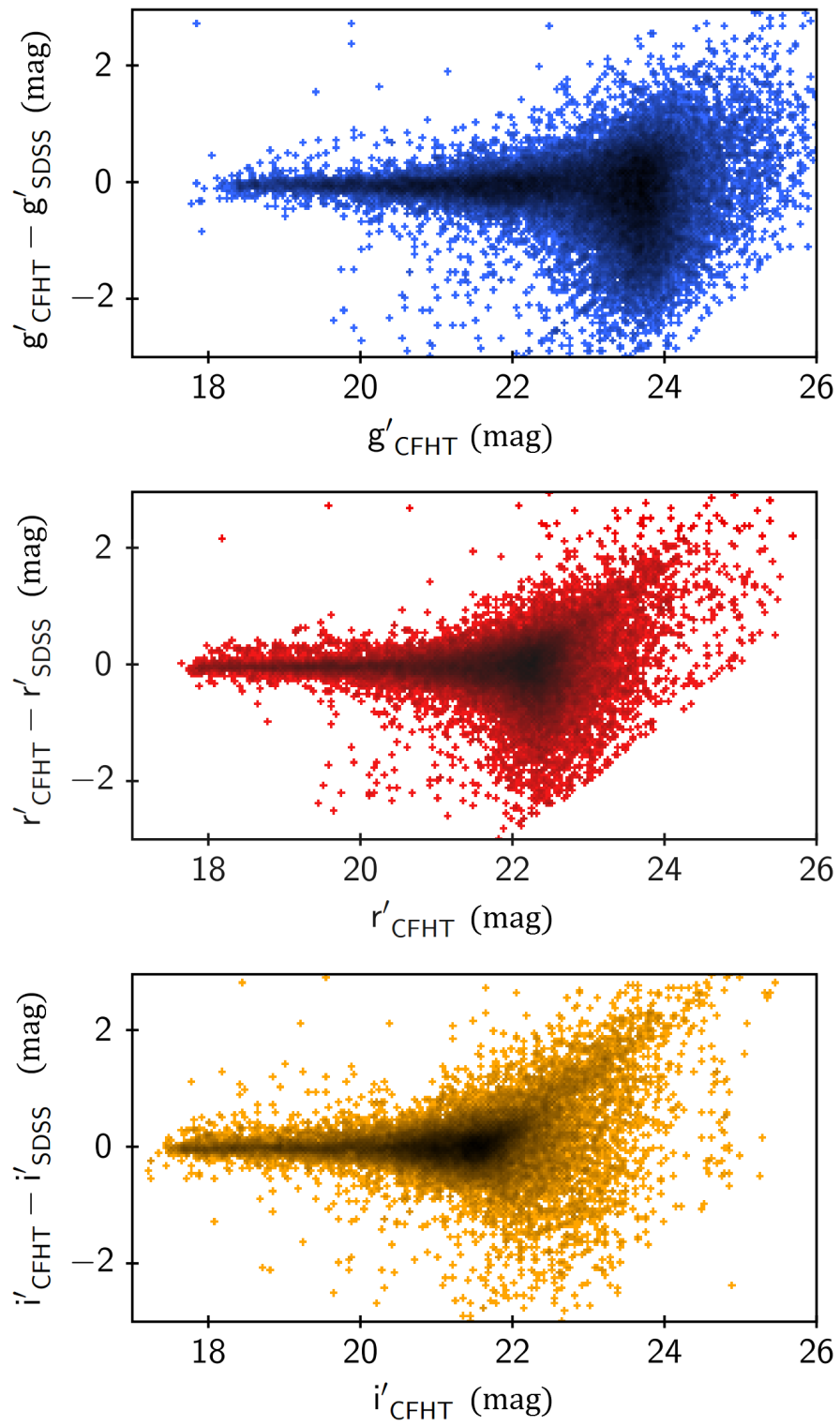


Figure 3.21: Comparison between the calibrated CFHT magnitudes in this study and magnitudes from the SDSS catalogue.

Chapter 4

Leavitt Laws

With calibrated magnitudes for stars in M33 now available, empirical Leavitt Laws can be constructed for the galaxy to acquire a distance and to investigate the effects of metallicity on Cepheids.

4.1 Identifying the Cepheids

The Hartman catalogue contains 2272 candidate Cepheids with their positions, periods, *instrumental* mean r' -band magnitudes and other parameters. No attempts were made in identifying additional Cepheids in M33 as the image data that were provided for this project are either single epoch in nature or composite stacks. To identify which of the stars in the CFHT M33 photometry catalogue are Cepheids, the Cepheid positions and r' -band magnitudes from the Hartman catalogue were used as reference. While Hartman et al. state that their magnitudes should be treated as being instrumental, they should still be accurate to within a few tenths of a magnitude. The Cepheid matching procedure is as follows:

1. For each Cepheid in the Hartman catalogue, stars in the calibrated CFHT photometry catalogue that are within 2 arcseconds of the Cepheid's RA–Dec position are identified and listed.

2. If the list contains multiple CFHT stars, the star with the closest r' -band magnitude match is marked as a tentative CFHT Cepheid.
3. If the brightness difference between the tentative CFHT Cepheid and the reference Hartman Cepheid is less than 1 magnitude, a match is confirmed.

From the CFHT catalogue, 2060 stars were matched to the Hartman Cepheids.

An independent study of M33 by [Pellerin and Macri \(2011\)](#) in B , V , and I bands yielded a sample of 564 Cepheids with well determined periods. Their Cepheid catalogue contains a mix of both fundamental and overtone mode pulsators which is evident in a period-luminosity plot (see [Figure 4.1](#)). To exclude the overtone mode Cepheids, Cepheids with periods shorter than 8 days and with I -band magnitudes brighter by 0.5 mag than a fitted Leavitt Law of $I = -2.979 \log P + 23.07$ are removed from the catalogue. There are of course Cepheids in this catalogue that correspond to entries in the Hartman Cepheid catalogue. Of the fundamental mode Cepheids that are present in both catalogues, most of their reported periods are consistent with a mean difference of 0.05%. Entries in the Pellerin & Macri catalogue that are within 2 arcseconds of any Cepheid in the Hartman catalogue are removed. This leaves a pruned catalogue of an additional 135 fundamental mode Cepheids.

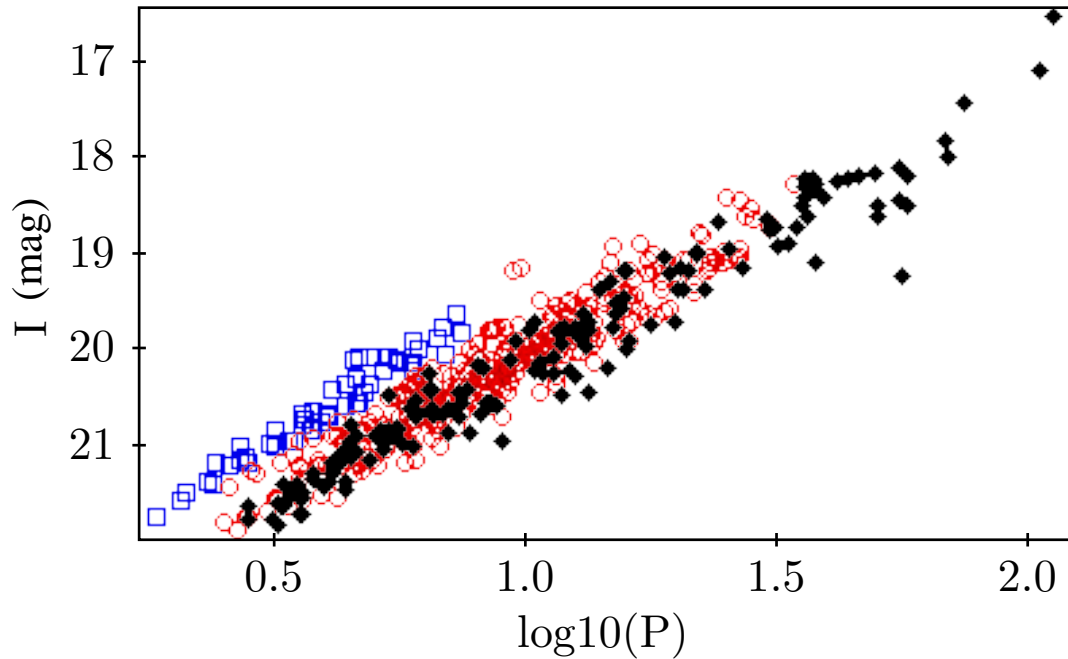


Figure 4.1: Period-luminosity plot of the 564 Cepheids from the [Pellerin and Macri \(2011\)](#) catalogue. Blue points are presumed overtone mode Cepheids. Black points are the Cepheids not present in the Hartman catalogue.

This supplementary sample of Cepheids exclusive to the Pellerin & Macri catalogue is matched against the CFHT M33 photometry catalogue with a procedure similar to the one used with the Hartman catalogue. The magnitude matching step compares I and i' magnitudes as no r' -band data are available in the Pellerin & Macri Cepheid catalogue. An additional 108 Cepheids are matched in this case. Combining the two catalogues gives a collection of 2168 fundamental mode Cepheids with Sloan-band magnitudes across M33. The spatial distribution of the Cepheids is shown in [Figure 4.2](#) where an association with the spiral arms is visible.

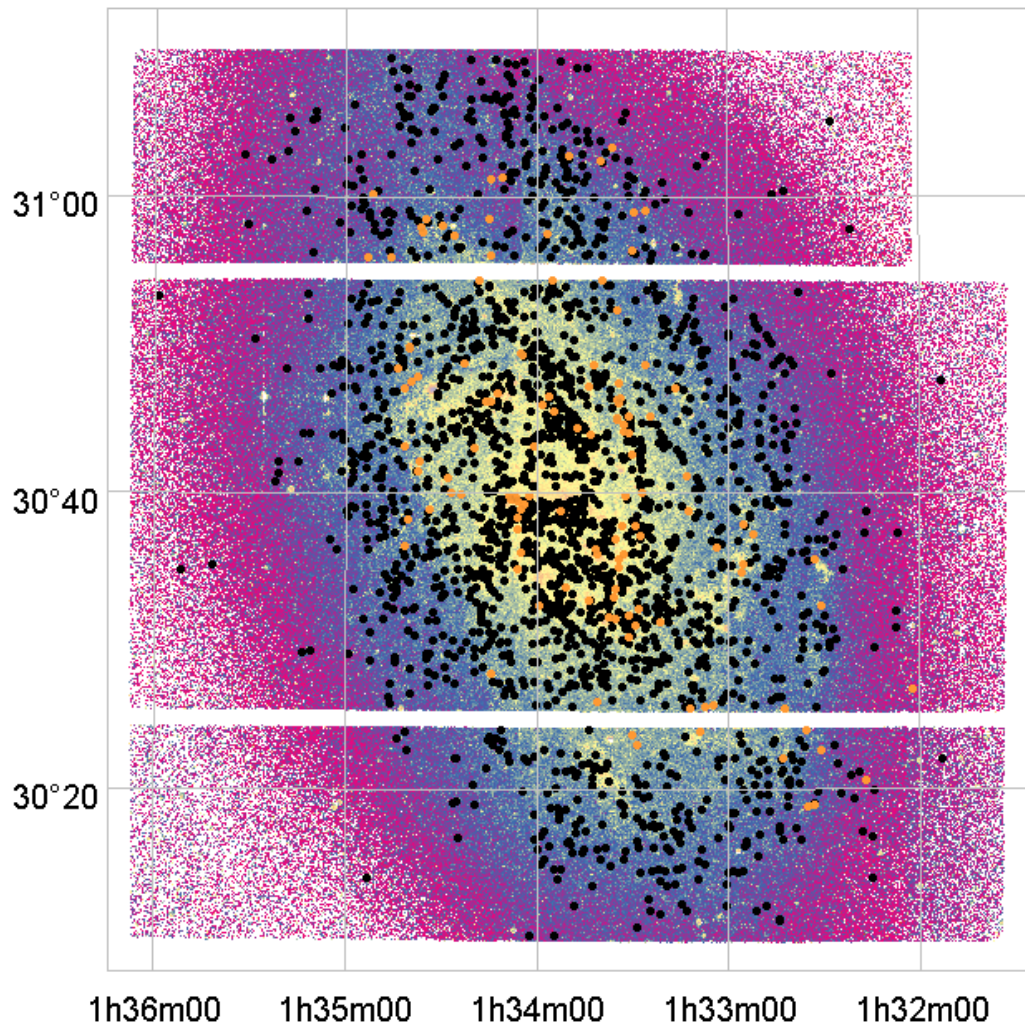


Figure 4.2: Stars from the CFHT stack of M33 images are the small points. Matched Hartman Cepheids are black circles. Matched Pellerin & Macri Cepheids are orange circles.

The quality of the calibrated magnitudes of the Cepheids can be assessed through CMDs. In the r' vs $g' - r'$ CMD, the majority of Cepheids are located between the two branches at $g' - r' \approx -0.2$ mag and $g' - r' \approx 1.4$ mag (see Figure 4.3). There are Cepheids with anomalous $g' - r'$ colours that place them well beyond the blue and red edges of the instability strip which are very approximately placed in Figure 4.3. The blue edge is defined to be $r' = 22 - 10(g' - r')$ and the red edge by $r' = 31 - 10(g' - r')$. By colouring the Cepheid data points according to their photometry flag values as reported by SExtractor, a correspondence between anomalous colour and flag value is hinted at (see Figure 4.4). It is likely that the photometry of these Cepheids has been contaminated by stars that are sufficiently bright and close that PSF photometry has

difficulty in disentangling them, yielding inaccurate magnitudes and therefore colours.

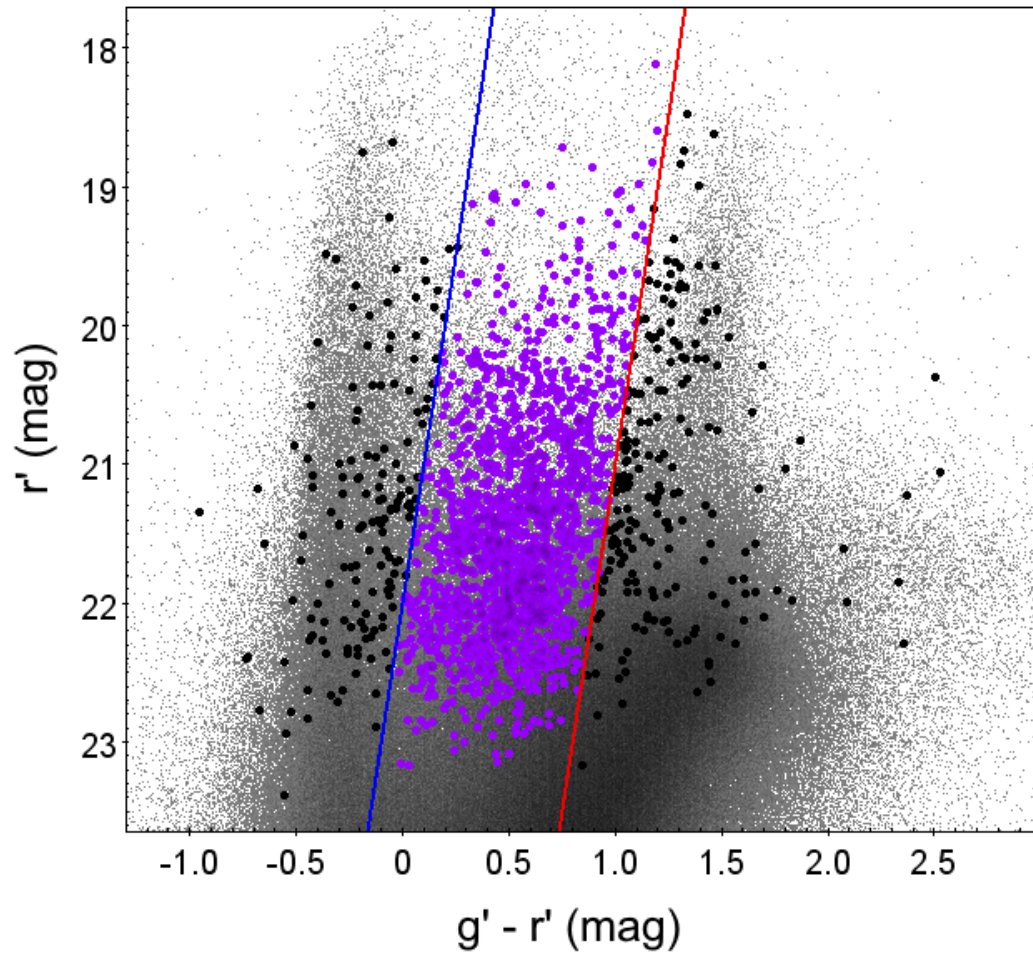


Figure 4.3: CMD of M33 stars (gray points), Cepheids with anomalous $g' - r'$ colours (black points) and Cepheids with acceptable $g' - r'$ colours (magenta points). The blue and red lines mark the approximate edges of the instability strip.

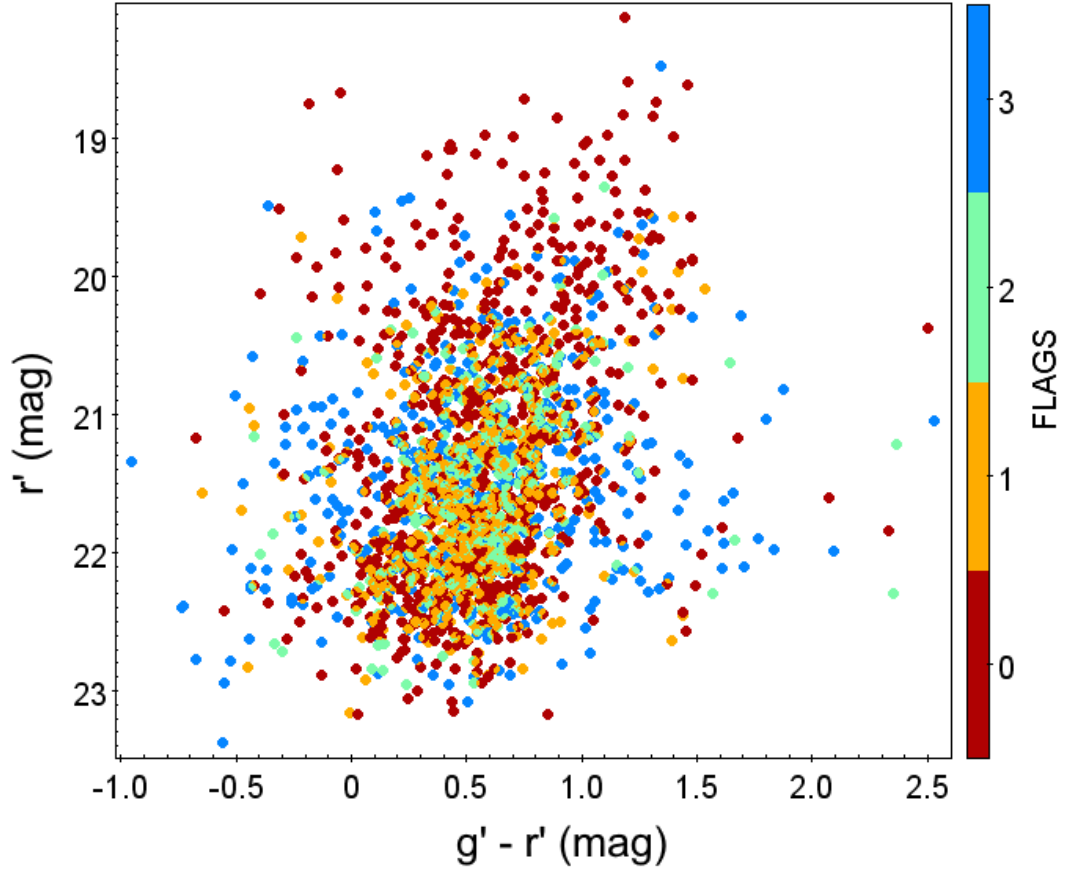


Figure 4.4: CMD of Cepheids coloured by SExtractor flag value. Cepheids with questionable $g' - r'$ colours tend to have high FLAG values.

By excluding the Cepheids with anomalous $g' - r'$ colours, a significantly smaller but still substantial catalogue of 1587 Cepheids remains.

4.2 Deprojection

A change in the zero-point of the Leavitt Law translates directly into a change in the Cepheid distance modulus $\mu = m - M$. The variation in observed distance modulus as a function of metallicity, $\gamma = \Delta\mu/\Delta[Z]$, can be equivalently framed as the change in the distance modulus as a function of galactocentric radius, assuming the slope of the Leavitt Law does not also vary. Converting between the relations simply requires a value for the metallicity gradient:

$$\gamma = \frac{\Delta\mu}{\Delta[Z]} = \frac{\Delta\mu}{\Delta\rho} \times \frac{\Delta\rho}{\Delta[Z]} \quad (4.1)$$

where ρ is galactocentric radius.

γ is often referred to as the metallicity parameter or correction. Positive values for γ correspond to Cepheids of higher metallicity being intrinsically dimmer, leading to an increase in apparent distance moduli.

For now, galactocentric radius will be used as a proxy for metallicity; various metallicity gradient values will later be assessed.

Deprojecting the galactocentric angular distance into physical distances requires known values for the distance to M33, its inclination and its position angle. Since many metallicity gradient studies are based on an assumed distance of 840 kpc to M33, that value will be adopted here to maintain ease of comparability. From Table 2.1, an inclination of 53° and a position angle of 22° are used.

Figure 4.5 shows the spatial distribution of the Cepheids colour-codes by their galactocentric radius and Figure 4.6 shows the radial distribution of the Cepheids.

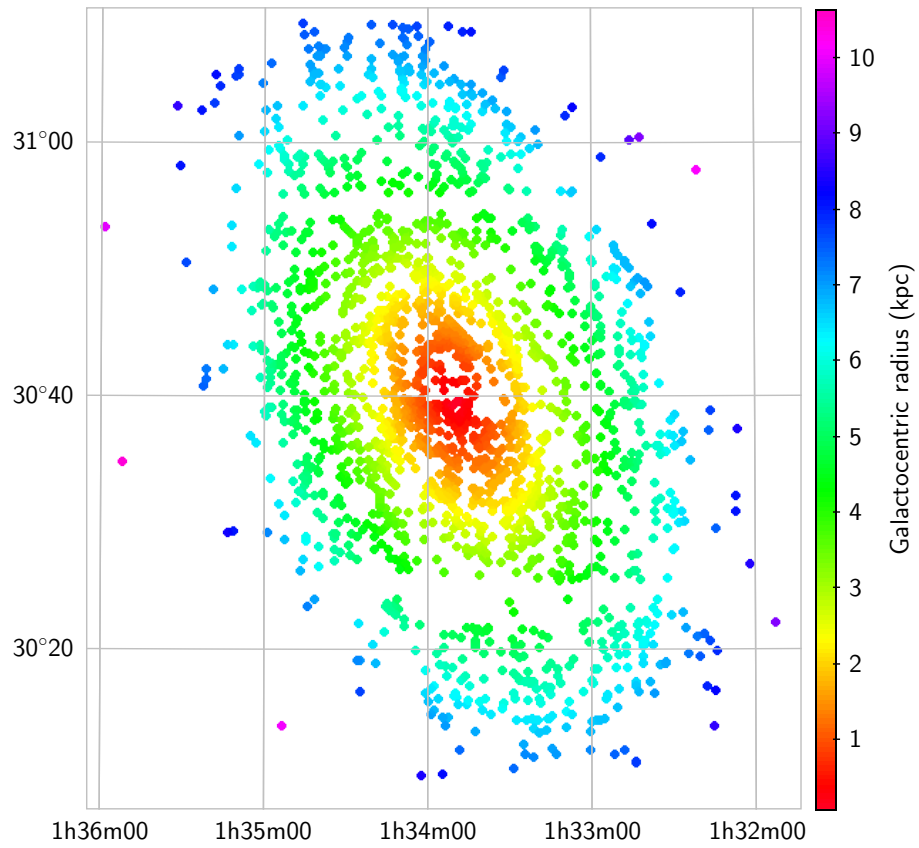


Figure 4.5: Spatial distribution of Cepheids coloured by galactocentric radius.

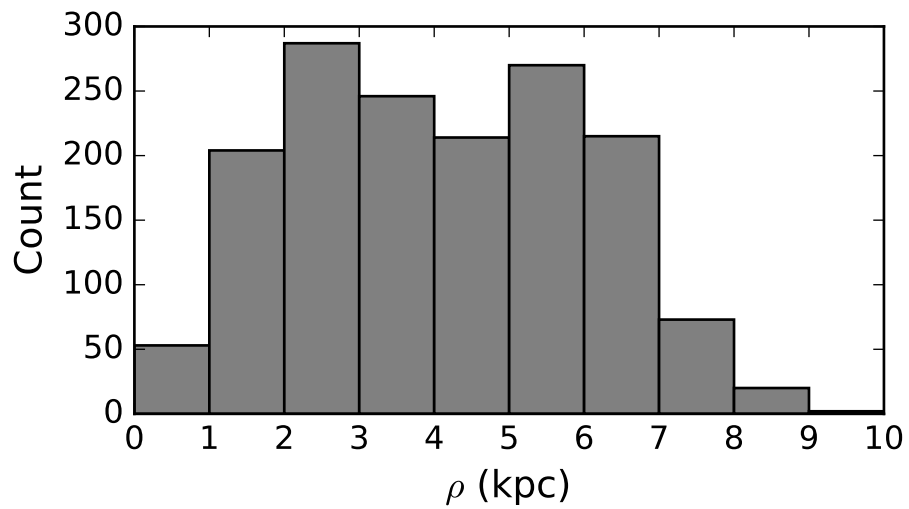


Figure 4.6: Radial distribution of Cepheids.

4.3 Wesenheit magnitudes

For a star with measured magnitudes in two or more different filters, a new magnitude-like quantity called the Wesenheit¹ index or magnitude can be constructed where the effects of extinction and reddening are negated (Madore, 1982). For example, with a known value for the reddening law (ratio of total-to-selective extinction)

$R_{BV}^V = A_V/E(B - V)$, and apparent B and V magnitudes, the Wesenheit magnitude W_{BV}^V is defined as

$$\begin{aligned}
 W_{BV}^V &= V - R_{BV}^V \times (B - V) \\
 &= V_0 + A_V - R_{BV}^V \times ((B - V)_0 + E(B - V)) \\
 &= V_0 + A_V - R_{BV}^V \times (B - V)_0 - \frac{A_V}{E(B - V)} \times E(B - V) \\
 &= V_0 - R_{BV}^V \times (B - V)_0
 \end{aligned} \tag{4.2}$$

The Wesenheit magnitude W_{BV}^V is effectively reddening-independent despite being composed of magnitudes and colours affected by reddening.

A reddening law of $R_{BV}^V = 3.1$ is typically adopted for photometric studies of M33 and is also used here with the implicit assumption that it remains constant across the galaxy. With the magnitudes in the three Sloan filters, six Wesenheit magnitudes can be constructed. For clarity, the apostrophes in the filter names will not be shown hereafter.

¹German for “essence”.

$$W_{gi}^g = g - R_{gi}^g \times (g - i)$$

$$W_{ri}^r = r - R_{ri}^r \times (r - i)$$

$$W_{gr}^g = g - R_{gr}^g \times (g - r)$$

(4.3)

$$W_{ri}^g = g - R_{ri}^g \times (r - i)$$

$$W_{gi}^r = r - R_{gi}^r \times (g - i)$$

$$W_{gr}^i = i - R_{gr}^i \times (g - r)$$

The six Sloan-band reddening parameter R values are determined using the parameterisation developed by [Cardelli et al. \(1989\)](#). With $R_{BV}^V = 3.1$, $\lambda_g = 0.4686 \mu\text{m}$, $\lambda_r = 0.6166 \mu\text{m}$ and $\lambda_i = 0.7480 \mu\text{m}$, extinction ratios between the gri and V filters are calculated to be

$$\frac{A_g}{A_V} = 1.222$$

$$\frac{A_r}{A_V} = 0.880 \tag{4.4}$$

$$\frac{A_i}{A_V} = 0.676$$

Figure 4.7 shows the variation of the extinction ratio as a function of wavelength.

With these ratios, the Sloan-band R values are: $R_{gi}^g = 2.24$, $R_{ri}^r = 4.31$, $R_{gr}^g = 3.57$,

$$R_{ri}^g = 5.99, R_{gi}^r = 1.61, \text{ and } R_{gr}^i = 1.97.$$

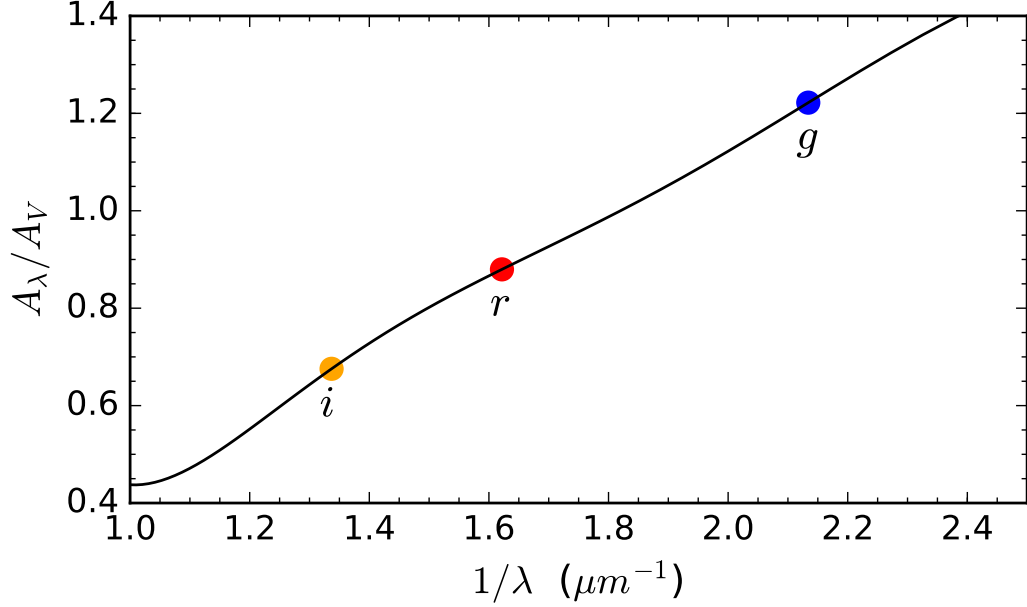


Figure 4.7: Sloan-band extinction ratios with reddening law $R_{BV}^V = 3.1$.

4.4 Theoretical and semi-empirical Sloan-band Leavitt Laws

Empirical determinations of the Leavitt Law have primarily been undertaken through the Johnson-Cousins BVR_{IJK} filters. With the steadily increasing presence of wide-band studies using Sloan filters, the characterisation of Cepheids in such filters is crucial. With this motivation, [Ngeow and Kanbur \(2007\)](#) developed semi-empirical Sloan-band Leavitt Laws while theoretical Laws were created by [Di Criscienzo et al. \(2013\)](#).

[Ngeow and Kanbur \(2007\)](#) took a sample of LMC Cepheids in the period range $0.4 < \log P < 1.8$ with BVI magnitudes from the OGLE database ([Udalski et al., 1999](#)) and applied bolometric corrections to acquire bolometric magnitudes. Sloan-band bolometric corrections were then computed and applied to the bolometric magnitudes to

arrive at semi-empirical *ugriz* magnitudes. With these new magnitudes, they derived semi-empirical Sloan-band Leavitt Laws which are reproduced here in Table 4.1.

Di Criscienzo et al. (2013), with non-linear convective stellar pulsation models from Bono et al. (2002) and references therein, determined theoretical bolometric light curves, effective temperatures and static luminosities of Cepheid models of a range of masses, periods and metallicities. These predicted quantities were transformed into the SDSS bands with model atmospheres and SDSS transmission functions; intensity-averaged mean magnitudes in the Sloan bands for Cepheids at Milky Way, LMC and SMC metallicities were then acquired. For each *ugriz* filter and metallicity, various theoretical Leavitt Law slopes were determined by selecting Cepheids in various period ranges. The theoretical Leavitt Law slopes for Cepheids at LMC metallicity ($Z = 0.008$) and with periods $\log P < 1.5$ are reproduced here in Table 4.1.

	Band	Slope	Zero-point	σ
Semi-empirical	<i>u</i>	-1.981 ± 0.046	18.195 ± 0.035	0.338
	<i>g</i>	-2.518 ± 0.036	17.165 ± 0.027	0.262
	<i>r</i>	-2.819 ± 0.027	17.027 ± 0.020	0.193
	<i>i</i>	-2.928 ± 0.023	17.032 ± 0.018	0.171
	<i>z</i>	-3.007 ± 0.022	17.064 ± 0.017	0.160
Theoretical	<i>u</i>	-2.498 ± 0.015		
	<i>g</i>	-2.855 ± 0.012		
	<i>r</i>	-3.056 ± 0.009		
	<i>i</i>	-3.137 ± 0.008		
	<i>z</i>	-3.192 ± 0.007		

Table 4.1: Semi-empirical Sloan-band Leavitt Laws for LMC Cepheids from Ngeow and Kanbur (2007) and theoretical Sloan-band Leavitt Law slopes from Di Criscienzo et al. (2013).

4.5 Empirical Leavitt Laws and the distance to M33

A “true” distance modulus and an $E(B - V)$ reddening value for M33 can be inferred by creating Leavitt Laws from a sample of Cepheids in M33 with metallicities similar to that of the LMC. By using M33 Cepheids with LMC metallicity, potential differences in magnitudes caused by differing metallicity are negated.

Because of the finite temperature width of the instability strip and uncertainties in the photometry and calibration procedures, there will be an intrinsic scatter in the period-luminosity plots. The linear regression algorithm developed by [Akritas and Bershadsky \(1996\)](#) is used to determine the slopes and zero-points of the Leavitt Laws. This algorithm is built upon the ordinary least squares method and allows for measurement errors on both the dependent and independent variables, permits a dependency between the errors on the two variables, allows the size of the errors to depend on the measurements themselves, and incorporates the intrinsic scatter of the data, making it well suited for this study. For this work, the fitting algorithm has been modified to also fit with a pre-determined slope if necessary. The accuracy of the non-empirical Leavitt Laws will be assessed through comparisons with fitted empirical period-luminosity relations.

4.5.1 The $[Z] = [Z]_{\text{LMC}}$ Cepheid Sample

From their study of blue supergiant (BSG) star spectra to acquire iron and magnesium abundances, [Urbaneja et al. \(2017\)](#) obtained an LMC metallicity of $[Z]_{\text{LMC}} = -0.35 \pm 0.09$ dex. For the sake of consistency in metallicity tracer (BSG stars) and measure ($[Z]$), a metallicity gradient for M33 derived from BSG stars of $d[Z]/d\rho = -0.082 \pm 0.010$ dex/kpc from [U et al. \(2009\)](#) is adopted (after rescaling from their acquired M33 distance of 968 kpc to 840 kpc). Their central abundance of $[Z] = 0.09 \pm 0.04$ dex is also used. [U et al. \(2009\)](#) determined the abundance of heavy elements such as iron and titanium for the majority (late B and early A supergiants) of their BSG sample while for the early B supergiants, they obtained an average of the oxygen, magnesium and silicon abundances.

The galactocentric radius at which the heavy metal abundance of M33 is similar to the LMC is $\rho_{Z(\text{LMC})} = 5.37 \pm 0.61$ kpc (see [Figure 4.8](#)). Within this radial range, there are 320 Cepheids.

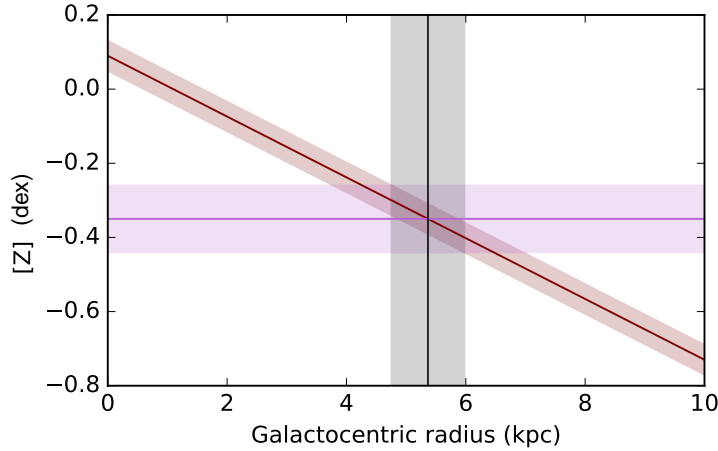


Figure 4.8: The metallicity gradient of M33 is represented with the red line (U et al., 2009), the metallicity of the LMC with the magenta line (Urbaneja et al., 2017), and the galactocentric radial range where the two overlap with the grey line.

One way to gauge the similarity of the $[Z] = [Z]_{\text{LMC}}$ sample of M33 Cepheids with that of the LMC Cepheids themselves is to compare the distribution of pulsation amplitudes. Szabados and Klagyivik (2012) demonstrated the existence of a weak relationship between pulsation amplitude and $[\text{Fe}/\text{H}]$ metallicity; expressed qualitatively, they find that metal-poor Cepheids possess larger amplitudes of pulsation. This effect is strongest for Cepheids pulsating in the first overtone mode and for short-period ($\log P < 1.02$) Cepheids pulsating in the fundamental mode.

A true comparison of Cepheid amplitude distributions for the LMC and M33 requires the amplitudes from the two systems to be measured through the same filter since observed pulsation amplitudes are wavelength dependent. If the $[Z] = [Z]_{\text{LMC}}$ subsample of M33 Cepheids are indeed LMC-like in terms of iron abundance, then the amplitude distributions should be similar, with all else being equal.

The OGLE-III catalogue of LMC Cepheids provides I -band amplitudes for over 1800 fundamental mode Cepheids (Soszynski et al., 2008); 1716 of these Cepheids possess short pulsation periods and they will be used to create the fiducial amplitude distribution. To compare like-for-like, it is necessary to use I -band amplitudes for the subsample of M33 Cepheids. The Pellerin & Macri catalogue (Pellerin and Macri, 2011) provides such amplitudes; it is worth noting that the number of short-period, fundamental

mode Cepheids in their catalogue that are located in the radial range $\rho = 5.37 \pm 0.61$ kpc is only 50. The amplitude distributions of LMC Cepheids and M33 Cepheids with LMC-like metallicity are both shown in Figure 4.9. The two distributions agree moderately well despite the low number of suitable M33 Cepheids.

The consistency of the two amplitude distributions at low amplitude values points towards an absence of blending effects in the Pellerin & Macri catalogue of M33 Cepheids. A blended Cepheid would present smaller pulsational amplitudes than an identical Cepheid that is otherwise uncontaminated. If blending effects were significant in the Pellerin & Macri catalogue, the distribution of Cepheid amplitudes would be biased towards smaller values.

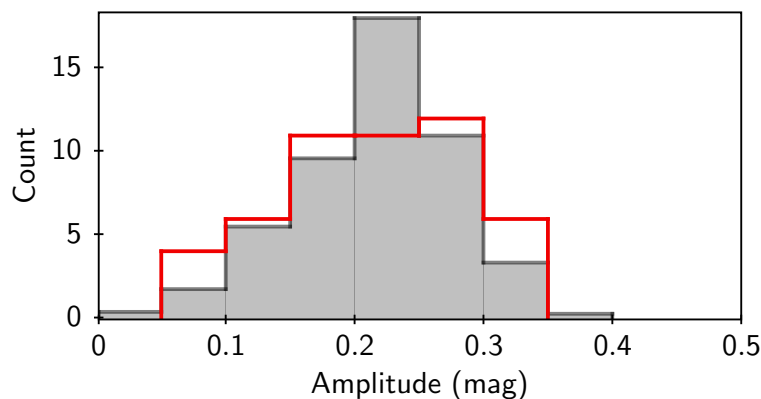


Figure 4.9: Amplitude distributions of LMC Cepheids (grey filled histogram) and the subsample of M33 Cepheids (red histogram) in the I band. The LMC Cepheid distribution has been normalised against the size of the M33 Cepheid subsample ($N = 50$).

Another diagnostic of the similarity of the two Cepheid samples is the comparison of period distributions. Szabados and Klagyivik (2012) also showed that pulsation periods mildly depends on iron abundance in the sense that an increase in $[\text{Fe}/\text{H}]$ is correlated with an increase in pulsation period. Fortunately, period data is available for the entire collection of M33 Cepheids with what is expected to be LMC-like metallicity ($N = 320$). The period distributions of the two Cepheid samples are shown in Figure 4.10 and show excellent agreement, implying that the two samples share similar distributions in metallicity.

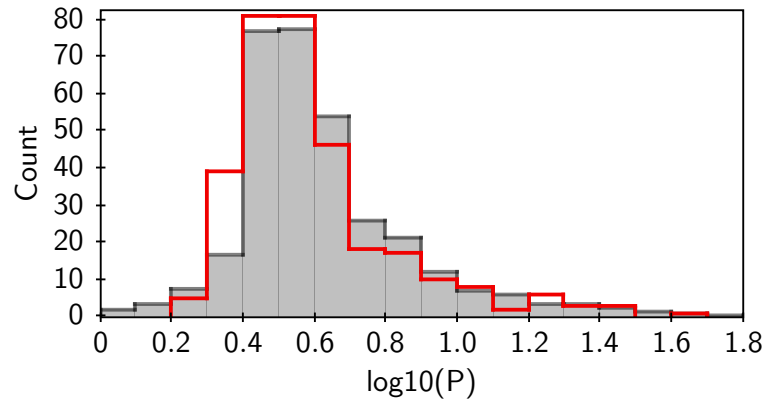


Figure 4.10: Period distributions of LMC Cepheids (grey filled histogram) and the subsample of M33 Cepheids (red histogram). The LMC Cepheid distribution has been normalised against the size of the M33 Cepheid subsample ($N = 320$).

Creating and comparing Sloan-band Leavitt Laws

Period-luminosity relations are fitted to the Cepheids of LMC-like metallicity with both fixed and non-fixed slopes. The results are plotted in Figure 4.11 and tabulated in Table 4.2.

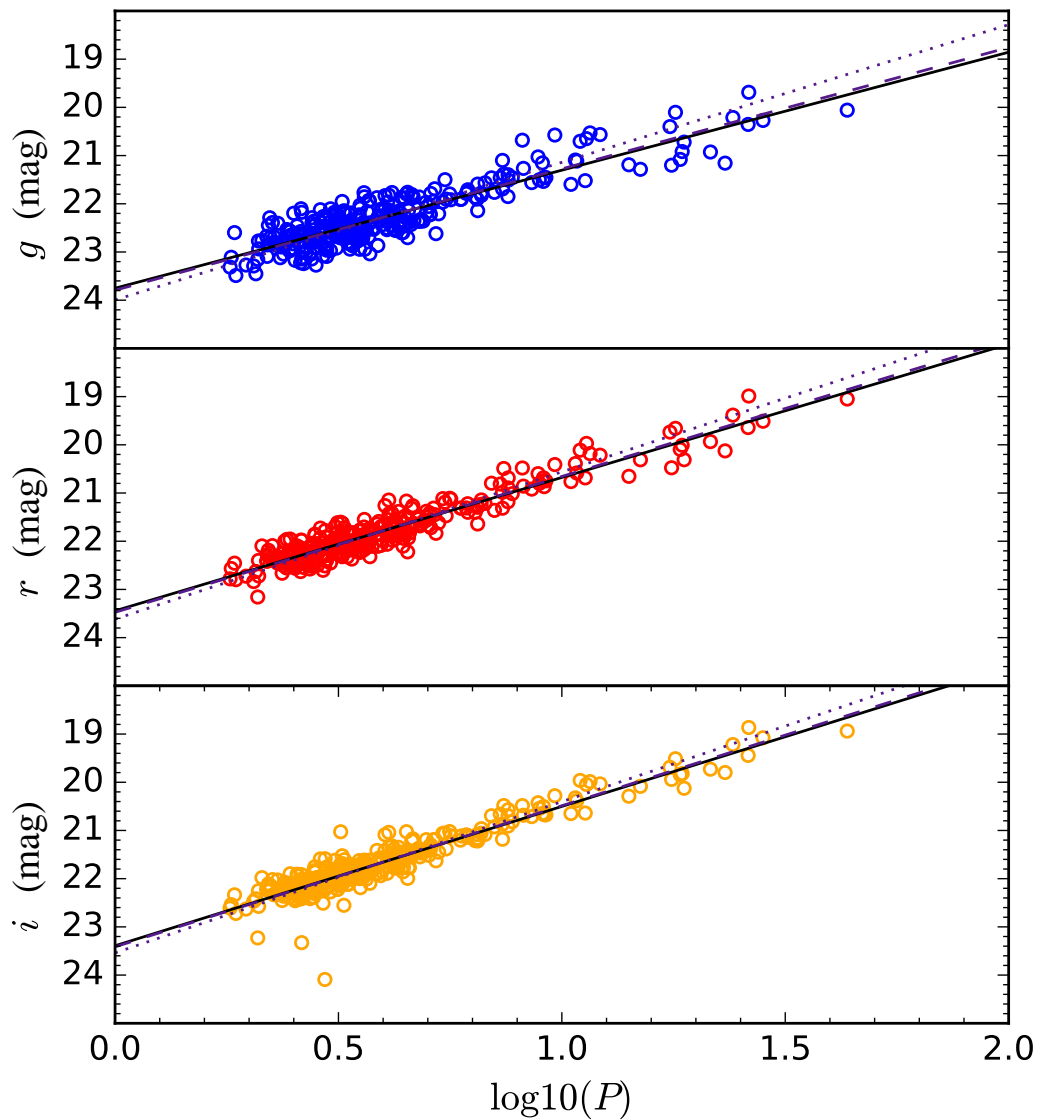


Figure 4.11: Sloan-band period-luminosity relations of Cepheids in M33 with LMC-like metallicities. The solid lines are the fully-empirical fits. The dashed lines represents the fits where the slopes are fixed to the semi-empirical values. The dotted lines are the fits where the slopes are fixed to the theoretical values.

For each filter, the three slopes appear to be in good agreement. To better illustrate the level of consistency between the slopes, a clearer visual comparison of the empirically-determined slopes with those predicted by [Ngeow and Kanbur \(2007\)](#) and [Di Criscienzo et al. \(2013\)](#) is shown in [Figure 4.12](#). It is revealed that there are clear systematic offsets between each set of slopes. Both the semi-empirical and theoretical sets of slopes are steeper than those empirically measured here, though the semi-empirical

	Band	Slope	Zero-point
Empirical	<i>g</i>	-2.448 ± 0.088	23.751 ± 0.052
	<i>r</i>	-2.766 ± 0.065	23.443 ± 0.039
	<i>i</i>	-2.890 ± 0.059	23.392 ± 0.040
N&K Fixed-slope	<i>g</i>	-2.518	23.793 ± 0.017
	<i>r</i>	-2.819	23.475 ± 0.012
	<i>i</i>	-2.928	23.414 ± 0.013
DC+ Fixed-slope	<i>g</i>	-2.855	23.995 ± 0.016
	<i>r</i>	-3.056	23.617 ± 0.012
	<i>i</i>	-3.137	23.539 ± 0.014

Table 4.2: Sloan band Leavitt Laws using M33 Cepheids with LMC metallicity.

slopes by [Ngeow and Kanbur \(2007\)](#) lie comfortably within the errors. The significant disparities between the theoretical and the (semi-)empirical slopes suggests that the theoretical models used by [Di Criscienzo et al. \(2013\)](#) do not fully reproduce the physical behaviour and the observed characteristics of Cepheids. As stated by [Di Criscienzo et al. \(2013\)](#), the models they used do not incorporate core overshooting nor is rotation taken into account. It is possible that the exclusion of these factors contribute to the observed systematic differences in slopes.

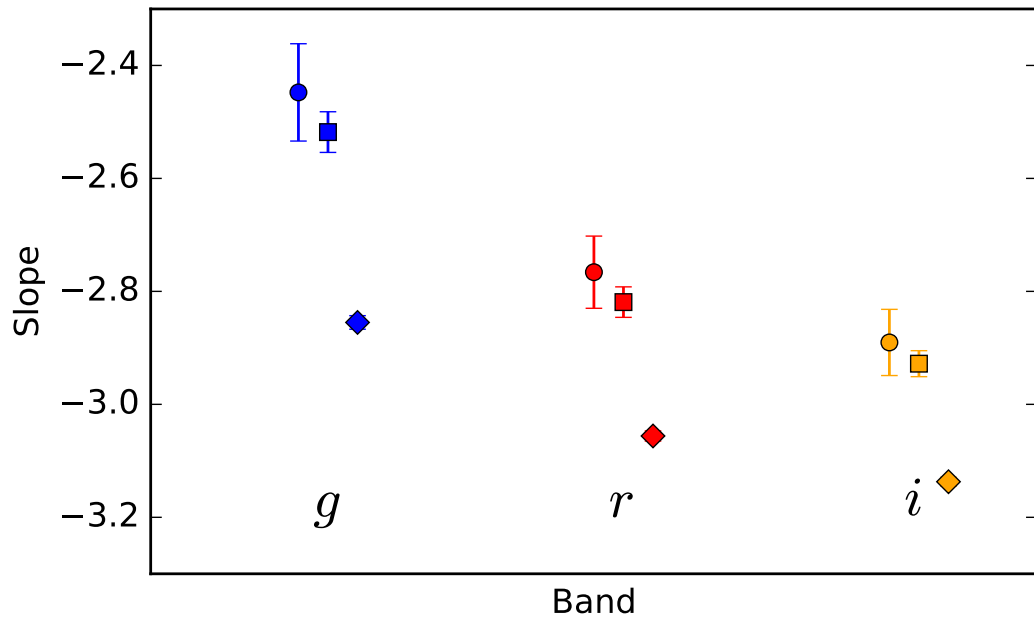


Figure 4.12: Comparison between empirical and predicted slopes. Circular points are empirically derived slopes, square points are the semi-empirical slopes from [Ngeow and Kanbur \(2007\)](#), and diamond points are the theoretical slopes from [Di Criscienzo et al. \(2013\)](#).

By adopting the semi-empirical Leavitt Laws and using their slopes during the fitting procedures, apparent distance moduli can be estimated by taking the difference between the measured M33 intercepts and semi-empirical LMC intercepts

$$\mu_{\lambda} = \mu_{\text{LMC}} + (ZP_{\lambda} - ZP_{\lambda,\text{LMC}}) \quad (4.5)$$

where μ_{λ} is the apparent distance modulus to M33 in the filter λ , ZP_{λ} is the measured intercept in that filter using a fixed-slope fit, $ZP_{\lambda,\text{LMC}}$ is the semi-empirical intercept in that filter for the LMC Cepheids, and μ_{LMC} is the distance modulus to the LMC which is taken to be the canonical value of 18.50 mag. The apparent M33 distance moduli as measured in the Sloan bands are: $\mu_g = 25.128 \pm 0.031$ mag, $\mu_r = 24.948 \pm 0.024$ mag and $\mu_i = 24.882 \pm 0.22$ mag.

The reddened, apparent distance modulus is a linear function of the total-to-selective extinction ratio with the reddening as the multiplicative factor

$$\begin{aligned}\mu_\lambda &= \mu_0 + A_\lambda \\ \mu_\lambda &= \mu_0 + E(B - V) \times \frac{A_\lambda}{E(B - V)} \\ \mu_\lambda &= \mu_0 + E(B - V) \times R_{BV}^\lambda\end{aligned}\tag{4.6}$$

where μ_0 is the true distance modulus.

With the parameterisation of [Cardelli et al. \(1989\)](#), the total-to-selective extinction ratios in the three Sloan filters are: $R_{BV}^g = 3.79$, $R_{BV}^r = 2.73$, and $R_{BV}^i = 2.09$. A linear fit between the apparent moduli and ratios gives a reddening of $E(B - V) = 0.144 \pm 0.020$ mag and, by extrapolating to zero reddening, a true distance modulus of $\mu_0 = 24.57 \pm 0.06$ mag. [Figure 4.13](#) shows the plot of apparent distance moduli against ratios. With a known value for reddening, the extinctions in the three Sloan filters can be calculated. [Table 4.3](#) lists the apparent distances, extinctions and extinction-corrected distances in the three filters.

λ	μ_λ (mag)	A_λ (mag)	$\mu_\lambda - A_\lambda$ (mag)
<i>g</i>	25.128 ± 0.031	0.547 ± 0.076	24.582 ± 0.082
<i>r</i>	24.948 ± 0.024	0.394 ± 0.055	24.555 ± 0.059
<i>i</i>	24.882 ± 0.022	0.302 ± 0.042	24.580 ± 0.047

Table 4.3: Apparent distance moduli, extinctions and extinction-corrected distance moduli in the Sloan bands.

The reddening of $E(B - V) = 0.144$ mag determined from $[Z] = [Z]_{\text{LMC}}$ Cepheids is — for now — assumed for all Cepheids regardless of radial position. For comparison, [Massey et al. \(1995\)](#) found an average reddening of $E(B - V) = 0.13 \pm 0.01$ mag with individual values ranging from 0.08 to 0.33 mag from their photometry and spectroscopy of massive OB stars across 8 fields in the disk of M33. A later study by [Massey et al. \(2007\)](#) finds a similar value of $E(B - V) = 0.12 \pm 0.02$ mag by using the plume of blue supergiant stars on a CMD of M33 stars. Given that the two studies made use of stellar populations that are similar to Cepheids and that they find

reddening values that are compatible with the value determined here, the application of a constant average reddening of 0.144 mag for all Cepheids is supported.

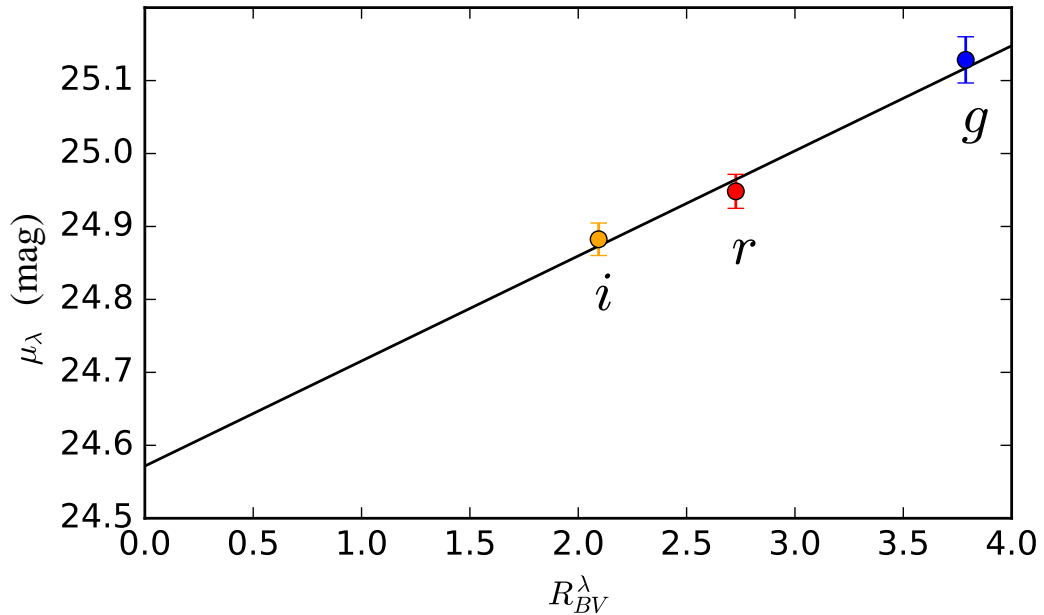


Figure 4.13: Apparent distance moduli vs total-to-selective extinction ratios in the Sloan bands. The zero-point of the fit yields the true distance modulus and the gradient gives the reddening.

The true distance modulus of 24.57 ± 0.06 mag is superimposed on a sample of previous distance estimates collated by [de Grijs and Bono \(2014\)](#) in Figure 4.14.

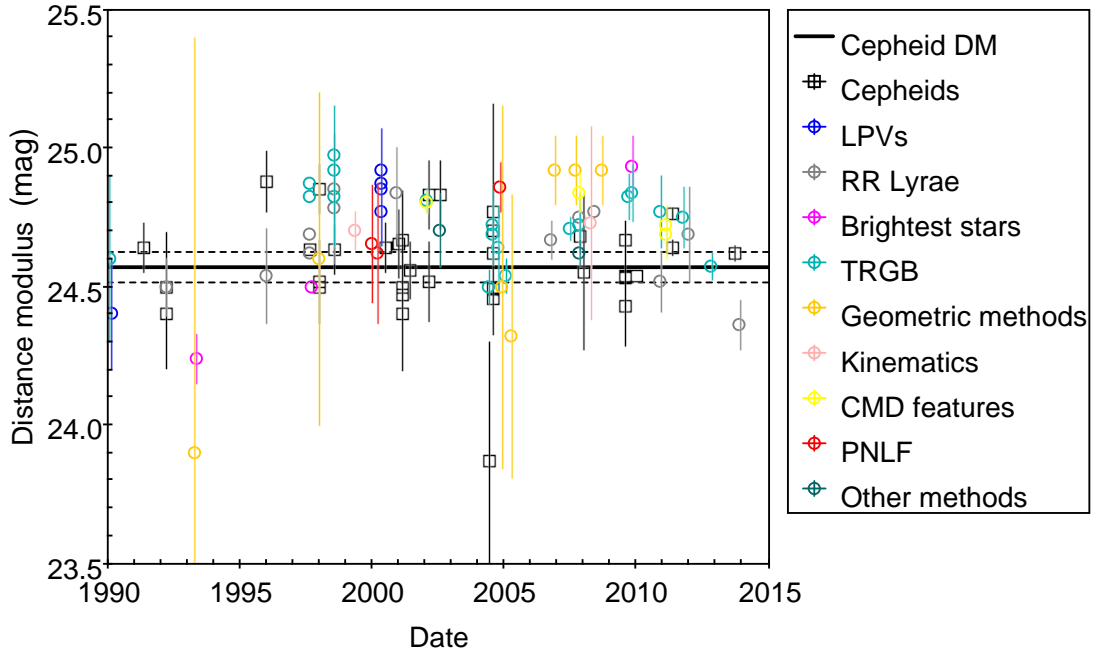


Figure 4.14: M33 distance estimates collated by [de Grijs and Bono \(2014\)](#). The distance modulus of $\mu = 24.57 \pm 0.06$ mag derived here is indicated by the solid and dashed horizontal lines.

4.5.2 Creating and comparing period-Wesenheit relations

With the Wesenheit formulations in Equation 4.3 and the semi-empirical Leavitt Laws by [Ngeow and Kanbur \(2007\)](#), it is possible to construct semi-empirical period-Wesenheit (PW) relations through simple substitution. For example, the slope and zero-point for the W_{gi}^g period-Wesenheit relation are predicted in the following way:

$$\begin{aligned}
 W_{gi}^g &= g - R_{gi}^g \times (g - i) \\
 &= (a_g \log P + b_g) - R_{gi}^g \times ((a_g \log P + b_g) - (a_i \log P + b_i)) \\
 &= (a_g - R_{gi}^g (a_g - a_i)) \log P + (b_g - R_{gi}^g (b_g - b_i)) \\
 &= a_{gi}^g \log P + b_{gi}^g
 \end{aligned} \tag{4.7}$$

Table 4.4 lists the predicted slopes and intercepts for the period-Wesenheit relations.

Band	Predicted Slope	Predicted Zero-point
W_{gi}^g	-3.435 ± 0.068	16.868 ± 0.052
W_{ri}^r	-3.289 ± 0.133	17.049 ± 0.102
W_{gr}^g	-3.593 ± 0.134	16.672 ± 0.100
W_{ri}^g	-3.170 ± 0.215	17.195 ± 0.163
W_{gi}^r	-3.479 ± 0.074	16.813 ± 0.056
W_{gr}^i	-3.522 ± 0.092	16.760 ± 0.069

Table 4.4: Predicted semi-empirical Sloan-band period-Wesenheit relations for LMC Cepheids.

Wesenheit magnitudes are determined for each Cepheid with Equations 4.3. With the modified Akritas and Bershadsky (1996) OLS fitting algorithm to account for the intrinsic scatter, fits are made to the Wesenheit magnitude against period data with slopes that are allowed to float and slopes that are fixed to the predicted values (see Figure 4.15). No rejection procedures were applied. Table 4.5 lists the results of the fits and Figure 4.16 compares the predicted and measured slopes.

The scatters in the Wesenheit plots are considerably larger than those of the single filters plots. The CFHT stacks comprise at most 17 input frames so the light curves of the Cepheids may not be sampled sufficiently. The apparent brightnesses of the Cepheids in the CFHT stacks therefore may not accurately reflect their true average brightnesses. Amplitudes of Cepheid light curves increase monotonically for decreasing wavelength. The greater the amplitude, the larger the potential discrepancy between a Cepheid's measured stacked magnitude and the Cepheid's true average magnitude. Given that the construction of Wesenheit indices is essentially a linear combination of two or more magnitudes, uncertainties for said magnitudes are compounded into the final uncertainty for the Wesenheit index. The coefficient on the colour term will also act to amplify the errors.

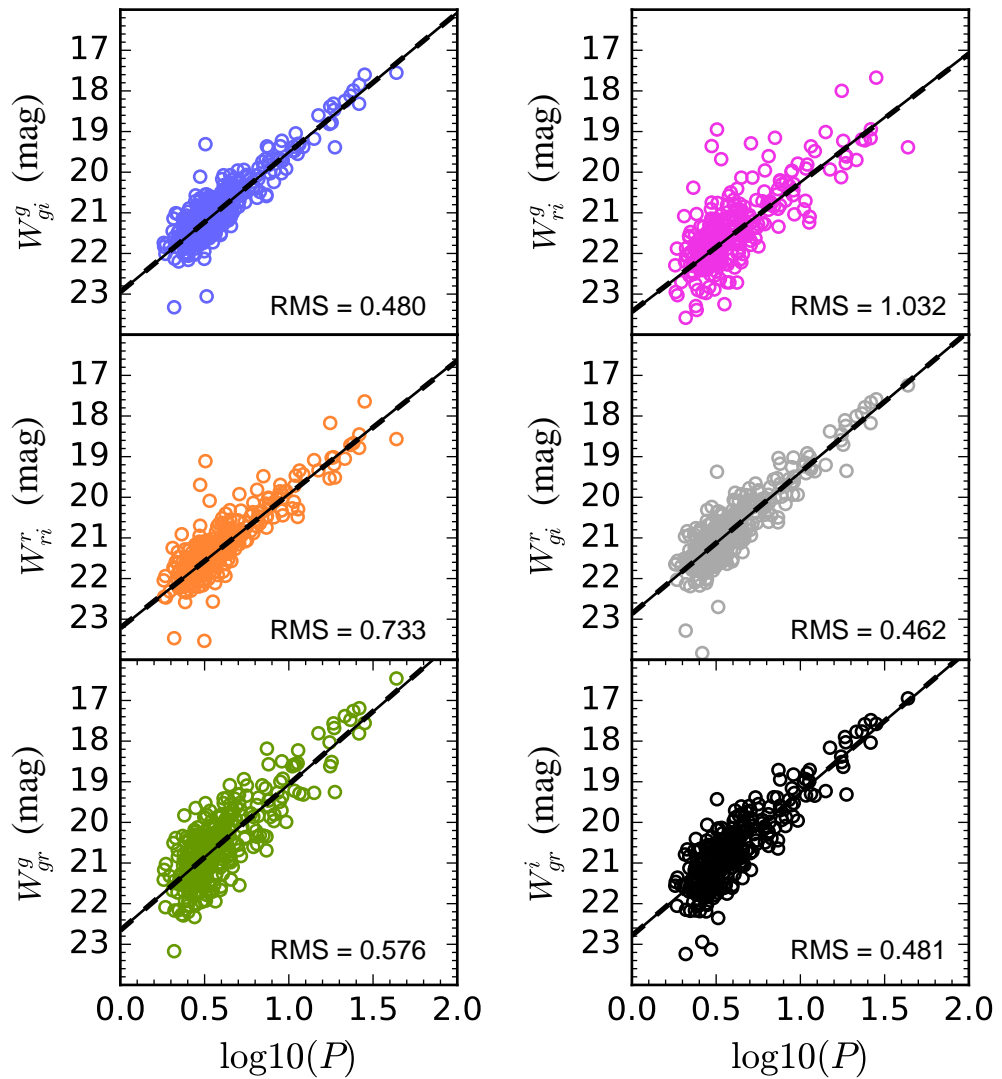
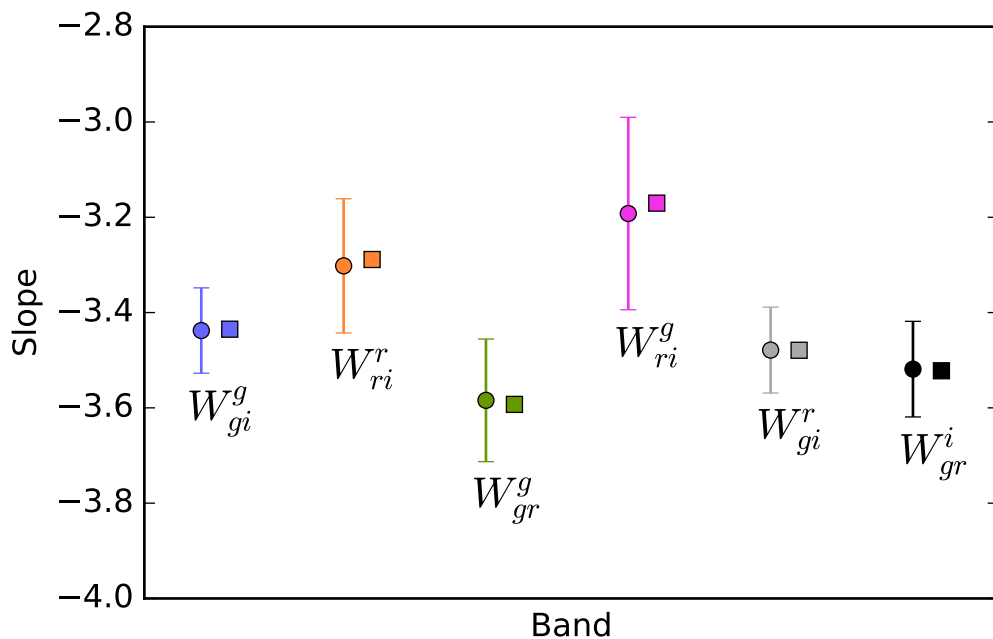


Figure 4.15: Fitted Sloan-band period-Wesenheit relations. The solid lines represents the free-slope fits and the barely visible dashed lines represent the fits with fixed slopes. The RMS scatter for each fixed-slope fit is listed for each plot.

	Band	Slope	Zero-point	RMS
Empirical	W_{gi}^g	-3.438 ± 0.092	22.948 ± 0.072	0.480
	W_{ri}^r	-3.302 ± 0.137	23.222 ± 0.110	0.732
	W_{gr}^g	-3.584 ± 0.126	22.652 ± 0.083	0.576
	W_{ri}^g	-3.192 ± 0.196	23.443 ± 0.154	1.034
	W_{gi}^r	-3.479 ± 0.095	22.865 ± 0.069	0.462
	W_{gr}^i	-3.519 ± 0.102	22.784 ± 0.071	0.480
	N&K Fixed-slope	W_{gi}^g	-3.435	22.946 ± 0.027
W_{ri}^r		-3.289	23.214 ± 0.041	0.733
W_{gr}^g		-3.593	22.657 ± 0.033	0.576
W_{ri}^g		-3.170	23.430 ± 0.058	1.032
W_{gi}^r		-3.479	22.865 ± 0.025	0.462
W_{gr}^i		-3.522	22.786 ± 0.026	0.481

Table 4.5: Sloan-band period-Wesenheit relations using M33 Cepheids with LMC metallicity.

Figure 4.16: Slopes from empirical and predicted period-Wesenheit relations. Circular points are empirically-derived slopes and square points are slopes predicted using combinations of single-filter slopes from [Ngeow and Kanbur \(2007\)](#).

Nevertheless, the slopes from the empirical fits agree extremely well with the predicted semi-empirical values. The fits of the Wesenheit data with the predicted slopes yield

six additional estimates for the distance to M33; no reddening correction is needed here as the Cepheid Wesenheit magnitudes are by definition reddening-free. The estimated distances from the single-filter band Leavitt Laws and period-Wesenheit relations are collated in Table 4.6 and plotted in Figure 4.17 along with the true distance modulus.

Band	Distance modulus (mag)
g_0	24.583 ± 0.082
r_0	24.555 ± 0.059
i_0	24.581 ± 0.047
W_{gi}^g	24.578 ± 0.059
W_{ri}^r	24.665 ± 0.110
W_{gr}^g	24.485 ± 0.105
W_{ri}^g	24.735 ± 0.174
W_{gi}^r	24.552 ± 0.062
W_{gr}^i	24.527 ± 0.074

Table 4.6: Distance moduli in various bands determined from Cepheids of LMC metallicity in M33.

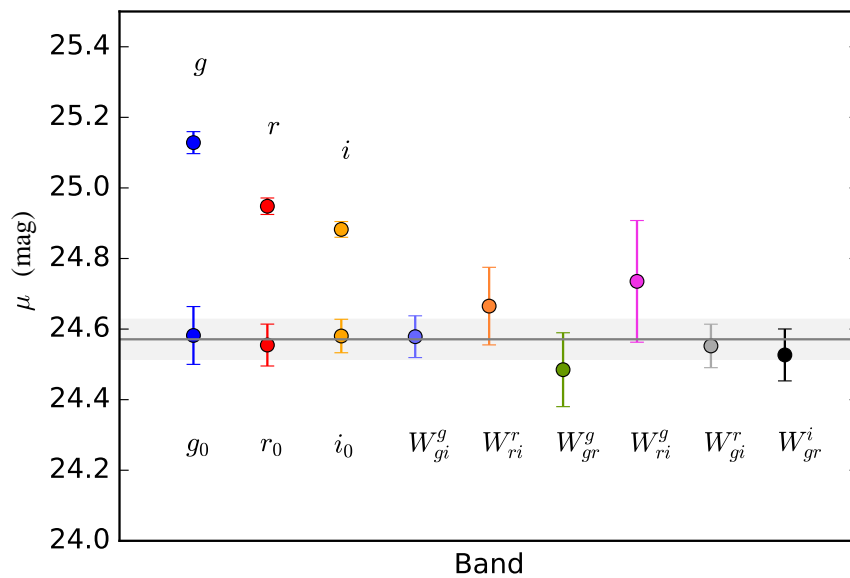


Figure 4.17: Distance estimates for M33 derived from reddening-corrected single-band and reddening-free Wesenheit magnitudes in the Sloan filters. The solid horizontal line is the true distance modulus and the shaded region is its error. Reddened single-filter distance moduli are also shown and are labelled as g , r and i .

4.6 Effects of metallicity on the period-luminosity relation

To assess the metallicity effects on Cepheid luminosities, period-luminosity relations are fitted against Cepheids from a series of galactocentric radial bins. The Cepheids are binned into a series of galactocentric annuli starting at a radius of 0.5 kpc and ending at 10.5 kpc with a bin thickness of 1 kpc. The first bin encompasses the radial range $0.5 < \rho < 1.5$ kpc, the second $1.5 < \rho < 2.5$ kpc, the third $2.5 < \rho < 3.5$ kpc, etc. For each annular sample of Cepheids and magnitude band or Wesenheit index, period-luminosity relations are fitted twice using the linear regression method by [Akritas and Bershady \(1996\)](#). One fit is performed with no constraints on the slope and another fit is made with the slope fixed to the semi-empirical value specific to that particular band or index. The extinction values in [Table 4.3](#) are applied to all single-filter tests.

4.6.1 Slopes

First, the dependency of the slopes of the period-luminosity relations on metallicity in various bands is assessed. [Figure 4.18](#) shows the variations in the freely-fitted slope as a function of galactocentric radius in all single-filter bands and Wesenheit indices.

The freely-fitted slopes in all single-filter bands show no strong trend with galactocentric radius beyond 3 kpc, suggesting the lack of a slope-metallicity dependence and are consistent with the semi-empirical determinations. For the Wesenheit-index fits, the slopes exhibit greater levels of variation. A slight radial trend appears to be present in the W_{ri}^g plot though it may be spurious given the large uncertainties for each data point.

In the central region $\rho < 3$ kpc, a correlation between fitted slope and radius is apparent. It is possible that this is a sign of a metallicity-slope relation that is present only in metal-rich environments. A more likely cause for the slope-radius relation is flux contamination effects — a phenomenon that is not unexpected in such regions of high

stellar density.

Flux contamination

For the sake of simplicity, let us assume that all the Cepheids in a given radial bin experience the same level of flux contamination, that is, measurements of the Cepheids' flux are all overestimated by the same amount. The additional flux makes up a greater fraction of the total measured flux for the intrinsically faint Cepheids than it does for intrinsically brighter Cepheids. The greater fractional flux change for dimmer Cepheids consequently imparts a greater change in magnitude than for brighter Cepheids. This differential change in magnitude as a function of intrinsic brightness (and therefore period) has the effect of producing period-luminosity relations of shallower slopes. With decreasing galactocentric radius, the level of flux contamination increases, leading to increasingly shallower slopes. This effect is seen in all plots of Figure 4.18.

To verify flux contamination as a probable cause of shallow slopes, Cepheids that have bright neighbours or are blended² are removed and period-luminosity relations are re-fitted to each bin of Cepheids. The flag value SExtractor provides for each Cepheid during photometry is used to identify those that are likely isolated and therefore subjected to little flux contamination; there are 797 Cepheids that satisfy these conditions. Plots of Leavitt Law and period-Wesenheit relation slopes from Cepheids with little to no flux contamination are shown in Figure 4.19. The correlation between slope and radius near the galactic centre is less pronounced in the new fits while the slopes beyond $\rho = 3$ kpc remain for the most part unchanged. Figure 4.20 shows the change in slopes between the two sets of fits.

Period distribution

Another contributing factor to the shallow slopes is the period distribution of the observable Cepheids. There is a selection bias towards the brighter and, hence, longer-period Cepheids near the centre of M33 because of the high stellar crowding. The

²SExtractor's definition of "blended" is used here.

correlation between pulsation period and metallicity (Szabados and Klagyivik, 2012) and the metal-rich nature of the central Cepheids further biases the period distribution to larger values. A comparison of the period distributions of Cepheids in the LMC and Cepheids in the inner regions of M33 is shown in Figure 4.21. There is a clear disparity between the two period distributions.

Given that the semi-empirical Leavitt Laws by Ngeow and Kanbur (2007) were derived from a sample of LMC Cepheids over a period range of $0.4 < \log P < 1.8$, and that there is a paucity of detectable short-period Cepheids near the centre of M33, the shallow slopes may also be a symptom of the putative break in linearity of the period-luminosity relation. The linearity break is usually framed as the slope of the Leavitt Law being shallower at longer periods ($\log P > 1$) than short ($\log P < 1$). Since there is a larger presence of Cepheids with long periods than short in the central region of M33, the slopes of the Leavitt Laws derived from such Cepheids are expected to be shallower than anticipated.

Acceptable radial range

Beyond $\rho = 8$ kpc, the slopes strongly diverge from previous values. The numbers of Cepheids sharply diminish (see Figure 4.6), leading to inaccurate determinations of Leavitt Law slopes and zero-points. For these reasons, only the Cepheids within $3 \leq \rho \leq 8$ kpc are used to determine effects of metallicity hereafter. This sample of Cepheids covers a range in metallicity of $-0.566 < [Z] < -0.156$ dex when using the metallicity profile of $[Z] = (0.09 \pm 0.04) - (0.082 \pm 0.010)\rho$ dex from U et al. (2009).

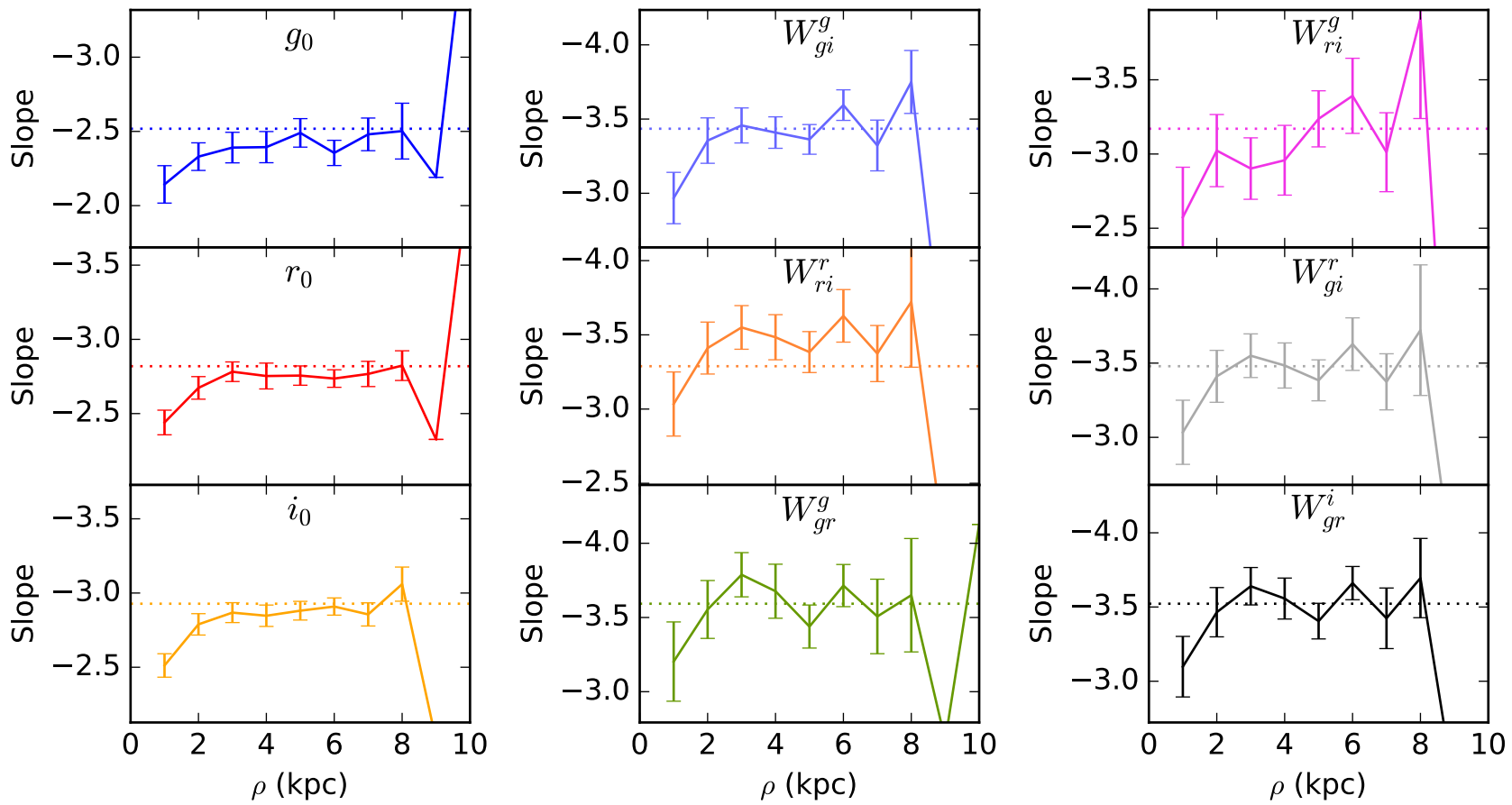


Figure 4.18: Variations in slopes with galactocentric radius. Dotted lines represent the semi-empirical values.

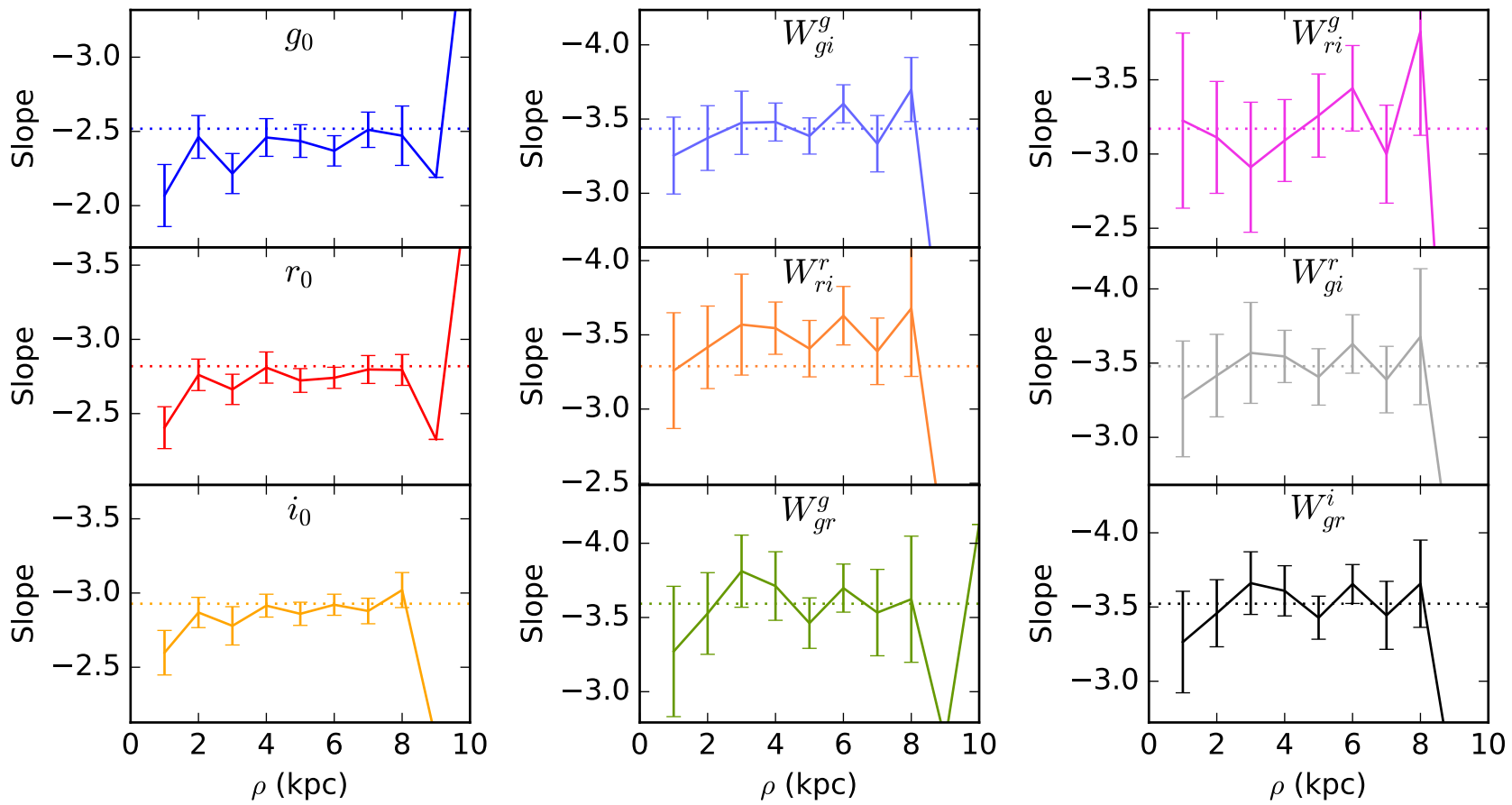


Figure 4.19: Same as Figure 4.18 but with only non-contaminated Cepheids.

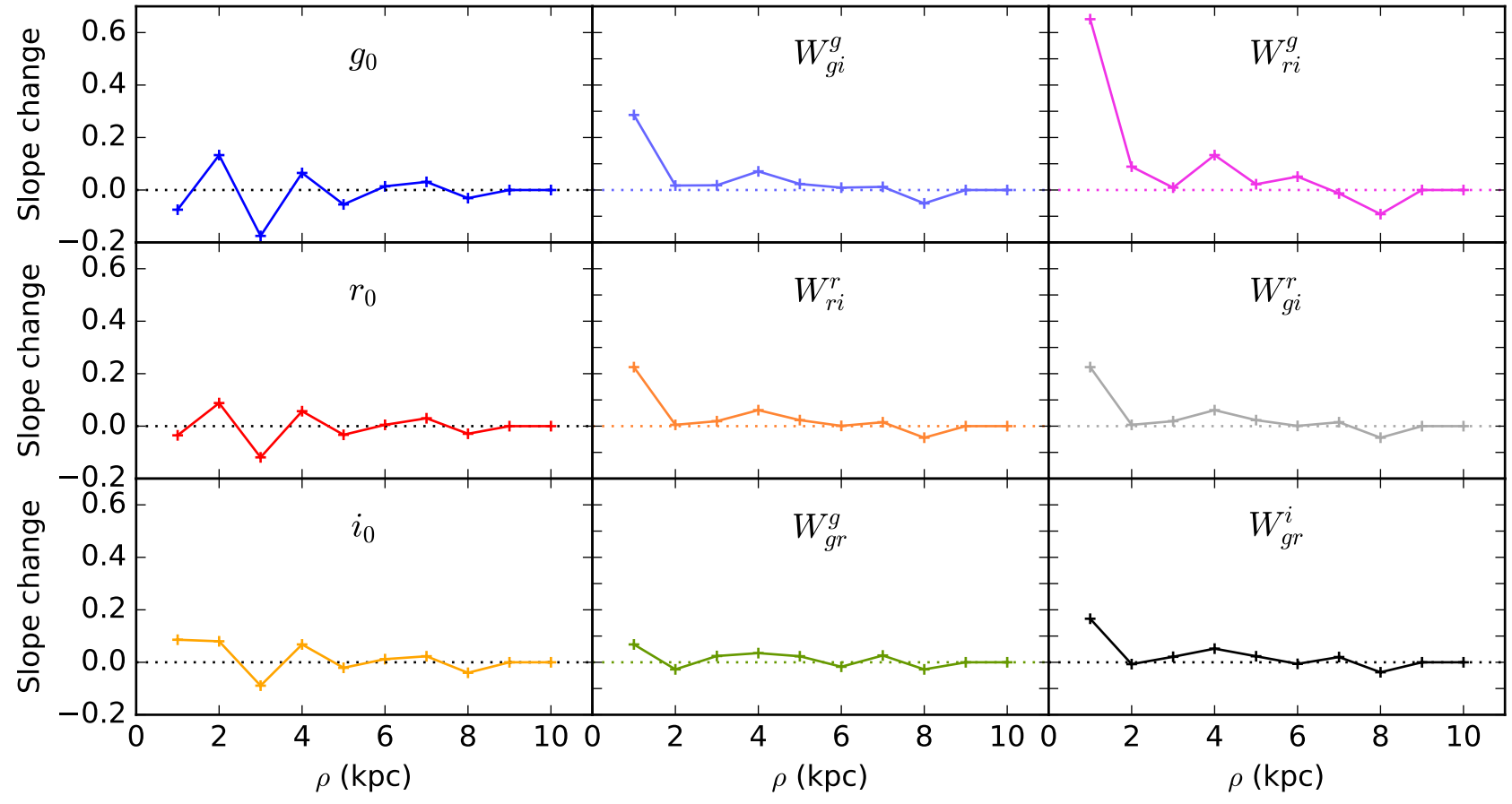


Figure 4.20: Changes in Leavitt Law slopes between fitting all Cepheids and using only isolated Cepheids.

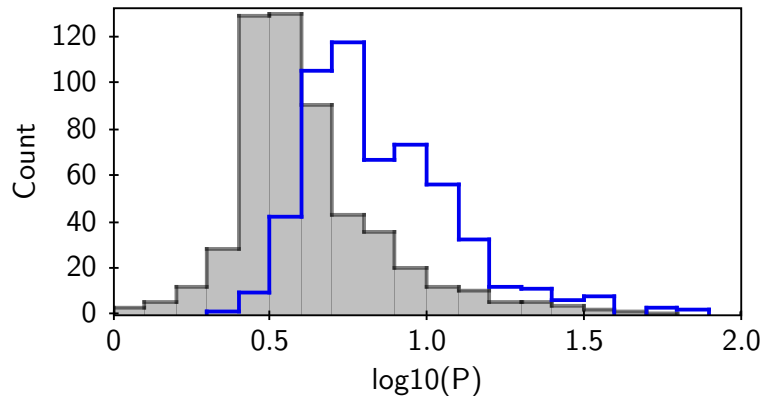


Figure 4.21: Period distributions of LMC Cepheids (grey filled histogram) and Cepheids at the centre of M33 (blue histogram).

4.6.2 Zero-points

The consistency of the empirically-fitted slopes with the predicted semi-empirical slopes gives credence to the results from the fixed-slope fits. For each annular sample of Cepheids, distance moduli are derived from the zero-points of the fixed-slope fits and are shown in Figure 4.22. A correlation between measured distance moduli and galactocentric radius is apparent.

Linear fits to the distance modulus gradients are listed in Table 4.7. For the single filter results, the steepness of the gradient increases with increasing wavelength. In the g band, the result is consistent with there being no effect. The Wesenheit gradients are consistent with each other though considerably steeper than those of the single filter fits. There are several possible causes for these observed distance modulus gradients: a radial gradient in reddening, stellar crowding, and metallicity effects.

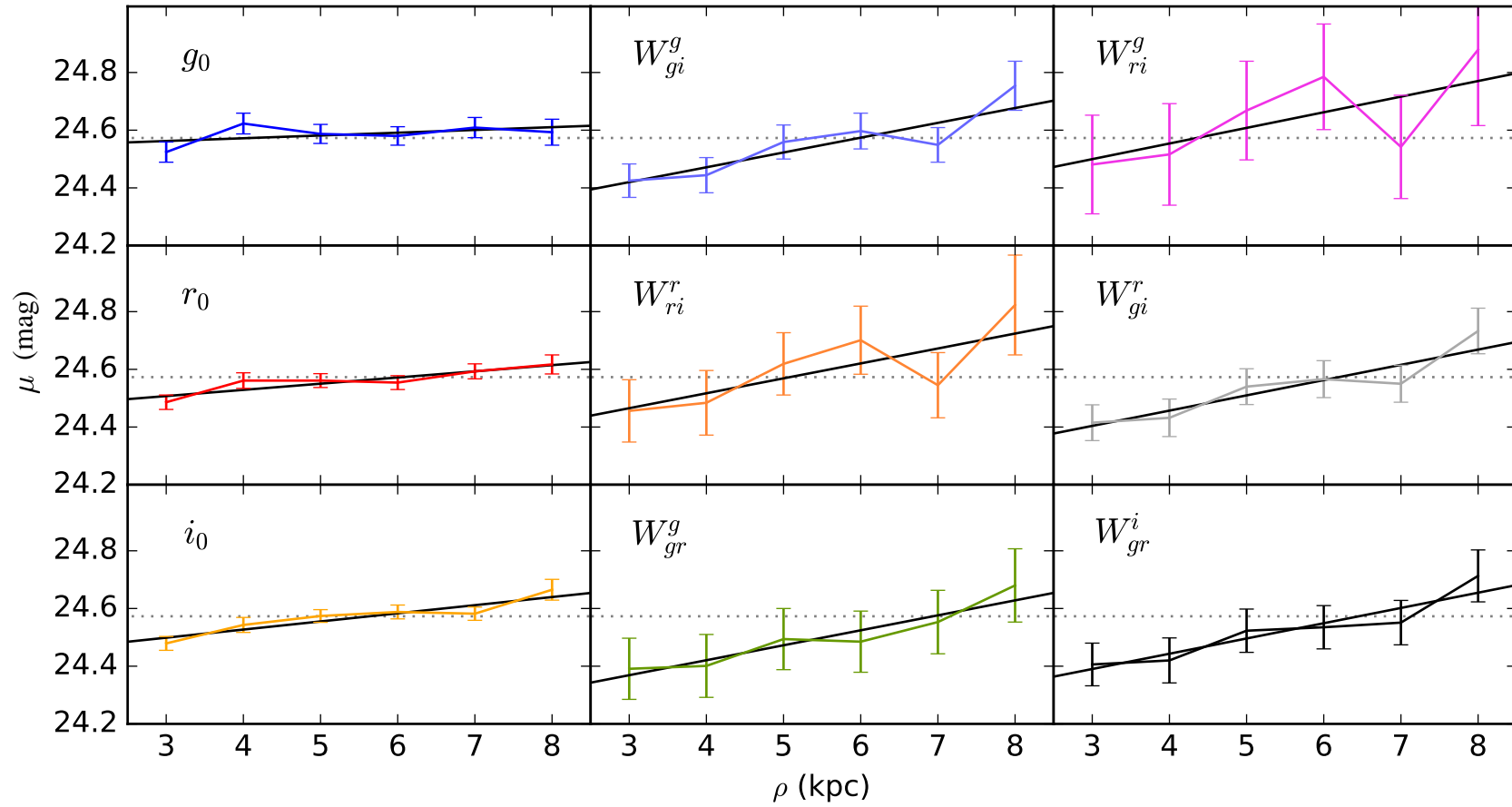


Figure 4.22: Variations in observed distance modulus with galactocentric radius and their linear fits. The dotted horizontal line marks the true distance modulus to M33 as determined from $[Z] = [Z]_{\text{LMC}}$ Cepheids.

Band	$\Delta\mu/\Delta\rho$ (mag/kpc)	Intercept (mag)
<i>g</i>	0.010 ± 0.012	24.534 ± 0.068
<i>r</i>	0.021 ± 0.008	24.443 ± 0.044
<i>i</i>	0.028 ± 0.009	24.414 ± 0.050
W_{gi}^g	0.051 ± 0.020	24.266 ± 0.109
W_{ri}^r	0.052 ± 0.033	24.310 ± 0.178
W_{gr}^g	0.052 ± 0.013	24.213 ± 0.074
W_{ri}^g	0.054 ± 0.044	24.337 ± 0.241
W_{gi}^r	0.053 ± 0.017	24.245 ± 0.093
W_{gr}^i	0.053 ± 0.015	24.232 ± 0.081

Table 4.7: Changes in observed distance modulus against galactocentric radius.

Reddening gradient

A radial variation in reddening may produce the observed changes in distance moduli in the single-filter Leavitt Law fits but not in the Wesenheit fits as they are by definition reddening-free. Variations in the reddening parameter R_V , however, can produce the changes in the distance moduli measured in Wesenheit indices. The Wesenheit plots in Figure 4.22 show that Cepheids appear dimmer the further they are from the centre which would require — all else being equal — the R_V value to increase as a function of galactocentric radius. Larger values for the reddening parameter results in extinctions that are not as chromatically sensitive and physically corresponds to the presence of larger dust grains along the line of sight. This would imply an unlikely scenario where the “dustiness” of M33 is greater in the outskirts than the central region.

From OB stars, Massey et al. (1995) acquire an average reddening of $E(B - V) = 0.13 \pm 0.01$ mag for M33 with no obvious signs of systematic spatial dependence, though they describe the reddening in M33 as being “patchy”. U et al. (2009) determined individual $E(B - V)$ reddening values for 22 blue supergiant stars across M33 (see Figure 4.23). They find an average reddening of $E(B - V) = 0.083$ mag and no significant radial reddening gradient. With the spectroscopic data from the study of HII regions by Rosolowsky and Simon (2008), U et al. (2009) determined

an independent distribution of reddening values, averaging around $E(B - V) = 0.11$ mag. While there is considerable scatter, they again find no radial dependency. The lack of a reddening gradient rules out reddening variations as a probable cause for the gradients in distance moduli seen in the single-filter bands.

Furthermore, if changes in reddening were the cause of apparent distance variations, the gradients in distance modulus should be steeper for decreasing wavelength. For a given difference in reddening $\Delta E(B - V)$ across a range in radius, the changes in extinctions — hence, distance modulus — in the three bands should follow $\Delta A_g > \Delta A_r > \Delta A_i$. This is not seen in the plots of distance moduli against galactocentric radius (Figure 4.22).

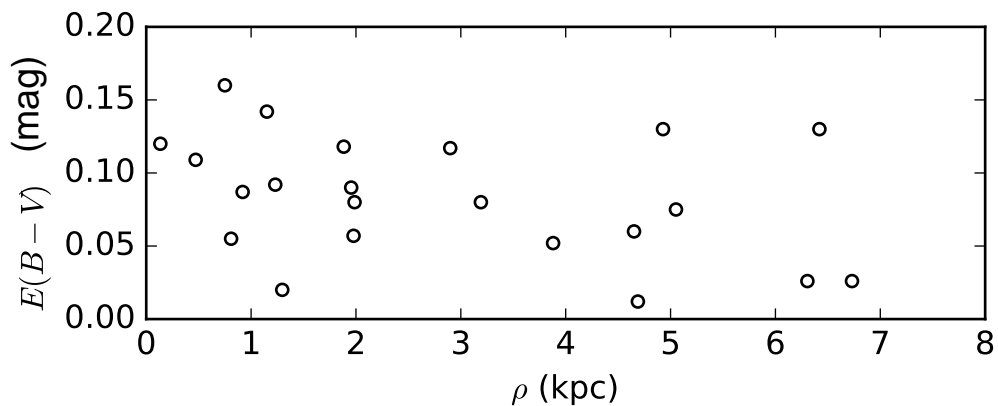


Figure 4.23: Reddening across M33 from observations of blue supergiant stars (U et al., 2009).

Blending and crowding

Crowding and blending could conceivably cause changes in the observed distance moduli by biasing the measurements of Cepheid magnitudes so that they appear brighter in denser regions. To test this possibility, the analysis of changes in observed distance moduli as a function of galactocentric radius is undertaken once more but with only the Cepheids that SExtractor report as being isolated.

Plots of the measured distance moduli from isolated Cepheids against galactocentric radius are shown in Figure 4.24. As with the previous case in which all Cepheids were

used, trends in measured distances with galactocentric radius in the range $3 < \rho < 8$ kpc are also present and are also numerically consistent with the results of the larger Cepheid sample (see Figure 4.25). Differences in stellar crowding are therefore unlikely to be the main or sole contributor to the gradients in measured Cepheid distance moduli.

Cepheids that are truly blended with another star will evade being filtered out with the aforementioned method as the companion is by definition unresolvable from the Cepheid and therefore undetected by SExtractor. Chavez et al. (2012) have quantified the effects of the blending of Cepheids in M33 through the comparison of ground-based Wisconsin–Indiana–Yale–NOAO (WIYN) photometry and Hubble Space Telescope photometry. They acquire their Cepheid sample from Pellerin and Macri (2011), whose images had a typical seeing of $0.75''$ which is similar to that of the CFHT stacks used here. Over half of the Cepheids were found not to be affected by blending in the ground-based V and I images. Of the Cepheids with companions, around 70% are photometrically affected below the 10% level. Supposing that the CFHT stacks also suffer from the same level of contamination, the overall effect of blending should not be significant here.

Binarity

Around 80% of Cepheids in the Milky Way are expected to be members of binary systems (Kervella et al., 2019). Flux from the companions will contribute to the measured flux of such Cepheids, introducing systematic errors into the apparent magnitudes and colours. Supposing that the companion in a binary system is a blue main-sequence star, the severity of the additional flux is expected to be relatively small; the apparent magnitudes and colour indices of the Cepheid can shift by several hundredths of a magnitude (Szabados, 2003).

Presuming that a similar fraction of Cepheids in M33 are in binary systems, a considerable number of the Cepheids used here will have companions, slightly biasing their apparent magnitudes and colours. Unless Cepheid binarity becomes more pronounced

as the galactocentric distance increases and contributes significantly to the observed Cepheid brightnesses, there is unlikely to be a scenario where binarity leads to the observed changes in distance modulus as a function of galactocentric radius.

Metallicity

Variations in metallicity are thus the most likely explanation for the observed changes in distance moduli. Recent observational studies into the effect of metallicity on the Leavitt Laws in non-Sloan filters reveal the presence of the same phenomenon: the brightening of Cepheids with increasing metallicity. See [Sasselov et al. \(1997\)](#), [Scowcroft et al. \(2009\)](#), [Gerke et al. \(2011\)](#), [Storm et al. \(2011\)](#), [Shappee and Stanek \(2011\)](#), [Mager et al. \(2013\)](#), [Fausnaugh et al. \(2015\)](#), [Gieren et al. \(2018\)](#) for such examples.

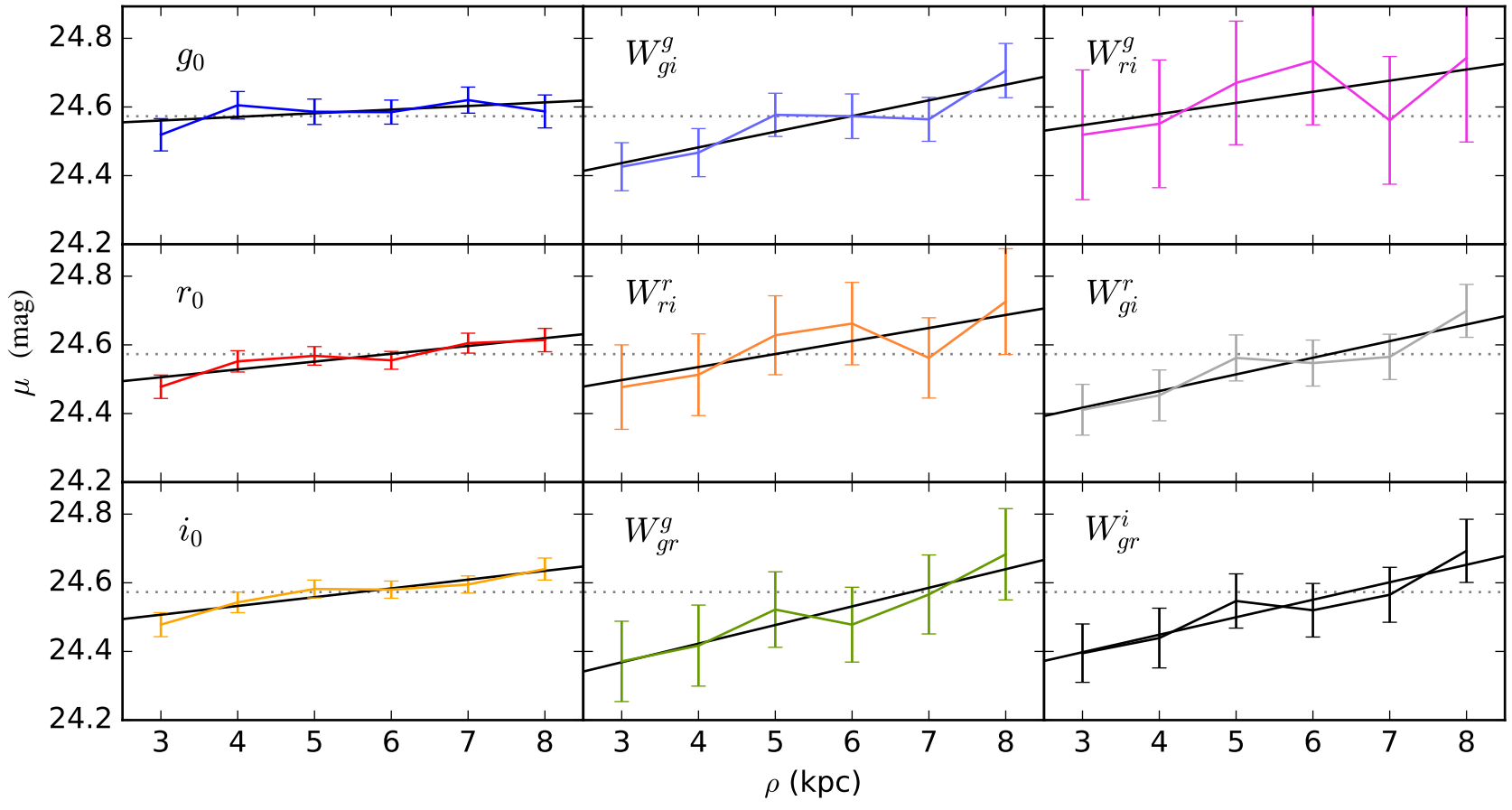


Figure 4.24: Same as Figure 4.22 but from only isolated Cepheids.

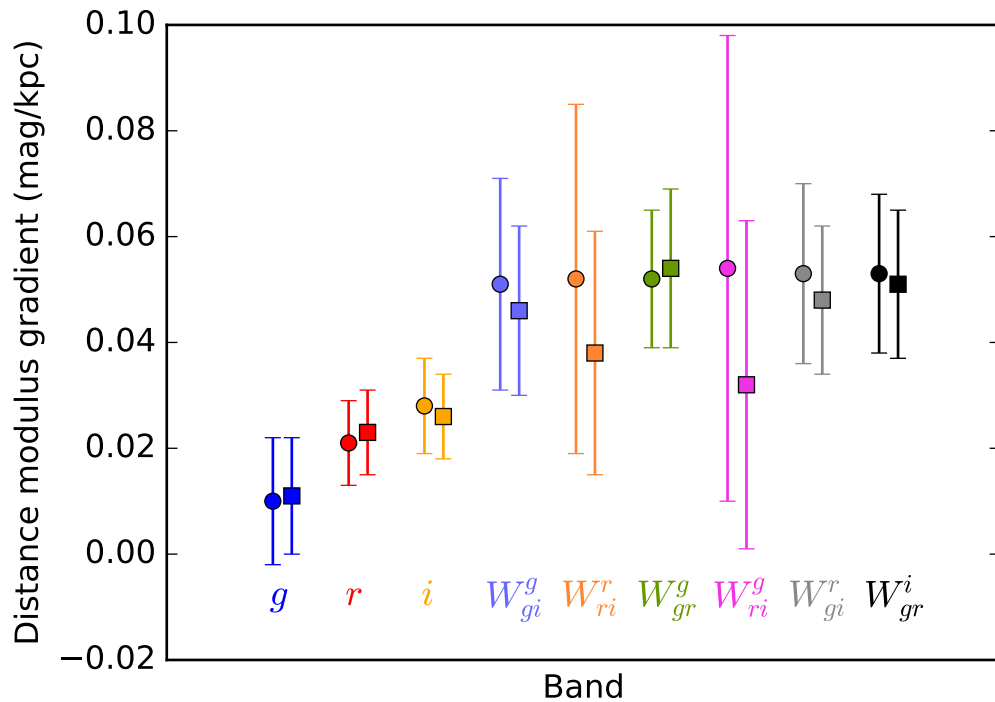


Figure 4.25: Observed gradients in distance modulus from all Cepheids (circles) and Cepheids with no bright stellar neighbours (squares).

4.6.3 Metallicity correction values

Potential values for the magnitude-metallicity parameters ($\gamma_\lambda = \Delta\mu_\lambda/\Delta[\text{Metal}]$) are inferred by taking the gradients in distance modulus from Table 4.7 and dividing by a range of metallicity gradients (see Equation 4.1), and are shown in Figure 4.26.

With these metallicity-correction curves, several recent metallicity gradients obtained from different tracers are evaluated: the stellar metallicity gradient of $d[Z]/d\rho = -0.082 \pm 0.010$ dex/kpc derived from blue supergiant stars (U et al., 2009), the stellar gradient of $d[Z]/d\rho = -0.112$ dex/kpc derived from beat Cepheids (Beaulieu et al., 2006)³, and the gas-phase gradient of $d[\text{O}/\text{H}]/d\rho = -0.024 \pm 0.004$ dex/kpc from HII regions (Lin et al., 2017). Table 4.8 lists the resulting metallicity correction values.

³With updated deprojected radii

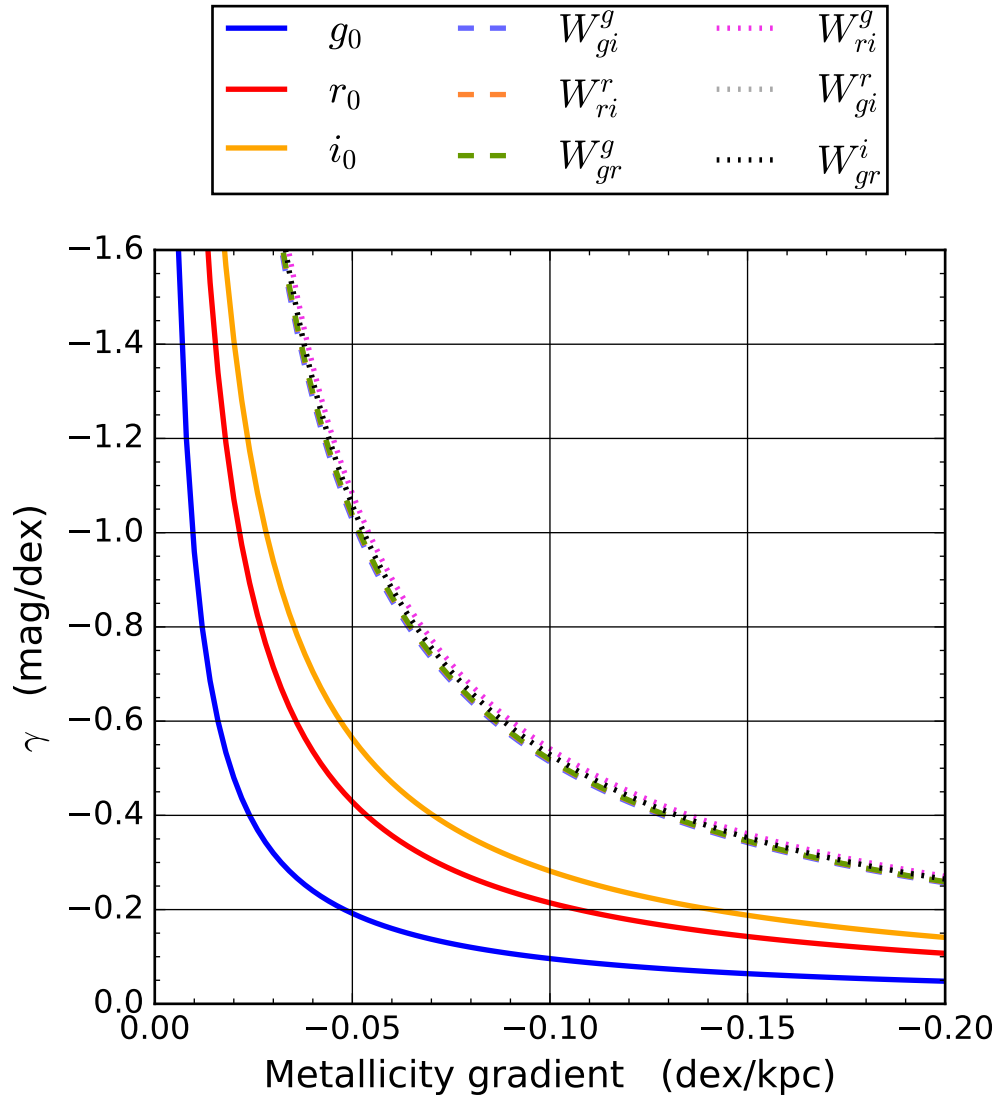


Figure 4.26: Curves of potential metallicity parameter values.

Band	γ (mag/dex) BSGs: $d[Z]/d\rho = -0.082$	γ (mag/dex) BCs: $d[Z]/d\rho = -0.112$	γ (mag/dex) HII regions: $d[\text{O}/\text{H}]/d\rho = -0.024$
g	-0.122 ± 0.146	-0.089 ± 0.107	-0.417 ± 0.500
r	-0.256 ± 0.098	-0.188 ± 0.071	-0.875 ± 0.333
i	-0.341 ± 0.110	-0.250 ± 0.080	-1.167 ± 0.375
W_{gi}^g	-0.622 ± 0.244	-0.455 ± 0.179	-2.125 ± 0.833
W_{ri}^r	-0.634 ± 0.402	-0.464 ± 0.295	-2.167 ± 1.375
W_{gr}^g	-0.634 ± 0.159	-0.464 ± 0.116	-2.167 ± 0.542
W_{ri}^g	-0.659 ± 0.537	-0.482 ± 0.393	-2.250 ± 1.833
W_{gi}^r	-0.646 ± 0.207	-0.473 ± 0.152	-2.208 ± 0.708
W_{gr}^i	-0.646 ± 0.183	-0.473 ± 0.134	-2.208 ± 0.625

Table 4.8: Metallicity correction values for various metallicity gradients.

For fairly steep gradients from stellar tracers, the metallicity correction values are mostly within reasonable limits. For the shallow metallicity gradient derived from HII regions, however, the resulting correction values are exceedingly large in all but the g filter. One simplistic explanation for the large values is that M33 does not possess a shallow metallicity gradient and that the gradients listed in Table 2.3 corresponding to HII regions are erroneous. A more realistic explanation is that chemical abundances derived from spectroscopic observations of HII regions at various radii are valid but are not representative of the metallicities of Cepheids at the same radii. As can be seen in Table 2.3, the gradients derived from stellar tracers tend to be steeper than those of HII regions, supporting the second option.

The fact that the metallicity gradients as traced by individual stars are steeper than those traced by HII regions is perhaps not unexpected. [Beasley et al. \(2015\)](#) acquired metallicities for 77 stellar clusters of various ages across M33 and find that the older stellar clusters yield steeper metallicity gradients. In other words, the metallicity gradient of M33 as traced by star clusters flattens with time. Since HII regions are younger than the stars that are used here, one would expect that metallicity gradients derived from such tracers will be flatter than stellar-based determinations.

However, the age difference between stellar tracers and HII regions may not be large

enough to allow for a significant change in metallicity gradient. Other potential sources of the discrepancy in gradient steepness are the systematic uncertainties associated with the methods with which chemical abundances are determined. As discussed by [Kudritzki and Urbaneja \(2012\)](#), the “strong line method” of determining the oxygen content of HII regions involves large uncertainties; in particular, by adopting different calibrations of the strong line method, the steepness of a measured metallicity gradient can change from being significant to being non-existent, and the measured absolute values of metallicity can change by as much as 0.6 dex. Most of the metallicity determinations of HII regions by [Lin et al. \(2017\)](#) made use of the strong line method.

[Shappee and Stanek \(2011\)](#) arrived at a value for γ in the V_{IG} Wesenheit index of $\gamma_{VI} = -0.80$ mag/dex by comparing the magnitudes of Cepheids of different metallicities in separate fields of M101. The consequences of such a large metallicity correction were explored by [Majaess et al. \(2011\)](#). They find that applying such a metallicity correction to Cepheid-based distances to the Magellanic Clouds yields distances that significantly disagree with those derived from other methods. Metallicity corrections of $\gamma \sim -2$ mag/dex in [Table 4.8](#) are clearly intolerable; chemical abundances determined from HII regions are not a suitable proxy for Cepheid metallicities.

[Hoffmann and Macri \(2015\)](#) acquired a Cepheid-based distance to the maser-hosting galaxy NGC 4258 with Sloan-band data. The maser in NGC 4258 provides a precise and accurate independent distance estimate via very-long-baseline interferometry, against which the Cepheid Leavitt Law can be calibrated. Like [Ngeow and Kanbur \(2007\)](#), they construct semi-empirical Leavitt Laws in Sloan filters which they then fit to almost 100 Cepheids. Their slopes agree well with those of [Ngeow and Kanbur \(2007\)](#) and, therefore, to those empirically determined here. Theoretical Leavitt Laws were also created following the method used by [Di Criscienzo et al. \(2013\)](#) and were also found to be consistent. Unfortunately, NGC 4258 features an LMC-like metallicity throughout its disk ([Bresolin, 2011a](#)), rendering a test of the Sloan-band metallicity effect on Cepheids (à la [Majaess et al. 2011](#)) infeasible. An ideal candidate for evaluating the validity of the Sloan-band metallicity corrections is the Small Magellanic Cloud. This nearby system hosts almost 3000 Cepheids pulsating in the fundamental

mode (Soszyński et al., 2015), possesses a metallicity that is ~ 0.4 dex below that of the LMC, and has distance estimates from a variety of methods (de Grijs and Bono, 2015). However, no Sloan-band data is currently available to enable such a test.

The beat Cepheid metallicity gradient of $d[Z]/d\rho = -0.112$ dex/kpc is adopted and the metallicity parameter values listed under that gradient in Table 4.8 are chosen to be the final — though tentative — results. The metallicity gradient acquired from the updated linear fit to the metallicities of 5 beat Cepheids against their galactocentric position in Section 2.1.2 was presented without any errors. The error associated with each γ value should therefore be taken as the lower limit as no error from the metallicity gradient has been propagated into the final values. By assuming a generous error of 0.056 dex/kpc on the metallicity gradient and propagating that value, the error on γ increases by as little as 0.009 mag/dex in g and by as much as 0.144 mag/dex in W_{gr}^g .

The small spread of the Wesenheit-band metallicity parameters suggests that a single quantity γ_W can encompass the effect of metallicity in all Sloan Wesenheit indices. A weighted mean gives $\gamma_W = -0.468$ mag/dex.

A recent multi-band study into the effects of metallicity on Cepheid brightnesses by Gieren et al. (2018) find metallicity correction values in optical and near-infrared bands (see Table 4.10) that are comparable to the ones determined here though they use a different filter system. Their $V, (V - I)$ Wesenheit metallicity parameter of -0.335 ± 0.059 mag/dex is also consistent with the parameters measured here with Sloan-band Wesenheit indices. No wavelength dependency is seen in their results, however. Their method of acquiring metallicity parameters relies upon accurate distances determined with a Baade-Wesselink method to a sample of SMC Cepheids to establish absolute magnitude Leavitt Laws. With Leavitt Laws of fixed identical slopes for the Milky Way, LMC and SMC, they quantified the correlation between zero-point and metallicity.

Another recent multi-band study by Wielgórski et al. (2017) found metallicity parameter values in all bands consistent with zero, a finding that is incompatible with the results reported here. To acquire their metallicity corrections, they compare the rela-

tive distance difference between the LMC and the SMC as determined from eclipsing binary systems with the relative distance determined from Cepheids. As noted by [Gieren et al. \(2018\)](#), the determination of the metallicity parameters by [Wielgórski et al. \(2017\)](#) is strongly predicated on the adopted relative distance difference between the two Magellanic Clouds; a decrease in the distance to the SMC of 0.07 mag in distance modulus is sufficient to increase the size of the metallicity effect to ~ -0.2 mag/dex in all bands, bringing them in line with the values measured here.

The first two columns of Table 4.10 present the Wesenheit metallicity parameters and errors determined in this work and the final results from [Gieren et al. \(2018\)](#), [Wielgórski et al. \(2017\)](#) in a variety of passbands. Results from [Storm et al. \(2011\)](#) are also included though they do not report their errors. The errors reported in the present study are considerably larger than those given by [Gieren et al. \(2018\)](#) and [Wielgórski et al. \(2017\)](#) in the Wesenheit indices. This may in part be due to the differing method with which the errors in the zero-points of the period-Wesenheit relations were estimated and the propagation of those errors. In this study, the slopes and zero-points of the period-Wesenheit relations were determined with a linear regression algorithm that incorporates the intrinsic scatter of the relations ([Akritas and Bershady, 1996](#)), while the two earlier studies rely on the standard least squares method. By not incorporating the intrinsic scatter of the period-Wesenheit relations during the fitting procedures, the errors on the zero-points are likely to be underestimates.

Most empirical studies into the Cepheid metallicity effect observe that Cepheids of higher metallicity are more luminous in optical wavelengths than their metal-poor counterparts of the same period. Counter to the majority of observational results, theoretical investigations into the role of metallicity on Cepheid brightnesses suggest that the effect exists but in the opposite direction where metal-rich Cepheids are dimmer than those that are metal-poor of the same period ([Caputo et al. 2000](#), [Bono et al. 2008](#)). The fact that theory and observation contradict each other points towards some unknown mechanisms in either approach to the study of the metallicity effect, or perhaps to too strong a reliance on certain assumptions (such as minimal blending on the observational side and the efficacy of pulsation and atmospheric models on the theo-

retical side). On this topic, [Gieren et al. \(2018\)](#) stated that the uncertainties associated with the metallicity effects determined from pulsation theory are still substantial.

4.6.4 Period-luminosity-metallicity relations

A metallicity term is now appended to the usual form of the Leavitt Law:

$$m = a \log P + b + \gamma ([Z] - [Z_{\text{LMC}}]) \quad (4.8)$$

The terms in the period-luminosity-metallicity relations in the single-filter bands and Wesenheit indices are listed in [Table 4.9](#).

Band	a	b (mag)	γ (mag/dex)
g	-2.518	23.793 ± 0.017	-0.089 ± 0.107
r	-2.819	23.475 ± 0.012	-0.188 ± 0.071
i	-2.928	23.414 ± 0.013	-0.250 ± 0.080
W_{gi}^g	-3.435	22.946 ± 0.027	-0.455 ± 0.179
W_{ri}^r	-3.289	23.214 ± 0.041	-0.464 ± 0.295
W_{gr}^g	-3.593	22.657 ± 0.033	-0.464 ± 0.116
W_{ri}^g	-3.170	23.430 ± 0.058	-0.482 ± 0.393
W_{gi}^r	-3.479	22.865 ± 0.025	-0.473 ± 0.152
W_{gr}^i	-3.522	22.786 ± 0.026	-0.473 ± 0.134

Table 4.9: Sloan-band Leavitt Law terms with metallicity corrections for Cepheids in M33.

4.7 Predicting Wesenheit metallicity parameters

When the Leavitt Laws were predicted in Wesenheit indices in Section 4.5.2, the slopes and zero-points were determined by substituting the single-band magnitude terms in Equations 4.3 with their Leavitt Law equivalents. The metallicity parameters in the Wesenheit indices can be predicted in the same manner by using the metallicity parameters found for the single-band Leavitt Laws. For example, the metallicity parameter in the W_{gi}^g band is predicted in the following way:

$$\gamma_{gi}^g = \gamma_g - R_{gi}^g \times (\gamma_g - \gamma_i) \quad (4.9)$$

Predictions and comparisons are made using the Sloan single-band results determined here and also from non-Sloan single-band results in the literature (see Table 4.10). The results from the multi-band studies on the effects of metallicity on Cepheids by Gieren et al. (2018), Wielgórski et al. (2017) and Storm et al. (2011) are presented here to demonstrate the efficacy of the predictions, independent of the results determined here.

The predicted metallicity parameters in the Sloan Wesenheit indices all cluster around $\gamma = -0.450$ mag/dex and are also consistent with their corresponding measured values. For each of the other multi-band studies, the predicted and measured parameters also agree well (see Figure 4.27), indicating that the prediction procedure is valid.

4.8 Wavelength dependency

A plot of the metallicity parameters as a function of the wavelength through which they were measured reveals a tentative relation between the two quantities: the metallicity effect becomes stronger at longer wavelengths (see Figure 4.28). An unweighted linear fit is made to the three single-filter metallicity corrections against inverse wavelength, giving $\gamma = 0.09 \times \lambda^{-1} - 0.448$ mag/dex where λ is given in μm . The SDSS filter

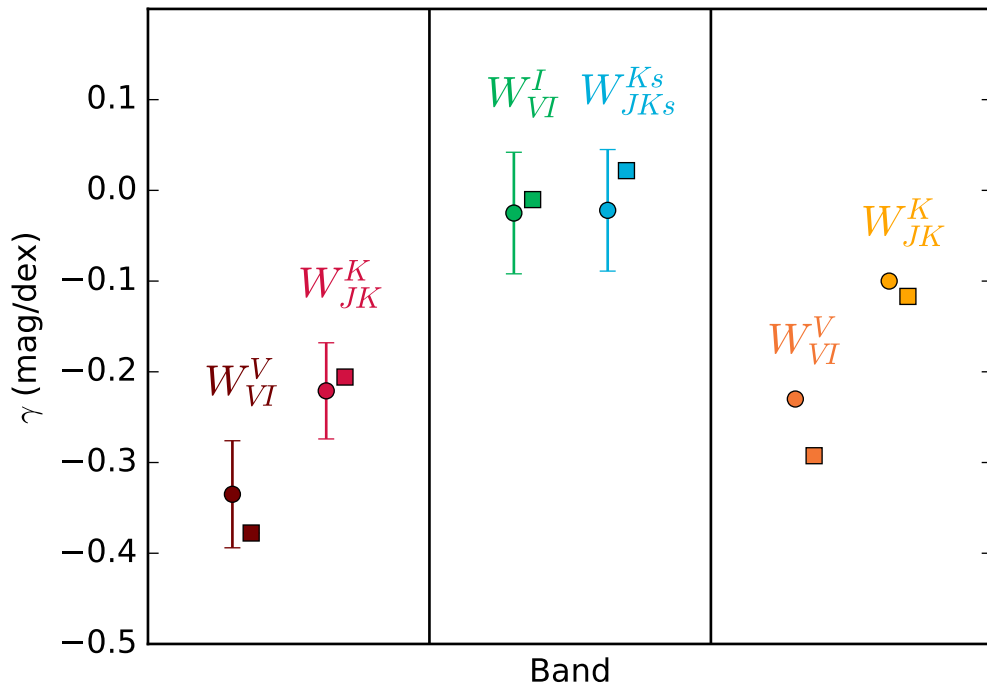


Figure 4.27: Comparison of measured metallicity correction values in the literature (circles) and predicted values (squares). *Left*: values are from [Gieren et al. \(2018\)](#). *Centre*: values are from [Wielgórski et al. \(2017\)](#). *Right*: values are from [Storm et al. \(2011\)](#).

set includes two additional filters: u for ultraviolet and z for infrared with central wavelengths of $0.3551 \mu\text{m}$ and $0.8932 \mu\text{m}$ respectively. Assuming that the linear fit between wavelength and metallicity correction persists beyond the g filter into the ultraviolet regime and below i , the metallicity correction in the u band is predicted to be $+0.049 \text{ mag/dex}$, while for z it is -0.292 mag/dex .

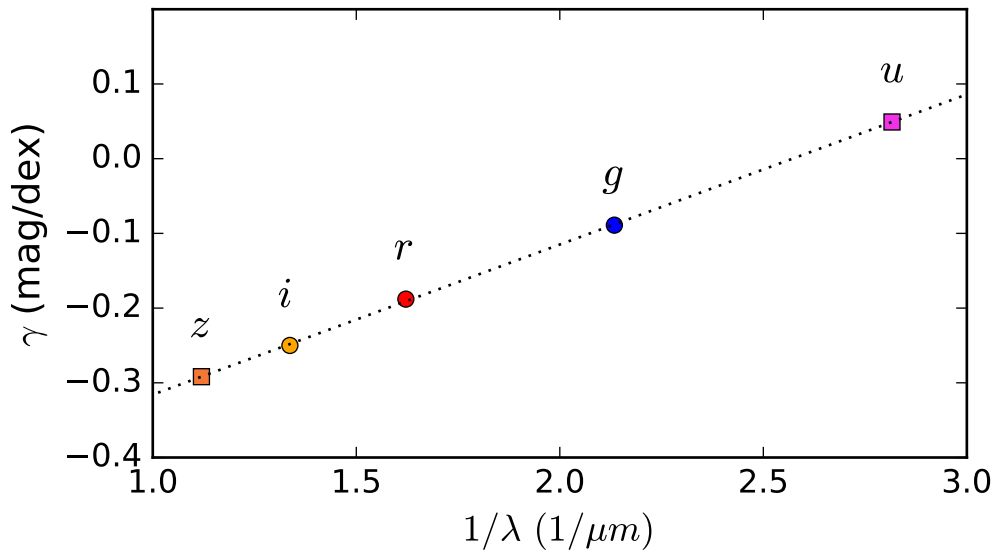


Figure 4.28: Metallicity corrections against wavelength. The circular points denote the empirical measurement. Square points mark the predicted corrections in the other Sloan filters. The line is the unweighted linear fit using the three single-filter metallicity corrections.

In their multi-wavelength study of metallicity effects on LMC Cepheids, [Freedman and Madore \(2011\)](#) also find a monotonic correlation with wavelength in the same direction — that is, the metallicity parameter is more negative at longer wavelengths. However, they determine positive values for the metallicity parameter in optical bands and negative values in the mid-infrared. In this work with Sloan-band data, the metallicity parameters start off negative in the optical ($\gamma_g = -0.089 \pm 0.107$ mag/dex) and become progressively more negative at longer wavelengths.

As stated in [Freedman and Madore \(2011\)](#), the trend in metallicity parameter with wavelength is consistent with line blanketing effects. Flux at short wavelengths is preferentially absorbed and re-emitted at longer wavelengths by metals in Cepheid atmospheres. In the case of this work, flux from photons with wavelengths shorter than that of the g filter appears to be redistributed to longer wavelengths as evidenced by the negative signs of the metallicity parameters in g , r and i filters.

Band	γ (mag/dex)	Predicted γ (mag/dex)	Source
W_{gi}^g	-0.455 ± 0.179	-0.450	This work
W_{ri}^r	-0.464 ± 0.295	-0.455	
W_{gr}^g	-0.464 ± 0.116	-0.442	
W_{ri}^g	-0.482 ± 0.393	-0.460	
W_{gi}^r	-0.473 ± 0.152	-0.447	
W_{gr}^i	-0.473 ± 0.134	-0.445	
V	-0.238 ± 0.186		
I	-0.293 ± 0.150		
W_{VI}^V	-0.335 ± 0.059	-0.378	
J	-0.270 ± 0.108		
K	-0.232 ± 0.064		
W_{JK}^K	-0.221 ± 0.053	-0.206	
V	-0.022 ± 0.076		Wielgórski et al. (2017)
I	-0.015 ± 0.071		
W_{VI}^I	-0.025 ± 0.067	-0.010	
J	-0.042 ± 0.069		
H	-0.012 ± 0.069		
Ks	-0.017 ± 0.069		
W_{JKs}^{Ks}	-0.022 ± 0.067	+0.022	
V	+0.09		Storm et al. (2011)
I	-0.06		
W_{VI}^V	-0.23	-0.29	
J	-0.10		
K	-0.11		
W_{JK}^K	-0.10	-0.12	

Table 4.10: Metallicity parameters from several studies using multi-band data. Predicted values are calculated using the corresponding single-band results.

Chapter 5

Tip of the Red Giant Branch

With the available catalogue of M33 stars, an independent, non-Cepheid method to determine the distance to M33 is possible through the use of the tip of the red giant branch (TRGB). Section 1.5.3 gives a basic overview of a typical procedure to identify the magnitude at which the tip is located.

The TRGB magnitude is conventionally measured with the Cousins I filter where the effects of metallicity on the TRGB luminosity are minimised. No empirical calibrations of the TRGB in Sloan bands are available, though Bellazzini (2008) provide preliminary theoretical values on the basis of stellar models. They find absolute magnitudes of the TRGB in Sloan i and z filters of $M_i^{\text{TRGB}} = -3.44 \pm 0.1$ mag for $[\text{Fe}/\text{H}] \leq -1.0$ dex, and $M_z^{\text{TRGB}} = -3.67 \pm 0.1$ mag for $[\text{Fe}/\text{H}] \leq -0.4$ dex (see Figure 5.1).

In the previous chapter, Cepheids were binned into galactocentric annuli to assess the variation in distance modulus with galactocentric radius. The same approach will be used here: RGB stars will be binned into a series of galactocentric annuli, from which individual TRGB distances will be measured with i -band data. With Cepheids, variations in distance moduli were observed and were attributed to metallicity effects after crowding and reddening variations were ruled out. Under the presumption that there is no reddening variation and that crowding effects are minimal, TRGB distances are not expected to vary significantly as a function of radius. However, because the TRGB method is only applicable at metallicities of $[\text{Fe}/\text{H}] \leq -1.0$ dex in the i band, the use

of this method is permitted only in metal-poor regions of M33, limiting its efficacy to the outer regions of the galaxy.

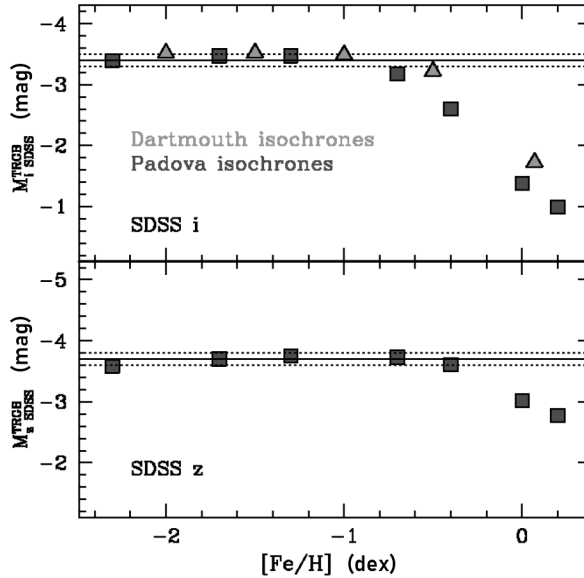


Figure 5.1: Absolute magnitudes of the TRGB in the Sloan i and z filters as a function of $[\text{Fe}/\text{H}]$ metallicity as determined from two sets of stellar models. Figure from [Bellazzini \(2008\)](#).

5.1 Locating the tip

From the CFHT catalogue of ~ 1.4 million M33 stars, candidate RGB stars near the TRGB are identified by their positions on the i against $r - i$ CMD. The stars in the region demarcated by the following relations

$$20 < i < 22, \quad 23 - 3.5(r - i) < i < 26 - 3.5(r - i) \quad (5.1)$$

are used to locate the apparent TRGB magnitude (see [Figure 5.2](#)). Stars that raise a non-zero SExtractor photometry flag value (i.e., stars that are not isolated) are discarded from the sample. This additional constraint acts to lessen the number of stars with potentially contaminated magnitude and colour measurements. The presence of such contaminated stars would otherwise have increased the dispersion in the data, reducing the precision with which the TRGB can be discerned. It should be noted that

no attempts have been made at removing foreground stars from the sample.

This subset of stars is separated into radial bins of 0.5 kpc thickness out to a maximum galactocentric radius of 10 kpc. For each binned sample of RGB stars, a luminosity function (LF) is constructed where a magnitude interval size of 0.05 mag is used. The location of the TRGB in the LF — if clearly present — is marked by a sharp change (discontinuity) in the number of stars across a small change in magnitude. To computationally acquire the magnitude at which the discontinuity occurs, the LF is convolved with an edge-detection kernel. The kernel is of the form $[-1, -2, 0, +2, +1]$; at a given magnitude bin centred on M^j , the output (response function) of the convolution of the kernel with the LF is equal to $-1(N^{j-2}) - 2(N^{j-1}) + 2(N^{j+1}) + 1(N^{j+2})$ where N^j is the number of stars in the magnitude bin around M^j . The output of the edge-detection convolution peaks at the LF discontinuity and the magnitude at which the peak occurs is read off accordingly as the TRGB magnitude.

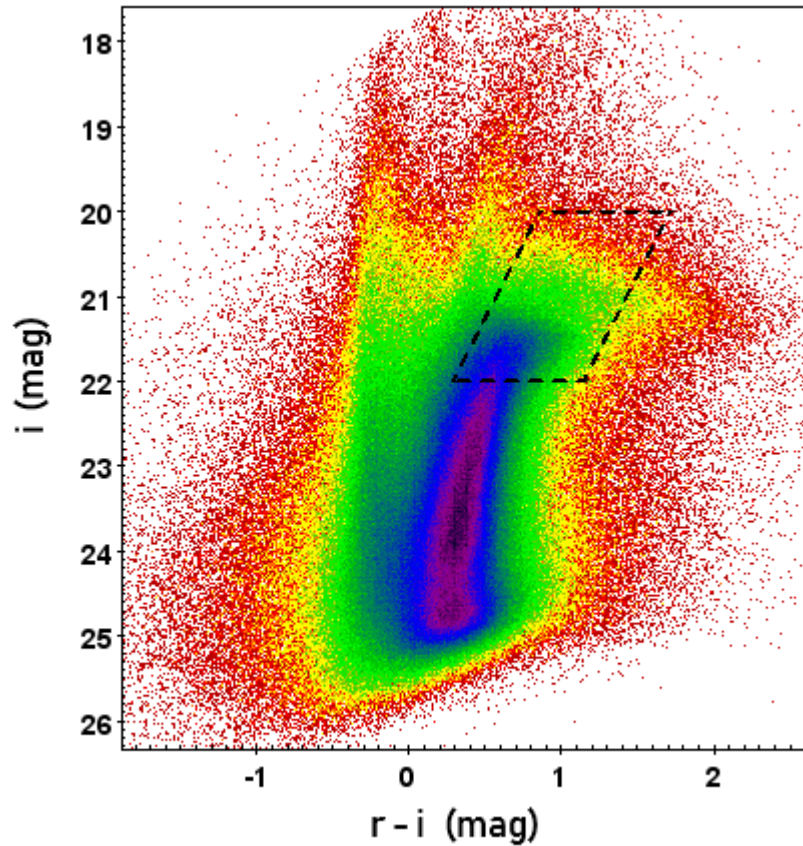


Figure 5.2: *i* vs *r* - *i* CMD with the TRGB region bounded by dashed lines.

5.2 TRGB distances

Figure 5.4 presents, for each radial bin, a 2D density plot of $r - i$ colour against i magnitude (i.e., a CMD rotated by 90°), a histogram showing the distribution of i -band magnitudes in orange (i.e., the LF of the stars in the annular bin), and the response of the convolution of the LF with the edge-detection kernel in black.

Tiede et al. (2004) obtained an M33 RGB metallicity gradient of $[\text{Fe}/\text{H}] = (-0.07 \pm 0.01)\rho - (0.48 \pm 0.04)$ dex by combining their chemical abundance determinations for RGB stars located beyond 8 kpc from the galactic centre with those determined by Kim et al. (2002) for inner field RGB stars (see Figure 5.3). The radius at which the RGB metallicity falls to $[\text{Fe}/\text{H}] = -1$ dex is ~ 7.4 kpc; at smaller radii (higher metallicity), the TRGB method is expected to no longer be a reliable distance estimator. The presence of a sharp, unambiguous, dominant peak in the convolution output is seen in bins at radii $\rho > 5.5$ kpc except at $7.0 < \rho < 7.5$ kpc.

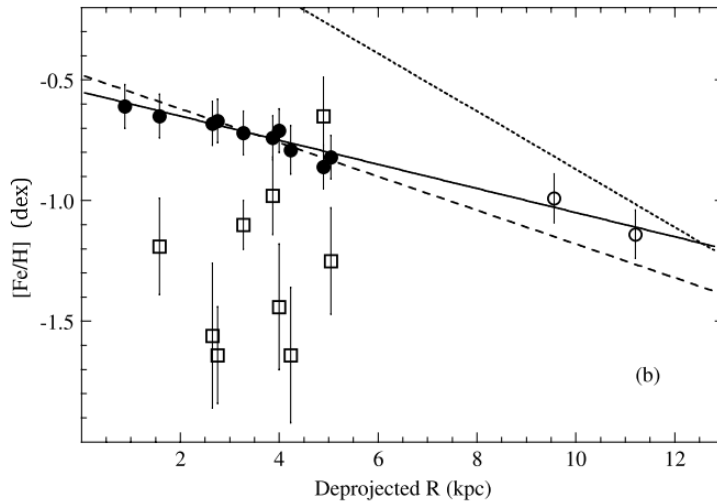


Figure 5.3: RGB metallicities as a function of galactocentric radius. Filled circles are from Kim et al. (2002), open circles from Tiede et al. (2004), and squares are halo globular cluster metallicities from Sarajedini et al. (2000). The RGB metallicity gradient used here is represented by the dashed line which is a linear fit to the filled circles (except the innermost two points). Figure from Tiede et al. (2004).

The series of convolution outputs in Figure 5.4 (black response functions) are collated into a heatmap to better illustrate the effectiveness of the TRGB-identification proce-

dure as a function of galactocentric radius (see Figure 5.5). Before they are placed side by side, the response function for a given bin is normalised by dividing by the maximum value of the response in that bin and negative values are set to 0; this is to ensure that the variations in each response function remain visible when juxtaposed.

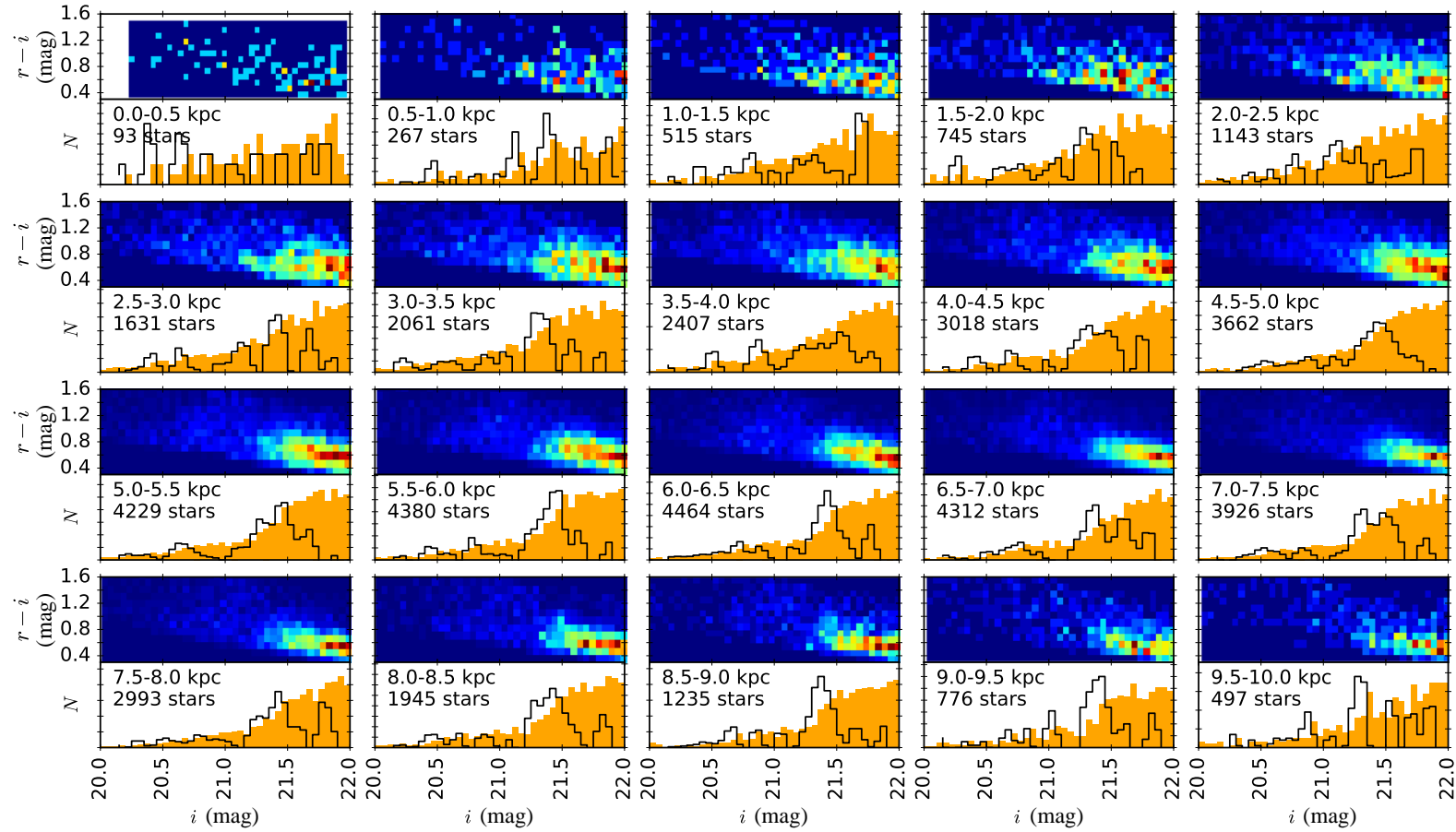


Figure 5.4: Stars in the TRGB region are binned into galactocentric annuli. The coloured density plot (rotated CMD) shows $r - i$ colour against i magnitude with denser regions being redder. The luminosity function of the stars in a given annular bin is presented below its associated CMD as the filled orange histogram. The convolution of the LF with an edge-detection kernel is superimposed on the LF in black (values below 0 are omitted). The peak in a convolution output corresponds to the discontinuity in the LF and to the TRGB magnitude.

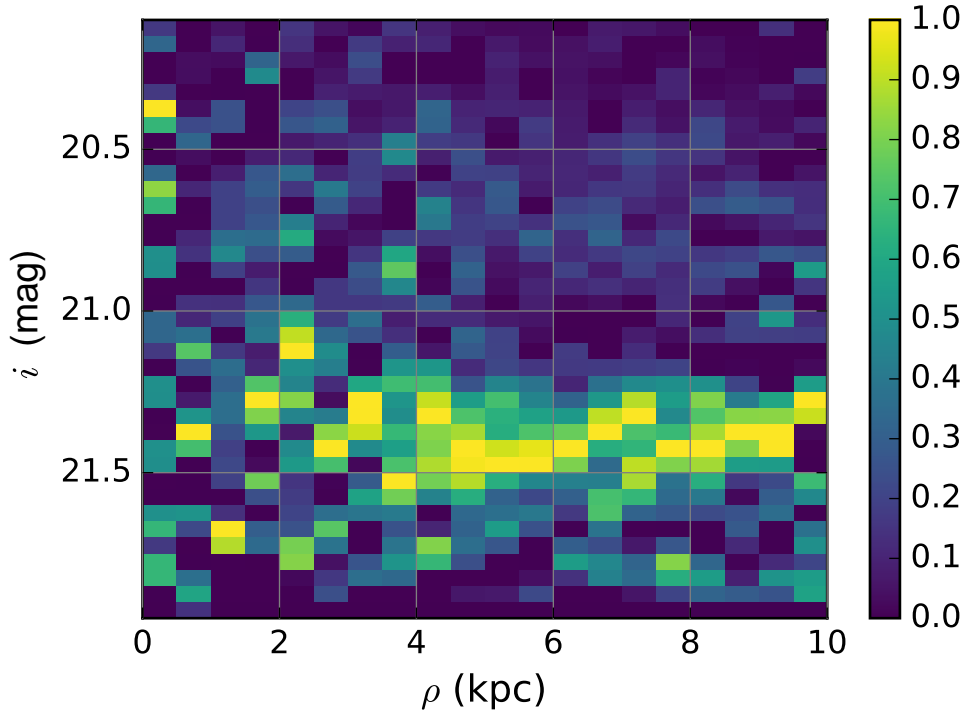


Figure 5.5: The response functions from Figure 5.4 collated and displayed as a heatmap after normalisation. For each radial bin, the peak in the heatmap corresponds to the peak in the response function, i.e., the TRGB magnitude.

With a measured apparent TRGB magnitude and known extinction in the i band, the distance modulus is given by

$$\begin{aligned}
 \mu &= m_i^{\text{TRGB}} - M_i^{\text{TRGB}} \\
 &= m_{i, \text{app}}^{\text{TRGB}} - A_i - M_i^{\text{TRGB}} \\
 &= m_{i, \text{app}}^{\text{TRGB}} - 0.30 + 3.44
 \end{aligned} \tag{5.2}$$

The extinction value is obtained from Table 4.3 and is presumed to be consistent across the entire radial range.

By applying a translation of $-0.30 + 3.44$ mag to the y-axis of Figure 5.5, the y-axis becomes distance modulus (see Figure 5.6). The Cepheid-derived distance modulus

of 24.57 ± 0.06 mag is superimposed on the heatmap as the solid and dashed lines. At the radii where the TRGB can be located unambiguously, the TRGB distances are well-matched with that of the Cepheid distance.

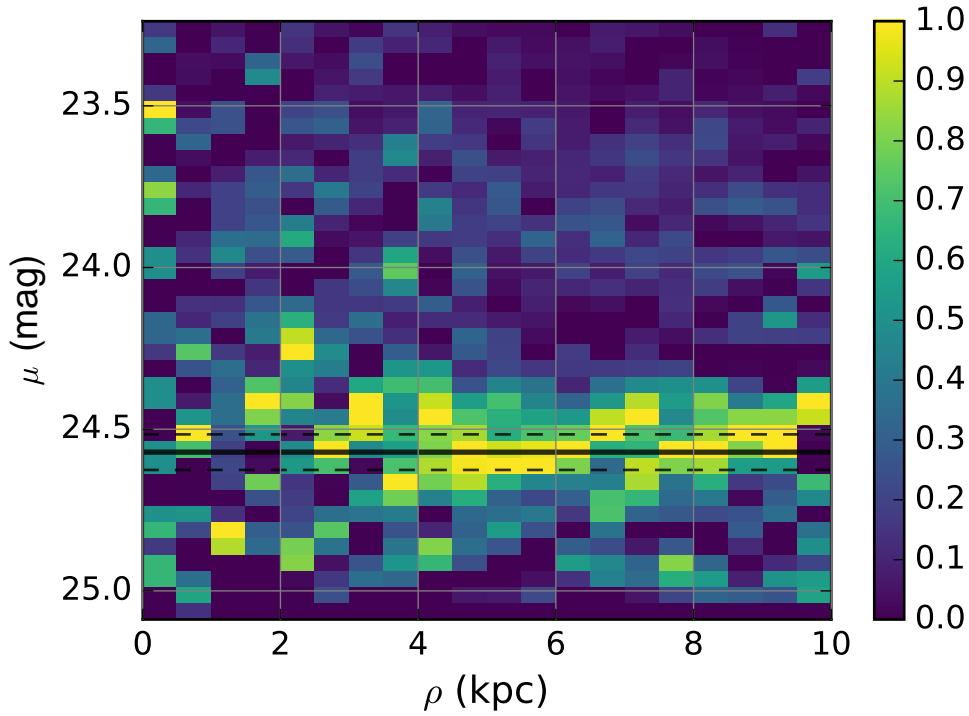


Figure 5.6: Same as Figure 5.5 but with distance modulus as the y-axis and with the Cepheid distance and its error overlaid as the black lines.

For each response function with a well-defined peak, the peak is isolated by identifying the magnitude bins on either side of the peak where the value of the response function first falls to 20% of the peak value. A Gaussian function is then fitted to the isolated peak to obtain values for the TRGB magnitude. Figure 5.7 shows the response functions as the solid line, the isolated peaks are blue, and the fitted Gaussians are the red dashed lines.

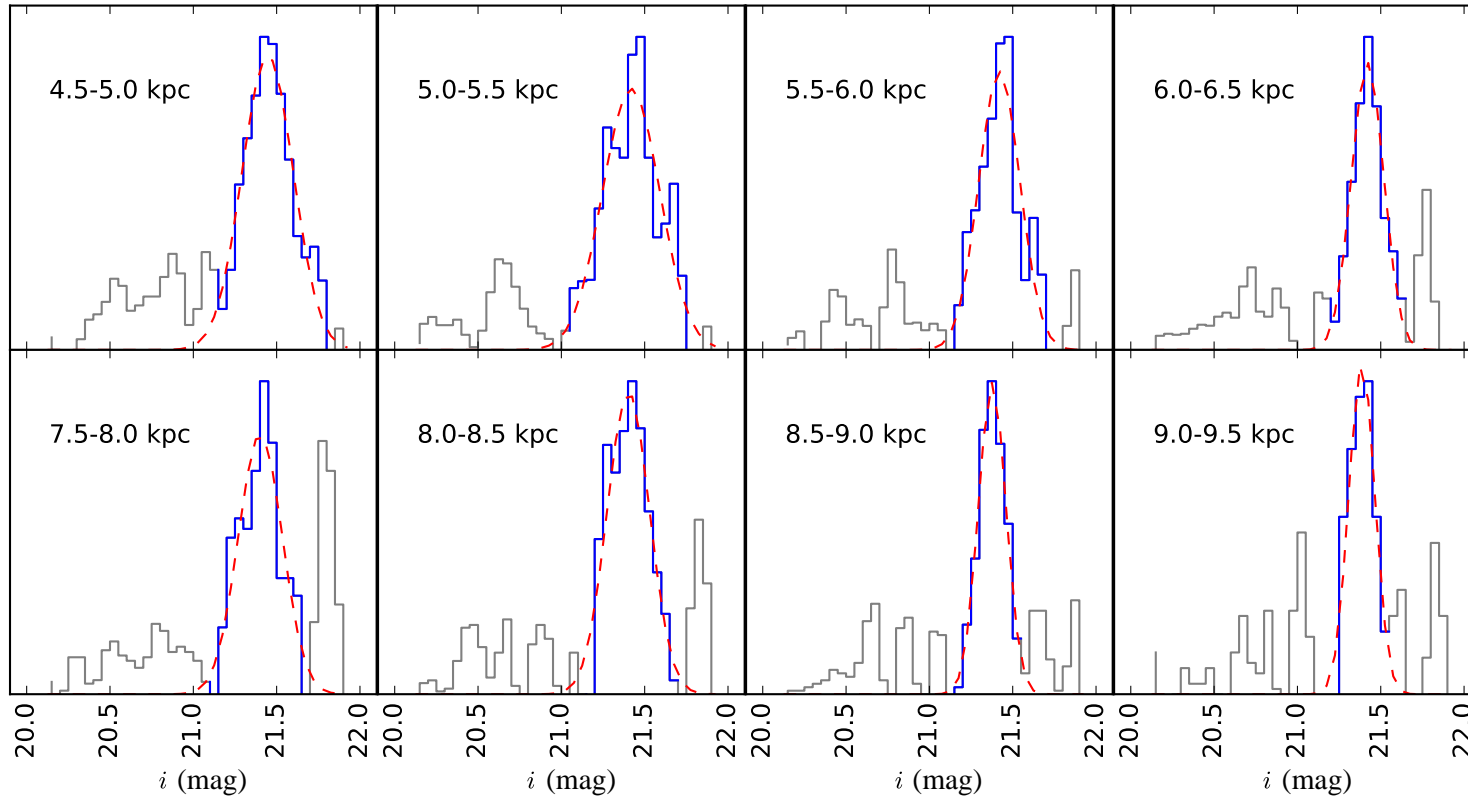


Figure 5.7: Response functions and fitted Gaussians for various annular bins of RGB stars. In each subplot, the solid black line is the response function with the isolated peak in blue and its fitted Gaussian function as the red dashed lines.

Distance moduli are obtained from the TRGB magnitudes and plotted against galactocentric radius in Figure 5.8 with errors given as the magnitude bin width of 0.05 mag. A slight trend in distance modulus with galactocentric radius is apparent; the TRGB distances obtained from RGB stars closer to the galactic centre are larger than those from the outer regions. However, since the metallicities of RGB stars at $\rho < 7.4$ kpc are expected to be too high ($[\text{Fe}/\text{H}] > -1$ dex), the distances obtained at those radii are rendered undependable and, given the sizes of the errors, the tentative gradient in distance modulus may be a spurious artefact. By discarding the four inner distance measurements and taking the mean of the remaining outer distance estimates, and by considering the uncertainty on the absolute i -band TRGB magnitude, an average TRGB distance modulus of 24.53 ± 0.11 mag is obtained, consistent with the value of 24.57 ± 0.06 mag determined from Cepheids with LMC-like metallicity.

It should be noted, however, that the sample of stars extracted from the CMD in Figure 5.2 for use in identifying the TRGB magnitude most likely comprises RGB stars of a wide age range and non-RGB stars (e.g. foreground stars). As the calibration of the absolute I -band TRGB magnitude is typically achieved through measurements of old, metal-poor RGB stars in globular clusters, the use of the TRGB method with “young” stellar populations may be susceptible to age effects. Salaris and Girardi (2005) caution against the use of the TRGB method for galaxies with a complex star formation history, even if the TRGB is appears well defined. They find that the I -band TRGB magnitude as determined from intermediate-age RGB stars may be offset from the “true” value on the order of 0.1 mag. Similar age effects may be present in the Sloan i -band.

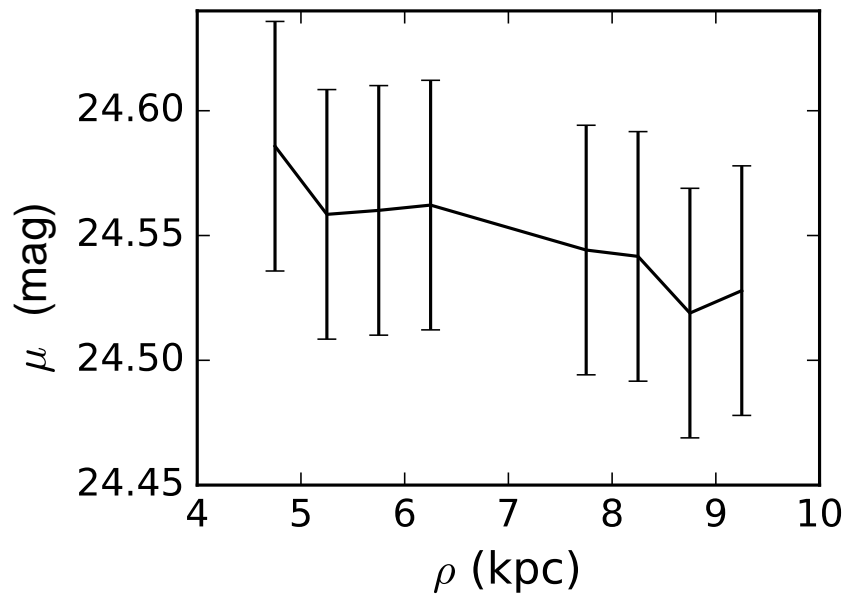


Figure 5.8: TRGB distance against galactocentric radius.

Chapter 6

Conclusions

6.1 Summary

The main results of this thesis are the following:

1. Sloan-band magnitudes for over 1.3 million stars in M33 were measured.
2. Sloan-band Leavitt Laws and PW relations were empirically determined.
3. A Cepheid-based average distance modulus of 24.57 ± 0.06 mag to M33 was obtained.
4. The effects of metallicity on the Sloan-band Leavitt Laws have been quantified. In g, r, i bands and Wesenheit indices, a Cepheid of higher metallicity is brighter than a Cepheid of lower metallicity of the same period. The strength of the metallicity effect increases with decreasing wavelength. No significant Leavitt Law slope-metallicity dependence was seen.
5. An independent distance estimate of 24.53 ± 0.11 mag was acquired with the TRGB method using stars from the outer disk of M33.

Cepheids have played a vital role as accurate distance determinators over the past century, enabling the calibration of standard candles suited for cosmologically significant

distance determinations and local measurements of the Hubble constant. It is crucial that uncertainties in the behaviour of Cepheids be properly understood, particularly those regarding metallicity. To that end, a large sample of Cepheids in the nearby spiral galaxy M33 were used to investigate the effects of metallicity on the Leavitt Law in Sloan bands.

PSF photometry of deep Sloan-band stacks of M33 yielded a catalogue of over 1.3 million stars. Through matching with existing Cepheid catalogues and by inspecting their locations on a colour-magnitude diagram, 1587 of these stars were identified as fundamental mode Cepheids with acceptable colours. These Cepheids were found throughout the disk of the galaxy and so sample the galaxy's gradient in chemical abundance.

Cepheids with metallicities similar to that of the LMC were identified and were used to empirically determine the slopes for Sloan-band Leavitt Laws. The slopes of these Leavitt Laws were found to be very consistent with those derived by [Ngeow and Kanbur \(2007\)](#) on a semi-empirical basis. By adopting their semi-empirical slopes and by comparing the resulting zero-points, a distance modulus to M33 of 24.57 ± 0.06 mag (equivalent to 820 ± 23 kpc) was obtained. A reddening of $E(B - V) = 0.144 \pm 0.020$ mag was also determined.

The extensive collection of Cepheids was then binned into a series of galactocentric annuli to sample the range in metallicity that is present in M33. Leavitt Laws were fitted against each binned sample of Cepheids and variations in slopes and zero-points were measured. The slopes were found to not change significantly and are consistent with semi-empirical determination, supporting the idea of a universal slope. A correlation between metallicity and zero-points was found in all bands: the higher the metallicity of a sample of Cepheids, the lower the Leavitt Law zero-point will be. In terms of Cepheid properties, a metal-rich Cepheid is measured to be brighter than a metal-poor Cepheid of the same pulsation period. Without a metallicity correction, two Cepheids with differing metallicity — all else being equal (period, distance from an observer, etc.) — will be of different brightnesses, leading to different distance moduli.

The strength of the metallicity effect was found to be weakest in the g band and becomes stronger at longer wavelengths. The metallicity corrections were determined to be -0.089 ± 0.107 mag/dex in g , -0.188 ± 0.071 mag/dex in r and -0.250 ± 0.080 mag/dex in i . In all Wesenheit indices, the values cluster around -0.468 mag/dex. These values are predicated upon the chosen metallicity gradient of M33; in this case, the gradient derived from beat Cepheids (Beaulieu et al., 2006) was selected.

A subset of stars in the outer region of M33 ($\rho > 7.4$ kpc) was used to determine an independent distance estimate via the TRGB method. The TRGB method is conventionally performed with stellar magnitudes in the Cousins I band. However, the M33 photometry catalogue comprises magnitudes in the Sloan bands, and there exists no empirical calibration of the TRGB magnitude in those filters. A theoretical i -band absolute TRGB magnitude was relied upon though it requires a sufficiently low RGB metallicity to be valid. A TRGB distance estimate of 24.53 ± 0.11 mag was obtained and is consistent with the Cepheid-based distance.

6.2 M33 metallicity gradient

Various published metallicity gradients for M33 were assessed. Shallow gradients determined from spectroscopy of HII region were found to produce unreasonably large metallicity corrections while steeper stellar determinations of the gradient yielded acceptable results. There are large systematic uncertainties inherent to the “strong line method” that is typically used to obtain metallicities of HII regions, while the uncertainties involved with stellar metallicity determinations tend to be considerably smaller. These suggest that the use of metallicities obtained from HII regions as a proxy for Cepheid metallicities is unsuitable.

While the metallicity gradient obtained from beat Cepheids may be the most appropriate gradient to choose from when ascertaining the metallicity effect on Cepheids in this work, that gradient was derived from a sample of only five beat Cepheids. To identify those double mode Cepheids, Beaulieu et al. (2006) made use of the survey data from

Hartman et al. (2006); more specifically, they analysed the light curves of Cepheids to find those pulsating in both the fundamental and first overtone modes with a period ratio $P_1/P_0 \approx 0.7$. The original variable star survey provided around 33 measurements for each star which, while sufficient to classify the variable stars into their respective families (Cepheids, LPVs, etc.), is insufficient in identifying — with completeness — all the Cepheids that are pulsating simultaneously in two modes. For comparison, the extensive OGLE survey of the LMC has catalogued over 2000 Cepheids pulsating exclusively in the fundamental mode and almost 100 beat Cepheids pulsating in both the fundamental and first overtone modes (Soszyński et al., 2015). As M33 contains a similar number of fundamental mode Cepheids as the LMC, one might expect that the same applies to the number of beat Cepheids. With a comprehensive catalogue of beat Cepheids in M33 and with well-sampled light curves, an extremely robust stellar metallicity gradient will be obtained. With such a metallicity gradient, the values obtained for the Cepheid metallicity correction will be improved.

6.3 Outlook

The Sloan filter set was introduced over two decades ago for use with the Sloan Digital Sky Survey (Fukugita et al., 1996). The Sloan filters have since then been extensively used in studies into myriad astrophysical phenomena; despite this, Sloan-band photometric studies of Cepheids are few and far between. With the LSST forecasted to begin high cadence observations of the southern sky with Sloan filters early next decade, a surge in the availability of Cepheid magnitudes in the those bands is expected. In both the Magellanic Clouds, there exist thousands of Cepheids, making them excellent targets for LSST. Photometry of those Cepheids with LSST will provide an independent empirical determination of the Sloan-band Leavitt Laws and will supplement the already comprehensive survey by the OGLE team.

There are 77 dwarf or spiral galaxies out to a distance of ~ 10 Mpc in the southern sky that are conducive to Cepheid studies with LSST (Hoffmann and Macri, 2015). The majority of those galaxies have had distances determined with the tip of the red

giant branch method; only a dozen or so, however, have Cepheid-based distances measurements. With such a bounty of untapped Cepheids in a multitude of environments, many long-standing idiosyncrasies of Cepheids will soon be understood to a better degree, further solidifying their use as test beds for stellar models and their reliability as tracers of many astrophysical characteristics.

Appendix A

CFHT calibration solutions

Table A.1: Calibration solutions for the CFHT chips.

Filter	Z	c	d	e	RMS
Chip 0					
g'	-30.193	-0.173	$+4.372 \times 10^{-5}$	$+1.175 \times 10^{-5}$	0.038
r'	-29.897	-0.008	-3.660×10^{-5}	$+0.410 \times 10^{-5}$	0.013
i'	-30.098	-0.062	$+0.270 \times 10^{-5}$	$+0.530 \times 10^{-5}$	0.021
Chip 1					
g'	-30.092	-0.167	-1.962×10^{-5}	$+1.723 \times 10^{-5}$	0.029
r'	-30.111	-0.013	-1.240×10^{-5}	$+1.430 \times 10^{-5}$	0.022
i'	-30.583	-0.062	-1.830×10^{-5}	$+3.820 \times 10^{-5}$	0.022
Chip 2					
g'	-29.674	-0.175	$+4.835 \times 10^{-5}$	-2.755×10^{-5}	0.046
r'	-30.456	-0.015	$+0.930 \times 10^{-5}$	$+2.900 \times 10^{-5}$	0.026
i'	-30.717	-0.080	-0.820×10^{-5}	$+4.380 \times 10^{-5}$	0.011
Chip 3					
g'	-27.965	-0.137	-9.068×10^{-5}	-7.569×10^{-5}	0.053
r'	-28.482	-0.005	-27.340×10^{-5}	$+3.360 \times 10^{-5}$	0.048
i'	-30.791	-0.092	$+1.950 \times 10^{-5}$	$+3.840 \times 10^{-5}$	0.029
Chip 4					
g'	-30.120	-0.159	$+1.250 \times 10^{-5}$	$+0.205 \times 10^{-5}$	0.026
r'	-29.669	-0.023	-1.440×10^{-5}	-0.550×10^{-5}	0.020
i'	-30.106	-0.070	-0.180×10^{-5}	$+0.730 \times 10^{-5}$	0.022

Filter	Z	c	d	e	RMS
Chip 5					
<i>g'</i>	-29.605	-0.128	-2.718×10^{-5}	-0.162×10^{-5}	0.021
<i>r'</i>	-29.989	-0.017	-1.630×10^{-5}	$+1.430 \times 10^{-5}$	0.018
<i>i'</i>	-30.119	-0.074	-1.170×10^{-5}	$+1.400 \times 10^{-5}$	0.028
Chip 6					
<i>g'</i>	-30.576	-0.216	$+2.818 \times 10^{-5}$	$+1.564 \times 10^{-5}$	0.039
<i>r'</i>	-31.137	-0.026	$+3.150 \times 10^{-5}$	$+4.310 \times 10^{-5}$	0.027
<i>i'</i>	-31.328	-0.096	$+4.460 \times 10^{-5}$	$+4.100 \times 10^{-5}$	0.031
Chip 7					
<i>g'</i>	-23.855	-0.136	-25.598×10^{-5}	-12.051×10^{-5}	0.041
<i>r'</i>	-27.159	0.029	-20.690×10^{-5}	$+2.550 \times 10^{-5}$	0.020
<i>i'</i>	-35.213	-0.034	$+23.330 \times 10^{-5}$	$+8.770 \times 10^{-5}$	0.049
Chip 9					
<i>g'</i>	-29.564	-0.214	-2.395×10^{-5}	-0.750×10^{-5}	0.010
<i>r'</i>	-29.805	-0.007	-1.770×10^{-5}	-0.690×10^{-5}	0.027
<i>i'</i>	-30.046	-0.028	-5.090×10^{-5}	$+4.180 \times 10^{-5}$	0.049
Chip 10					
<i>g'</i>	-29.426	-0.154	-14.625×10^{-5}	$+1.244 \times 10^{-5}$	0.041
<i>r'</i>	-29.441	-0.027	-4.050×10^{-5}	-2.660×10^{-5}	0.045
<i>i'</i>	-29.658	-0.071	-4.370×10^{-5}	-1.470×10^{-5}	0.026
Chip 11					
<i>g'</i>	-29.869	-0.173	-2.173×10^{-5}	$+0.496 \times 10^{-5}$	0.019
<i>r'</i>	-29.945	-0.033	$+1.240 \times 10^{-5}$	-0.160×10^{-5}	0.029
<i>i'</i>	-29.852	-0.077	-0.770×10^{-5}	-0.790×10^{-5}	0.026
Chip 12					
<i>g'</i>	-29.990	-0.167	$+1.940 \times 10^{-5}$	-1.082×10^{-5}	0.029
<i>r'</i>	-29.877	-0.058	$+0.240 \times 10^{-5}$	-0.390×10^{-5}	0.028
<i>i'</i>	-30.246	-0.081	$+2.200 \times 10^{-5}$	$+0.280 \times 10^{-5}$	0.035
Chip 13					
<i>g'</i>	-29.792	-0.182	-0.904×10^{-5}	-0.486×10^{-5}	0.030
<i>r'</i>	-29.654	-0.022	-2.730×10^{-5}	$+0.350 \times 10^{-5}$	0.043
<i>i'</i>	-29.945	-0.072	-1.700×10^{-5}	$+1.210 \times 10^{-5}$	0.037
Chip 14					
<i>g'</i>	-29.378	-0.154	-0.910×10^{-5}	-3.260×10^{-5}	0.032
<i>r'</i>	-29.219	-0.029	-2.810×10^{-5}	-2.190×10^{-5}	0.026
<i>i'</i>	-29.123	-0.088	-3.450×10^{-5}	-2.830×10^{-5}	0.023
Chip 15					
<i>g'</i>	-30.567	-0.155	$+3.859 \times 10^{-5}$	$+0.348 \times 10^{-5}$	0.025
<i>r'</i>	-30.010	-0.015	$+1.360 \times 10^{-5}$	-0.820×10^{-5}	0.020
<i>i'</i>	-30.060	-0.067	$+1.900 \times 10^{-5}$	-1.640×10^{-5}	0.024

Filter	Z	c	d	e	RMS
Chip 16					
g'	-30.733	-0.179	$+2.684 \times 10^{-5}$	$+2.698 \times 10^{-5}$	0.048
r'	-30.362	0.000	$+1.720 \times 10^{-5}$	$+1.180 \times 10^{-5}$	0.003
i'	-30.019	-0.048	-0.770×10^{-5}	$+0.970 \times 10^{-5}$	0.030
Chip 17					
g'	-30.506	-0.182	-0.033×10^{-5}	$+4.884 \times 10^{-5}$	0.046
r'	-29.877	-0.019	-1.050×10^{-5}	$+1.170 \times 10^{-5}$	0.013
i'	-30.526	-0.085	$+1.700 \times 10^{-5}$	$+1.760 \times 10^{-5}$	0.017
Chip 18					
g'	-29.570	-0.211	-1.305×10^{-5}	-2.268×10^{-5}	0.032
r'	-29.794	-0.007	-4.480×10^{-5}	-0.850×10^{-5}	0.023
i'	-29.611	-0.028	-8.740×10^{-5}	$+0.100 \times 10^{-5}$	0.028
Chip 19					
g'	-29.488	-0.204	-6.806×10^{-5}	-1.434×10^{-5}	0.026
r'	-30.040	-0.012	-0.230×10^{-5}	$+1.030 \times 10^{-5}$	0.032
i'	-29.163	-0.045	-14.400×10^{-5}	-3.030×10^{-5}	0.049
Chip 20					
g'	-29.689	-0.288	-2.387×10^{-5}	$+1.165 \times 10^{-5}$	0.025
r'	-29.950	-0.020	$+0.040 \times 10^{-5}$	$+0.210 \times 10^{-5}$	0.028
i'	-29.660	-0.080	-3.970×10^{-5}	-1.480×10^{-5}	0.028
Chip 21					
g'	-29.263	-0.158	-0.810×10^{-5}	-7.215×10^{-5}	0.034
r'	-30.610	0.003	$+7.960 \times 10^{-5}$	$+0.440 \times 10^{-5}$	0.045
i'	-30.214	-0.073	$+7.240 \times 10^{-5}$	-4.090×10^{-5}	0.039
Chip 22					
g'	-29.669	-0.197	-1.115×10^{-5}	-2.272×10^{-5}	0.038
r'	-29.923	-0.041	-1.750×10^{-5}	$+2.810 \times 10^{-5}$	0.029
i'	-29.731	-0.100	-2.790×10^{-5}	$+0.570 \times 10^{-5}$	0.030
Chip 23					
g'	-30.040	-0.159	$+0.149 \times 10^{-5}$	$+0.474 \times 10^{-5}$	0.017
r'	-29.902	-0.034	-1.700×10^{-5}	$+2.610 \times 10^{-5}$	0.030
i'	-29.933	-0.086	-1.060×10^{-5}	$+0.730 \times 10^{-5}$	0.020
Chip 24					
g'	-30.573	-0.171	$+5.133 \times 10^{-5}$	-1.601×10^{-5}	0.022
r'	-30.146	-0.022	$+1.780 \times 10^{-5}$	-0.420×10^{-5}	0.017
i'	-29.922	-0.067	-0.120×10^{-5}	-1.230×10^{-5}	0.023
Chip 25					
g'	-30.572	-0.149	$+3.880 \times 10^{-5}$	$+1.209 \times 10^{-5}$	0.027
r'	-29.080	-0.011	-5.020×10^{-5}	$+0.370 \times 10^{-5}$	0.044
i'	-30.015	-0.073	$+2.090 \times 10^{-5}$	-3.400×10^{-5}	0.036

Filter	Z	c	d	e	RMS
Chip 26					
g'	-29.181	-0.175	-2.174×10^{-5}	-4.541×10^{-5}	0.046
r'	-29.125	-0.083	-2.080×10^{-5}	-4.770×10^{-5}	0.016
i'	-33.833	-0.108	$+23.100 \times 10^{-5}$	-3.860×10^{-5}	0.014
Chip 27					
g'	-29.796	-0.216	-0.695×10^{-5}	$+2.493 \times 10^{-5}$	0.041
r'	-29.630	-0.010	-6.140×10^{-5}	$+1.540 \times 10^{-5}$	0.045
i'	-29.684	-0.020	-7.320×10^{-5}	-0.280×10^{-5}	0.045
Chip 28					
g'	-29.655	-0.196	-5.228×10^{-5}	$+0.323 \times 10^{-5}$	0.046
r'	-29.488	-0.019	-7.700×10^{-5}	-4.150×10^{-5}	0.031
i'	-29.704	-0.060	-7.260×10^{-5}	$+0.580 \times 10^{-5}$	0.021
Chip 29					
g'	-30.046	-0.220	$+4.277 \times 10^{-5}$	-0.115×10^{-5}	0.048
r'	-29.878	-0.039	$+2.230 \times 10^{-5}$	-4.700×10^{-5}	0.049
i'	-30.145	-0.107	$+4.390 \times 10^{-5}$	-1.360×10^{-5}	0.029
Chip 30					
g'	-29.615	-0.183	-2.807×10^{-5}	-1.016×10^{-5}	0.030
r'	-29.969	-0.025	$+1.250 \times 10^{-5}$	-1.240×10^{-5}	0.041
i'	-29.997	-0.085	$+1.020 \times 10^{-5}$	-1.890×10^{-5}	0.030
Chip 31					
g'	-29.744	-0.158	-2.127×10^{-5}	$+1.256 \times 10^{-5}$	0.031
r'	-29.472	-0.014	-4.360×10^{-5}	$+1.620 \times 10^{-5}$	0.041
i'	-29.750	-0.073	-2.470×10^{-5}	$+1.250 \times 10^{-5}$	0.031
Chip 32					
g'	-29.741	-0.169	-1.648×10^{-5}	$+1.665 \times 10^{-5}$	0.017
r'	-29.837	-0.028	-0.990×10^{-5}	$+4.170 \times 10^{-5}$	0.014
i'	-29.830	-0.062	-1.760×10^{-5}	$+1.560 \times 10^{-5}$	0.015
Chip 33					
g'	-30.060	-0.166	$+0.592 \times 10^{-5}$	$+1.755 \times 10^{-5}$	0.018
r'	-29.913	-0.017	-0.240×10^{-5}	$+3.890 \times 10^{-5}$	0.026
i'	-30.174	-0.067	$+1.010 \times 10^{-5}$	$+2.000 \times 10^{-5}$	0.020
Chip 34					
g'	-29.127	-0.161	-5.716×10^{-5}	$+3.171 \times 10^{-5}$	0.019
r'	-29.328	0.006	-3.790×10^{-5}	$+1.710 \times 10^{-5}$	0.016
i'	-29.281	-0.045	-1.860×10^{-5}	-10.300×10^{-5}	0.031
Chip 35					
g'	-30.238	-0.171	$+1.222 \times 10^{-5}$	$+1.700 \times 10^{-5}$	0.019
r'	-29.582	-0.028	$+0.330 \times 10^{-5}$	-1.430×10^{-5}	0.034
i'	-29.065	-0.069	-3.250×10^{-5}	$+2.080 \times 10^{-5}$	0.033

Bibliography

- M. G. Akritas and M. A. Bershady. Linear Regression for Astronomical Data with Measurement Errors and Intrinsic Scatter. *ApJ*, 470:706, October 1996. doi: 10.1086/177901.
- L. H. Aller. The Spectra of the Emission Nebulosity in Messier 33. *ApJ*, 95:52, January 1942. doi: 10.1086/144372.
- R. I. Anderson. Homing in on Polaris: A $7 M_{\odot}$ first-overtone Cepheid entering the instability strip for the first time. *A&A*, 611:L7, April 2018. doi: 10.1051/0004-6361/201832585.
- R. I. Anderson, S. Ekström, C. Georgy, G. Meynet, N. Mowlavi, and L. Eyer. On the effect of rotation on populations of classical Cepheids. I. Predictions at solar metallicity. *A&A*, 564:A100, April 2014. doi: 10.1051/0004-6361/201322988.
- M. Annunziatella, A. Mercurio, M. Brescia, S. Cavuoti, and G. Longo. Inside Catalogs: A Comparison of Source Extraction Software. *PASP*, 125:68, January 2013. doi: 10.1086/669333.
- E. Antonello, E. Poretti, and L. Reduzzi. The separation of S-Cepheids from classical Cepheids and a new definition of the class. *A&A*, 236:138–148, September 1990.
- W. Baade. Über eine Möglichkeit, die Pulsationstheorie der δ Cephei-Veränderlichen zu prüfen. *Astronomische Nachrichten*, 228:359, October 1926. doi: 10.1002/asna.19262282003.
- R. Baranowski, R. Smolec, W. Dimitrov, T. Kwiatkowski, A. Schwarzenberg-Czerny, P. Bartczak, M. Fagas, W. Borczyk, K. Kamiński, P. Moskalik, R. Ratajczak, and

- A. Rožek. V440 Per: the longest-period overtone Cepheid. *MNRAS*, 396:2194–2200, July 2009. doi: 10.1111/j.1365-2966.2009.14865.x.
- M. K. Barker, A. Sarajedini, D. Geisler, P. Harding, and R. Schommer. The Stellar Populations in the Outer Regions of M33. II. Deep ACS Imaging. *AJ*, 133:1125–1137, March 2007. doi: 10.1086/511185.
- M. A. Beasley, I. San Roman, C. Gallart, A. Sarajedini, and A. Aparicio. Evidence for temporal evolution in the M33 disc as traced by its star clusters. *MNRAS*, 451:3400–3418, August 2015. doi: 10.1093/mnras/stv943.
- R. L. Beaton, G. Bono, V. F. Braga, M. Dall’Ora, G. Fiorentino, I. S. Jang, C. E. Martínez-Vázquez, N. Matsunaga, M. Monelli, J. R. Neeley, and M. Salaris. Old-Aged Stellar Population Distance Indicators. *ArXiv e-prints*, August 2018.
- J. P. Beaulieu, P. Grison, W. Tobin, J. D. Pritchard, R. Ferlet, F. Lepeintre, A. Vidal-Madjar, E. Maurice, L. Prevot, C. Gry, J. Guibert, O. Moreau, F. Tajhamady, E. Aubourg, P. Bareyre, C. Coutures, M. Gros, B. Laurent, M. Lachieze-Rey, E. Lesquoy, C. Magneville, A. Milsztajn, L. Moscoso, F. Queinnec, C. Renault, J. Rich, M. Spiro, L. Vigroux, S. Zylberajch, R. Ansari, F. Cavalier, and M. Moniez. EROS variable stars: fundamental-mode and first-overtone Cepheids in the bar of the Large Magellanic Cloud. *A&A*, 303:137, Nov 1995.
- J. P. Beaulieu, D. D. Sasselov, C. Renault, P. Grison, R. Ferlet, A. Vidal-Madjar, E. Maurice, L. Prevot, E. Aubourg, P. Bareyre, S. Brehin, C. Coutures, N. Delabrouille, J. de Kat, M. Gros, B. Laurent, and et al. The effect of metallicity on the Cepheid distance scale and its implications for the Hubble constant (H_0) determination. *A&A*, 318:L47–L50, February 1997.
- J.-P. Beaulieu, J. R. Buchler, J.-B. Marquette, J. D. Hartman, and A. Schwarzenberg-Czerny. Detection of Beat Cepheids in M33 and Their Use as a Probe of the M33 Metallicity Distribution. *ApJl*, 653:L101–L104, December 2006. doi: 10.1086/510453.

- M. Bellazzini. The Tip of the Red Giant Branch. *Mem. Soc. Astron. Italiana*, 79:440, 2008.
- E. Bertin. Automated Morphometry with SExtractor and PSFEx. In I. N. Evans, A. Accomazzi, D. J. Mink, and A. H. Rots, editors, *Astronomical Data Analysis Software and Systems XX*, volume 442 of *Astronomical Society of the Pacific Conference Series*, page 435, July 2011.
- E. Bertin and S. Arnouts. SExtractor: Software for source extraction. *A&AS*, 117:393–404, June 1996. doi: 10.1051/aas:1996164.
- M. Betoule, J. Murrain, N. Regnault, J.-C. Cuillandre, P. Astier, J. Guy, C. Balland, P. El Hage, D. Hardin, R. Kessler, L. Le Guillou, J. Mosher, R. Pain, P.-F. Rocci, M. Sako, and K. Schahmaneche. Improved photometric calibration of the SNLS and the SDSS supernova surveys. *A&A*, 552:A124, April 2013. doi: 10.1051/0004-6361/201220610.
- A. Bhardwaj, S. M. Kanbur, H. P. Singh, L. M. Macri, and C.-C. Ngeow. On the variation of Fourier parameters for Galactic and LMC Cepheids at optical, near-infrared and mid-infrared wavelengths. *MNRAS*, 447:3342–3360, March 2015. doi: 10.1093/mnras/stu2678.
- A. Bhardwaj, S. M. Kanbur, L. M. Macri, H. P. Singh, C.-C. Ngeow, and E. E. O. Ishida. Large Magellanic Cloud Near-Infrared Synoptic Survey - III. A statistical study of non-linearity in the Leavitt Laws. *MNRAS*, 457:1644–1665, April 2016. doi: 10.1093/mnras/stw040.
- J. C. Bird, K. Z. Stanek, and J. L. Prieto. Using Ultra Long Period Cepheids to Extend the Cosmic Distance Ladder to 100 Mpc and Beyond. *ApJ*, 695:874–882, April 2009. doi: 10.1088/0004-637X/695/2/874.
- A. Z. Bonanos, K. Z. Stanek, R. P. Kudritzki, L. Macri, D. D. Sasselov, J. Kaluzny, D. Bersier, F. Bresolin, T. Matheson, B. J. Mochejska, N. Przybilla, A. H. Szentgyorgyi, J. Tonry, and G. Torres. The First DIRECT Distance to a Detached

- Eclipsing Binary in M33. *Ap&SS*, 304:207–209, August 2006. doi: 10.1007/s10509-006-9112-1.
- G. Bono, F. Caputo, V. Castellani, and M. Marconi. Theoretical Models for Classical Cepheids. II. Period-Luminosity, Period-Color, and Period-Luminosity-Color Relations. *ApJ*, 512:711–723, February 1999a. doi: 10.1086/306815.
- G. Bono, M. Marconi, and R. F. Stellingwerf. Classical Cepheid Pulsation Models. I. Physical Structure. *The Astrophysical Journal Supplement Series*, 122:167–205, May 1999b. doi: 10.1086/313207.
- G. Bono, M. A. T. Groenewegen, M. Marconi, and F. Caputo. On the Distance of Magellanic Clouds: First Overtone Cepheids. *ApJL*, 574:L33–L37, July 2002. doi: 10.1086/342211.
- G. Bono, M. Marconi, S. Cassisi, F. Caputo, W. Gieren, and G. Pietrzynski. Classical Cepheid Pulsation Models. X. The Period-Age Relation. *ApJ*, 621:966–977, March 2005. doi: 10.1086/427744.
- G. Bono, F. Caputo, G. Fiorentino, M. Marconi, and I. Musella. Cepheids in External Galaxies. I. The Maser-Host Galaxy NGC 4258 and the Metallicity Dependence of Period-Luminosity and Period-Wesenheit Relations. *ApJ*, 684:102–117, September 2008. doi: 10.1086/589965.
- G. Bono, F. Caputo, M. Marconi, and I. Musella. Insights into the Cepheid Distance Scale. *ApJ*, 715:277–291, May 2010. doi: 10.1088/0004-637X/715/1/277.
- F. Bresolin. Revisiting the Abundance Gradient in the Maser Host Galaxy NGC 4258. *ApJ*, 729:56, March 2011a. doi: 10.1088/0004-637X/729/1/56.
- F. Bresolin. The Abundance Scatter in M33 from H II Regions: Is There Any Evidence for Azimuthal Metallicity Variations? *ApJ*, 730:129, April 2011b. doi: 10.1088/0004-637X/730/2/129.
- F. Bresolin, G. Stasińska, J. M. Vílchez, J. D. Simon, and E. Rosolowsky. Planetary nebulae in M33: probes of asymptotic giant branch nucleosynthesis and inter-

- stellar medium abundances. *MNRAS*, 404:1679–1697, June 2010. doi: 10.1111/j.1365-2966.2010.16409.x.
- R. S. Brooks, C. D. Wilson, and W. E. Harris. The Metallicity Distribution in the Outer Halo of M33. *AJ*, 128:237–244, July 2004. doi: 10.1086/421850.
- J. R. Buchler. The State of Cepheid Pulsation Theory. In J. A. Guzik and P. A. Bradley, editors, *American Institute of Physics Conference Series*, volume 1170 of *American Institute of Physics Conference Series*, pages 51–58, September 2009. doi: 10.1063/1.3246556.
- F. Caputo, M. Marconi, I. Musella, and P. Santolamazza. Theoretical models for classical Cepheids. VII. Metallicity effects on the Cepheid distance scale. *A&A*, 359:1059–1067, July 2000.
- J. A. Cardelli, G. C. Clayton, and J. S. Mathis. The relationship between infrared, optical, and ultraviolet extinction. *ApJ*, 345:245–256, October 1989. doi: 10.1086/167900.
- W. C. Carroll and D. A. Ostlie. *An Introduction to Modern Astrophysics*. Pearson, San Francisco, California, United States of America, 2nd edition, 2007. ISBN 0321442849.
- J. M. Chavez, L. M. Macri, and A. Pellerin. Blending of Cepheids in M33. *AJ*, 144:113, October 2012. doi: 10.1088/0004-6256/144/4/113.
- C. Chiosi, G. Bertelli, and A. Bressan. New developments in understanding the HR diagram. *ARA&A*, 30:235–285, 1992. doi: 10.1146/annurev.aa.30.090192.001315.
- R. F. Christy. The Hertzsprung progression in Cepheid calculations. *NASA Special Publication*, 383, 1975.
- R. Ciardullo, P. R. Durrell, M. B. Laychak, K. A. Herrmann, K. Moody, G. H. Jacoby, and J. J. Feldmeier. The Planetary Nebula System of M33. *ApJ*, 614:167–185, October 2004. doi: 10.1086/423414.

- M.-R. L. Cioni. The metallicity gradient as a tracer of history and structure: the Magellanic Clouds and M33 galaxies. *A&A*, 506:1137–1146, November 2009. doi: 10.1051/0004-6361/200912138.
- G. Clementini, A. Garofalo, T. Muraveva, and V. Ripepi. Gaia, Stellar Populations and the Distance Scale. In J. Jensen, editor, *Stellar Populations and the Distance Scale*, volume 514 of *Astronomical Society of the Pacific Conference Series*, page 89, November 2018.
- N. R. Crockett, D. R. Garnett, P. Massey, and G. Jacoby. Neon and Oxygen Abundances in M33. *ApJ*, 637:741–751, February 2006. doi: 10.1086/498424.
- A. K. Dambis, L. N. Berdnikov, A. Y. Kniazev, V. V. Kravtsov, A. S. Rastorguev, R. Seifako, and O. V. Vozyakova. RR Lyrae variables: visual and infrared luminosities, intrinsic colours and kinematics. *MNRAS*, 435:3206–3220, November 2013. doi: 10.1093/mnras/stt1514.
- R. de Grijs. *An Introduction to Distance Measurement in Astronomy*. Wiley, Chichester, West Sussex, United Kingdom, 1st edition, 2011. ISBN 9780470511794.
- R. de Grijs and G. Bono. Clustering of Local Group Distances: Publication Bias or Correlated Measurements? II. M31 and Beyond. *AJ*, 148:17, July 2014. doi: 10.1088/0004-6256/148/1/17.
- R. de Grijs and G. Bono. Clustering of Local Group Distances: Publication Bias or Correlated Measurements? III. The Small Magellanic Cloud. *AJ*, 149:179, June 2015. doi: 10.1088/0004-6256/149/6/179.
- M. Di Criscienzo, M. Marconi, I. Musella, M. Cignoni, and V. Ripepi. Predicted properties of galactic and magellanic classical Cepheids in the SDSS filters. *MNRAS*, 428:212–219, January 2013. doi: 10.1093/mnras/sts023.
- A. S. Eddington. *The Internal Constitution of the Stars*. Cambridge University Press, Cambridge, Cambridgeshire, United Kingdom, 1926.

- Y. N. Efremov. Cepheids in LMC Clusters and the Period-Age Relation. *Astronomy Reports*, 47:1000–1012, December 2003. doi: 10.1134/1.1633613.
- N. R. Evans, L. Berdnikov, J. Lauer, D. Morgan, J. Nichols, H. M. Günther, N. Gorynya, A. Rastorguev, and P. Moskalik. Binary Properties from Cepheid Radial Velocities (CRaV). *AJ*, 150(1):13, Jul 2015. doi: 10.1088/0004-6256/150/1/13.
- N. R. Evans, M. Karovska, H. E. Bond, G. H. Schaefer, K. C. Sahu, J. Mack, E. P. Nelan, A. Gallenne, and E. D. Tingle. The Orbit of the Close Companion of Polaris: Hubble Space Telescope Imaging, 2007 to 2014. *ApJ*, 863:187, August 2018. doi: 10.3847/1538-4357/aad410.
- L. Eyer, G. Clementini, L. P. Guy, L. Rimoldini, F. Glass, M. Audard, B. Holl, J. Charnas, J. Cuypers, J. D. Ridder, D. W. Evans, G. J. de Fombelle, A. Lanzafame, and et al. Pulsating star research and the Gaia revolution. In *European Physical Journal Web of Conferences*, volume 152 of *European Physical Journal Web of Conferences*, page 02002, September 2017. doi: 10.1051/epjconf/201715202002.
- M. M. Fausnaugh, C. S. Kochanek, J. R. Gerke, L. M. Macri, A. G. Riess, and K. Z. Stanek. The Cepheid distance to the maser-host galaxy NGC 4258: studying systematics with the Large Binocular Telescope. *MNRAS*, 450:3597–3619, July 2015. doi: 10.1093/mnras/stv881.
- J. D. Fernie. The Period-Luminosity Relation: A Historical Review. *PASP*, 81:707, December 1969. doi: 10.1086/128847.
- G. Fiorentino, F. Caputo, M. Marconi, and I. Musella. Theoretical Models for Classical Cepheids. VIII. Effects of Helium and Heavy-Element Abundance on the Cepheid Distance Scale. *ApJ*, 576:402–412, September 2002. doi: 10.1086/341731.
- G. Fiorentino, M. Marconi, I. Musella, and F. Caputo. Classical Cepheid pulsation models. XI. Effects of convection and chemical composition on the period-luminosity and period-Wesenheit relations. *A&A*, 476:863–879, December 2007. doi: 10.1051/0004-6361:20077587.

- P. Fouque and W. P. Gieren. An improved calibration of Cepheid visual and infrared surface brightness relations from accurate angular diameter measurements of cool giants and supergiants. *A&A*, 320:799–810, April 1997.
- W. L. Freedman. Cosmology at a crossroads. *Nature Astronomy*, 1:0121, May 2017. doi: 10.1038/s41550-017-0121.
- W. L. Freedman and B. F. Madore. The Hubble Constant. *ARA&A*, 48:673–710, September 2010. doi: 10.1146/annurev-astro-082708-101829.
- W. L. Freedman and B. F. Madore. Two New Tests of the Metallicity Sensitivity of the Cepheid Period-luminosity Relation (the Leavitt Law). *ApJ*, 734:46, June 2011. doi: 10.1088/0004-637X/734/1/46.
- W. L. Freedman, B. F. Madore, B. K. Gibson, L. Ferrarese, D. D. Kelson, S. Sakai, J. R. Mould, R. C. Kennicutt, Jr., H. C. Ford, J. A. Graham, J. P. Huchra, S. M. G. Hughes, G. D. Illingworth, L. M. Macri, and P. B. Stetson. Final Results from the Hubble Space Telescope Key Project to Measure the Hubble Constant. *ApJ*, 553: 47–72, May 2001. doi: 10.1086/320638.
- W. L. Freedman, B. F. Madore, V. Scowcroft, A. Monson, S. E. Persson, M. Seibert, J. R. Rigby, L. Sturch, and P. Stetson. The Carnegie Hubble Program. *AJ*, 142:192, December 2011. doi: 10.1088/0004-6256/142/6/192.
- M. Fukugita, T. Ichikawa, J. E. Gunn, M. Doi, K. Shimasaku, and D. P. Schneider. The Sloan Digital Sky Survey Photometric System. *AJ*, 111:1748, April 1996. doi: 10.1086/117915.
- A. Gallenne, A. Mérand, P. Kervella, J. D. Monnier, G. H. Schaefer, R. M. Roettenbacher, W. Gieren, G. Pietrzyński, H. McAlister, T. ten Brummelaar, J. Sturmann, L. Sturmann, N. Turner, and R. I. Anderson. Multiplicity of Galactic Cepheids from long-baseline interferometry - III. Sub-percent limits on the relative brightness of a close companion of δ Cephei. *MNRAS*, 461:1451–1456, September 2016. doi: 10.1093/mnras/stw1375.

- S. Galleti, M. Bellazzini, and F. R. Ferraro. The distance of M 33 and the stellar population in its outskirts. *A&A*, 423:925–934, September 2004. doi: 10.1051/0004-6361:20040489.
- A. García-Varela, B. E. Sabogal, and M. C. Ramírez-Tannus. A study on the universality and linearity of the Leavitt law in the LMC and SMC galaxies. *MNRAS*, 431: 2278–2284, May 2013. doi: 10.1093/mnras/stt325.
- A. García-Varela, J. R. Muñoz, B. E. Sabogal, S. Vargas Domínguez, and J. Martínez. The Influential Effect of Blending, Bump, Changing Period, and Eclipsing Cepheids on the Leavitt Law. *ApJ*, 824:74, June 2016. doi: 10.3847/0004-637X/824/2/74.
- D. R. Garnett, G. A. Shields, E. D. Skillman, S. P. Sagan, and R. J. Dufour. Interstellar Abundance Gradients in NGC 2403: Comparison to M33. *ApJ*, 489:63–86, November 1997. doi: 10.1086/304775.
- T. Gastine and B. Dintrans. Direct numerical simulations of the κ -mechanism. II. Non-linear saturation and the Hertzsprung progression. *A&A*, 490:743–752, November 2008. doi: 10.1051/0004-6361:200809891.
- A. Gautschy. On the Baade-Wesselink method. *Vistas in Astronomy*, 30:197–241, 1987. doi: 10.1016/0083-6656(87)90002-X.
- A. Gautschy. The history of radial stellar pulsation theory. *Eidgenössische Technische Hochschule Zürich, ETH Bibliothek*, 2003. doi: 10.3929/ethz-a-005091311.
- J. R. Gerke, C. S. Kochanek, J. L. Prieto, K. Z. Stanek, and L. M. Macri. A Study of Cepheids in M81 with the Large Binocular Telescope (Efficiently Calibrated with Hubble Space Telescope). *ApJ*, 743:176, December 2011. doi: 10.1088/0004-637X/743/2/176.
- W. Gieren, M. Górski, G. Pietrzyński, P. Konorski, K. Suchomska, D. Graczyk, B. Pilecki, F. Bresolin, R.-P. Kudritzki, J. Storm, P. Karczmarek, A. Gallenne, P. Calderón, and D. Geisler. The Araucaria Project. A Distance Determination to the Local Group Spiral M33 from Near-infrared Photometry of Cepheid Variables. *ApJ*, 773:69, August 2013. doi: 10.1088/0004-637X/773/1/69.

- W. Gieren, J. Storm, P. Konorski, M. Górski, B. Pilecki, I. Thompson, G. Pietrzyński, D. Graczyk, T. G. Barnes, P. Fouqué, N. Nardetto, A. Gallenne, P. Karczmarek, K. Suchomska, P. Wielgórski, and et al. The effect of metallicity on Cepheid period-luminosity relations from a Baade-Wesselink analysis of Cepheids in the Milky Way and Magellanic Clouds*. *A&A*, 620:A99, December 2018. doi: 10.1051/0004-6361/201833263.
- W. P. Gieren, T. J. Moffett, T. G. Barnes, III, J. M. Matthews, and M. L. Frueh. The short-period Cepheid EU Tau. II - Physical properties of the star. *AJ*, 99:1196–1206, April 1990. doi: 10.1086/115408.
- S. D. J. Gwyn. MegaPipe: The MegaCam Image Stacking Pipeline at the Canadian Astronomical Data Centre. *PASP*, 120:212, February 2008. doi: 10.1086/526794.
- J. D. Hartman, D. Bersier, K. Z. Stanek, J.-P. Beaulieu, J. Kaluzny, J.-B. Marquette, P. B. Stetson, and A. Schwarzenberg-Czerny. Deep Canada-France-Hawaii Telescope photometric survey of the entire M33 galaxy - I. Catalogue of 36000 variable point sources. *MNRAS*, 371:1405–1417, September 2006. doi: 10.1111/j.1365-2966.2006.10764.x.
- E. Hertzsprung. Über die räumliche Verteilung der Veränderlichen vom δ Cephei-Typus. *Astronomische Nachrichten*, 196:201, November 1913.
- S. L. Hoffmann and L. M. Macri. Cepheid Variables in the Maser-host Galaxy NGC 4258. *AJ*, 149:183, June 2015. doi: 10.1088/0004-6256/149/6/183.
- M. Hoskin. Goodricke, Pigott and the Quest for Variable Stars. *Journal for the History of Astronomy*, 10:23, 1979.
- E. P. Hubble. Cepheids in Spiral Nebulae. *Popular Astronomy*, 33, 1925.
- L. Jiang, X. Fan, F. Bian, I. D. McGreer, M. A. Strauss, J. Annis, Z. Buck, R. Green, J. A. Hodge, A. D. Myers, A. Rafiee, and G. Richards. The Sloan Digital Sky Survey Stripe 82 Imaging Data: Depth-optimized Co-adds over 300 deg² in Five Filters. *The Astrophysical Journal Supplement Series*, 213:12, July 2014. doi: 10.1088/0067-0049/213/1/12.

- P. Kervella, D. Bersier, D. Mourard, N. Nardetto, P. Fouqué, and V. Coudé du Foresto. Cepheid distances from infrared long-baseline interferometry. III. Calibration of the surface brightness-color relations. *A&A*, 428:587–593, December 2004a. doi: 10.1051/0004-6361:20041416.
- P. Kervella, N. Nardetto, D. Bersier, D. Mourard, and V. Coudé du Foresto. Cepheid distances from infrared long-baseline interferometry. I. VINCI/VLTI observations of seven Galactic Cepheids. *A&A*, 416:941–953, March 2004b. doi: 10.1051/0004-6361:20031743.
- P. Kervella, B. Trahin, H. E. Bond, A. Gallenne, L. Szabados, A. Mérand, J. Breitterfelder, J. Dailloux, R. I. Anderson, P. Fouqué, W. Gieren, N. Nardetto, and G. Pietrzyński. Observational calibration of the projection factor of Cepheids. III. The long-period Galactic Cepheid RS Puppis. *A&A*, 600:A127, April 2017. doi: 10.1051/0004-6361/201630202.
- P. Kervella, A. Mérand, A. Gallenne, B. Trahin, S. Borgniet, G. Pietrzynski, N. Nardetto, and W. Gieren. Optical interferometry and Gaia parallaxes for a robust calibration of the Cepheid distance scale. In A. Recio-Blanco, P. de Laverny, A. G. A. Brown, and T. Prusti, editors, *IAU Symposium*, volume 330 of *IAU Symposium*, pages 305–308, April 2018. doi: 10.1017/S1743921317006792.
- P. Kervella, A. Gallenne, N. Remage Evans, L. Szabados, F. Arenou, A. Mérand, Y. Proto, P. Karczmarek, N. Nardetto, W. Gieren, and G. Pietrzynski. Multiplicity of Galactic Cepheids and RR Lyrae stars from Gaia DR2. I. Binarity from proper motion anomaly. *A&A*, 623:A116, Mar 2019. doi: 10.1051/0004-6361/201834210.
- M. Kim, E. Kim, M. G. Lee, A. Sarajedini, and D. Geisler. Determination of the Distance to M33 Based on the Tip of the Red Giant Branch and the Red Clump. *AJ*, 123:244–254, January 2002. doi: 10.1086/324639.
- P. Klagyivik and L. Szabados. Observational studies of Cepheid amplitudes. I. Period-amplitude relationships for Galactic Cepheids and interrelation of amplitudes. *A&A*, 504:959–972, September 2009. doi: 10.1051/0004-6361/200811464.

- M. Kodric, A. Riffeser, S. Seitz, J. Snigula, U. Hopp, C.-H. Lee, C. Goessl, J. Koppenhoefer, R. Bender, and W. Gieren. The M31 Near-infrared Period-Luminosity Relation and its Non-linearity for δ Cep Variables with $0.5 \leq \log(P) \leq 1.7$. *ApJ*, 799(2):144, February 2015. doi: 10.1088/0004-637X/799/2/144.
- M. Kodric, A. Riffeser, S. Seitz, U. Hopp, J. Snigula, C. Goessl, J. Koppenhoefer, and R. Bender. M31 PAndromeda Cepheid Sample Observed in Four HST Bands. *ApJ*, 864:59, September 2018. doi: 10.3847/1538-4357/aad4a1.
- M. König and S. Binnewies. *The Cambridge Photographic Atlas of Galaxies*. Cambridge University Press, Cambridge, Cambridgeshire, United Kingdom, 1st edition, 2017. ISBN 9781316995303.
- R.-P. Kudritzki and M. A. Urbaneja. Distances to galaxies from the brightest stars in the universe. *Astrophysics and Space Science*, 341(1):131–142, Sep 2012. ISSN 1572-946X. doi: 10.1007/s10509-012-1016-7.
- R.-P. Kudritzki, M. A. Urbaneja, F. Bresolin, Jr. Hosek, M. W., and N. Przybilla. Stellar Metallicity of the Extended Disk and Distance of the Spiral Galaxy NGC 3621. *ApJ*, 788(1):56, June 2014. doi: 10.1088/0004-637X/788/1/56.
- H. S. Leavitt. 1777 variables in the Magellanic Clouds. *Annals of Harvard College Observatory*, 60:87–108.3, 1908.
- H. S. Leavitt and E. C. Pickering. Periods of 25 Variable Stars in the Small Magellanic Cloud. *Harvard College Observatory Circular*, 173:1–3, March 1912.
- C.-H. Lee, M. Kodric, S. Seitz, A. Riffeser, J. Koppenhoefer, R. Bender, U. Hopp, C. Gössl, J. Snigula, W. S. Burgett, K. C. Chambers, H. Flewelling, K. W. Hodapp, N. Kaiser, R.-P. Kudritzki, P. A. Price, J. L. Tonry, and R. J. Wainscoat. Properties of M31. III. Candidate Beat Cepheids from PS1 PAndromeda Data and Their Implication on Metallicity Gradient. *ApJ*, 777:35, November 2013. doi: 10.1088/0004-637X/777/1/35.

- M. G. Lee, W. L. Freedman, and B. F. Madore. The Tip of the Red Giant Branch as a Distance Indicator for Resolved Galaxies. *ApJ*, 417:553, November 1993. doi: 10.1086/173334.
- M. G. Lee, M. Kim, A. Sarajedini, D. Geisler, and W. Gieren. Determination of the Distance to M33 Based on Single-Epoch I-Band Hubble Space Telescope Observations of Cepheids. *ApJ*, 565:959–965, February 2002. doi: 10.1086/324719.
- Z. Lin, N. Hu, X. Kong, Y. Gao, H. Zou, E. Wang, F. Cheng, G. Fang, L. Lin, and J. Wang. Spectroscopic Observation and Analysis of H II Regions in M33 with MMT: Temperatures and Oxygen Abundances. *ApJ*, 842:97, June 2017. doi: 10.3847/1538-4357/aa6f14.
- T. E. Lutz and D. H. Kelker. On the Use of Trigonometric Parallaxes for the Calibration of Luminosity Systems: Theory. *PASP*, 85(507):573, Oct 1973. doi: 10.1086/129506.
- X. Ma, P. F. Hopkins, C.-A. Faucher-Giguère, N. Zolman, A. L. Muratov, D. Kereš, and E. Quataert. The origin and evolution of the galaxy mass-metallicity relation. *MNRAS*, 456:2140–2156, February 2016. doi: 10.1093/mnras/stv2659.
- W. J. Maciel, R. D. D. Costa, and M. M. M. Uchida. An estimate of the time variation of the O/H radial gradient from planetary nebulae. *A&A*, 397:667–674, January 2003. doi: 10.1051/0004-6361:20021530.
- L. M. Macri, K. Z. Stanek, D. Bersier, L. J. Greenhill, and M. J. Reid. A New Cepheid Distance to the Maser-Host Galaxy NGC 4258 and Its Implications for the Hubble Constant. *ApJ*, 652:1133–1149, December 2006. doi: 10.1086/508530.
- B. F. Madore. The period-luminosity relation. IV - Intrinsic relations and reddenings for the Large Magellanic Cloud Cepheids. *ApJ*, 253:575–579, February 1982. doi: 10.1086/159659.
- B. F. Madore and W. L. Freedman. The Cepheid distance scale. *PASP*, 103:933–957, September 1991. doi: 10.1086/132911.

- V. A. Mager, B. F. Madore, and W. L. Freedman. The Metallicity Dependence of the Cepheid P - L Relation in M101. *ApJ*, 777:79, November 2013. doi: 10.1088/0004-637X/777/1/79.
- L. Magrini, J. M. Vílchez, A. Mampaso, R. L. M. Corradi, and P. Leisy. The metallicity gradient of M 33: chemical abundances of H ii regions. *A&A*, 470:865–874, August 2007. doi: 10.1051/0004-6361:20077445.
- L. Magrini, L. Stanghellini, and E. Villaver. The Planetary Nebula Population of M33 and its Metallicity Gradient: A Look Into the Galaxy’s Distant Past. *ApJ*, 696:729–740, May 2009. doi: 10.1088/0004-637X/696/1/729.
- L. Magrini, L. Stanghellini, E. Corbelli, D. Galli, and E. Villaver. Metal production in M 33: space and time variations. *A&A*, 512:A63, March 2010. doi: 10.1051/0004-6361/200913564.
- L. Magrini, L. Coccato, L. Stanghellini, V. Casasola, and D. Galli. Metallicity gradients in local Universe galaxies: Time evolution and effects of radial migration. *A&A*, 588:A91, April 2016. doi: 10.1051/0004-6361/201527799.
- D. Majaess, D. Turner, and W. Gieren. Concerning the Classical Cepheid VI_C Wesenheit Function’s Strong Metallicity Dependence. *ApJL*, 741:L36, November 2011. doi: 10.1088/2041-8205/741/2/L36.
- M. Marconi, I. Musella, and G. Fiorentino. Cepheid Pulsation Models at Varying Metallicity and $\Delta Y/\Delta Z$. *ApJ*, 632:590–610, October 2005. doi: 10.1086/432790.
- M. Marconi, I. Musella, G. Fiorentino, G. Clementini, A. Aloisi, F. Annibali, R. Contreras Ramos, A. Saha, M. Tosi, and R. P. van der Marel. Pulsation Models for Ultra-low ($Z = 0.0004$) Metallicity Classical Cepheids. *ApJ*, 713:615–625, April 2010. doi: 10.1088/0004-637X/713/1/615.
- P. Massey, T. E. Armandroff, R. Pyke, K. Patel, and C. D. Wilson. Hot, Luminous Stars in Selected Regions of NGC 6822, M31, and M33. *AJ*, 110:2715, December 1995. doi: 10.1086/117725.

- P. Massey, K. A. G. Olsen, P. W. Hodge, G. H. Jacoby, R. T. McNeill, R. C. Smith, and S. B. Strong. A Survey of Local Group Galaxies Currently Forming Stars. II. UBVRI Photometry of Stars in Seven Dwarfs and a Comparison of the Entire Sample. *AJ*, 133:2393–2417, May 2007. doi: 10.1086/513319.
- M. L. Mateo. Dwarf Galaxies of the Local Group. *ARA&A*, 36:435–506, 1998. doi: 10.1146/annurev.astro.36.1.435.
- A. W. McConnachie, M. J. Irwin, A. M. N. Ferguson, R. A. Ibata, G. F. Lewis, and N. Tanvir. Determining the location of the tip of the red giant branch in old stellar populations: M33, Andromeda I and II. *MNRAS*, 350:243–252, May 2004. doi: 10.1111/j.1365-2966.2004.07637.x.
- C. L. Miller, H. R. Neilson, N. Remage Evans, S. G. Engle, and E. Guinan. Rotation, convective core overshooting, and period changes in classical Cepheid stellar evolution models. *ArXiv e-prints*, May 2018.
- M. I. Monteverde, A. Herrero, D. J. Lennon, and R.-P. Kudritzki. The Stellar Oxygen Abundance Gradient in M33. *ApJL*, 474:L107–L110, January 1997. doi: 10.1086/310441.
- T. Muraveva, H. E. Delgado, G. Clementini, L. M. Sarro, and A. Garofalo. RR Lyrae stars as standard candles in the Gaia Data Release 2 Era. *MNRAS*, 481:1195–1211, November 2018. doi: 10.1093/mnras/sty2241.
- P. Murdin, editor. *Encyclopedia of Astronomy & Astrophysics*. Nature Publishing Group and Institute of Physics Publishing Co, New York and London, 2001. ISBN 9780750304405.
- N. Nardetto, E. Poretti, M. Rainer, A. Fokin, P. Mathias, R. I. Anderson, A. Gallenne, W. Gieren, D. Graczyk, P. Kervella, A. Mérand, D. Mourard, H. Neilson, G. Pietrzynski, B. Pilecki, and J. Storm. HARPS-N high spectral resolution observations of Cepheids I. The Baade-Wesselink projection factor of δ Cep revisited. *A&A*, 597:A73, January 2017. doi: 10.1051/0004-6361/201629400.

- H. R. Neilson, M. Cantiello, and N. Langer. The Cepheid mass discrepancy and pulsation-driven mass loss. *A&A*, 529:L9, May 2011. doi: 10.1051/0004-6361/201116920.
- C. Ngeow and S. M. Kanbur. Nonlinear Period-Luminosity Relation for the Large Magellanic Cloud Cepheids: Myths and Truths. *ApJ*, 650:180–188, October 2006. doi: 10.1086/507419.
- C. Ngeow and S. M. Kanbur. Semiempirical Cepheid Period-Luminosity Relations in Sloan Magnitudes. *ApJ*, 667:35–37, September 2007. doi: 10.1086/520802.
- C.-C. Ngeow, S. M. Kanbur, S. Nikolaev, J. Buonaccorsi, K. H. Cook, and D. L. Welch. Further empirical evidence for the non-linearity of the period-luminosity relations as seen in the Large Magellanic Cloud Cepheids. *MNRAS*, 363(3):831–846, Nov 2005. doi: 10.1111/j.1365-2966.2005.09477.x.
- C.-C. Ngeow, W. Gieren, and C. Klein. Distance determination from the Cepheid and RR Lyrae period-luminosity relations. In J. A. Guzik, W. J. Chaplin, G. Handler, and A. Pigulski, editors, *Precision Asteroseismology*, volume 301 of *IAU Symposium*, pages 123–128, February 2014. doi: 10.1017/S1743921313014208.
- P. Th. Oosterhoff. U Trianguli Australis, a classical Cepheid with secondary period. *Bulletin of the Astronomical Institutes of the Netherlands*, 13:317, Oct 1957.
- D. E. Osterbrock. Walter Baade, observational astrophysicist, (3): Palomar and Göttingen 1948 - 1960 (Part B). *Journal for the History of Astronomy*, 29:345–377, November 1998.
- A. Pellerin and L. M. Macri. The M 33 Synoptic Stellar Survey. I. Cepheid Variables. *ApJL*, 193:26, April 2011. doi: 10.1088/0067-0049/193/2/26.
- J. O. Petersen. Masses of double mode cepheid variables determined by analysis of period ratios. *A&A*, 27:89, Aug 1973.
- M. M. Phillips. The absolute magnitudes of Type IA supernovae. *ApJL*, 413:L105–L108, August 1993. doi: 10.1086/186970.

- M. J. Pierce, J. S. Jurcevic, and D. Crabtree. Period-luminosity relations for red supergiant variables - I. The calibration. *MNRAS*, 313:271–280, April 2000. doi: 10.1046/j.1365-8711.2000.03196.x.
- G. Pietrzyński, W. Gieren, A. Udalski, I. Soszyński, F. Bresolin, R.-P. Kudritzki, A. Garcia, D. Minniti, R. Mennickent, O. Szewczyk, M. Ł Szymański, M. Kubiak, and L. Wyrzykowski. The Araucaria Project: The Distance to the Local Group Galaxy WLM from Cepheid Variables Discovered in a Wide-Field Imaging Survey. *AJ*, 134(2):594–603, August 2007. doi: 10.1086/518599.
- B. Ł Pilecki, W. Gieren, G. Pietrzyński, I. B. Thompson, R. Ław Smolec, D. Graczyk, M. Taormina, A. Udalski, J. Storm, N. Nardetto, A. Gallenne, P. Kervella, I. Soszyński, M. Górski, P. Wielgórski, K. Suchomska, P. Karczmarek, and B. Zgirski. The Araucaria Project: High-precision Cepheid Astrophysics from the Analysis of Variables in Double-lined Eclipsing Binaries. *ApJ*, 862(1):43, Jul 2018. doi: 10.3847/1538-4357/aacb32.
- Planck Collaboration:, N. Aghanim, M. Ashdown, J. Aumont, C. Baccigalupi, M. Ballardini, A. J. Banday, R. B. Barreiro, N. Bartolo, S. Basak, R. Battye, K. Benabed, J.-P. Bernard, M. Bersanelli, and et al. Planck intermediate results. XLVI. Reduction of large-scale systematic effects in HFI polarization maps and estimation of the reionization optical depth. *A&A*, 596:A107, December 2016. doi: 10.1051/0004-6361/201628890.
- Planck Collaboration:, N. Aghanim, Y. Akrami, M. Ashdown, J. Aumont, C. Baccigalupi, M. Ballardini, A. J. Banday, R. B. Barreiro, N. Bartolo, S. Basak, R. Battye, K. Benabed, J.-P. Bernard, and et al. Planck 2018 results. VI. Cosmological parameters. *ArXiv e-prints*, July 2018.
- R. Poleski. Period Changes of LMC Cepheids in the OGLE and MACHO Data. *Acta Astronomica*, 58:313, December 2008.
- A. A. Ponomareva, M. A. W. Verheijen, R. F. Peletier, and A. Bosma. The multiwave-

- length Tully-Fisher relation with spatially resolved H I kinematics. *MNRAS*, 469: 2387–2400, August 2017. doi: 10.1093/mnras/stx1018.
- A. G. Riess, L. M. Macri, S. L. Hoffmann, D. Scolnic, S. Casertano, A. V. Filippenko, B. E. Tucker, M. J. Reid, D. O. Jones, J. M. Silverman, R. Chornock, P. Challis, W. Yuan, P. J. Brown, and R. J. Foley. A 2.4% Determination of the Local Value of the Hubble Constant. *ApJ*, 826:56, July 2016. doi: 10.3847/0004-637X/826/1/56.
- A. G. Riess, S. Casertano, W. Yuan, L. Macri, B. Bucciarelli, M. G. Lattanzi, J. W. MacKenty, J. B. Bowers, W. Zheng, A. V. Filippenko, C. Huang, and R. I. Anderson. Milky Way Cepheid Standards for Measuring Cosmic Distances and Application to Gaia DR2: Implications for the Hubble Constant. *ApJ*, 861:126, July 2018. doi: 10.3847/1538-4357/aac82e.
- V. Ripepi, R. Molinaro, I. Musella, M. Marconi, S. Leccia, and L. Eyer. A re-classification of Cepheids in the Gaia Data Release 2. *ArXiv e-prints*, October 2018.
- A. Ritter. Untersuchungen über die Höhe der Atmosphäre und die Constitution gasförmiger Weltkörper. *Annalen der Physik*, 241:543–558, 1878. doi: 10.1002/andp.18782411207.
- M. Romaniello, F. Primas, M. Mottini, S. Pedicelli, B. Lemasle, G. Bono, P. François, M. A. T. Groenewegen, and C. D. Laney. The influence of chemical composition on the properties of Cepheid stars. II. The iron content. *A&A*, 488:731–747, September 2008. doi: 10.1051/0004-6361:20065661.
- P. Rosenfield, L. Girardi, B. F. Williams, L. C. Johnson, A. Dolphin, A. Bressan, D. Weisz, J. J. Dalcanton, M. Fouesneau, and J. Kalirai. A New Approach to Convective Core Overshooting: Probabilistic Constraints from Color-Magnitude Diagrams of LMC Clusters. *ApJ*, 841:69, June 2017. doi: 10.3847/1538-4357/aa70a2.
- E. Rosolowsky and J. D. Simon. The M33 Metallicity Project: Resolving the Abundance Gradient Discrepancies in M33. *ApJ*, 675:1213–1222, March 2008. doi: 10.1086/527407.

- S. Sakai, L. Ferrarese, R. C. Kennicutt, Jr., and A. Saha. The Effect of Metallicity on Cepheid-based Distances. *ApJ*, 608:42–61, June 2004. doi: 10.1086/386540.
- M. Salaris and S. Cassisi. *Evolution of Stars and Stellar Populations*. John Wiley & Sons Ltd, Hoboken, New Jersey, United States, 1st edition, 2005. ISBN 9780470033456.
- M. Salaris and L. Girardi. Tip of the Red Giant Branch distances to galaxies with composite stellar populations. *MNRAS*, 357:669–678, February 2005. doi: 10.1111/j.1365-2966.2005.08689.x.
- A. Sarajedini, D. Geisler, R. Schommer, and P. Harding. Hubble Space Telescope WFPC2 Photometry of M33: Properties of the Halo Star Clusters and Surrounding Fields. *AJ*, 120:2437–2459, November 2000. doi: 10.1086/316807.
- A. Sarajedini, M. K. Barker, D. Geisler, P. Harding, and R. Schommer. RR Lyrae Variables in M33. I. Evidence for a Field Halo Population. *AJ*, 132:1361–1371, September 2006. doi: 10.1086/506152.
- D. D. Sasselov, J. P. Beaulieu, C. Renault, P. Grison, R. Ferlet, A. Vidal-Madjar, E. Maurice, L. Prevot, E. Aubourg, P. Bareyre, S. Brehin, C. Coutures, N. Delabrouille, J. de Kat, M. Gros, B. Laurent, and et al. Metallicity effects on the Cepheid extragalactic distance scale from EROS photometry in the Large Magellanic Cloud and the Small Magellanic Cloud. *A&A*, 324:471–482, August 1997.
- V. Scowcroft, D. Bersier, J. R. Mould, and P. R. Wood. The effect of metallicity on Cepheid magnitudes and the distance to M33. *MNRAS*, 396:1287–1296, July 2009. doi: 10.1111/j.1365-2966.2009.14822.x.
- P. Senchyna, L. C. Johnson, J. J. Dalcanton, L. C. Beerman, M. Fouesneau, A. Dolphin, B. F. Williams, P. Rosenfield, and S. S. Larsen. Panchromatic Hubble Andromeda Treasury. XIV. The Period-Age Relationship of Cepheid Variables in M31 Star Clusters. *ApJ*, 813:31, November 2015. doi: 10.1088/0004-637X/813/1/31.
- H. Shapley. On the Nature and Cause of Cepheid Variation. *ApJ*, 40:448, December 1914. doi: 10.1086/142137.

- B. J. Shappee and K. Z. Stanek. A New Cepheid Distance to the Giant Spiral M101 Based on Image Subtraction of Hubble Space Telescope/Advanced Camera for Surveys Observations. *ApJ*, 733:124, June 2011. doi: 10.1088/0004-637X/733/2/124.
- N. R. Simon and E. G. Schmidt. Evidence Favoring Nonevolutionary Cepheid Masses. *ApJ*, 205:162–164, April 1976. doi: 10.1086/154259.
- D. M. Skowron, I. Soszyński, A. Udalski, M. K. Szymański, P. Pietrukowicz, J. Skowron, R. Poleski, Ł. Wyrzykowski, K. Ulaczyk, S. Kozłowski, P. Mróz, and M. Pawlak. OGLE-ing the Magellanic System: Photometric Metallicity from Fundamental Mode RR Lyrae Stars. *Acta Astronomica*, 66:269–292, September 2016.
- R. Smolec. Unstable standard candles. Periodic light-curve modulation in fundamental mode classical Cepheids. *MNRAS*, 468:4299–4310, July 2017. doi: 10.1093/mnras/stx679.
- J. G. Sorce, H. M. Courtois, R. B. Tully, M. Seibert, V. Scowcroft, W. L. Freedman, B. F. Madore, S. E. Persson, A. Monson, and J. Rigby. Calibration of the Mid-infrared Tully-Fisher Relation. *ApJ*, 765:94, March 2013. doi: 10.1088/0004-637X/765/2/94.
- I. Soszynski, R. Poleski, A. Udalski, M. K. Szymanski, M. Kubiak, G. Pietrzynski, L. Wyrzykowski, O. Szewczyk, and K. Ulaczyk. The Optical Gravitational Lensing Experiment. The OGLE-III Catalog of Variable Stars. I. Classical Cepheids in the Large Magellanic Cloud. *Acta Astronomica*, 58:163–185, September 2008.
- I. Soszyński, R. Poleski, A. Udalski, M. K. Szymański, M. Kubiak, G. Pietrzyński, Ł. Wyrzykowski, O. Szewczyk, and K. Ulaczyk. The Optical Gravitational Lensing Experiment. The OGLE-III Catalog of Variable Stars. VII. Classical Cepheids in the Small Magellanic Cloud. *Acta Astronomica*, 60(1):17–39, Mar 2010.
- I. Soszyński, A. Udalski, M. K. Szymański, D. Skowron, G. Pietrzyński, R. Poleski, P. Pietrukowicz, J. Skowron, P. Mróz, S. Kozłowski, Ł. Wyrzykowski, K. Ulaczyk, and M. Pawlak. The OGLE Collection of Variable Stars. Classical Cepheids in the Magellanic System. *Acta Astronomica*, 65:297–312, December 2015.

- I. Soszyński, A. Udalski, M. K. Szymański, Ł. Wyrzykowski, K. Ulaczyk, R. Poleski, P. Pietrukowicz, S. Kozłowski, D. M. Skowron, J. Skowron, P. Mróz, M. Pawlak, K. Rybicki, and A. Jacyszyn-Dobrzyniecka. The OGLE Collection of Variable Stars. Classical, Type II, and Anomalous Cepheids toward the Galactic Center. *Acta Astronomica*, 67:297–316, December 2017.
- P. B. Stetson. DAOPHOT - A computer program for crowded-field stellar photometry. *PASP*, 99:191–222, March 1987. doi: 10.1086/131977.
- P. B. Stetson. The center of the core-cusp globular cluster M15: CFHT and HST Observations, ALLFRAME reductions. *PASP*, 106:250–280, March 1994. doi: 10.1086/133378.
- J. Storm, W. Gieren, P. Fouqué, T. G. Barnes, I. Soszyński, G. Pietrzyński, N. Nardetto, and D. Quetz. Calibrating the Cepheid period-luminosity relation from the infrared surface brightness technique. II. The effect of metallicity and the distance to the LMC. *A&A*, 534:A95, October 2011. doi: 10.1051/0004-6361/201117154.
- L. Szabados. Database on Binaries among Galactic Classical Cepheids. *Information Bulletin on Variable Stars*, 5394:1, Mar 2003.
- L. Szabados and P. Klagyivik. Observational studies of Cepheid amplitudes. II. Metallicity dependence of pulsation amplitudes. *A&A*, 537:A81, January 2012. doi: 10.1051/0004-6361/201117815.
- R. Szabó, J. R. Buchler, and J. Bartee. The Cepheid Phase Lag Revisited. *ApJ*, 667: 1150–1160, October 2007. doi: 10.1086/520917.
- G. A. Tammann, A. Sandage, and B. Reindl. New Period-Luminosity and Period-Color relations of classical Cepheids: I. Cepheids in the Galaxy. *A&A*, 404:423–448, June 2003. doi: 10.1051/0004-6361:20030354.
- M. B. Taylor. TOPCAT & STIL: Starlink Table/VOTable Processing Software. In P. Shopbell, M. Britton, and R. Ebert, editors, *Astronomical Data Analysis Software and Systems XIV*, volume 347 of *Astronomical Society of the Pacific Conference Series*, page 29, December 2005.

- G. P. Tiede, A. Sarajedini, and M. K. Barker. The Stellar Populations in the Outer Regions of M33. I. Metallicity Distribution Function. *AJ*, 128:224–236, July 2004. doi: 10.1086/421369.
- L. Toribio San Cipriano, G. Domínguez-Guzmán, C. Esteban, J. García-Rojas, A. Mesa-Delgado, F. Bresolin, M. Rodríguez, and S. Simón-Díaz. Carbon and oxygen in H II regions of the Magellanic Clouds: abundance discrepancy and chemical evolution. *MNRAS*, 467:3759–3774, May 2017. doi: 10.1093/mnras/stx328.
- R. B. Tully and J. R. Fisher. A new method of determining distances to galaxies. *A&A*, 54:661–673, February 1977.
- V. U, M. A. Urbaneja, R.-P. Kudritzki, B. A. Jacobs, F. Bresolin, and N. Przybilla. A New Distance to M33 Using Blue Supergiants and the FGLR Method. *ApJ*, 704: 1120–1134, October 2009. doi: 10.1088/0004-637X/704/2/1120.
- A. Udalski, I. Soszynski, M. Szymanski, M. Kubiak, G. Pietrzynski, P. Wozniak, and K. Zebrun. The Optical Gravitational Lensing Experiment. Cepheids in the Magellanic Clouds. I. Double-Mode Cepheids in the Small Magellanic Cloud. *Acta Astronomica*, 49:1–44, Mar 1999.
- M. A. Urbaneja, A. Herrero, R.-P. Kudritzki, F. Najarro, S. J. Smartt, J. Puls, D. J. Lennon, and L. J. Corral. Blue Luminous Stars in Nearby Galaxies: Quantitative Spectral Analysis of M33 B-Type Supergiant Stars. *ApJ*, 635:311–335, December 2005. doi: 10.1086/497528.
- M. A. Urbaneja, R.-P. Kudritzki, W. Gieren, G. Pietrzyński, F. Bresolin, and N. Przybilla. LMC Blue Supergiant Stars and the Calibration of the Flux-weighted Gravity-Luminosity Relationship. *AJ*, 154:102, September 2017. doi: 10.3847/1538-3881/aa79a8.
- R. P. van der Marel, M. Fardal, G. Besla, R. L. Beaton, S. T. Sohn, J. Anderson, T. Brown, and P. Guhathakurta. The M31 Velocity Vector. II. Radial Orbit toward the Milky Way and Implied Local Group Mass. *ApJ*, 753:8, July 2012. doi: 10.1088/0004-637X/753/1/8.

- K. Viironen, G. Delgado-Inglada, A. Mampaso, L. Magrini, and R. L. M. Corradi. The S2N2 metallicity calibrator and the abundance gradient of M33. *MNRAS*, 381: 1719–1726, November 2007. doi: 10.1111/j.1365-2966.2007.12357.x.
- R. Wagner-Kaiser, A. Sarajedini, J. J. Dalcanton, B. F. Williams, and A. Dolphin. Panchromatic Hubble Andromeda Treasury XIII: The Cepheid period-luminosity relation in M31. *MNRAS*, 451:724–738, July 2015. doi: 10.1093/mnras/stv880.
- M. Wenger, F. Ochsenbein, D. Egret, P. Dubois, F. Bonnarel, S. Borde, F. Genova, G. Jasniewicz, S. Laloë, S. Lesteven, and R. Monier. The SIMBAD astronomical database. The CDS reference database for astronomical objects. *A&AS*, 143:9–22, April 2000. doi: 10.1051/aas:2000332.
- A. J. Wesselink. The observations of brightness, colour and radial velocity of δ Cephei and the pulsation hypothesis (Errata: 10 258, 310). *Bulletin of the Astronomical Institutes of the Netherlands*, 10:91, January 1946.
- P. Wielgórski, G. Pietrzyński, W. Gieren, M. Górski, R.-P. Kudritzki, B. Zgirski, F. Bresolin, J. Storm, N. Matsunaga, D. Graczyk, and I. Soszyński. A Precision Determination of the Effect of Metallicity on Cepheid Absolute Magnitudes in VI-JHK Bands from Magellanic Cloud Cepheids. *ApJ*, 842:116, June 2017. doi: 10.3847/1538-4357/aa7565.
- J. A. Willick and P. Batra. A Determination of the Hubble Constant from Cepheid Distances and a Model of the Local Peculiar Velocity Field. *ApJ*, 548:564–584, February 2001. doi: 10.1086/319005.
- S. P. Willner and K. Nelson-Patel. Neon Abundances in the H II Regions of M33. *ApJ*, 568:679–688, April 2002. doi: 10.1086/339032.
- S.-C. Yang, A. Sarajedini, J. A. Holtzman, and D. R. Garnett. RR Lyrae Variables in M33. II. Oosterhoff Properties and Radial Trends. *ApJ*, 724:799–817, November 2010. doi: 10.1088/0004-637X/724/1/799.

- W. Yuan, L. M. Macri, A. Javadi, Z. Lin, and J. Z. Huang. Near-infrared Mira Period-Luminosity Relations in M33. *AJ*, 156:112, September 2018. doi: 10.3847/1538-3881/aad330.
- M. V. Zabolotskikh, M. E. Sachkov, L. N. Berdnikov, A. S. Rastorguev, and I. E. Egorov. The Classification of Cepheids by Pulsation Modes and the Problem of the Distance scale. In C. Turon, K. S. O’Flaherty, and M. A. C. Perryman, editors, *The Three-Dimensional Universe with Gaia*, volume 576 of *ESA Special Publication*, page 723, January 2005.
- D. Zaritsky, R. C. Kennicutt, Jr., and J. P. Huchra. H II regions and the abundance properties of spiral galaxies. *ApJ*, 420:87–109, January 1994. doi: 10.1086/173544.